

*INVESTIGATION OF TRANSIENT AND
SAFETY ISSUES IN GAS INSULATED
SYSTEMS*

Jonathan James

Advanced High Voltage Engineering Research Centre

School of Engineering

Cardiff University / Prifysgol Caerdydd



**This thesis is being submitted in partial fulfilment of the requirements for the
degree of Doctor of Philosophy**

March 2022

SUMMARY

This thesis investigates the occurrence, characteristics and effects of Very Fast Transients (VFTs) associated with disconnecter switching operations in Gas Insulated Substations. VFTs are analysed and efforts are made to elucidate their behaviour through advanced simulation techniques.

The initial motivation for this work was the occurrence of a surface flashover at a spacer, leading to a prolonged outage of the circuit in question and a significant repair effort. While post failure investigations were carried out by the manufacturer and yielded no significant observations, through modelling and measurements efforts while working towards this thesis, a phenomenon that could have led or contributed to the failure.

VFTs at a live, operational 400kV Substation (un-named for confidentiality but termed throughout as Substation ‘A’) are quantified through both modelling and measurements. Significant progress in the modelling of VFTs and TEVs is demonstrated. Numerical Electromagnetic Analysis is shown to be most effective method in studying the behaviour of the GIS and earthing systems. Multiple NEA techniques are utilised, all solving a full-Maxwell’s equations through a Wave equation. The behaviour of the system (both internally and externally) is captured with great accuracy and lucidity, without the need to use analytic approximations or assumed parameters, which has traditionally been the case. Detailed models were built using equipment drawings from Substation ‘A’ for the GIB, spacer-flange assembly, double-elbow assembly, disconnecter, gas to air bushing. Frequency and time domain behaviour is analysed and a potential contributor to the failure at Substation ‘A’ is identified. Furthermore, elements of the earthing system were evaluated for effectiveness in mitigating TEVs.

The methods highlight some of flaws and inaccuracies that are present with existing ‘standard practice’ modelling efforts. The need for circuit-based modelling for VFT studies is apparent, as NEA techniques at very high frequencies are limited in their interaction with the wider system. Efforts are therefore made to enhance circuit-based models; utilising NEA methods and Vector Fitting to produce accurate, large bandwidth equivalent circuits, which demonstrate the computed frequency responses of the various

GIS equipment types studied. Vector Fit models at lower orders of approximation are prone to unstable time domain responses, leading to numerical oscillations or even a complete divergence from a solution. A method was developed to identify model orders that demonstrate stability in the time domain, allowing the lowest model order of approximation to be selected, thereby reducing the additional computational requirements of very high orders of approximation, while retaining accuracy and stability in the time and frequency domains. The conversion process is augmented with a new method for identifying model orders that will be stable in the time domain.

Several measurement techniques and sensors were developed to capture the entire cycle of transients associated with disconnecter operations. Device prototypes were designed and optimised through NEA/circuit-based modelling, prior to undergoing laboratory-based measurements. Laboratory based testing was conducted using a custom built, half scale GIB, with impedance matching cones at each end to allow measurement and signal generating equipment to be connected with minimal interference.

While, essential, laboratory-based measurements will never replicate the transient and high EMI environmental conditions seen at a live GIS, therefore, the bulk of the measurement efforts were focused on live measurements at Substation 'A'. Throughout the course of this project several opportunities to undertake measurements were presented and a significant amount of data was recorded. Each measurement also identified areas for improvement of the measurement systems.

ACKNOWLEDGEMENTS

This research was carried out with the Advanced High Voltage Engineering Research Center (AHIVE), Cardiff University.

I would firstly like to state my gratitude and appreciation to Professor A. (Manu) Haddad and Dr Maurizio Albano, for your guidance, knowledge and trust throughout this challenging and stimulating project. I have always felt confident under your supervision and could not have progressed without you.

I would like to give thanks to the all other members of the AHIVE during my time there, including Emeritus Professor Ronald T. Waters, Dr David Clark, Mr Chris Stone, Mrs Kate Osbaldston, Dr Mohammed El Amine, Dr Stephen Robson, Dr Daniel Carr, Dr Salah Mousa, Dr Housseem Nechmi, Dr Alistair Reid, Dr Athanasios Mermigkas and Dr Daniel Mitchard. I was always treated as a fellow researcher, not a student and I am deeply thankful for your support. I would like to give a special mention to my PhD colleague Michail Michelarakis. We shared knowledge, stress and laughs, I know we will remain life-long friends.

Further appreciation goes to the Cardiff University support facility staff with a big mention to Mr Denley Slade and his staff, who always found time to help.

I would also like to thank Network Operator, for the funding, access to live assets and support. I would like to give a special mention Dr Dongsheng Guo, Richard Williams, Steven Welti and Adrian Brown, for the extra support and efforts to assist my research.

Finally, I thank my loving wife Rebecca, daughters Layla and Eva, my parents and step-parents, this achievement would not have been possible without your patience and support.

LIST OF PUBLICATIONS

Conferences

J. James, M. Albano and A. M. Haddad, “Finite Element Modelling of Gas Insulated Bus for Very Fast Transients,” 11th Universities High Voltage Network Colloquium (UHVnet), 2018.

J. James, M. Albano, D. Guo, and A. M. Haddad, “Application of Multiple Modelling Techniques for Analysis of Very Fast Transient Overvoltages in GIS,” *IEEE Dielectr. Electr. Insul. Eng.*, 2018, doi: [10.1109/ICHVE.2018.8642189](https://doi.org/10.1109/ICHVE.2018.8642189).

J. James, M. Albano and A. M. Haddad, “Enhanced Circuit Models for Very Fast Transients in Gas Insulated Substations,” 12th Universities High Voltage Network Colloquium (UHVnet), 2019.

J. James, M. Albano, , D. Guo and A. M. Haddad, “Blackbox Modelling of Gas Insulated Substations for Very Fast Transient Analysis,” 13th Universities High Voltage Network Colloquium (UHVnet), 2020.

Journals

J. James, M. Albano, D. Clark, D. Guo, and A. M. Haddad, “Analysis of Very Fast Transients Using Black Box Macromodels in ATP-EMTP,” doi: [10.3390/en13030698](https://doi.org/10.3390/en13030698).

CONTENTS

1 INTRODUCTION	1
2 A REVIEW OF VERY FAST TRANSIENTS IN GAS INSULATED SYSTEMS; GENERATION, CONSEQUENCES AND MITIGATION	7
2.1 BREAKDOWN IN SF ₆	7
2.2 VERY FAST TRANSIENTS	10
2.2.1 Breakdown mechanisms and VFT generation in a GIS disconnecter	11
2.2.2 Risks of VFTs and TEVs	13
2.2.3 Effects of Trapped charge on Very Fast Transients	14
2.2.4 VFT Waveshape	15
2.2.5 Impact of VFTO	17
2.2.6 Breakdown of SF ₆ during VFTs	18
2.2.7 Effect of VFTs on Spacers	19
2.2.8 Secondary Effects of VFTs	21
2.3 MITIGATION TECHNIQUES	22
2.3.1 Surge arresters	22
2.3.2 Damping resistor	23
2.3.3 Ferrite Rings	24
2.3.4 HF resonator	24
2.4 TRANSIENT ENCLOSURE VOLTAGES AND EARTHING SYSTEM RESPONSE	25
2.4.1 Electromagnetic Coupling at Bushing and spacer-flange	25
2.4.2 Calculation of TEVs	27
2.4.3 Effects of TEV	29
2.4.4 Earthing, Bonding and Shielding	31
2.4.5 Soil characteristics - frequency dependence	32
2.4.6 Earthing system elements	32
2.5 MODELLING CONSIDERATIONS FOR VFTs AND TEVs	35
2.6 EXISTING MEASUREMENT TECHNIQUES FOR VFTs AND TEVs	37
2.6.1 Full voltage measurement	38
2.6.2 TEV Measurement	38
2.6.3 Current Measurement	40
2.6.4 Trapped Charge Measurement	40
2.6.5 Low voltage measurement	41
2.7 CONCLUSION	43

3 NUMERICAL MODELS OF AN OPERATIONAL GAS INSULATED SUBSTATION TO DETERMINE VERY HIGH FREQUENCY BEHAVIOUR	46
3.1 INTRODUCTION	46
3.2 FINITE ELEMENT MODELS FOR THE STUDY OF VERY FAST TRANSIENTS	47
3.2.1 <i>Spacer-flange assembly</i>	50
3.2.2 <i>Elbow</i>	60
3.2.3 <i>Disconnecter</i>	64
3.2.4 <i>Gas to Air Bushing</i>	65
3.3 EXTERNAL TRANSIENTS	72
3.3.1 <i>TEVs – above ground propagation</i>	72
3.3.2 <i>Multiple enclosure propagation</i>	79
3.4 CONCLUSION	83
4 THE RESPONSE OF EARTHING SYSTEMS TO TRANSIENT ENCLOSURE VOLTAGES	85
4.1 INTRODUCTION	85
4.2 MODELLING OF EARTH ELECTRODES FOR VERY HIGH FREQUENCIES	86
4.3 MODELLING THE VERY HIGH FREQUENCY RESPONSE OF EARTHING SYSTEM ELEMENTS	87
4.3.1 <i>High frequency rods</i>	87
4.3.2 <i>Downlead and rod</i>	89
4.3.3 <i>Impact of a downlead-meshed grid</i>	94
4.3.4 <i>Response of GIS model with substation earthing system</i>	96
4.4 SOIL IONISATION FOR VERY HIGH FREQUENCY MODELLING OF EARTHING SYSTEMS	100
4.5 CONCLUSION	101
5 A CIRCUIT BASED MODEL FOR THE STUDY OF VFTS AND TEVS	102
5.1 INTRODUCTION	102
5.2 CIRCUIT MODEL ELEMENTS	104
5.2.1 <i>Gas/Air Bushing</i>	104
5.2.2 <i>Metal Oxide Surge Arresters</i>	104
5.2.3 <i>Disconnecter model</i>	108
5.2.4 <i>Disconnecter – breakdown curves from measurements</i>	113
5.3 EQUIVALENT MODEL GENERATION	116
5.3.1 <i>RLCG equivalent extraction</i>	116
5.3.2 <i>Generation of finite element derived blackbox models for ATP-EMTP</i>	118

5.4 SUBSTATION ‘A’ 400kV GIS EMT MODEL	126
5.4.1 <i>Switching regime</i>	131
5.4.2 <i>Simulated Coupling at MOSA</i>	131
5.4.3 <i>Effect of Bus Capacitance</i>	133
5.5 CONCLUSION	134
6 DEVELOPMENT OF MEASUREMENT SYSTEMS FOR FIELD BASED MEASUREMENTS	137
6.1 INTRODUCTION	137
6.2 CALIBRATION VESSEL	138
6.3 HIGH FREQUENCY CURRENT TRANSFORMERS	140
6.4 ULTRA-HIGH FREQUENCY SENSOR COUPLER UNIT	144
6.4.1 <i>Termination of the UHF sensor</i>	146
6.4.2 <i>Bandwidth test of the UHF sensor coupler unit</i>	148
6.5 DEVELOPMENT OF A D-DOT SENSOR FOR GIB MEASUREMENTS	150
6.6 DEVELOPMENT OF A HIGH BANDWIDTH ANALOGUE FIBRE OPTIC LINK	160
6.7 CONCLUSION	166
7 MEASUREMENTS OF TRANSIENTS GENERATED BY GIS SWITCHING OPERATIONS	168
7.1 INTRODUCTION	168
7.2 HFCT MEASUREMENTS	170
7.3 SURGE COUNTER INCREMENTATION	178
7.4 D-DOT INSTALLATION AND MEASUREMENTS	183
7.5 HIGH FREQUENCY EARTHING MEASUREMENTS	185
7.6 MEASUREMENT OBSERVATIONS	188
7.7 CONCLUSION	191
8 CONCLUSION AND FUTURE WORK	194
8.1 CONCLUSION	194
8.2 FUTURE WORK	198
REFERENCES	200
APPENDICES	212

LIST OF TABLES

TABLE 3.1: BULK MATERIAL PARAMETERS	48
TABLE 3.2: FINITE ELEMENT MODEL PARAMETERS	49
TABLE 5.1: POLE RESIDUE EQUIVALENT MODEL EXTRACTION TERMS.	121
TABLE 5.2: COMPUTED SPACER-FLANGE AND ELBOW MODEL PERFORMANCE FOR RANGE OF TERMINATIONS.	123
TABLE 6.1: CALCULATED MUTUAL CAPACITANCE MATRIX.	145
TABLE 6.2: D-DOT CALCULATED MUTUAL CAPACITANCE MATRIX.	155
TABLE 7.1 21ST OCTOBER 2020 SWITCHING SCHEDULE.	169
TABLE 7.2: 21/10/2020 HFCT MEASURED VALUES – AMPLITUDE AND FREQUENCY CONTENT.	173
TABLE 7.3: 21/10/2020 HFCT MEASURED VALUES – NUMBER OF TRANSIENTS AND DURATION.	175

LIST OF FIGURES

FIGURE 2.1: IONISATION COEFFICIENT GROWTH	8
FIGURE 2.2: PASCHEN'S CURVE SHOWING BREAKDOWN VOLTAGE AS A FUNCTION OF PRESSURE AND DISTANCE	9
FIGURE 2.3: PROBABILITY DENSITY OF TCV BASED ON 1000 MONTE CARLO SIMULATIONS	15
FIGURE 2.4: SOURCE AND LOAD SIDE VOLTAGES DURING OPENING OPERATION	16
FIGURE 2.5: SOURCE AND LOAD SIDE VOLTAGES DURING CLOSING OPERATION	16
FIGURE 2.6: TYPICAL HIGHER FREQUENCY SOURCE AND LOAD SIDE VFTO WAVEFORMS	16
FIGURE 2.7: DOMINANT SOURCE AND LOAD SIDE VFTO WAVEFORMS OVER SEVERAL MICROSECONDS	16
FIGURE 2.8: SOURCE AND LOAD SIDE OSCILLATIONS BETWEEN GIS AND TRANSFORMER	17
FIGURE 2.9: VFT AND LI VOLTAGE-TIME CURVES	20
FIGURE 2.10: INSULATOR AGEING FACTORS	21
FIGURE 2.11: HF RESONATOR DESIGN	24
FIGURE 2.12: BASICS OF COUPLING AT SPACER-FLANGE DISCONTINUITY	27
FIGURE 2.13: BASIC COUPLING MECHANISM AT GAS/AIR BUSHING	28
FIGURE 2.14: SIMPLIFIED EQUIVALENT CIRCUIT REPRESENTING THE THREE TRANSMISSION LINES	29
FIGURE 2.15: ENCLOSURE SHIELDING	31
FIGURE 2.16: ENCLOSURE BONDING ARRANGEMENTS	32
FIGURE 2.17: MEASURED WAVEFORMS	34
FIGURE 2.18: LOCAL FIELD ENHANCEMENT AT GROUNDED PROTRUSION	35
FIGURE 2.19: ARTIFICIAL GENERATION OF VFT IN LABORATORY SET-UP	37
FIGURE 2.20: CVD PORT-HOLE CONSTRUCTION	38
FIGURE 2.21: NEWI PROBE	39

FIGURE 2.22: CALIBRATION OF SPHERICAL FIELD SENSOR	39
FIGURE 2.23: MEASUREMENT OF TEV USING HIGH VOLTAGE PROBES ACROSS INSULATED FLANGES	39
FIGURE 2.24: MEASUREMENT FROM FLANGE TO REFERENCE EARTH	40
FIGURE 2.25: TRAPPED CHARGE MONITORING	41
FIGURE 2.26: USING FIBRE OPTIC CABLE TO FURTHER REDUCE INTERFERENCE	41
FIGURE 2.27: LOW VOLTAGE PRESTRIKE SIMULATION USING DC SUPPLY AND MERCURY RELAY SWITCH	42
FIGURE 2.28: LV TEV PROPAGATION TRACING	42
FIGURE 2.29: TEV WAVEFORM MEASURED AT 27M FROM THE SOURCE	43
FIGURE 2.30: EMTP MODEL VALIDATION	43
FIGURE 3.1: 3D MODEL VIEW OF SUBSTATION 'A' CIRCUIT 1 (BUS SUPPORTS EXCLUDED).	47
FIGURE 3.2: SIDE 2D VIEW OF SUBSTATION 'A' CIRCUIT 1 OUTDOOR GIS/AIS LAYOUT.	48
FIGURE 3.3: SPACER-FLANGE FINITE ELEMENT MODEL.	51
FIGURE 3.4: SPACER-FLANGE COMPUTATION FOR PERFECTLY GROUNDED AND UNGROUNDED BOLTS	52
FIGURE 3.5: SPACER FIELD DISTRIBUTION	54
FIGURE 3.6: SPACER FIELD DISTRIBUTION COLOUR PLOT	54
FIGURE 3.7: COMPUTED BOLT CONDUCTIVITY VS REFLECTION/TRANSMISSION COEFFICIENTS.	55
FIGURE 3.8: ELECTRIC FIELD AT SPACER INTERFACE FOR FLOATING BOLT MODEL	56
FIGURE 3.9: SPACER-FLANGE MODEL FOR TEV COUPLING.	57
FIGURE 3.10: S-PARAMETERS DETAILING TRANSMITTANCE FROM INTERNAL EXCITATION PORT TO EXTERNAL ENCLOSURE 6M AWAY ALONG A PERFECT GROUND.	58
FIGURE 3.11: FORMATION OF ELECTRIC DIPOLE ACROSS THE SPACER-FLANGE, APPEARANCE OF RADIATING FIELDS.	59

FIGURE 3.12: FAR FIELD PLOTS VIEWED ON HORIZONTAL PLANE	59
FIGURE 3.13: 3D REPRESENTATION OF THE DOUBLE ELBOW FOR FINITE ELEMENT ANALYSIS.	60
FIGURE 3.14: S-PARAMETERS OF DOUBLE-ELBOW FOR BONDED AND FLOATING BOLTS ARRANGEMENTS.	61
FIGURE 3.15: DERIVED IMPEDANCE OF DOUBLE-ELBOW MODELS FOR BONDED AND FLOATING BOLTS ARRANGEMENTS.	62
FIGURE 3.16: PEAK E FIELD ALONG SPACER SURFACE VS FREQUENCY	63
FIGURE 3.17: E FIELD ALONG SPACER SURFACE FROM HV CONDUCTOR TO ENCLOSURE (ARC LENGTH)	63
FIGURE 3.18: TRANSIENT DOUBLE ELBOW SIMULATION, INPUT VOLTAGE STEP SHOWING REFLECTIONS.	64
FIGURE 3.19: 3D MODEL OF OPEN DISCONNECTOR AND FREQUENCY RESPONSE	65
FIGURE 3.20: 3D BUSHING MODEL	66
FIGURE 3.21: BUSHING BASE OPTIMISED DOWNLEAD ARRANGEMENT TAPERED MULTIPLE DOWNLEAD TO 4.8M EARTH ROD	68
FIGURE 3.22: BUSHING S-PARAMETERS FOR 1 AND 8 DOWNLEAD ARRANGEMENTS.	69
FIGURE 3.23: INTERNAL PORT TO GIB ENCLOSURE PORT TRANSMISSION COEFFICIENT MAGNITUDE AND PHASE FOR 1 AND 8 DOWNLEAD MODELS.	69
FIGURE 3.24: INPUT IMPEDANCE TO THE BUSHING, TERMINATED 6M WITH THE CHARACTERISTIC IMPEDANCE OF THE AIB.	70
FIGURE 3.25: 1MHZ POWER FLOW VECTOR PLOT FROM 8 DOWNLEAD BUSHING MODEL.	71
FIGURE 3.26: 10MHZ POWER FLOW VECTOR PLOT FROM 8 DOWNLEAD BUSHING MODEL.	71
FIGURE 3.27: GIB PROPAGATION MODES	74
FIGURE 3.28 – PENETRATION DEPTH	76
FIGURE 3.29: COMPUTED WAVELENGTH AND VELOCITY OVER FREQUENCY.	77

FIGURE 3.30: IMPEDANCE CALCULATED USING EMTP LCC ROUTINE AND EIGENMODE ANALYSIS.	78
FIGURE 3.31: OUT OF PLANE (Z - DIRECTION OF PROPAGATION) E FIELD AT 1 AND 20MHZ.	79
FIGURE 3.32: Z COMPONENT CONTOUR WITH X AND Y COMPONENT E FIELD.	79
FIGURE 3.33: SUBSTATION 'A' GIB/AIB COMPLETE MODEL CALCULATED VOLTAGES FOR INTERNAL 6NS STEP VOLTAGE EXCITATION.	81
FIGURE 3.34: FULL-SCALE SUBSTATION 'A' CIRCUIT 1 FINITE ELEMENT MODEL, EXTERNAL FIELD PROPAGATION	82
FIGURE 3.35: SUBSTATION 'A' GIB/AIB COMPLETE MODEL ENCLOSURE MODAL VOLTAGES FOR 1P.U. INTERNAL EXCITATION.	82
FIGURE 3.36: OUTER ENCLOSURE ELECTRIC FIELD STREAMLINES AT 300NS.	83
FIGURE 4.1: SEGMENTATION REQUIRED FOR A 4.8M VERTICAL ROD IN 100ΩM SOIL AT 50MHZ.	87
FIGURE 4.2: HF ROD CDEGS MODEL.	88
FIGURE 4.3: HF ROD IMPEDANCE	89
FIGURE 4.4 – INPUT IMPEDANCE OF 3M DOWNLEAD TO 4.8M ROD FOR UNIFORM SOILS	90
FIGURE 4.5 – VERTICAL DOWNLEAD EXCITATION ELECTRIC FIELD VECTORS	92
FIGURE 4.6 – COMPARISON OF DOWNLEAD-ROD IMPEDANCE CALCULATED USING CDEGS AND COMSOL.	92
FIGURE 4.7 – TAPERED MULTI-DOWNLEAD	94
FIGURE 4.8 – INPUT IMPEDANCE DOWNLEAD TO 5M GRID	95
FIGURE 4.9: DOWNLEAD-GRID IMPEDANCE FOR VARIOUS GRID DIMENSIONS AND DENSITIES.	96
FIGURE 4.10: CDEGS WIREFRAME REPRESENTATION OF GIS ENCLOSURE.	97
FIGURE 4.11: SIMPLIFIED 'COAXIAL CABLE' REPRESENTATION OF GIS ENCLOSURE.	97
FIGURE 4.12: SUBSTATION 'A' HIGH FREQUENCY EARTHING MODEL WITH SIMPLIFIED GIS AT 40MHZ.	98

FIGURE 4.13: IMPEDANCE-FREQUENCY PLOT - VARIOUS GROUNDING CONFIGURATIONS FOR SIMPLIFIED GIS ENCLOSURE MODEL.	99
FIGURE 4.14: SEGMENT GPR MIDBUS VARIOUS GROUNDING CONFIGURATIONS FOR SIMPLIFIED GIS ENCLOSURE MODEL.	99
FIGURE 4.15: ELECTRIC FIELD ABOVE SOIL IONISATION THRESHOLD.	100
FIGURE 5.1: SECTION OF DEVELOPED SUBSTATION 'A' ATP-EMTP RED PHASE GIB MODEL.	103
FIGURE 5.2: SLD DETAILING GENERATION SOURCE TO SUBSTATION 'A' MAIN AND RESERVE BUS.	104
FIGURE 5.3: MOSA – IEEE MODEL WITH DOWNLEAD AND EQUIVALENT ROD TERMINATION OPTIONS	105
FIGURE 5.4: MOSA INSTALLATION AT SUBSTATION 'A'.	106
FIGURE 5.5: MOSA – IEEE MODEL NONLINEAR CHARACTERISTICS	107
FIGURE 5.6: MOSA HF ROD AT SUBSTATION 'A' BLACKBOX MODEL COMPUTED FREQUENCY RESPONSE (A) MAGNITUDE (B) PHASE.	107
FIGURE 5.7: THREE PHASE DISCONNECTOR MODEL – GROUPED.	109
FIGURE 5.8: CUSTOM DISCONNECTOR MODEL PARAMETERISATION.	110
FIGURE 5.9: 3 PHASE (R/Y/B) DISCONNECTOR MODEL – INTERNAL DECOUPLED GROUP.	110
FIGURE 5.10: SCHWAIGER UNIFORMITY CURVES [5].	111
FIGURE 5.11: INHERENT BREAKDOWN STRENGTH (CURVE 2) AND MEASURED BREAKDOWN STRENGTH OF COAXIAL ARRANGEMENT	112
FIGURE 5.12: LINEAR BREAKDOWN VOLTAGE VS GAP DISTANCE FOR A RANGE OF FIELD UNIFORMITIES.	112
FIGURE 5.13: STEPWISE BREAKDOWN PATTERN GENERATED USING CUSTOM DISCONNECTOR MODEL.	113
FIGURE 5.14: NORMALISED PEAKS – DS2 CLOSE 4 21/10/20.	114
FIGURE 5.15: EXAMPLE OF MEASURED (ORIGINAL-NORMALISED) WAVEFORMS WITH FITTED BREAKDOWN CURVES – DS CLOSE OPERATION.	115

FIGURE 5.16: TRANSIENT INITIATING PHASE IDENTIFICATION AND GENERATION OF LINEAR APPROXIMATION BREAKDOWN CURVE.	116
FIGURE 5.17: EXTRACTED CIRCUIT PARAMETERS.	118
FIGURE 5.18: IDENTIFICATION OF STABLE MODEL ORDER.	120
FIGURE 5.19: 1ST ORDER, TWO PORT POLE-RESIDUE EQUIVALENT CIRCUIT.	120
FIGURE 5.20: GIS BLACKBOX MACROMODEL GENERATION AT MINIMUM ORDER FOR STABILITY ALGORITHM.	122
FIGURE 5.21: 90° ELBOW - EMTP vs. ADS TRANSIENT RESPONSE COMPARISON FOR MODEL WITH OHL TERMINATION.	123
FIGURE 5.22: VOLTAGE AT GAS-AIR BUSHING FOR CIRCUIT-BASED MODEL	124
FIGURE 5.23: VOLTAGE AT GAS-AIR BUSHING FOR POLE-RESIDUE MODEL	124
FIGURE 5.24: FINITE ELEMENT MODEL AND POLE-RESIDUE EQUIVALENT IMPEDANCE COMPARISON.	125
FIGURE 5.25: TRANSIENT OVERVOLTAGE AT BUSHING POLE-RESIDUE MODEL FOR A 1P.U. 6NS STEP INPUT VOLTAGE.	125
FIGURE 5.26: SECTION OF SUBSTATION ‘A’ SLD.	127
FIGURE 5.27: COMPUTED DS2 CLOSE SINGLE TRANSIENT AT MOSA DOWNLEAD – CB1 OPEN, DS1 OPEN, DS3 OPEN.	127
FIGURE 5.28: COMPUTED DS2 CLOSE SINGLE TRANSIENT (WITH -1P.U. TRAPPED CHARGE) AT MOSA DOWNLEAD– CB1 OPEN, DS1 OPEN, DS3 OPEN.	128
FIGURE 5.29: COMPUTED DS2 CLOSE SINGLE TRANSIENT AT MOSA DOWNLEAD FIRST TRANSIENT – CB1 OPEN, DS1 CLOSED, DS3 OPEN.	128
FIGURE 5.30: COMPUTED DS2 CLOSE SINGLE TRANSIENT (WITH -1P.U. TRAPPED CHARGE) AT MOSA DOWNLEAD – CB1 OPEN, DS1 CLOSED, DS3 OPEN.	129
FIGURE 5.31: COMPUTED LINE SIDE VOLTAGE AT ELBOW - DS2 CLOSE, DS1 CLOSED, CB1 OPEN, DS3 OPEN.	129
FIGURE 5.32: COMPUTED VOLTAGE WAVEFORM AT BUSHING – DS2 CLOSE, DS1 CLOSED, CB1 OPEN, DS3 OPEN.	130
FIGURE 5.33: COMPUTED DS2 CLOSE SINGLE TRANSIENT (WITH -1P.U. TRAPPED CHARGE) AT ADJACENT CIRCUIT – CB1 OPEN, DS1 CLOSED, DS3 OPEN,	130

FIGURE 5.34: COMPUTED LINE SIDE ENERGISATION, DS1 CLOSE, CB1 OPEN, DS2 OPEN, DS3 OPEN.	132
FIGURE 5.35: COMPUTED DS2 CLOSE CURRENT COUPLING MECHANISM THROUGH MOSA – CB1 OPEN, DS1 CLOSED	132
FIGURE 5.36: COMPUTED DS2 CLOSE CURRENT COUPLING MECHANISM THROUGH MOSA – CB1 OPEN, DS1 CLOSED, RESISTIVE CURRENTS ONLY	133
FIGURE 5.37: COMPUTED VOLTAGE COLLAPSE AT EITHER SIDE OF DS2 FOR ACTUAL MODEL	133
FIGURE 5.38: COMPUTED VOLTAGE COLLAPSE AT EITHER SIDE OF DS2 FOR MODEL WITH ADDITIONAL 1NF CAPACITANCE ON ISOLATED BUS	134
FIGURE 5.39: COMPUTED VOLTAGE COLLAPSE AT EITHER SIDE OF DS2 FOR MODEL WITH ADDITIONAL 1NF CAPACITANCE ON ISOLATED BUS	134
FIGURE 6.1: CALIBRATION VESSEL INSTALLED IN EMI CHAMBER.	139
FIGURE 6.2: VESSEL MEASURED S-PARAMETERS.	139
FIGURE 6.3: HFCT MOUNTED INSIDE IP RATED ALUMINIUM ENCLOSURE.	142
FIGURE 6.4: DEVELOPED HFCT AND ENCLOSURE FINITE ELEMENT MODEL COMPONENTS	142
FIGURE 6.5: VNA FREQUENCY RESPONSE MEASUREMENT SETUP.	143
FIGURE 6.6: VNA MEASURED HFCT WITH ENCLOSURE RESPONSE.	144
FIGURE 6.7: HFCT ENCLOSURE INSTALLATION AT SUBSTATION ‘A’.	144
FIGURE 6.8: UHF SENSOR AND BUS SECTION FINITE ELEMENT MODEL.	145
FIGURE 6.9: TRANSMISSION CHARACTERISTICS BETWEEN HV CONDUCTOR AND UHF COUPLER.	146
FIGURE 6.10: ADS CIRCUIT WITH EM MODEL VIEW.	148
FIGURE 6.11: DOUBLE EXPONENTIAL (5NS/50NS) RESPONSE.	148
FIGURE 6.12: UHF SENSOR COUPLER	149
FIGURE 6.13: TRANSMISSION LOSS COMPARISON MODELLED AND MEASURED RESULTS.	150

FIGURE 6.14: ELECTRIC FIELD (kV/MM) PROFILE AT SPACER SURFACE FOR 400kV INTERNAL BUS EXCITATION.	151
FIGURE 6.15: D-DOT SENSOR DESIGN INSTALLED AROUND SPACER DIELECTRIC.	151
FIGURE 6.16: D-DOT CAPACITANCES (FLOATING GROUND)	154
FIGURE 6.17: SIMPLIFIED 2D AXISYMMETRIC MODEL OF GIB WITH SENSOR ATTACHED TO SPACER OUTER SURFACE. COLOUR BAR 1 ELECTRIC POTENTIAL (V) - BUS, ENCLOSURE AND INTERNAL SF6 SPACE. COLOUR BAR 2 ELECTRIC POTENTIAL (V) – SENSOR AND AIR SPACE AROUND SENSOR.	155
FIGURE 6.18: D-DOT SECTION CHEMICALLY ETCHED ONTO PYRALUX® FLEXIBLE SUBSTRATE	156
FIGURE 6.19: D-DOT INTEGRATION MODE VS FREQUENCY.	157
FIGURE 6.20: D-DOT IMPULSE MEASUREMENT SETUP	158
FIGURE 6.21: D-DOT IMPULSE MEASUREMENTS	159
FIGURE 6.22: D-DOT LABORATORY FREQUENCY RESPONSE MEASUREMENTS.	159
FIGURE 6.23: D-DOT S-PARAMETERS	160
FIGURE 6.24: FIBRE OPTIC LINK – TRANSMITTER CIRCUIT.	162
FIGURE 6.25: FIBRE OPTIC LINK – RECEIVER CIRCUIT.	162
FIGURE 6.26: FIBRE OPTIC LINK CIRCUIT DESIGN PROCESS (SHOWING PROTOTYPE).	163
FIGURE 6.27: FIBRE OPTIC LINK PROTOTYPE (AS BUILT).	163
FIGURE 6.28: FIBRE OPTIC TRANSMITTER IN CAST ALUMINIUM CASE.	164
FIGURE 6.29: OPTICAL LINK TEST ARRANGEMENT.	164
FIGURE 6.30: INPUT WAVEFORM	165
FIGURE 6.31: D-DOT AND CABLE/OPTICAL LINK MEASUREMENT SETUP	165
FIGURE 6.32: D-DOT SINUSOIDAL RESPONSE (BLUE) FOR 10MHZ INPUT (RED)	166
FIGURE 7.1: SUBSTATION ‘A’ CIRCUIT 1 SLD.	169
FIGURE 7.2: DATA ACQUISITION SYSTEM.	170
FIGURE 7.3: DS3 OPEN TRANSIENTS – SWITCHING SEQUENCE 6.	171

FIGURE 7.4: SINGLE TRANSIENT MAGNIFIED, 1 MS CAPTURE – SWITCHING SEQUENCE 6.	171
FIGURE 7.5: FREQUENCY SPECTRUM SINGLE TRANSIENT – SWITCHING SEQUENCE 6.	171
FIGURE 7.6: CLIPPED WAVEFORM AND DECLIPPING ACTION.	173
FIGURE 7.7: TRANSIENTS MEASURED THROUGHOUT DS2 OPEN 4 – DS1 CLOSED POSITION - SWITCHING SEQUENCE 11.	176
FIGURE 7.8: SINGLE TRANSIENT MAGNIFIED (HIGHEST AMPLITUDE) DS2 OPEN 4 – DS1 CLOSED POSITION - SWITCHING SEQUENCE 11.	176
FIGURE 7.9: FREQUENCY PERSISTENCE SPECTRUM DS2 OPEN 4 – DS1 CLOSED POSITION - SWITCHING SEQUENCE 11.	177
FIGURE 7.10: OBSERVED COUPLING OF TRANSIENTS TO ALL PHASES - SWITCHING SEQUENCE 11.	177
FIGURE 7.11: OBSERVED COUPLING OF TRANSIENTS TO ALL PHASES (MAGNIFIED) - SWITCHING SEQUENCE 11.	178
FIGURE 7.12: CB1 CLOSE TRANSIENTS - SWITCHING SEQUENCE 12.	179
FIGURE 7.13: CB1 CLOSE LINE VOLTS SINGLE TRANSIENT - SWITCHING SEQUENCE 12.	179
FIGURE 7.14: CB1 CLOSE TRANSIENT FREQUENCY SPECTRUM - SWITCHING SEQUENCE 12.	180
FIGURE 7.15: DS2 CLOSE TRANSIENTS - SWITCHING SEQUENCE 8.	181
FIGURE 7.16: DS2 CLOSE MAGNIFIED SINGLE TRANSIENT - SWITCHING SEQUENCE 8.	181
FIGURE 7.17: DS2 CLOSE TRANSIENT FREQUENCY SPECTRUM - SWITCHING SEQUENCE 10.	182
FIGURE 7.18: CB CLOSE CB1 TRANSIENT – TOTAL CHARGE OVER CB OPERATION.	182
FIGURE 7.19: DS2 CLOSE TRANSIENT – TOTAL CHARGE OVER DS OPERATION - SWITCHING SEQUENCE 10.	182
FIGURE 7.20: INSTALLATION OF THE D-DOT PROBE (WITHOUT SHIELD).	183

FIGURE 7.21: 200MS CAPTURE DURING CLOSE OPERATION – SWITCHING SEQUENCE 7.	184
FIGURE 7.22: SINGLE TRANSIENT MAGNIFIED – 10MS CAPTURE – SWITCHING SEQUENCE 7.	185
FIGURE 7.23: FREQUENCY SPECTRUM AND TIME-FREQUENCY SPECTROGRAM – SWITCHING SEQUENCE.	185
FIGURE 7.24: EARTHING MEASUREMENT SETUP AT SUBSTATION ‘A’.	186
FIGURE 7.25: EARTHING MEASUREMENT AT DOWNLEAD ARRANGEMENT DIAGRAM.	186
FIGURE 7.26: MEASURED IMPEDANCE MAGNITUDE.	187
FIGURE 7.27: MEASURED IMPEDANCE PHASE.	188
FIGURE 7.28: DS2 CLOSE MAXIMUM TRANSIENT (DS1 CLOSED – 1P.U. TRAPPED CHARGE)	189

LIST OF ABBREVIATIONS AND ACRONYMS

AC	Alternating Current
ADS	Advanced Design System
AIB	Air Insulated Bus
AIS	Air Insulated Substation
ATP	Alternative Transients Program
BIL	Basic Insulation Level
BVP	Boundary Value Problem
CB	Circuit Breaker
CT	Current Transformer
CVD	Capacitive Voltage Divider
DC	Direct Current
DoF	Degrees of Freedom
DS	Disconnecter
EHV	Extra High Voltage
EM	Electro-magnetic
EMC	Electromagnetic Compatibility
EMI	Electromagnetic Interference
EMP	Electromagnetic Pulse
EMT	Electromagnetic Transient
EMTP	Electromagnetic Transients Program
ESL	Equivalent Series Inductance
ESR	Equivalent Series Resistance
FD	Frequency Domain
FDTD	Finite Difference Time Domain
FEA	Finite Element Analysis
FEM	Finite Element Modelling
FFT	Fast Fourier Transform
FSR	First Series Resonance
GIB	Gas Insulated Bus
GIS	Gas Insulated Substation
GPR	Ground Potential Rise
GS	Grounding Switch
HF	High Frequency
HFCT	High Frequency Current Transformer
HPC	High Performance Computing
HV	High Voltage
IBC	Impedance Boundary Condition
IMS	Impedance Measurement System
LCC	Line and Cable Constants

LDO	Low Drop Out
LED	Light Emitting Diode
LI	Lightning Impulse
LIWL	Lightning Impulse Withstand Level
LIWV	Lightning Impulse Withstand Voltage
LV	Low Voltage
MES	Main Earthing System
MoM	Method of Moments
MOSA	Metal Oxide Surge Arrester
MOV	Metal Oxide Varistor
NEA	Numerical Electromagnetic Analysis
OHL	Overhead Line
PCB	Printed Circuit Board
PD	Partial Discharge
PEC	Perfect Electrical Conductor
PEEC	Partial Element Equivalent Circuit
PMC	Perfect Magnetic Conductor
PML	Perfectly Matched Layer
POF	Plastic Optical Fibre
RAM	Random Access Memory
RF	Radio Frequency
RMS	Root Mean Square
SE	Shielding Effectiveness
SF ₆	Sulphur Hexafluoride
SGT	Supergrid Transformer
SLD	Single-Line Diagram
SMA	SubMiniature version A
SMD	Surface Mounted Device
SRF	Series Resonance Frequency
STFT	Short-Time Fourier Transform
TC	Trapped Charge
TCV	Trapped Charge Voltage
TD	Time Domain
TDR	Time Domain Reflectometry
TE	Transverse Electric
TEM	Transverse Electromagnetic
TEPR	Transient Earth Potential Rise
TEV	Transient Enclosure Voltage
TGPR	Transient Ground Potential Rise
TLA	Transmission Line Approximation

TLM	Transmission Line Matrix
TM	Transverse Magnetic
UHF	Ultra High Frequency
ULM	Universal Line Model
UV	Ultra-Violet
VF	Vector Fitting
VFT	Very Fast Transient
VFTC	Very Fast Transient Current
VFTO	Very Fast Transient Overvoltage
VHF	Very High Frequency
VNA	Vector Network Analyser
VSWR	Voltage Standing Wave Ratio
VT	Voltage Transformer
ZNO	Zinc Oxide

LIST OF SYMBOLS

a_n	Reflection coefficient
B	Magnetic flux density (T)
b_n	Transmission coefficient
C	Capacitance (F)
d	distance (m)
D	Displacement flux density (C/m ²)
E	Electric field (V/m)
$(E/P)_0$	Breakdown field strength (V/m bar)
E	Electric field (V/m)
f	Frequency (Hz)
G	Conductance (S)
H	Magnetic field (A/m)
k	Reduction factor of incident wave
k	Wavenumber
k_0	Wavenumber in free spacer
K_T	Toepler's Spark Constant
L	Inductance (H)
l	Length (m)
n	Unit vector
R	Resistance (Ω)
R_b	Body resistance (Ω)
Y	Admittance (Ω^{-1})
Z	Impedance (Ω)
Z_0	Reference impedance (Ω)
Z_c	Characteristic impedance (Ω)
α	Attenuation constant (Np/m)
β	Phase constant (rads/m)
γ	Propagation Constant
δ	Skin depth (m)
δ_G	penetration depth (m)
ϵ	Permittivity (F/m)
η	Field utilisation factor
η_{EFF}	Effective mode index
θ	Phase angle (degrees)
λ	Wavelength (m)
μ	Permeability (H/m)
v	Velocity (m/s)
π	Archimede's Constant

ρ	Resistivity (Ωm)
ρ_g	gas pressure (bar)
σ	Conductivity (S/m)
τ	Time delay
ω	$2\pi f$ (rad/s)

LIST OF APPENDICES

A - RELEVANT PARAMETERS WHEN INVESTIGATING ELECTROMAGNETIC WAVE PROBLEMS	213
B - NUMERICAL ELECTROMAGNETIC ANALYSIS	216
C - CIRCUIT BASED MODELLING FOR VFTs AND TEVs IN ATP-EMTP	220
D - DISCONNECTOR 'MODELS' CODE	224
E - GIS FINITE ELEMENT MODEL CONVERSION TO BLACKBOX MACROMODELS	234
F - DATA ACQUISITION AND CALIBRATION TECHNIQUES	236
G - FURTHER MEASUREMENT RESULTS	238

1 INTRODUCTION

Gas Insulated Substations (GIS), also referred to as Gas Insulated Switchgear and bus only elements as Gas Insulated Buses (GIB), were introduced in the 1960s and have become a popular choice for substation designers, particularly when land or climatic constraints exist. The first complete GIS, a 550kV GIS was installed in Japan in 1976 and since then over 50000 bays have been installed [1]. GIS have many advantages over Air Insulated Substations (AIS) including [1]:

- Reduced maintenance requirements.
- Reduced space requirements -occupying 10-20% of the space required for AIS.
- Weather independent operation – can be installed within climate-controlled buildings in any environment.
- Increased reliability – operating life greater than 50 years.

The many advantages that GIS possess are mainly attributed to the encapsulated design, made possible by use of SF₆ as the insulating medium. SF₆ has a breakdown strength approximately three times greater than air and, when pressurised, its breakdown strength increases significantly. The mechanisms that govern its high dielectric strength and breakdown characteristics are discussed in Chapter 2. SF₆ is however considered a 'brittle' gas and when the electric field strength threshold is exceeded, breakdown occurs extremely rapidly. This rapid collapse of voltage results in travelling electromagnetic waves that propagate in both directions along the bus, these transients are known as VFTs. Partial reflections occur at discontinuities and the superposition of incident and reflected electromagnetic waves can give rise to overvoltages known as

VFTOs. These high magnitude transient overvoltages stress insulation and can result in further, more significant breakdowns.

One of the most commonly associated sources of VFT is disconnector operation. A disconnector is used to provide isolation of a part of a circuit, usually to allow maintenance activities. Disconnectors are not used for on load switching and are only rated for switching of small capacitive currents. During opening and closing of a disconnector, multiple breakdowns of the dielectric occur between the moving and fixed contacts, resulting in the generation of many VFTs. Mitigation measures proposed in recent years show promise, although, at present, they can only achieve minor reductions in magnitude and rise time of VFTs.

In addition to the primary generation of VFTs and the internal GIS issues attributed to them, there are secondary issues that result from electromagnetic coupling and radiation. One of the main concerns, also not well understood is the generation of TEVs also known as TGPR, or TEPR. TEVs exist through the coupling of internal transients to the enclosure that can develop at discontinuities (i.e. changes in surge impedance). TEV are primarily a shock hazard. However, further problems are caused by sparking at insulated/inadequately earthed joints. A correctly designed high frequency earthing system is considered the most effective countermeasure against TEV, and significant reductions in magnitude can be achieved, although limited to a great extent by the length of a downlead, connecting the enclosure to the main grounding system or discrete high frequency rods at multiple points over the system. Secondary coupling onto control cables and electromagnetic radiation is known to be responsible for the damage of equipment, which can result in the loss of critical assets and significant downtime of a substation. The primary mitigation methods listed in literature include the proper screening of cables, shielding and earthing.

The study of VFTs for a particular substation using a time domain transient simulation program such (an EMTP) is ubiquitous. EMTPs or more specifically assumes TEM mode of propagation and is not considered to be accurate for very high frequencies where waveforms may achieve higher order modes [2]. More in-depth studies of field interactions can be carried out using NEA. NEA techniques are extremely powerful, although inherently difficult to use and computationally demanding.

While computer simulations are essential when analysing transients in GIS, modelling errors are quite easily made, often due to lack of available information, or due to

incorrect assumption of modelling parameters. It is, therefore, imperative that measurement of VFT/TEV is carried out for model validation and for initial capture of the transients generated during switching. A number of measurement techniques have been developed in this thesis; most are modified or extended versions of power frequency measurement devices.

The generation of VFTs has been encountered since the introduction of GIS in the 1960s and although significant research has been published surrounding the issue, the issue remains complex and generally not well understood. In response to this, several working groups have been formed, including more recently, the formation of the CIGRE Working Group ‘Traceable measurement techniques for very fast transients’, WG D1.60, established in 2015, which aims to provide contribution towards a future IEC TC 42 release on the measurement of VFTs. The Working Group ‘EMC related very-fast transients in gas-insulated substations- EMC interferences, measured characteristics, modelling and simulations, WG C4.55, further explores in detail the measurement and modelling concepts utilised to date, contributions and findings from the work that culminated in this thesis are to be included in the upcoming technical brochure.

Due to the frequencies associated with VFTs and TEVs, strategies and concepts more commonly associated with RF and EMC engineering were investigated and applied, along with more traditional high voltage fundamentals.

The objective of this thesis is the investigation of the very high frequency transient events associated with disconnector operations; all gas insulated systems. This is investigated through:

- A detailed and thorough review of existing literature.
- The application of numerical modelling techniques and circuit-based techniques to visualise and quantify the behaviour of a GIS during VFTs and TEVs.
- The development of new, mobile sensors and data acquisition systems, for improved high-bandwidth measurements, providing validation of modelling efforts.
- Laboratory based low voltage measurements.
- Site based high voltage measurements.
- The analysis and comparison of measured and simulated data.

Contributions of this thesis are summarised as follows:

- State of the art review of existing literature.
- Numerical Electromagnetic Analysis methods used for the investigation of VFTs and TEVs. A live 400kV substation (termed Substation 'A' throughout) was the focus of the modelling, producing detailed, realistic models of various GIS components to understand the generation, propagation and coupling of VFTs and TEVs. Further quantification of coupling at the bushing is explored through a detail bushing/earthing model. The factors that could have contributed towards a surface flashover of the spacer at Substation 'A' are investigated and a possible contender for promoting flashover is identified.
- The response of earthing system elements is investigated. Options for improvement of the response to TEVs are proposed.
- Circuit based modelling techniques for the study of VFTs/TEVs are explored and enhancements to circuit-modelling practices are proposed.
- Several new sensors are developed for the capture of VFTs. Furthermore, a facility to aid the development and calibration of sensors is built.
- Several site-based, live measurements of Substation 'A' were carried out over multiple switching operations using a range of sensors and data acquisition systems. Full duration, disconnector transients were captured.
- Several potential areas for further research are explored.

A summary of each chapter follows:

Chapter 2

Explores in detail the progress made by the engineering community to date, while at the same time identifying gaps in existing knowledge and methods. The fundamentals of breakdowns in SF₆ are reviewed. The subsequent generation of VFTs and the factors that contribute to the magnitude and waveshape are explored, along with the effects and potential mitigation techniques. The coupling mechanisms, consequences and mitigation of TEVs is further examined, along with an overview of standard modelling practices.

Chapter 3

Further quantification and elucidation of the complex internal and external electromagnetic behaviour of the system during gas insulated disconnecter operations, highlighting some of the potential issues associated with a specific system at Substation 'A'. The behaviour of several 'key' pieces of GIS equipment, including the spacer-flange, elbow and bushing, in the time and frequency domains are explored, utilising numerical modelling techniques to solve an electromagnetic wave equation. A possible candidate for or contributor towards the surface flashover of the spacer at Substation 'A' is identified.

TEV propagation is studied through numerical eigenmode analysis. The limitations of transmission line approximations are made clear.

Chapter 4

Further numerical modelling and analysis of the response of earthing systems to high frequency transients are explored and options for mitigation and improvement are proposed. While Substation 'A' was the basis of the investigation, methods developed and the detailed account of the electromagnetic behaviour of the system are applicable across many other systems.

Chapter 5

Circuit based models are created for the study of VFTs/TEVs at Substation 'A'. An enhanced circuit-modelling method for the study of VFTs/TEVs within ATP-EMTP is developed, along with a unique algorithm which extracts accurate models through Vector Fitting and the identification of highly stable model orders of approximation.

Chapter 6

Several new sensors with the required frequency response and appropriate matching techniques are developed. The design philosophy for every sensor was based on a 'temporary' installation scheme, with all options being easy and quick to install and remove, without the need for permanent modification of the GIS, or even de-gassing of the bus. Sensors could be installed or removed in between switching operations, subject to the appropriate risk assessment and method statements

A laboratory based, half-scale (Substation 'A' bus replica) vessel was built and installed in an EMI chamber, for the purpose of testing and developing sensor prototypes. The

vessel featured a very low reflection response over 200MHz, appropriate for distortionless measurements. Measurements or the injection of high frequency waveforms were permitted through N-type connections, designed with tapered connections for impedance matching.

An analogue large bandwidth, low-cost fibre optic link was built to improve measurement captures and avoid coupling of 'unwanted' signals in a high EMI environment.

Chapter 7

Several site-based, live measurements of Substation 'A' were carried out over multiple switching operations using a range of sensors and data acquisition systems. Full duration, disconnector transients were captured. A number of observations are made through analysis of the measurement data and validation of models, including clarification of the coupling mechanisms at the surge arrester at Substation 'A', along with further clarity on the high counts present on the surge counters.

Chapter 8

Summary of thesis, contributions and discussion of options for future related work.

2 A REVIEW OF VERY FAST TRANSIENTS IN GAS INSULATED SYSTEMS; GENERATION, CONSEQUENCES AND MITIGATION

2.1 Breakdown in SF₆

As the generation of VFTs is a direct effect of breakdown in SF₆, it is necessary to have a good understanding of the breakdown mechanisms. SF₆ is an extremely effective gaseous dielectric, even at the relatively low operating pressures around 5 bar [3]. Its effectiveness as an insulating medium permits the clearance between conductors and between conductors and earth can be significantly reduced, allowing a compact design, which is one of the many advantages of GIS. SF₆ has a breakdown voltage threshold approximately three times greater than air; with a critical reduced field (threshold at which the net attachment and ionisation coefficients are equal) of approximately 89kV/cm bar compared to air at 27kV/cm bar [4]. The graph shown in Figure 2.1 demonstrates the steep growth of the ionisation coefficient when the critical reduced field for SF₆ is exceeded.

The behaviour of SF₆ as a dielectric is mainly a result of the molecules property of electronegativity and mean free path. This property also makes SF₆ an excellent arc quenching medium, hence the reason why its commonly used in circuit breakers. Electronegativity can be described as the tendency of a molecule to attract electrons, forming a dipole bond [5]. The fluorine and sulphur elements that form SF₆ both possess highly electronegative traits, with fluorine having an electronegativity

coefficient of 4 and sulphur 2.5, relative to air. There are two mechanisms that can explain the electronegativity of SF₆, resonance capture (SF₆ + e⁻ → SF₆⁻) and dissociative attachment of electrons (SF₆ + e⁻ → SF₅⁻ + F) [6]. Below the reduced critical field strength, any free electrons that are present quickly attach to the SF₆ molecules to form negative ions. The dominant negative ions formed have exceptionally high thresholds for collisional detachment, with a threshold energy of approximately 90eV for SF₆⁻ + SF₆ and 87eV for SF₅⁻ + SF₆, making a breakdown only possible under very high electric field strengths [6].

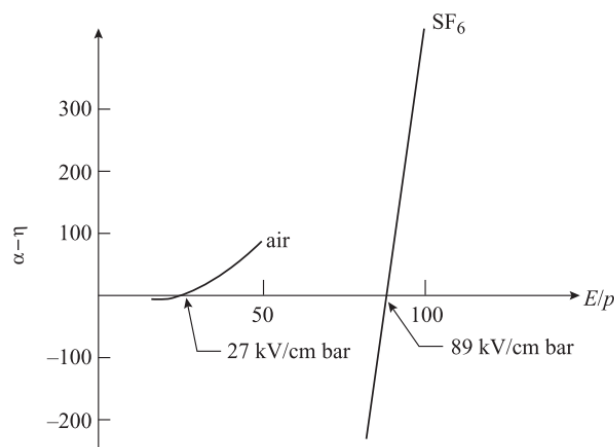


Figure 2.1: Ionisation coefficient growth [4].

The mean free path is defined as the distance an electron can travel before a collision with a molecule and is function of the molecules size and the gas pressure. As an electron requires a certain distance in order to accelerate to a velocity high enough to cause collisional detachment, a smaller mean free path indicates that electrons often do not attain a high enough velocity. In addition to this, a smaller mean free path makes attachment of free electrons to the electronegative SF₆ more efficient. SF₆ has a mean free path of 25×10^{-9} m, compared to nitrogen at 60×10^{-9} m [7].

The breakdown voltage of SF₆ is ultimately dependent on pressure and gap distance. The breakdown mechanism, however, can be considered as dependent on pressure, distance, field inhomogeneity and rise time. For uniform fields at low pd (pressure x gap distance), the Townsend mechanism of breakdown is considered to be responsible for breakdowns in SF₆ [5]. The Townsend mechanism is a succession of electron avalanches, growing exponentially towards the anode. The breakdown voltage required

for the Townsend mechanism can be explained using Paschen's law and illustrated with Paschen's curve in Figure 2.2.

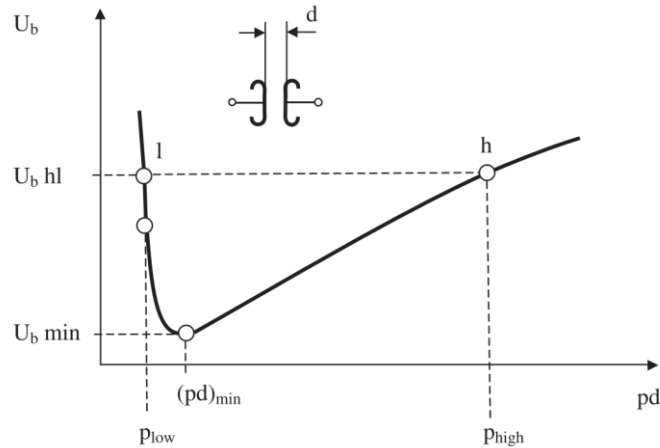


Figure 2.2: Paschen's curve showing breakdown voltage as a function of pressure and distance [5].

The curve shows that assuming a fixed distance, by increasing the pressure above the pd minimum threshold, the voltage required for breakdown increases almost linearly. If the pressure is decreased below the pd minimum threshold, fewer collisions occur due to the low density of gas and lower available energy for collision, resulting again in an increase in breakdown voltage.

At higher values of pd , the streamer-leader breakdown mechanism is considered to be responsible [5]. It is accepted that for GIS operating pressure (i.e. pressures exceeding 1 bar) the streamer breakdown mechanism is responsible under weakly non-uniform fields [4]. Streamer-leader breakdown is considered to be initiated following a single electron avalanche. When critical amplification of an avalanche is reached, space charge development within the avalanche has reached a high enough level for initiation of streamers [4]

The dielectric performance of SF_6 in the presence of defects when subject to slow varying fields (e.g. power frequency) may be temporarily enhanced by the formation of space charge, in a process known as corona stabilisation. The space charge cloud can effectively shield the defect [1] which can prevent discharges advancing to a full breakdown. As a result, defects will often only be detected during partial discharge testing. It is possible, however, that the same defect subjected to a VFT may not have

the time required for the space charge cloud to develop, and could result in a direct breakdown of the dielectric via a stepped leader [4].

2.2 Very Fast Transients

With the exception of some EMP phenomena, although sharing some similar traits, VFTs are the highest frequency class of transients that pose a direct threat to the insulation of high voltage equipment. VFTs are most commonly associated with GIS switching operations, particularly disconnector switching.

During GIS disconnector operation, the distance between stationary and moving contacts change relatively slowly (in comparison to circuit breaker operation speed), hence, changing the withstand voltage of the gap over the duration of operation. When the voltage across the gap, representing the difference between the source and disconnected bus (plus any trapped charge), exceeds the withstand voltage of the gap, a breakdown (prestrike or restrike) will occur. The rapid formation of the streamer/leader channel due to the physico-chemical properties of SF₆, leads to a collapsing voltage that provides excitation for electromagnetic waves, which propagation in every direction at close to the speed of light, reflecting and refracting at discontinuities. Multiple breakdowns of varying magnitude occur for each operation. Breakdown of the gap during a switching operation results in a rapid change between the source and TCV of disconnected section of bus/line. During breakdown and formation of an arc, capacitive currents flow, charging the line until the potential difference between the contacts decrease, eventually extinguishing the arc [8]. During breakdown, capacitive currents will flow across the arc channel, charging the disconnected section of bus, until eventually the arc extinguishes.

Following recovery of the withstand strength of the dielectric, further breakdowns are initiated when the voltage between contacts exceeds the withstand voltage of the gap. This cycle continues until either the withstand voltage gap has increased beyond the difference in potential between the contacts or when the switching operation is complete. This prestrike/restrike process can occur several hundred times during each operation due to the slow operation of the switch, with each VFT event usually lasting for up to 100 μ s [9]. Actual arcing times and arc quenching mechanisms for disconnector operations have a number of dependencies. Field and laboratory investigations by Neumann et al. [10] concluded that arcing time is highly dependent on the load current

of the disconnected bus and the characteristics of the connected network. Their experiments proved that while in the lab environment, for capacitive currents >100mA, arcing time was in the region of 10 μ s, appearing to coincide with the decay of the high frequency currents. However, for field tests with similar currents the arc did not extinguish following the decay of the high frequency oscillations, but up to 1ms after initial breakdown following sufficient decay of the lower frequency oscillations.

Recovery characteristics of the gas also have an impact on the number of sparking events for each full operation of a disconnector. A graph produced by Stosur et.al [9], charted the total number of sparks for one complete operation of a disconnector and concluded that there were approximately four times more sparks for closing operations. The number of breakdowns for a particular system is dependent on disconnector/GIS design and operating condition, the connected network characteristics and statistical/formative time lag.

2.2.1 Breakdown mechanisms and VFT generation in a GIS disconnector

The rapid formation of the streamer/leader channel due predominantly to the physico-chemical properties of SF₆. It is likely that a combination of the high fields and physical characteristics of the SF₆ molecules (short mean free path), along with the low inductance of the bus, lead to a rapid collapse of electric field between the contacts.

The electric field between disconnector contacts form an electric dipole, the arc causes collapse of the static field and it is this rapidly collapsing dipole that excites a short rise-time electromagnetic pulse, which propagates throughout the system at close to the velocity of light, reflecting at discontinuities and refracting externally at apertures. Forward and reverse travelling electromagnetic waves can superimpose leading to overvoltages termed VFTOs. VFTO have magnitudes up to 2.5 p.u, with frequencies extending up to 100 MHz [1]. Compared to disconnector operation in AIS, the magnitude of the transients in GIS are higher, with oscillations at frequencies up to a hundred times greater [11].

Due to the speed of breakdown in SF₆, VFT rise time is extremely steep and usually in the region of 5-20ns depending on field inhomogeneity [12]. Rise time can be estimated using Toepler's spark Equation, shown in Equation (2.1) from [3].

$$t_z = 13.3 \times \frac{K_T}{\left(\frac{E}{\rho}\right)_0 \times \rho \times \eta} \quad (2.1)$$

VFTs at any one point in the GIS are the superposition of the travelling electromagnetic waves; propagating within the metal-clad enclosure along the coaxial duct formed by the bus and enclosure with extremely low attenuation. The travelling waves, reflect and refract at each change in surge impedance, resulting in a dominant frequency that is dependent on the geometries and lengths of each section of GIS. The frequency range for the very fast class of transients is in the range 100 kHz to 50 MHz [3]. Based on the rise time alone, frequencies can reach in excess of 100 MHz. Higher frequencies are more likely to be present close to the disconnecter and in complex GIS geometries, such as those containing multiple ‘T’ junctions and other short sections. The dominant frequency of VFT can be estimated using Equation (2.2) [8].

$$f = \frac{1}{4\tau} \quad (2.2)$$

The propagation velocity is dependent on the inductance and capacitance of the bus-duct. However, if the velocity is assumed to be the speed of light, the frequency of the waveform at an open terminal can be estimated by the total length of the bus duct with Equation (2.3).

$$f = \frac{v}{4 \times l} \quad (2.3)$$

A lower frequency component, in the region of 1 MHz, usually accompanies the dominant frequency, which results from discharge of lumped capacitances in the system such as CVTs [13]. The actual frequency of this component will depend on the inductance and capacitance of the discharge loop. As VFTs are travelling waves, there will be a spatial distribution of VFTO along the bus, with the highest overvoltages usually present at the open end of the load side of the bus [8]. Magnitudes of VFTO typically do not exceed 2pu, although higher magnitudes are possible [13].

VFTOs are accompanied by large equivalent currents, referred to as Very Fast Transient Currents, with magnitudes reaching as high as 10kA [14], although related to the VFTO magnitude by the characteristic impedance of the bus. The magnitude of VFTO is dependent on a number of factors including:

- Trapped charge voltage.
- Rise time - shorter rise times result in increased magnitudes [15].

- Phase angle and polarity of source voltage – the most severe prestrike is anticipated when source side voltage is maximum and opposite polarity to trapped charge [6].
- Field inhomogeneity – a breakdown under a uniform field distribution results in a shorter rise time [15].
- Configuration of GIS - higher magnitudes were reported following simulations that included complex arrangement (multiple T junctions etc.) [8].
- Arc resistance – a significant source of attenuation of VFT and is included in modelling of GIS [16].
- Electromagnetic coupling - the highest portion of damping usually occurs due to out-coupling [17].
- Transformer entrance capacitance - increased capacitance decreases the magnitude of VFTO [15].
- Ratio of capacitance between source and load side - increased ratio results in increased overvoltage [11].
- distance from switching operation - while often assumed for modelling purposes, internal VFT propagation is not lossless and VFT will be subject to some attenuation.

2.2.2 Risks of VFTs and TEVs

For a disconnecter closing operation, the TCV present on the disconnected bus section is one of the most significant factors on magnitude during the initial prestrike event. Subsequent prestrikes are reported to be of reduced magnitude.

VFTs have been identified as a potential threat to insulation through ageing and surface breakdown and are also a significant source of interference to control systems through both conducted, near field and far field coupling [2]. VFTO waveforms will generally differ in shape and magnitude, both spatially and temporally. VFTs are considered to propagate internally along the coaxial bus, restricted by the skin effect. At unshielded apertures, such as the gas to air bushing or the spacer-flange, the transients will couple to the enclosure and will continue propagation, almost independently. This phenomenon is termed transient enclosure voltages. TEVs will propagate externally, presenting a personnel safety risk, in addition to the risk to equipment and control systems.

2.2.3 Effects of Trapped charge on Very Fast Transients

Trapped charges create an electric field along the floating section of a disconnected section of line, cable or bus. If left undisturbed, trapped charges dissipate slowly through the conductance spacers and can be present for many days. During operation of a disconnect switch, trapped charge shows as a DC voltage on the load side of the switch. The magnitude of TCV corresponds to the magnitude of the last restrike during opening operation and is, therefore, highly dependent on the speed of operation. High speed disconnectors usually result in higher levels of trapped charge but fewer strikes per operation. Correct assumption or calculation of trapped charge magnitude is very important when carrying out insulation coordination studies and for testing of GIS components. A worst-case magnitude of 1p.u. when carrying out VFT studies is commonly used. BS EN 62271-102 [18] recommends testing of GIS disconnectors to ensure that discharges to earth do not occur during the switching of charged bus currents; Test Duty no 1 (TD1) for 'switching of very short sections of bus duct' is used. TD1 corresponds to a bus charging switching duty with phase to earth 1.1p.u. at source side and load side pre-charged with negative DC -1.1p.u. (1.1 is safety factor on source and TCV equalling 20% total). A TCV of 1p.u. is likely with high-speed disconnectors which can result in VFTOs of 2.5-3p.u. in some cases. However, low speed disconnectors usually result in a maximum TCV of 0.5pu, and VFTOs would rarely exceed 1.5p.u. [19]. It should be noted that a TCV greater than 1p.u. is possible in the case of three phase GIS enclosures due to capacitive coupling [6].

While worst case assumptions provide a degree of conservatism, overly cautious assumptions can result in unnecessary downtime and additional costs. Many publications claim that a lower magnitude trapped charge is more realistic. Actual trapped charge magnitudes have many dependencies and are in fact a statistical quantity, following a Gaussian distribution [12]. To overcome inaccurate assumptions relating to trapped charge, statistical studies were carried out by Boggs et al. [12] using Monte Carlo techniques to randomise the phase of the source voltage at the time of contact separation for varying contact asymmetries. Results based on 1000 Monte Carlo simulations per degree of asymmetry revealed that a TCV of 0.1p.u. attained the highest probability density, dropping to very low probability around 0.3p.u. with an assumed contact asymmetry of 30%. The results are shown in Figure 2.3.

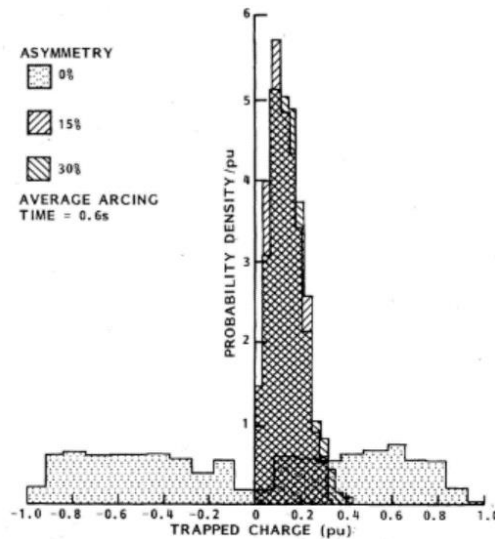


Figure 2.3: Probability density of TCV based on 1000 Monte Carlo Simulations [12].

Further statistical studies were carried out by a CIGRE working group using a 1100kV disconnector, the findings of which concluded that 99% of disconnector operations will result in a trapped charge below 0.24p.u. [14]. The same group also developed a new disconnector model which allowed calculation of actual trapped charge voltage, taking into account contact speed, gas pressure and dielectric design of the disconnector; further improving accuracy of simulation [20].

In addition to the increased overvoltages, a sustained high magnitude of trapped charge will contribute to surface charge accumulation. Surface charge accumulation can ultimately reduce the breakdown voltage while also reducing the time to breakdown.

2.2.4 VFT Waveshape

The complex waveshape of VFTs make it difficult to predict accurately the likely waveforms in a system without detailed knowledge of the GIS layout and geometry. The shape of the transient wave can vary but will retain the same initial fast front and high frequency content [1]. VFTs will follow the source side voltage, while the load side will follow a stepped pattern because of the recovery of the dielectric. Figure 2.4 to Figure 2.6 show the variation of source and load side voltages during switching.

On a nanosecond time frame, the VFTO waveform appears to be only the superposition of travelling waves. While the dominant frequency of the waveform may be a few tens of MHz and dependent on the total length of the bus, higher frequency transients (up to 100 MHz) caused by short reflections can superimpose on the waveform [21]. Typical waveforms of the initial VFTOs are shown in Figure 2.6.

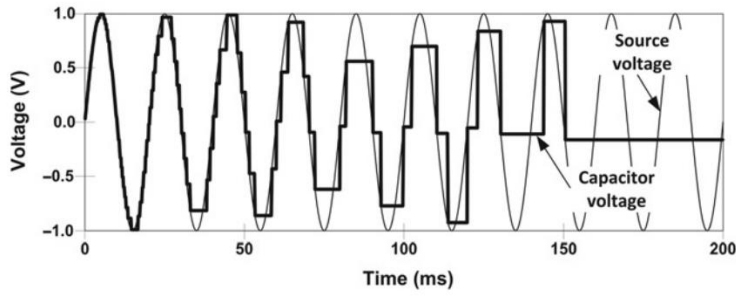


Figure 2.4: Source and load side voltages during opening operation [22].

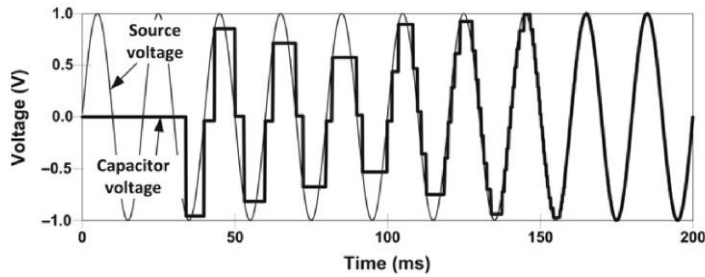


Figure 2.5: Source and load side voltages during closing operation [22].

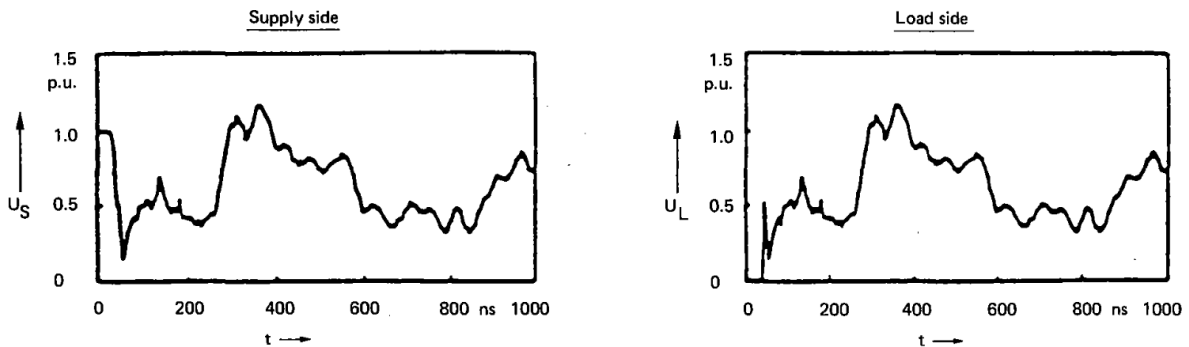


Figure 2.6: Typical higher frequency source and load side VFTO waveforms [21].

After several microseconds, the initial higher frequencies will have decayed, and the dominant frequency of VFTO will continue to oscillate as shown in Figure 2.7.

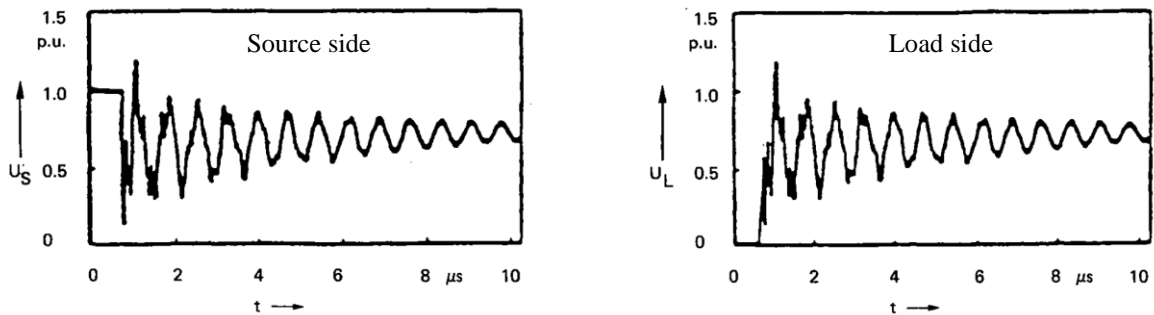


Figure 2.7: Dominant source and load side VFTO waveforms over several microseconds [21].

Eventually, after several hundred microseconds, oscillations of the overall system, which result from resonance between lumped capacitances and inductances in the system. Figure 2.8 shows damped oscillations resulting from GIS and transformer lumped characteristics.

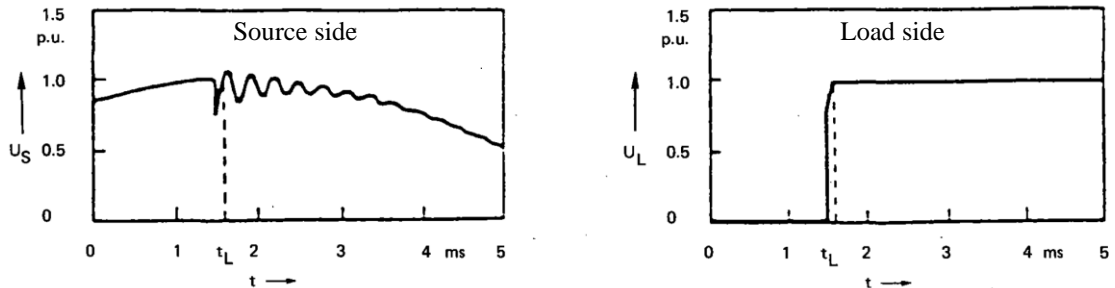


Figure 2.8: Source and load side oscillations between GIS and transformer [21].

A further parameter that is believed to have an effect on waveshape of the load side transients is the magnitude of trapped charge [15]. As reported by Babaei and Nourirad [15], the reduction of TCV results in a smoother wave shape. This implies that the capacitance of the disconnected bus with no pre-existing trapped charge provides an element of damping.

2.2.5 Impact of VFTO

In the special case that VFTOs exceed BIL/LIWV, a full breakdown and damage to equipment will likely occur. VFTOs are a more direct breakdown threat at the higher voltage levels, particularly, in the EHV and UHV range where the ratio of operating voltage to BIL is lower. At higher voltage levels, VFTOs can become a design limitation in addition to the LIWV. BS EN 62271-203 [23] lists switching impulse levels for operating voltages at 300kV and above. VFTOs can even become the limiting dielectric stress for which physical dimensions of the GIS would be defined [14]. According to the numerous probability studies that have been undertaken, this is unlikely to be the case, particularly, at lower operating voltage levels. However, even at lower magnitudes, the steep rate of rise of voltage can cause longer term damage and aging to insulation. A CIGRE working group [24] assessed the impact of fast transients on transformers and estimated that the 23% of failures have unknown origin and that proportion of these failures are attributed to VFT. VFTOs are of particular concern to power transformers as the full overvoltages may not be linearly distributed across the windings and can lead to inter-turn voltages that exceed the insulation level [25].

2.2.6 Breakdown of SF₆ during VFTs

VFTOs can result in local breakdown of the gas gap within the system, resulting in a phase to ground fault. Under uniform conditions, VFTOs of sufficient amplitude stressing the inter-electrode gap generally result in breakdowns at the same level or higher under lightning impulse, largely due to formative time lag [21]. Breakdowns are also subject to the statistical time lag associated with the availability of an avalanche causing free electron, making analysis of breakdowns inherently difficult with a large spread of results [21]. In addition to the associated time lags, breakdown conditions under VFTO are also dependent on polarity, frequency and field inhomogeneity.

Experiments carried out by Luxa et al. [26] determined that positive polarity breakdowns normally occur at lower voltage magnitudes and usually on the initial steep front. Negative polarity breakdowns typically develop on the oscillating tail, after longer formative time lags. Experiments carried out for inhomogeneous rod-plane gaps by Zhang et al. [27] showed that at higher pressures (GIS operating pressure range), breakdowns occurred at lower values for VFTO than lightning impulse. This was attributed to differences in the behaviour of space charge under VFTO in addition to the displacement current injected by VFTO wave fronts and oscillating tails.

Optical experiments using a high speed camera and UV/IR photomultipliers by Flohr et al. [28] investigated the effects of VFT frequency on the breakdown characteristics. The authors discovered that for the same amplitude, an increase of VFT frequency led to an increase in the voltage required for breakdown for both homogeneous and inhomogeneous arrangements. This is due to the obvious reduction in time for which the amplitude exceeds the critical threshold required to produce an avalanche inducing electron. In addition to this, to prevent streamer interruption, the amplitude must exceed a threshold for sufficient time to allow streamer propagation across the gap. The increase of dielectric strength with increased frequency was shown to plateau at higher pressure, following which a decrease in strength was observed for one of the frequencies tested under inhomogeneous fields; the overall trend continued to increase. A limitation of the experiments was that the VFT waveforms utilised for the experiments, consisted of a single frequency in contrast to the multiple frequencies present in real VFT waveforms. The process used does however allow estimation of the voltage required for breakdown for a particular frequency of VFT. Under the assumption of a single frequency (such as the dominant frequency of a real waveform),

it is possible to predict the ratio of VFTO amplitude for a particular frequency to the critical voltage required for a breakdown using Equation (2.4) [28].

$$\frac{VFT}{V_{crit}} = \frac{2}{1 + \cos(\pi * \frac{d}{V_s} * f_{VFT})} \quad (2.4)$$

where d is the gap distance (mm), V_s is the streamer velocity (mm/ns), f_{VFT} is the VFT frequency component in question.

2.2.7 Effect of VFTs on Spacers

Possibly of greatest concern in a GIS are the effects of overvoltages on insulating spacers. Spacers are considered to be the weakest insulation point within the GIS and are a common point of insulation failure within a system, having a breakdown voltage up to 10% less [29]. The withstand capability of spacers has also been shown to decrease with pressure, which implies that, at operating pressures, a breakdown is more likely to occur at a spacer. Even at power frequency, correct spacer design and manufacture is crucial for prevention of discharges under normal conditions. It is imperative that the correct materials are selected and the spacer profile is designed to minimise tangential fields on the surface. The area of greatest concern is the triple junction, an area usually associated with enhanced fields. This effect can be minimised with the use of correctly designed shielding or by embedding a field grading electrode into the epoxy resin [26]. However, spacers are often subjected to non-ideal conditions including surface charge accumulation, moisture, surface contamination from by-products or metallic particles, poor contact at connection point or even low gas density. A comparative study carried out by Luxa et al. [26] evaluated spacer flashover under VFT, lightning impulse and DC with superimposed VFT, for both particle contaminated and ‘correct’ (weakly non-uniform) insulation systems. The resulting voltage-time curves are shown in Figure 2.9. Under correct conditions, for a positive VFT, the voltage-time curve exhibits a flat trend, with breakdown voltages up to 20% higher than the corresponding positive lightning impulse. For a needle protrusion, breakdown voltages were lower than levels for the corresponding lightning impulse. Furthermore, on application of DC pre-stress with superimposed VFT of opposite polarity, a large reduction of insulating strength was apparent. The authors even imply that this may

constitute a design limit [26]. It was emphasised, however, that VFT breakdown data was subject to significant statistical scatter, with poor repeatability of results.

The effects of pre-stress were further investigated by Srivastava and Zhou [30], whom explored the mechanisms and effects of surface charging along with the consequences when subject to lightning impulse. Results implied that when subject to lightning impulse the polarity determined whether surface charging would increase or decrease local field enhancements; however, when an impulse of opposite polarity was applied the flashover voltage was significantly reduced, agreeing with experiments carried out by others. The authors concluded that pre-breakdown corona is the most likely source of surface charge accumulation.

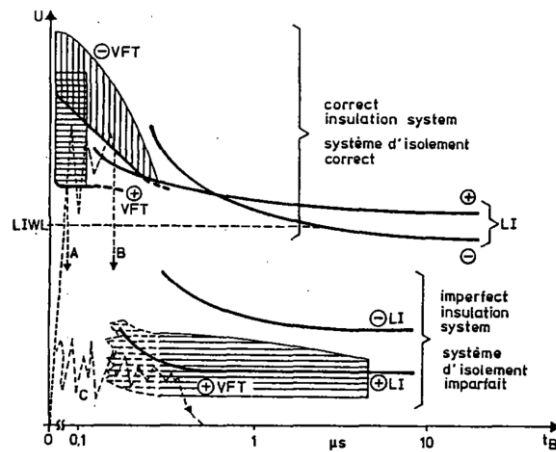


Figure 2.9: VFT and LI Voltage-Time curves [26].

In addition to the effects of VFTs on flashover voltages, VFTs are believed to contribute to accelerated ageing of insulating materials [12, 16, 28], owing to the very high dV/dt and the rate of occurrence, possibly leading to failed discharge events and subsequent degradation of the surface. Ageing is defined as an irreversible, deleterious change to the serviceability of an insulation system [32]. Ageing is generally considered to be a multifactor process and is a function of thermal, mechanical, environmental and electrical factors, as shown in Figure 2.10. Multifactor ageing models, presented by Gjerde [33], consider the synergy between ageing factors. However, the applicability of these synergistic relationships for insulators exposed to transients on a nanosecond timescale difficult to establish. Possibly more suitable for the estimation of lifetime under transient events is the exponential single factor electrical ageing model, as shown in Equation (2.5) [33].

$$L = a \exp^{-\frac{b}{E}} \quad (2.5)$$

where E is the electrical field strength (V/m), a and b are experimentally determined coefficients.

While the coefficients of this simple empirical model must to be determined experimentally, it can provide a reasonable quantitative estimation of life for insulators subject to high voltage stress, without the need for consideration of the underlying phenomena and specific geometries [33].

Despite the lack of published literature, the frequency dependence of dielectric performance is known to have an effect on ageing of a material and is one of the accepted accelerated electrical ageing processes [34]. While not well understood, some of the nonspecific degradation mechanisms associated with ageing includes surface and bulk partial discharge activity, surface discharges, tracking and space charge formation around defects [33].

Although not directly relative to the previous statement, Xie et al. [35] studied the surface flashover and ageing process of an Epoxy Resin insulator when subjected to VFTO. The ageing treatment consisted of multiple discharges across the surface of identical specimens, for a prolonged period, following which the by-products produced and the destructive effect on the insulator surface were analysed.

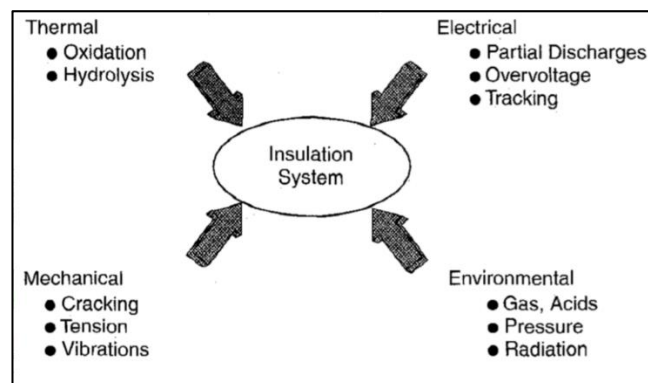


Figure 2.10: Insulator ageing factors [33].

2.2.8 Secondary Effects of VFTs

While breakdowns within the immediate system can result in complete system failure, secondary effects of VFTs are also problematic and include:

- Transient Enclosure Voltages.
- Tripping of protection.

- Surge arresters high conduction or advancement of surge counters [36].
- Coupling onto LV systems - peak voltages on cables connected to the bus duct proven to be in the range of 10kV [37].

It is also likely that the destructive effects of VFTOs are amplified at different sections of the GIS bus, namely at elbows and T junctions. Electric field distributions at these locations are likely to become distorted when compared to a straight section of bus. However, very little literature relating to this issue for VFT was found. Literature relating to partial discharge propagation at these areas exists [38]; it is likely that some correlation between propagation characteristics exist. For example, when considering partial discharge propagation in a GIS bus-duct, due to the frequencies of travelling waves that reach an elbow connection, the excitation of higher order modes is apparent [38]. Further research and modelling of field interactions at these locations when subjected to VFTs should provide a greater insight.

2.3 VFT Mitigation Techniques

Relatively limited guidance is provided for the mitigation and control by the relevant high voltage equipment standards [13][18]. Past failures were often attributed to poor design. In particular, early disconnecter designs often resulted in failure due to arc drifting, resulting in an uncontrolled arc that could bridge the gap between conductor and enclosure [39]. Optimisation of designs prevent this type of failure under normal conditions. Optimised design parameters of disconnectors include operating speed, shielding and limitation of contact asymmetry; all of which greatly influence the magnitudes of VFTO. Disconnector design aside, VFTs remain problematic and further mitigation techniques are required in future research. Identification of the requirement for mitigation of VFT may follow insulation coordination studies or investigative studies following a breakdown. Several publications have evaluated and progressed VFT mitigation technologies, although some are still in the development stages. Some of the existing mitigation techniques are explored below.

2.3.1 Surge arresters

While surge arresters are extremely important for establishing insulation coordination within a substation exposed to lightning and switching impulses, there are mixed opinions over their effectiveness when subjected to VFTO. Within the high and extra high voltage classes, VFTOs often do not attain sufficient magnitude for operation of

surge arresters, even though advancement of surge counters often occurs during disconnector operations [16]. Advancement of surge counters could be attributed to the high displacement currents due to large initial capacitance characteristic of a surge arrester in its non-conducting state and the sensitivity of the counters. Where the magnitude of transients is insufficient for activation of a surge arrester, VFTOs will appear across a surge arrester in a non-conducting state. Still, it is possible that surge arresters, even in their non-conducting state, contribute a minor change in VFTO characteristics. Tests carried out by members of CIGRE working group 33/13-09 [21] illustrated that, in its non-conducting state, a surge arrester appears as a capacitance; reducing the steepness and oscillations of VFTs, when compared to a section of GIS bus without a surge arrester.

In its conducting state, a surge arrester exhibits resistive-inductive characteristics. The impedance of the arrester was investigated by Chen et al. [40] by monitoring the phase difference between discharge current and residual voltage. Experiments concluded that, when subjected to VFTOs in its conducting state, a higher residual voltage would be apparent when compared to an arrester that was subjected to a lightning impulse. Simulations carried out by Rao et al. [36] show that when conducting, a surge arrester only has an effect on the amplitude of VFTO and results show no effect on steepness and the high frequency components.

The applicability of surge arresters as a mitigation technique for VFTs is also debated by some authors who consider that the response time of a surge arrester may be longer than the rise time of the VFTs, leading to possible delays or non-operation [41]. However, this theory does not appear to be the general consensus.

2.3.2 Damping resistor

Shunt damping resistors fitted to disconnectors are known to reduce both the amplitude and oscillations of VFTs [42]. It may be considered impractical to install damping resistors to pre-existing disconnectors, hence, the requirement for damping resistors must be identified prior to construction of a disconnector. The negative effects that damping resistors can have on system reliability should be of primary concern when considering this mitigation measure [36].

2.3.3 Ferrite Rings

Ferrite rings appear to be a suitable and realistic mitigation device. Ferrite rings could be installed as a minor modification to an existing GIS. When installed near the disconnect, they have been shown to attenuate and reduce the steepness of VFTOs with experimental results by Rama Rao et al. [43] reporting reductions of up to 62%. It does appear, however, that testing has previously been carried out at lower, and it is unclear if the saturation effects were fully appreciated. Saturation effects were considered by Riechert et al. [14] and a layering of ferrite rings was used to increase the threshold of saturation, although this resulted in a decrease in efficiency of damping. If the efficiency of ferrite rings under true VFT conditions is improved, it is likely that they will become a key VFT mitigation device for in-service GIS.

2.3.4 HF resonator

Another unique concept under development is the use of high frequency resonators for the damping of VFTs, as pictured in Figure 2.11.

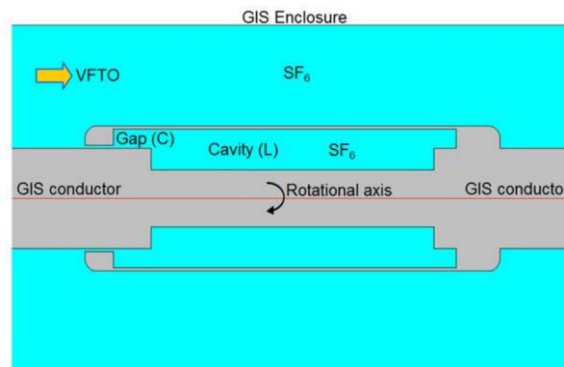


Figure 2.11: HF resonator design [44].

The resonator is designed to dissipate a portion of the VFT's energy in the gap by igniting an arc at a specific frequency. The frequency at which the device resonates is determined by the resonator's cavity (defining the inductance) and gap (capacitance). Smajic et al. [44] utilised eigenvalue analysis to calculate the resonance of the device to ensure that it resonated at a frequency corresponding to the dominant frequency of an expected VFT. Using this method a magnitude reduction of the dominant frequency up to 25% was possible [44]. Optimisation of the calculation method by using a simplified Vector FEM approach for extraction of eigenvalues in a later publication [45], led to reductions of up to 60%.

2.4 TEVs and Earthing System Response

TEVs are defined as the very fast transient phenomenon that appears on the external surface of the enclosure of gas insulated substations [46]. TEVs most often arise due to coupling between internal VFT and the external enclosure. The propagation of VFTs that originate from disconnecter operations remain internal due to the skin effect, but can emerge at discontinuities, causing TEVs. The location most commonly associated with this coupling is the gas to air bushing; other locations at which transient electromagnetic fields can emerge include flanges, insulated spacers for CTs and viewports [8].

Analogous to VFTs, TEV waveforms comprise at least two high/very high frequency components; the dominant frequency component, which is a function of the rise time of the initial TEV, and the length of the enclosure-ground plane. The resulting dominant oscillations are in the MHz range and a second, lower frequency component, usually in the kHz range, is a result of the discharge of capacitive devices (CVTs etc.) [8]. The rise time of TEVs are, generally, considered to be lower than that of VFT due to the lossy propagation of the enclosure-ground bus, although rise times can still be in the region of 20ns [8]. In addition to disconnecter switching, TEVs are also generated during a phase to ground fault, where the dominant frequency is dependent on external capacitance and the inductance of the discharge loop, with additional frequency composed of the superposition of reflected/refracted waves [47]. The magnitude of TEV due to discharge of external capacitance is dependent on the ratio of strap inductance to the impedance of the entire discharge loop and also the voltage on the external capacitance at the time of breakdown [48].

2.4.1 Electromagnetic Coupling at Bushing and spacer-flange

It is well known that the greatest electromagnetic coupling occurs at the insulated gas to air bushing, and is, therefore, considered as the largest source of TEV [1]. TEVs emerging at the bushing will have significant magnitude, primarily due to the continuous refractions at the bushing. Depending on the layout of the GIS, it is also worth considering that this magnitude is also affected by the low shielding effectiveness to VHF. Shielding effectiveness of a gas to air bushing was analysed by Rao et al. [49], using FDTD analysis and excitation of the conductor with both a derivative Gaussian pulse and sinusoidal VFTC current source (to demonstrate real application). The aim of the investigation was to determine radial and axial electric fields and azimuthal

magnetic fields for numerous configurations, with and without a bushing [49]. It was found that the shielding effectiveness for both magnetic and electric fields decreased with increased frequency; with no attenuation of magnetic fields above 55MHz and electric fields above 80MHz.

Analysis of electromagnetic fields at the bushing could provide a great deal of information about the coupling mechanisms and more accurate calculation of induced TEV. This method is, however, very time consuming and demanding from a computational point of view. Also, great care must be taken not to introduce inaccuracies due to the presence of other structures in the vicinity which can influence field magnitudes. A similar approach was used by Ruan et al. [50] to study the TEV generated on the enclosure of a 500kV SF₆ circuit breaker within a GIS. The enclosure was modelled as a simplified tubular wire mesh using the HIFREQ module of CDEGS software [51], which is used to solve Maxwell's Equations numerically. A double exponential switching surge was used to simulate VFTOs generated by disconnector switching [50]. The aim was to compare the results of this field theory-based technique with circuit theory-based techniques, while allowing computation of the effects of the earthing system.

While EM coupling at the gas to air bushing considered as the greatest source of TEVs, enclosure flanges securing insulating spacers are another known location of coupling. Many designs that use unshielded insulators usually have shorting links to allow a path for circulating currents. While these shorting links are adequate for power frequency currents, the links are too infrequent to effectively contain internal transients and leakage results [1]. The basic coupling mechanism at the spacer-flange discontinuity can be explained with the use of Figure 2.12. At the discontinuity, part of the incident wave will be reflected, part will continue in the same direction internally and part will refract out to the enclosure-ground plane in each direction. In Figure 2.12, this is indicated by subscripts i, f, T, L and R. Subscript 'i' is the internal incident wave, 'f' is the internally reflected wave at the discontinuity, 'T' is the internal transmitted wave at the discontinuity, 'L' is the externally refracted wave at the discontinuity (in the direction of internal incident wave propagation), 'R' is the externally refracted wave at the discontinuity (in the opposite direction to the internal incident wave).

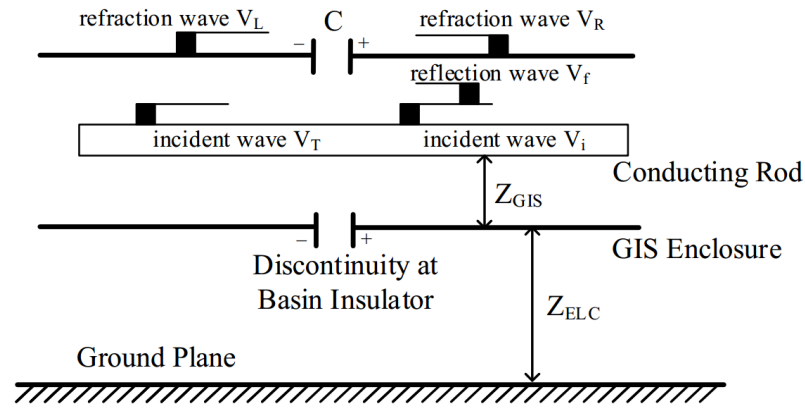


Figure 2.12: Basics of coupling at spacer-flange discontinuity [52].

Much of the research relating to coupling mechanisms at the GIS spacer-flange focusses on partial discharge propagation. Research undertaken by Okabe et al. [53] evaluated the propagation and coupling of high frequency surges at an isolated flange (with no spacer) for the purpose of enhancing circuit models. It was demonstrated that the joint could simply be represented as a capacitance derived from its geometrical characteristics; the impedance of which decreased with frequency. In addition, they inferred that the proportion of waveform that leaked through the joint to the grounding system decreased with increased frequency. Furthermore Okabe et al., evaluated the propagation of the electromagnetic wave when physically situated next to another enclosure (as is the case for multi-phase GIS). They found through measurement, and simulation through NEA, that the waveforms propagated between enclosures without directly generating a potential to ground in the adjacent enclosure, i.e. entirely tank to tank propagation (similar to aerial mode propagation of transmission lines). A potential to ground was, however, generated in the adjacent tank when the propagating waveform reached a discontinuity.

2.4.2 Calculation of TEVs

While knowledge of coupling mechanisms of electromagnetic fields at discontinuities aids understanding of the concept from a design point of view, the basic mechanism of the generation of TEVs is fundamentally based on the refraction of internal VFTs to the enclosure by a simple voltage division approach. This simplification allows TEVs to be estimated through circuit theory techniques using software such as EMTP [54]. It is possible to calculate more accurately TEV waveforms using EMTP, and this will be presented in a Chapters 3 and 4.

To calculate the magnitudes of TEV, the surge impedances of the GIB (Z_{GIS}), AIB/OHL (Z_{OH}) and enclosure-ground (Z_{ELC}) are utilised. The gas to air bushing can be considered as a junction forming the connection of three distinct transmission lines characterised by these individual surge impedances [55]. At the junction connecting the three transmission lines, as shown in Figure 2.13, the incident wave is partially reflected back towards the GIB, partially refracted, representing the coupling to the enclosure and partially continues in the original direction of propagation, towards the AIB, OHL or cable.

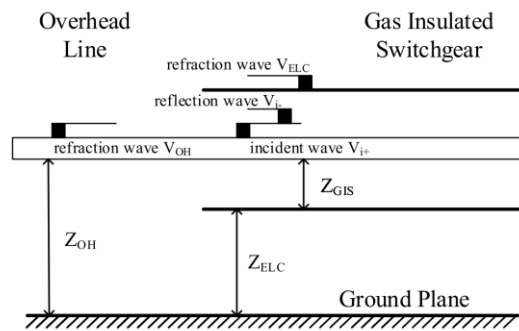


Figure 2.13: Basic coupling mechanism at gas/air bushing [52].

The magnitude of the initial TEV can be approximated simply by multiplying the magnitude of incident VFT by the ratio of the surge impedances of the three transmission lines (voltage divider), as shown in Equation 2.6 [48].

$$S_{31} = \frac{-2Z_{ELC}}{Z_{GIS} + Z_{OH} + Z_{ELC}} \quad (2.6)$$

where Z_{GIS} is the GIS bus surge impedance, Z_{OH} is the overhead line surge impedance, Z_{ELC} is the GIS enclosure surge impedance.

A simplified circuit model used for calculation of TEVs is shown in Figure 2.14. Each internal and external section is represented by a distributed inductance and capacitance, subscript 1 represents the GIB parameters, subscript 2 represents the AIB/OHL parameters and subscript 3 represents the enclosure-ground parameters.

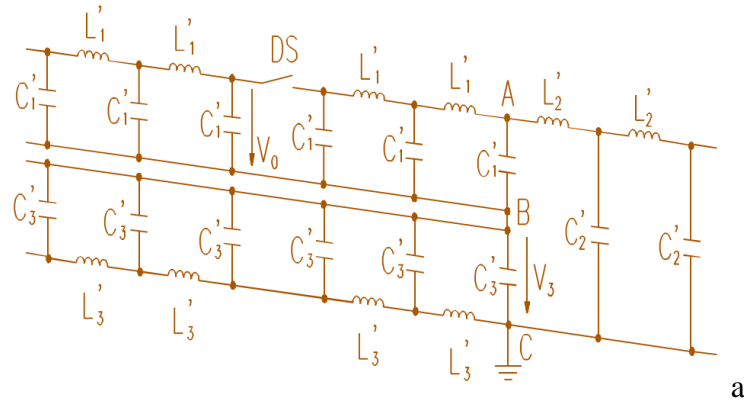


Figure 2.14: Simplified equivalent circuit representing the three transmission lines [8].

TEV magnitudes in excess of 0.5p.u. are possible, as measured by Fujimoto et al. [48], although 0.1 to 0.3p.u. reported in more recent publications [8]. The highest magnitudes will likely occur close to the gas/air bushing, decreasing closer to the main body of the GIS due to the lossy propagation.

2.4.3 Effects of TEV

In addition to the problems that can arise from internal transients, there are many additional issues that could arise as a result of TEV. Of greatest concern and possibly the least understood is the effect on safety as a direct or indirect result of electric shock. It is considered by many that the direct shock hazard is insignificant in most cases, with authors providing only anecdotal experience of the events [47]. From a safety perspective, there appears to be greater concern for the indirect effects of TEV, such as the startling effect which could lead to secondary injuries. While not conclusive, there has been several investigations into TEV and the effect on the body when subjected to impulse currents. Early studies on impulse currents by Dalziel [56] proposed a 13.5J for a body impedance of 500Ω. A later study by Ford and Geddes [47] applied Dalziel's limit to the calculation of body energies under various TEV generating events. Calculations were performed analytically, simplifying the TEV waveform as shown in Equation 2.7 [47].

$$V = V_L e^{-\alpha_L t} \cos \omega_L t + V_H e^{-\alpha_H t} \sin \omega_H t \quad (2.7)$$

where subscript L represents low frequency, subscript H represents high frequency, V is the magnitude of the frequency component, α is the attenuation factor of the frequency component.

Body energy can be calculated as the square of the voltage divided by the body resistance and integrated over the time period of the TEV. For the waveform Equation above, a simplified expression for the body energy is given in Equation 2.8 [47].

$$E \approx \frac{1}{4R_B} \left(\frac{V_L^2}{\alpha_L} + \frac{V_H^2}{\alpha_H} \right) \quad (2.8)$$

where R_b is the body resistance (Ω).

Ford and Geddes [47] calculated possible body shock energies for a number of typical GIS configurations. While shock energies for TEV events were found to be in excess of the recommended 13.5J, there were doubts on the suitability of body energy limits as the fundamental criteria for hazard classification. The main reason for doubt is the actual effects of high frequency currents on the body. Low frequency currents are known to cause muscular contraction and even ventricular fibrillation, they are generally considered to pose a far greater risk to the body. High frequency currents are believed to be restricted to the skin or very shallow depths. Even with this in mind, there is not enough conclusive evidence surrounding the effect of TEV on the human body. The 13.5J limit is still considered at present, and some utility providers even consider a reduced limit of 1J as more applicable [57].

In addition to the safety concerns, another phenomenon that regularly occurs during disconnecter switching is sparking across insulated and even uninsulated components (enclosure flanges, cable terminations, bolts etc.). In addition to the potential damage to insulation mentioned previously, this can cause significant problems where an insulated connection is strategically placed in order to limit the circulation of enclosure currents; which is one of the GIS earthing primary design requirements [46]. The energy due to a flashover caused by TEVs should not cause immediately significant damage, although aging will likely occur if the process was repeated regularly. A more problematic scenario in which immediate damage could occur, would be a flashover initially providing a path for the high frequency currents, that simultaneously provides a conductive path for power frequency currents [1]. Non-linear resistors or capacitors can be installed across insulating gaps at a GIS/cable junction to prevent the circulation of power frequency under normal conditions but allow TEVs to propagate across the gap [55].

2.4.4 Earthing, Bonding and Shielding

A recommended technique for reduction of TEVs is the use of a conductive shield, surrounding the enclosure, as shown in Figure 2.15 [58]. Magnitude reductions of up to 90% were reported in [37], with variations in effectiveness for different shield types. A shield installed around the enclosure would result in the partial reflection of TEVs. The magnitude reduction of the transmitted wave would depend on the shielding effectiveness. The positioning and possible effects of partially reflected waves requires careful consideration, so as to avoid the enhancement of TEVs at another vulnerable point of the system. The bonding arrangement of adjacent enclosures is also believed to have an impact on TEV magnitudes. The bonding arrangements shown in Figure 2.16 from [58], demonstrate the magnitude reductions possible for four bonding arrangements. The results imply that even the presence of the other two enclosures will reduce enclosure TEV magnitudes but bonding all three enclosures to each other and the earthing grid using a large metallic plate produces the best results. This arrangement could be relatively easy to implement at the entrance to the GIS hall, if not already bonded, although consideration of power frequency circulating currents is required.

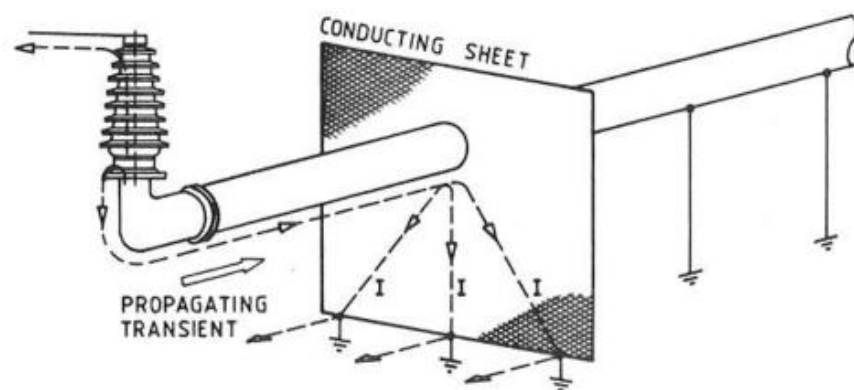


Figure 2.15: Enclosure shielding [58].

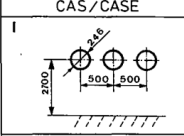
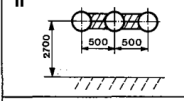
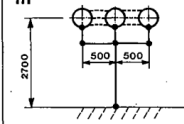
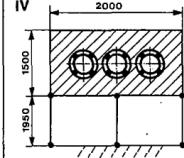
CAS / CASE	\hat{U}/U_0
	0,33
	0,15
	0,17 0,10 ^{II}
	0,06

Figure 2.16: Enclosure bonding arrangements [58].

2.4.5 Soil characteristics - frequency dependence

Soil characteristics are important for the study of TEV, as both soil resistivity and permittivity show significant frequency dependence [59]. Further dependence on soil water content and ground temperature was explored in [59] using a broadband dielectric spectrometer, for frequencies up to several tens of MHz. Soil characteristics greatly influence the behaviour of above and below ground transients. At lower frequencies, in the TEV range, soil characteristics are possibly dominated by the soil conductance. However, at higher frequencies, the soil behaves resistively and capacitively [60]. It is this frequency dependence, in addition to the frequency dependent effects of the electrode system, that characterise the complexity of earthing systems at high frequencies.

2.4.6 Earthing system elements

An effective earthing and bonding system provides the best mitigation results against TEVs. While designers of earthing systems for GIS primarily focus on earthing for power frequency faults and the prevention of circulating currents, little advice is given in earthing standards for effective high frequency earthing. This often results in an earthing system that may be effective at power frequencies but is ineffective for frequencies in the VHF range. This is possible because the behaviour of an earthing system when subject to impulse currents is completely different to its behaviour for power frequency faults.

Aside from soil characteristics, the main issues often faced are the number/spacing of ground straps and the length of ground straps exhibiting a considerable inductive reactance to TEVs [48].

Ground leads are usually considered too long and inductive for fast fronted transients. It is believed that shorter ground leads result in lower TEVs [1]. However, to achieve this requires a lower enclosure, which is often not a viable option. Ground lead effectiveness ultimately has many dependencies, including surge rise time, surge impedance, ground/soil characteristics and penetration depth etc. A simple calculation can determine the possible voltage that could develop across the inductance. Provided ground leads are installed with limited bend, an inductance of around 1 μ H/m can be assumed. For 10kA, a front of 1.2 μ s over a 3m ground lead would produce a voltage of 2.5kV across the ground lead. However, ignoring propagation effects and displacement fields to emphasize the point, a 10kA transient with a rise time of 10ns could in theory produce 3MV across the same ground lead. For this reason, ground leads cannot be ignored when considering earthing for TEVs. Their impact on various earthing configurations is investigated in Section 4.1.

Although the inductance significantly limits a ground lead's effectiveness, a division of a surge will still occur. Part of the surge will propagate down the ground lead towards the ground. An incident wave perpendicular to a conductive ground plane will only penetrate a short depth [61], a high proportion of the surge will reflect and can destructively superimpose with an oncoming surge. The reduction of the incident wave can be estimated by Equation (2.9) [8].

$$k = \frac{2Z_G}{2Z_G + Z_{enc}} \quad (2.9)$$

where Z_G is the ground surge impedance and Z_{ENC} is the enclosure surge impedance.

The presence of multiple, short ground straps provides the best attenuation in magnitude and duration of the TEV events [57]. Bonding the enclosure to the earth grid via ground straps of adequate size and length, spaced equally every 10m can reduce TEV by up to a factor of 0.8 at each strap and reduce the disturbance with a L/R time constant of around 50ns [57]. This attenuation is achieved by two mechanisms. The first mechanism is a reduction by voltage division at the 'T' junction formed by the enclosure and the ground strap. When TEVs propagate to this point, a transmission line division takes place

reducing the magnitude of the transmitted wave. This is the dominant attenuation process in long straps. Attenuation via this mechanism is usually small due to higher surge impedance of ground strap in comparison to the enclosure.

The second attenuation mechanism, dominant in the case of short ground straps has an immediate effect on the rise of the initial transient. When the transient reaches the low impedance of the earthing grid, it is reflected with opposite polarity. If the electrical length of the ground lead is such that twice the transit time of the transient (returning the transient to the T junction) is less than the rise time of the incident step, there will be a reduction in amplitude of the initial wave front [55]. The resulting TEV waveform that follows this reduced step surge is then dependent on the resultant standing waves that are associated with ground strap spacing and further VFTs [37].

Measurements of the initial step waveforms were taken in a laboratory set up by Fujimoto et al. [48]. Using a fast transmission divider, both with and without ground straps installed at the base of the gas to air bushing, they were able to compare the calculated and measured TEV and the effect on the waveforms. The waveforms captured by the oscilloscope in each case are shown in Figure 2.17.

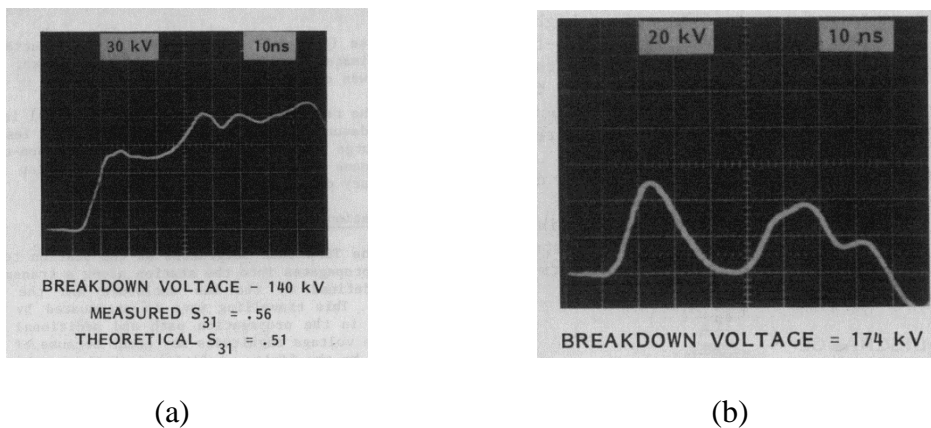


Figure 2.17: Measured waveforms (a) no ground straps (b) with ground straps.

Figure 2.17(a) appears to be a solely a step function without the characteristic oscillations. This was not the intended result and is possibly a result of the relatively small-scale laboratory set up. Waveforms measured on an actual GIS enclosure would have numerous reflections even without a ground connection, resulting in more of an oscillatory waveform overall. Figure 2.17(b) shows a reduced magnitude waveform with some oscillation as a result of the reflection from the ground strap.

While it is evident that ground straps have a significant effect on the magnitude and wave shape of TEVs, there are many other factors including the physical layout of the system and even the soil characteristics. While proper design of an earthing system is a priority, any additional TEV mitigation techniques may be limited by the physical design of the GIS. For example, a lower enclosure will not only reduce the required length of the ground straps, but also reduce the surge impedance and hence, the magnitude of transients that appear on the enclosure. Another factor more related to the location of a GIS is the soil characteristics. Earth resistivity affects both the magnitude and propagation velocity of TEVs. Increasing soil resistivity increases the attenuation of TEV and reduces the propagation velocity [62]. Low resistivity soils, however, result in waveforms that decay more quickly [50]. An optimised soil resistivity is, therefore, a possible mitigation technique. However, it is important to note that this will impact efficiency of the earthing system at power frequency.

Shielding, both internally and externally, is an additional mitigation technique. Although difficult to achieve, correct design of internal shielding can reduce the coupling of VFT to enclosures. External shielding will not only reduce coupling of VFT/TEV onto external circuits and structures, it is possible that strategically placed shields or metallic grounds can reduce the magnitude of TEV in problematic areas [49]. The location of shielding or other grounded structures must be carefully considered, as enhancement of electromagnetic fields is possible, as shown in Figure 2.18.

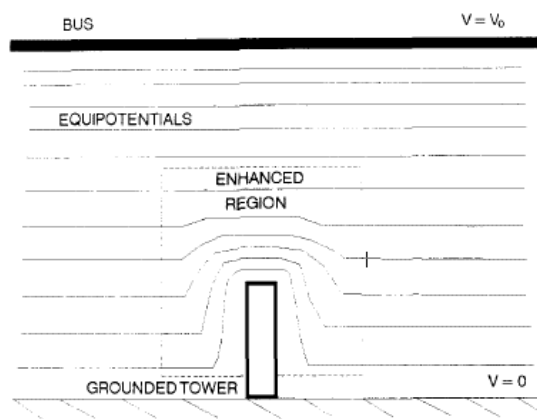


Figure 2.18: Local field enhancement at grounded protrusion [63].

2.5 Modelling considerations for VFTs and TEVs

The use of correct modelling and simulation techniques is essential for understanding and predicting the transients that are likely to exist in a system for a particular event.

From a design perspective, accurate simulations can minimise initial costs when considering insulation levels and sizing of equipment. In addition to this, when combined with data from a measurement system, an accurate model of a system can aid rectification efforts in the event of a failure. A brief overview of the considerations for modelling for VFTs is provided in this section, however a detailed overview of techniques used within this research will be provided in subsequent chapters.

There are two main choices of simulation method for high frequency transients in a power system; circuit theory based and field theory based. Circuit theory based techniques are relatively simple and non-computationally intensive. Circuit based techniques have the advantage that a large system and its interaction can be represented. This technique is considered reasonably accurate (providing correct representation of components) for waveforms that propagate in Transverse Electro-Magnetic (TEM) mode [64]. Unlike partial discharge propagation and archn flashover, VFTs are considered to propagate solely in TEM mode [45] and are therefore considered suitable for analysis in the time domain using software that employs circuit theory techniques, such as ATP-EMTP [65]. While EMTP requires knowledge of circuit parameters, it simplifies the process in a way by allowing computations using simplified representations of circuit parameters, usually solved analytically and with sufficient accuracy. Using EMTP, the differential Equations of lumped or distributed circuit elements are integrated using the trapezoidal rule to represent each element simply as a current source and resistor. A nodal conductance matrix is produced from the circuit elements and then solved for given voltage/current sources [2]. This process is carried out at each time step, for the desired length of a simulation. In addition, EMTP allows a more realistic representation of the wider system. Of primary concern when producing a circuit using EMTP is component behaviour. Most components behave very differently at very high frequencies. Modelling of each component requires careful consideration, particularly, with regards to the dominance of capacitances and the effects of travelling waves.

Field theory based methods, known collectively as Numerical Electromagnetic Analysis (NEA), can be applied with great effect and provide further insight into the electromagnetic phenomenon. NEA methods solve Maxwell's Equations directly, providing invaluable information about the field interactions for arbitrary geometries and are often used to extract equivalent electrical parameters for representation using circuit based methods. The methods are also not subject to the same limitations as

EMTP with regards to solving for the higher order propagation modes which are possible at very high frequencies. NEA methods are however, computationally intensive and require significantly greater geometric information components which is often difficult to acquire. NEA is also inherently more difficult to master, as a comprehensive understanding of electromagnetic field theory and the associated boundary conditions is a requirement for most NEA techniques. NEA techniques are generally better suited to smaller systems or even individual components as accurate representation of the wider system is difficult to include. NEA techniques include [64]:

- Finite Difference Time Domain (FDTD).
- Finite Element Modelling (FEM).
- Transmission Line Matrix (TLM).
- Method of Moments (MoM).
- Partial Element Equivalent Circuit (PEEC).

2.6 Existing Measurement Techniques for VFTs and TEVs

Measurement of transients within a system is an essential task for commissioning, condition monitoring, model validation or the acquisition of unknown circuit parameters. Measurement techniques have been utilised on test set ups within laboratories using small sections of GIS, and for in-service GIS. Laboratory testing of GIS would prove extremely useful when testing prototype mitigation devices; provided transient waveforms of a suitable rise time/frequency can be generated. A common method of generating a VFT waveform artificially involves the application of the output from a surge generator to a short section of GIS bus that contains a spark gap, as shown in Figure 2.19.

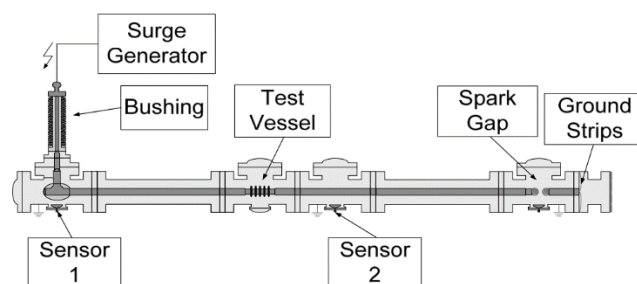


Figure 2.19: Artificial generation of VFT in laboratory set-up [14].

Measurements taken on in-service GIS during switching operations potentially allow the detection of sections of GIS that are prone to VFT (elbows, T junction etc.), either prior to an event in a condition monitoring capacity or following a breakdown to assist in determination of the cause. Considerable precautions must be taken to avoid interference for every measurement option, using as a minimum, doubly shielded cables and a Faraday cage housing for the measurement oscilloscope. Some of the measurement techniques published in literature follow.

2.6.1 Measurement of VFTs

The most common method of measurement of VFTs at operating voltages is achieved through the use of a CVD. Capacitive dividers built into port-holes tend to have better performance with respect to bandwidth [66] and have response times in the nanosecond/picosecond range. An example of CVD construction using a port-hole is shown in Figure 2.20. The disc electrode installed inside the duct along with the HV bus forms the first capacitor (HV) of the CVD. The second capacitor (LV) is formed between the electrode and port cover by a thin insulating film.

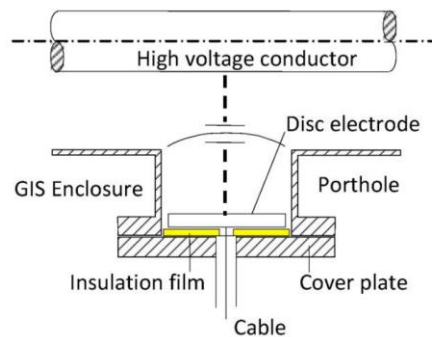


Figure 2.20: CVD port-hole construction [67].

2.6.2 TEV Measurement

Measurements of TEVs are commonly carried out using either an electric field sensor, or a special resistive characteristic impedance divider known as a Newi probe. Uncertainty of the effects of the geometry of the electric field sensor on the measured electric field meant that the Newi probes were often used [68]. An example set-up of a Newi measurement system is shown in Figure 2.21.

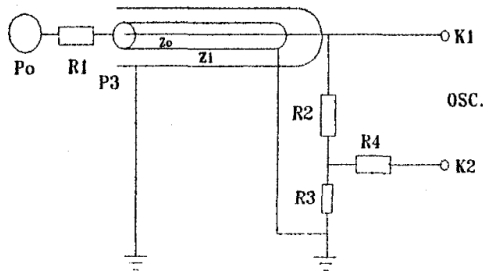


Figure 2.21: Newi Probe [68].

The effects of the geometry of the electric field probe can be corrected through calibration at a known voltage level, as shown in Figure 2.22.

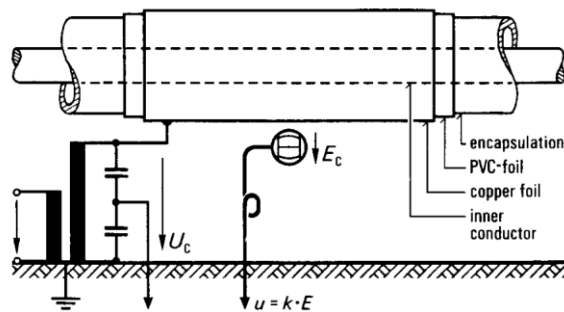


Figure 2.22: Calibration of spherical field sensor [69].

Other more recent measurement techniques involve the use of HV probes to measure directly TEVs at insulated flanges. Figure 2.23 and Figure 2.24 show measurement of TEVs both across the flange and between the flange and earth. Direct measurement may, however, be limited by the rated voltage of the measuring equipment.

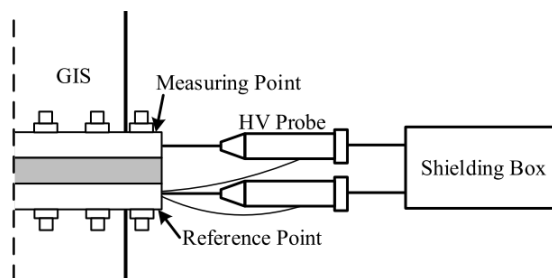


Figure 2.23: Measurement of TEV using High Voltage probes across insulated flanges [52].

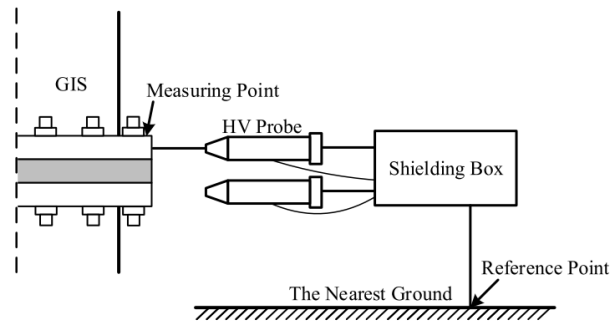


Figure 2.24: Measurement from flange to reference earth [52].

2.6.3 VFTC Measurement

Measurement of VFTCs, internally or externally is normally carried out with the use of Rogowski coils. The design of a Rogowski coil measurement system for VFTCs is complicated by the amplitude and rate of rise of current and the nature of travelling waves. The voltage induced across a coil is primarily dependent on the mutual inductance between the coil and primary conductor and the rate of change of current and can therefore become the limiting design factor [70]. It is possible that equipment damage could result due to the large voltages will be induced across a coil, even for relatively small currents and very low values of mutual inductance. For this reason, an element of isolation should be incorporated into designs such as through the use of optical transducers and fibre optic cabling [70]. Further insulation damage can occur as a result of the travelling wave phenomenon. Rogowski coils can appear electrically long compared to the rise time of the transients, leading to travelling waves and an uneven voltage distribution that can stress inter-winding insulation.

The very high rate of change of voltage associated with VFTOs and other external sources of noise, necessitate the need for shielding [71]. To ensure that the magnetic field can still couple with the coil, a slit is located in the shield.

2.6.4 Trapped Charge Measurement

Trapped charge can be monitored using a CVD arrangement of sufficiently low frequency response on the isolated bus section. Figure 2.25 shows the set up for monitoring trapped charge. The response time constant of the setup shown is down to 0.5 seconds which is suitable for monitoring of trapped charge [57].

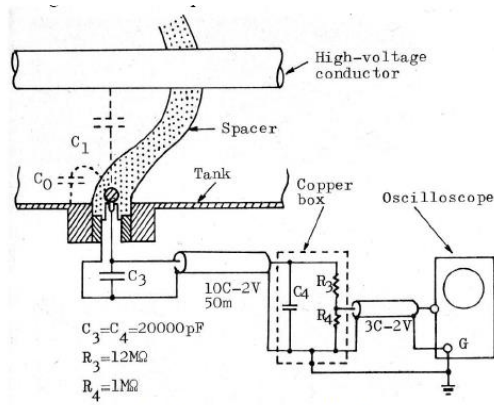


Fig. 3 Power Frequency Divider

Figure 2.25: Trapped charge monitoring [57].

An example of the minimisation of interference by using a fibre optic connection between the CVD circuit and oscilloscope is shown in Figure 2.26.

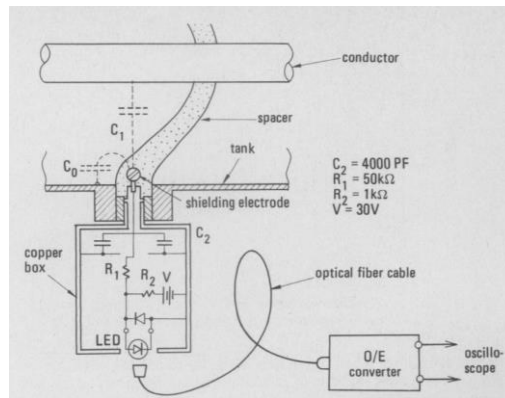


Figure 2.26: Using fibre optic cable to further reduce interference [72].

2.6.5 Estimation of TEVs via low voltage measurement

While high voltage measurements allow verification of transient response of a live system, there are drawbacks including temporary or permanent modification of a system (installation of a port-access CVD requires the system to be degassed and re-gassed before use) and often a limited time window in which to undertake the modifications. The whole process requires significant planning and coordination. Interference and statistical variation of parameters (trapped charge etc.) is also of great concern. Low voltage measurements could provide alternative means of estimating TEV magnitude and propagation. The use of a DC supply along with a mercury relay to simulate a prestrike arc across a disconnecter was utilised by Ogawa et al. [72], allowing

VFT/TEV coupling to be assessed using an oscilloscope with probes. An overview of the connection is shown in Figure 2.27.

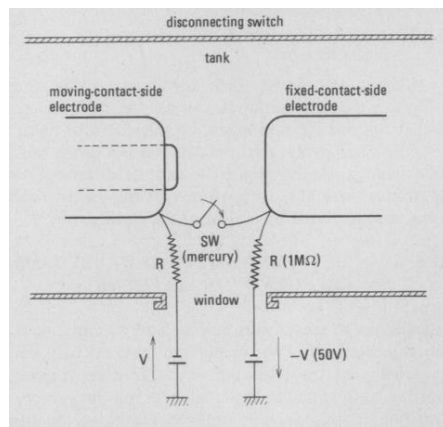


Figure 2.27: Low voltage prestrike simulation using DC supply and Mercury relay switch [72].

Dick et al. [57] further expands on LV testing/measurement of TEV, proposing an experimental set-up that uses Mercury relays, connected between enclosure and supports to identify the propagation of TEVs. Connection of the switch and results demonstrating accuracy as shown in Figure 2.28 to Figure 2.30.

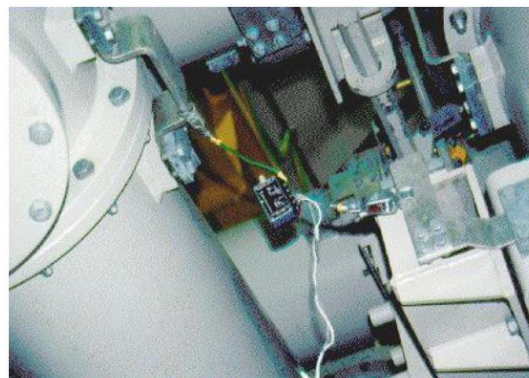


Figure 2.28: LV TEV propagation tracing [57].

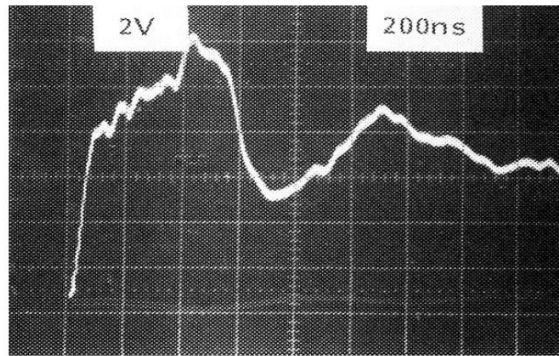


Figure 2.29: TEV waveform measured at 27m from the source [57].

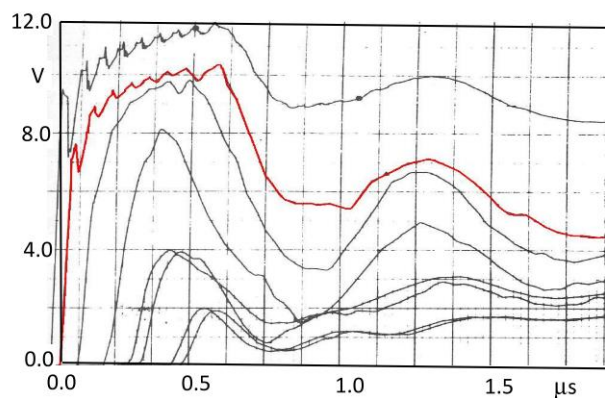


Figure 2.30: EMTP model validation [57].

2.7 Conclusion

A review of published literature surrounding the issue of VFTs in GIS has been presented. VFTs are ultimately the result of the rapid breakdown speed of SF₆. The breakdown process, when initiated, is extremely quick and usually in the region of 5-20ns for homogeneous field configurations. VFT generation is usually a result of disconnector operation with many tens or hundreds of breakdowns per operation. With the exception of the spacer-flange locations, internal propagation can generally be considered lossless. The waveform is dominated by a very high frequency component which is usually several tens of megahertz. However, a lower frequency is also present, which is attributed to the discharge of lumped capacitances. VFTOs are apparent at any point along the bus where the superposition of waves exceeds the rated voltage of the equipment, and generally have a magnitude of 1.5-2p.u. VFTOs can, in extreme cases, exceed the BIL of equipment, although greater concern is risk of insulation flashover or aging when subjected to their steep rate of rise, along with the additional risks of coupling to external equipment. One of the most significant factors of initial VFTO

magnitude is the trapped charge voltage (TCV) magnitude. For conservative results, TCV is often assumed to be 1p.u. (or 1.1p.u. if additional safety factor is considered) [18]. This is contested by many authors whom after carrying out statistical studies, calculate the highest probabilities of TCV to be between 0.1 and 0.3p.u. [12]. This observation highlights the need for proper evaluation of TCV, so as not to prompt unnecessary precautionary measures. A basic overview of published mitigation techniques has been explored; with recently developed techniques such as the use High Frequency Resonator, showing great promise. Further research and development is nevertheless required to make mitigation a viable option.

An important consequence of VFTs is the generation of TEVs through electromagnetic coupling. The most significant point of coupling of TEV is the gas/air bushing. Analogous to VFTs, the travelling waves that propagate on the enclosure-ground plane, reflect and refract at discontinuities. Propagation is lossy and attenuation of the waveform is apparent. Even so magnitudes in excess of 0.5p.u. are reported [48]. While TEVs are considered to be low energy, short duration events, they still present a significant shock hazard; principally due to the indirect (startling) effects that could lead to secondary accidents. In addition to this, TEVs can result in the flashover of insulating gaps at flanges/cable terminations. Flashover initiated by TEVs could subsequently initiate the flow of power frequency circulating currents/fault currents which would likely damage insulation and joints. Suitably designed high frequency earthing and bonding is the best available mitigation technique for the reduction of TEV; although its effectiveness is often limited by the appreciable length of enclosure to ground straps. Other indirect mitigation techniques that have successfully been implemented include shielding of control cabling and GIS structures.

Correct modelling practices for VFT/TEV are essential for undertaking insulation coordination, parametric or design studies. Variations of software based on the EMTP method are commonly used for the simulation of transients in the time domain. The correct representation of components according to their characteristics at very high frequencies is crucial for the accuracy of simulations. Basic modelling requirements have been presented within this chapter for some of the key components within a GIS system.

Measurement and testing of GIS is essential for condition monitoring, commissioning activities and model validation. Several measurement techniques were reviewed, and collectively allow a full suite of VFT related measurements to be carried out.

Techniques presented range from the measurement of VFTs/TEVs at full operating voltage during a switching event to testing on a laboratory set-up on a small section of GIS using low voltage approximated waveforms. While the measurement techniques explored are designed to capture frequencies in the VFT range, insufficient detail is provided by authors on impedance matching techniques, shielding and bonding measures and data acquisition systems; all highly relevant at very high frequencies and above, particularly in high EMI environments, of which a GIS during switching certainly is.

Breakdowns at GIS elbows/T-junctions due to VFTOs are assumed to be rare due to the lack of published literature. However, it is apparent from the fundamental requirement of this research and anecdotal notes from network operators, that further investigation is required. Modelling guidance suggests that an elbow is simply modelled as a lossless transmission line [8]. However, this guidance may prove insufficient in some cases. Further research could ascertain field interactions at these problematic areas. Finite Element Modelling is possibly the best method for elucidating these interactions and has briefly been explored in [73], although the primary motivation behind the article was the comparison of 2D axisymmetric and 3D modelling of GIS. Development of measurement techniques that can better monitor the propagation of VFTs at these problematic areas may shed further light on the matter. In addition, further investigation into surface discharges at insulators in these locations when subjected to VFT may provide explanation for gas breakdown.

3 NUMERICAL MODELS OF AN OPERATIONAL GAS INSULATED SUBSTATION TO DETERMINE VERY HIGH FREQUENCY BEHAVIOUR

3.1 Introduction

Electrical system behaviour can be broadly categorised by either lumped or distributed behaviour. For transients that have wavelengths that are comparable to or smaller than the physical length of equipment to be studied, as is the case for VFTs and TEVs in GIS, propagation delays must be considered. Transmission Line Approximations (TLA), adopted by EMTPs are useful and can provide a good insight into the behaviour of transients in a system. Across the wide bandwidth, multiple frequency VFT range, TLAs begin to lose accuracy and can even become numerical unstable. TLAs have the additional limitation that they are only applicable to TEM mode, i.e. both electric and magnetic fields are perpendicular to each other and the direction of propagation. It is demonstrated that higher order mode propagation is possible within the VFT/TEV frequency range. Beyond TEM mode and above their relative cut-off frequencies, TM modes, i.e. only the magnetic field is perpendicular to the direction of propagation, or transverse electric (TE) modes, i.e. only the electric field is perpendicular to the direction of propagation, along with hybrid modes are possible. Xue et al. show through an extended transmission line model that a mode transition to a surface wave (TM mode, Sommerfeld-Goubau) occurs for a GIB in the first few tens of MHz, even for low soil resistivity and permittivity [74].

Therefore, for the accurate study of VFTs and TEVs, it is necessary to solve full Maxwell's equations through Numerical Electromagnetic Analysis (NEA) methods. An overview of NEA, along with the identification of parameters relevant to the investigation of VFTs/TEVs as wave problems, is provided in Appendix B.

3.2 Finite element models for the study of Very Fast Transients

Finite Element modelling of GIS components improves the understanding of the behaviour of electric and magnetic fields in and around a system. Computation results can be used directly for plotting fields or visualising propagation, providing both quantitative results and elucidation of wave propagation phenomenon.

To solve for propagating electric and magnetic fields, we must solve full Maxwell's equations; models are, therefore, built to solve a weak form of an electromagnetic wave equation. In COMSOL, this is implemented using the RF module. It is first necessary to build discrete models of key components, to study the frequency response in isolation, followed by a complete circuit 1 model, to understand the interactions across the system. Detailed models for equipment specific to Substation 'A' are constructed, based on information obtained from the network operator. The layout of the Substation is shown in Figure 3.1 and Figure 3.2. Bus supports are insulated from the enclosures and are not included in the finite element models.

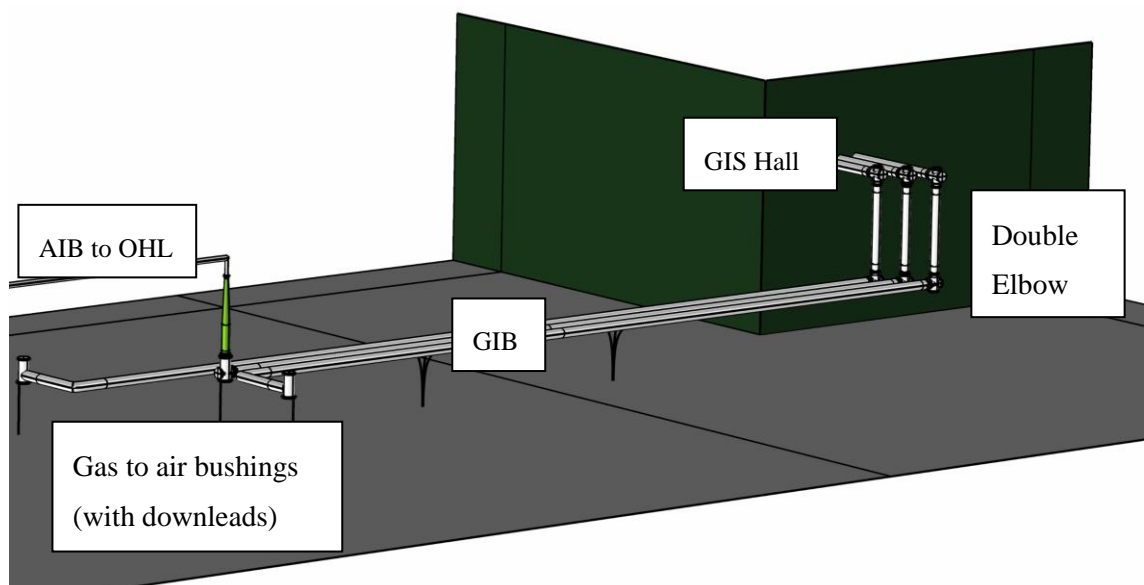


Figure 3.1: 3D model view of Substation 'A' Circuit 1 (bus supports excluded).

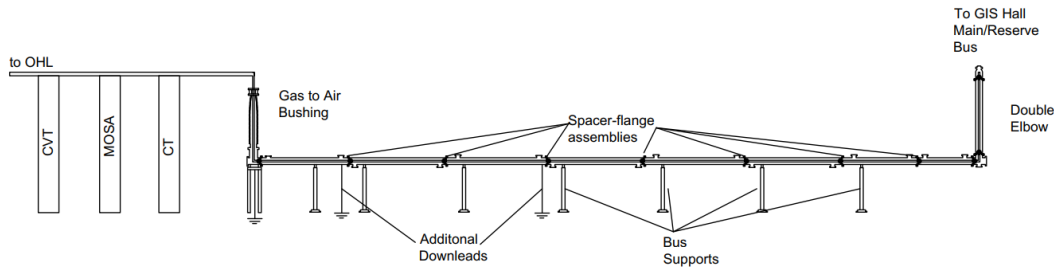


Figure 3.2: Side 2D view of Substation ‘A’ Circuit 1 outdoor GIS/AIS layout.

The models in this chapter are configured with an external air domain/ground, to assess the impact of each acting as an aperture and promoting coupling externally. Due to the potential excitation of higher order modes at discontinuities, each model is excited by a port boundary backed with an air domain and truncated with a PML. Excitation of models is achieved through the use of port boundary conditions, which concurrently allow the extraction of S-parameters.

For the models presented in this chapter, a list of material characteristics and boundary conditions applied are provided in Table 3.1 and Table 3.2, applicable to both frequency and time domain studies. Due to the ratio in scale of the geometries for the models, ranging from 1mm resolution to 70m, it would not be efficient or even possible to mesh all metallic components; a PEC or IBC is instead used as appropriate; the choice between the two depends on the simulation type and an assessment of the DoF/required computational resources. While the permittivity of metals tends to infinity, for simulation purposes a default of 1 can be used so long as the conductivity is set appropriately.

Table 3.1: Bulk Material parameters

Material	Conductivity (S/m)	Relative Permittivity (ϵ_r)	Relative Permeability (μ_r)
Air	0	1	1
SF ₆	0	1.002	1
Aluminium	3.77e7	1	1
Steel (assumed austenitic)	4.03e6	1	1
Epoxy	1E-17	4.1	1
Porcelain	1E-17	6	1

Soil	Range - 0.001 to 0.01	Range 1 - 40	1
Bolt insulation (unknown material-where applicable)	1E-17	1	1

Table 3.2: Finite element model parameters

Model	Component – Material - Boundary conditions
Spacer-flange	Bus and enclosure – Aluminium – IBC (FD), PEC (TD) Bolts – Steel - IBC (FD), PEC (TD) Bolt insulation (where applicable) Spacer - Epoxy Resin SF ₆ Air domain - external PML (FD), scattering boundary (TD) Ground – PEC (TD/FD) or IBC (FD where applicable)
Elbow	Bus and enclosure – Aluminium – IBC (FD), PEC (TD) Bolts – Steel - IBC (FD), PEC (TD) Bolt insert (where applicable) Spacer - Epoxy Resin SF ₆ Air domain - external PML (FD), scattering boundary (TD) Ground – PEC (TD/FD) or IBC (FD where applicable)
Bushing	Bus and enclosure – Aluminium – IBC (FD), PEC (TD) Bolts – Steel - IBC (FD), PEC (TD). Spacer - Epoxy Resin Bushing insulation – Porcelain SF ₆ Air domain - external PML (FD), scattering boundary (TD)

	Ground - Soil
Full scale GIS	Bus and enclosure – Aluminium – IBC (FD), PEC (TD) Bolts – Steel - IBC (FD), PEC (TD) Spacer - Epoxy Resin - (some spacers neglected to reduce model size) Bushing insulation – Porcelain SF ₆ Air domain - external PML (FD), scattering boundary (TD) Ground – PEC (TD/FD) or IBC (FD where applicable)

3.2.1 Spacer-flange assembly

Due to a previous spacer surface flashover at a Substation ‘A’, it was necessary to investigate the field distribution at the spacer-flange interface. The spacer-flange is of the unshielded type. To investigate the behaviour of fields at the spacer-flange interface several models were created; looking at strictly internal behaviour only and expanded for the study of the internal behaviour when the spacer as an aperture is considered (assuming the flange bolts are floating as an absolute worst case). Given the previous arcing problems witnessed at multiple bolt locations across the GIS, it does seem pertinent to investigate any possible consequences or risks to insulation that may also be present.

The spacer model, shown in Figure 3.3, consists of the detailed spacer profile, bus with a simplified shield arrangement and the detailed flange/enclosure assembly. The model is surrounded by an external air domain with a PML and 3m above a perfect ground plane and the enclosure is extended into the PML to avoid external reflections. Coaxial ports, with a characteristic impedance of 67.74Ω , separated by 1m across the spacer internally, both excites the bus with a controlled voltage and absorb transmitted and reflected electromagnetic waves.

A range of frequencies are selected for the simulation; ensuring frequencies relating to the dominant frequencies are present and at a fine enough resolution, will provide a more accurate response. For the frequency domain simulation, a time harmonic wave equation is solved for each frequency point.

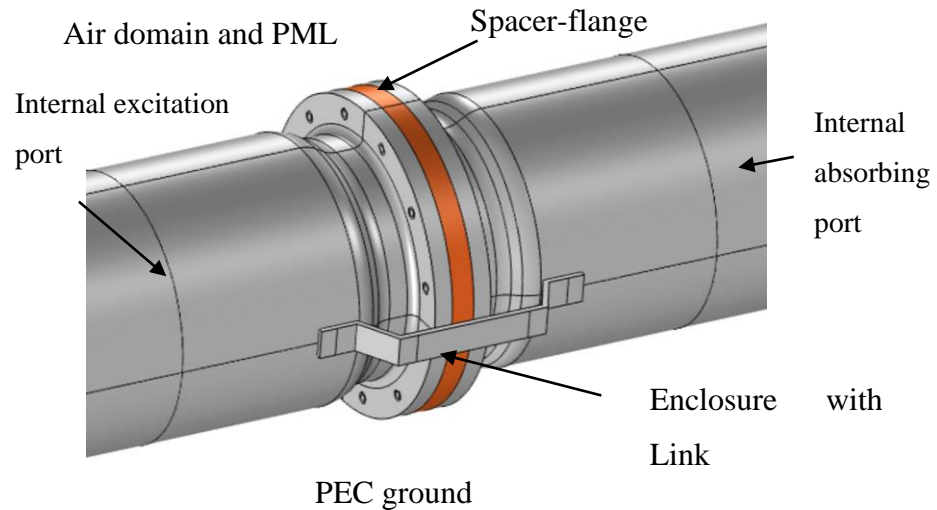


Figure 3.3: Spacer-flange finite element model.

The breakdown of dielectric gases under VFTOs is complex but is often compared to breakdowns under Lightning Impulse. Evidence suggests that under uniform field conditions, the VFTO magnitude required to initiate a breakdown is above the Lightning Impulse Withstand Limit (LIWL), for which system insulation levels are coordinated [21]. Under non-uniform field conditions, the voltage required for breakdown under VFTO can be considerably lower [75].

With this in mind and given the magnitudes calculated in initial simulations, under ideal conditions, there is unlikely to be a surface flashover of a spacer at the VFTO magnitudes anticipated. Nevertheless, even subtle changes in the field distribution, occurring due to particle contamination, excess moisture or even space charge accumulation, can reduce the dielectric strength of the spacer.

Non-ideal internal conditions aside, a possible candidate for promoting flashover due to fields, identified through these simulations, is ineffective bonding of the bolts securing the spacer flange assembly. This could occur where bolts are inserted through an insulated sleeve, compressed onto a painted surface or even a corroded connection. The enclosure links on the system in question, bonding one section of enclosure to another at the flange assembly, provide a path for power frequency return currents; simulation results suggest that they are ineffective at containing high frequency transients beyond a 20-30 MHz and it is well-known that fields can emerge at this location. A review of literature did not reveal any research that reports the effects of poor containment of fields on the internal VFTs, however, previous issues reported at Substation ‘A’ with sparking at bolts and enclosure links at numerous locations over the system during

disconnector operations implies that the flanges were not appropriately bonded, therefore some investigation of the cause is necessary. Initial models were built under the assumption that the bolts are galvanically connected to the enclosure. To investigate the effects of ineffective bonding (or even an intended disconnection), a floating bolt scenario was evaluated to demonstrate and compare both extremes.

3.2.1.1 Frequency response – bonded and floating bolts

For the frequency domain simulation, the calculated S-parameters for both an effectively shielded (perfect electrical connection between bolts and flange) and ineffectively shielded (floating bolts i.e. no galvanic connection) spacer. S-parameters and (following conversion) input impedance plots are presented in Figure 3.4 for both cases, a perfect connection and no direct connection between the bolts and the enclosure. It is clear that the reflectance for the floating bolt model becomes increasingly significant, reaching a peak at the quarter wave resonance. The quarter wave resonance occurs at a reduced frequency of 40MHz, compared with an anticipated 75MHz for an equivalent coaxial bus of the same dimensions, assuming no discontinuity between the ports. Appendix A provides an overview of the parameters utilised in the simulation results throughout.

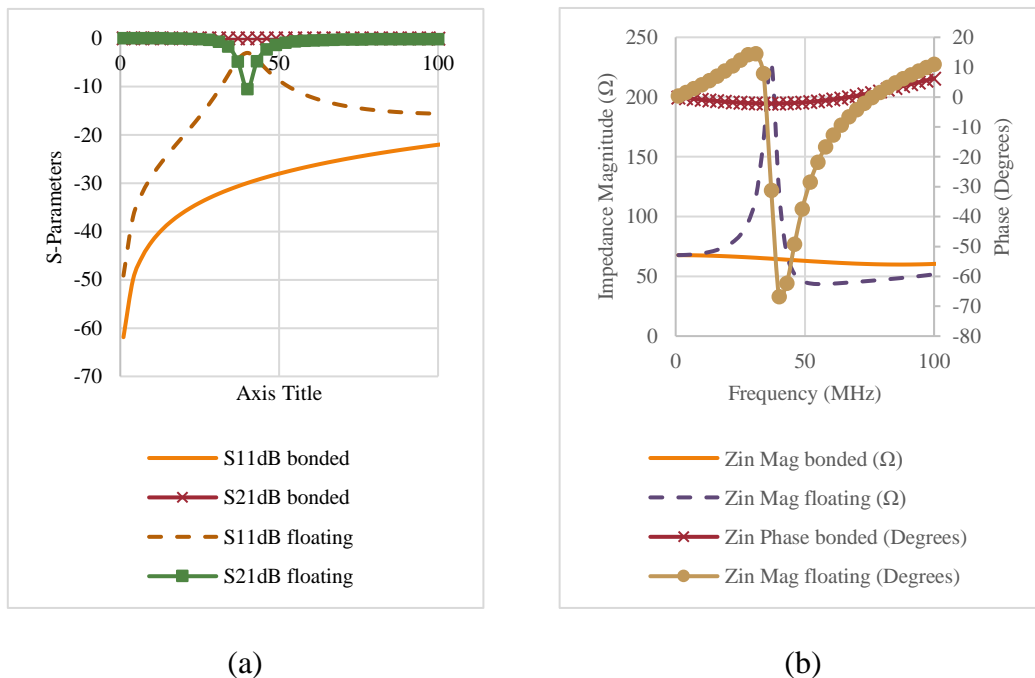


Figure 3.4: Spacer-flange computation for perfectly grounded and ungrounded bolts (a) S-parameters, (b) Impedance.

3.2.1.2 Electric field distribution – bonded and floating bolts

The maximum electric field, evaluated along a line that extends from the bus, along the spacer surface to the edge of the spacer, for both extremes is shown in Figure 3.5. The computed field at the surface is considered as the average of the fields at both sides of the boundary, i.e., the average of the field components immediately above the surface and the field immediately below the surface (in the bulk). The surface fields colour plot and magnitude are shown in Figure 3.6. For the bonded bolt model, the highest field is on the concave side, with the peak closer to the HV bus at 3.78 kV/mm. The floating bolt model presented much higher fields close to the triple junction on the side of the oncoming surge at 17.2 kV/mm.

The fields presented are based on the assumption that excitation of the bus at from 0 p.u. to 1 p.u occurs initially in one direction only. The end of the bus section includes a lumped element termination, equivalent to the characteristic impedance of the bus. The field magnitudes calculated do not consider any power frequency fields which in comparison of time frames would appear stationary. The transient fields could superimpose with the power frequency fields, leading to magnitudes in excess of those presented. The calculated peak steady state field of 2.75kV/mm, with the maximum VFT field for a floating bolt spacer-flange, assuming constructive superposition, could lead to a resultant field for a 2 p.u. VFTO of 19.9 kV/mm.

Considering the intrinsic breakdown strength of SF₆ is 8.9 kVmm⁻¹bar; and assuming a weakly non-uniform field and applying the suggested 0.75 factor for lightning impulse thresholds from [5], the reduced critical field strength for the system at 4 bar is 26.7 kV/mm. From the results presented, assuming VFTO at 2p.u., there should be no risk of discharge for the horizontal bonded/floating spacer-flange assembly in an ideal internal environment. The field is, however, relatively high from a spacer design perspective, easily exceeding the maximum 3-4kV/mm gradient for epoxy [29]. The breakdown threshold considering contamination or space charge accumulation could be further reduced, however, it is not possible to quantify directly from the models built. For the floating bolt model, the field magnitudes presented do not include the magnitudes computed at the bolts (which are considerably higher), due to the uncertainty of the bolt arrangements.

As discussed in Chapter 2, there is a statistical element to discharges under VFTs. If the waveform at a particular location is very oscillatory, there may not be sufficient time for

a discharge to propagate and therefore a breakdown is not guaranteed. Nevertheless, repeat failed VFT (creeping) discharges could degrade or age the spacer surface and thus promote breakdown at a lower threshold over time.

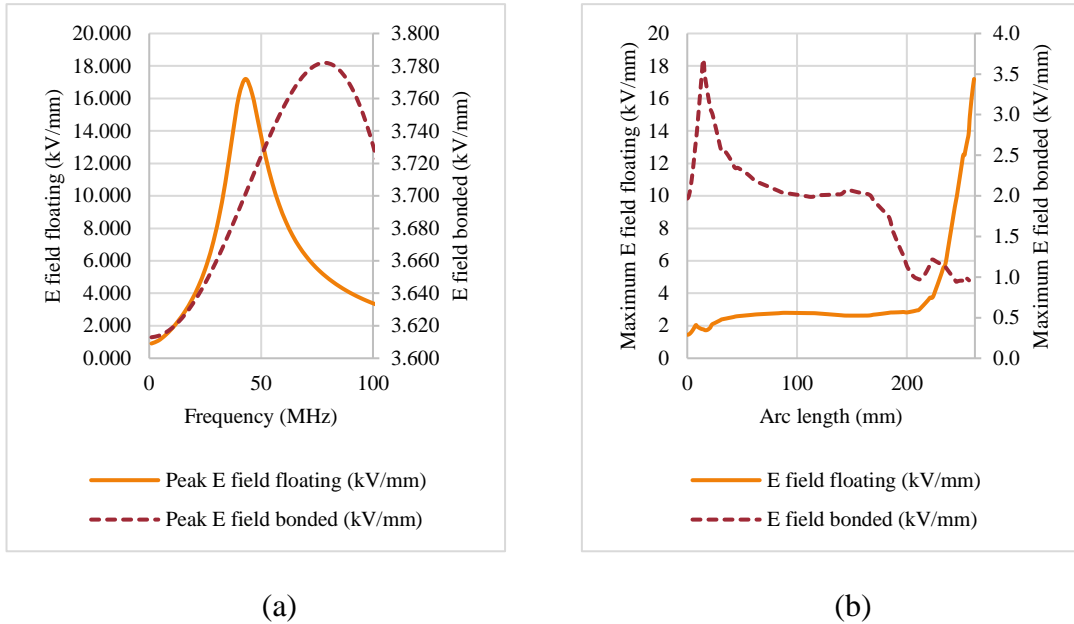


Figure 3.5: Spacer field distribution (a) peak E field vs frequency (b) peak E field profile along spacer corresponding to 40MHz.

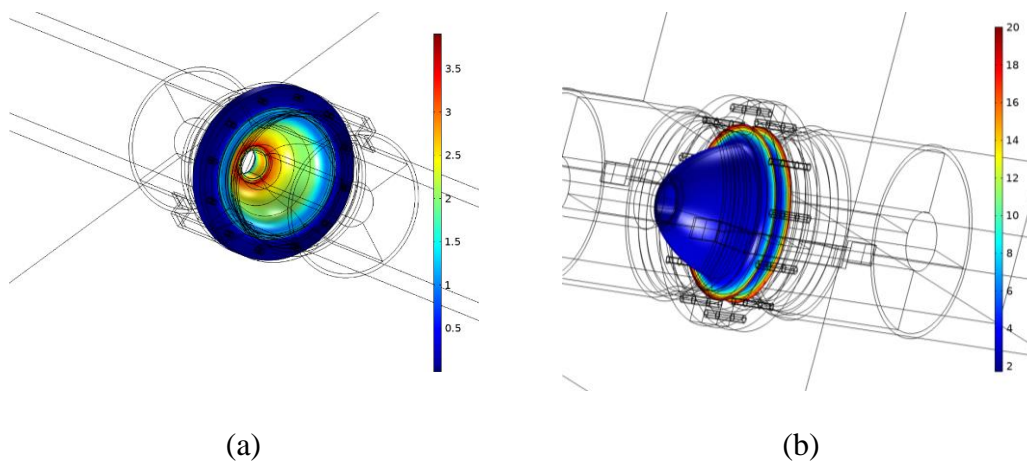


Figure 3.6: Spacer field distribution colour plot (a) bonded at 73MHz (b) floating at 40MHz.

A further scenario regarding the shielding effectiveness of the spacer-flange assembly, possibly one that is more credible than a floating bolt extreme, is a poor (although intended) electrical connection between the enclosure and the bolts. This has been

experienced previously at Substation ‘A’, evidenced by excessive arcing at bolts and rectified to some extent with serrated washers. The effect of the bolt’s resistance to the flange on the transmitted/reflected power can be demonstrated by varying the conductivity of the bolt insert. Alternatively adding lumped elements, transition boundary conditions or physically modelling a connection to the enclosure would work. S11dB and S21dB (reflection and transmission coefficients) for a coarse sweep of conductivity at 40MHz are shown in Figure 3.7. The plot demonstrates that for increased bolt conductivity, internal transmission increases, while internal reflection decreases.

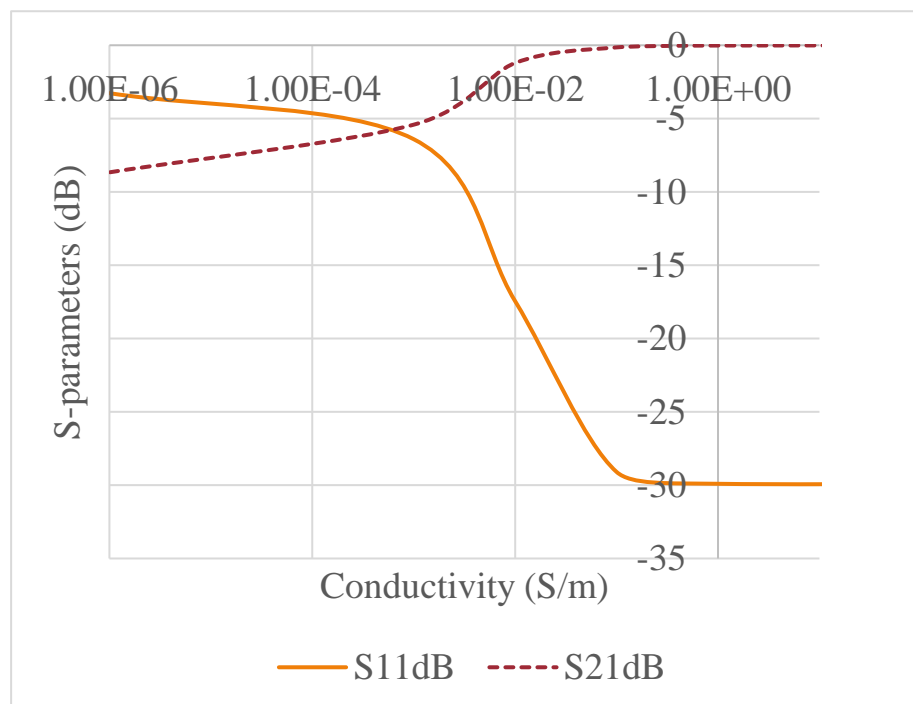


Figure 3.7: Computed bolt conductivity vs reflection/transmission coefficients.

It is possible to deduce a minimum conductivity for the bolts to the flange from Figure 3.7. A low reflectance, in terms of S11dB is generally considered to be anything below -15dB. To achieve this, the bolts would require a resistance to the enclosure/flange to be below approximately 100Ω , which, providing a clean connection is available, should be easily achievable.

Regarding internal propagation, a further point to note is the potential occurrence of wave tilt phenomenon. For an adequately shielded spacer, there does not appear to be any significant wave tilt effects and encouragement of higher order mode propagation in the VFT frequency range assessed (possibly some minor tilting of the E field at the bus

shield, Propagation following the spacer is quasi-TEM mode. For an ungrounded spacer-flange, there is an increase in out of plane field (in this case the y-component) throughout the spacer bulk around the resonant point, as shown by Figure 3.8. When looking at the resultant E field vector plot it is demonstrated that the majority of y-component field occurs through the spacer at the flanged section. This is essentially behaving like a feed point or excitation of a dipole antenna and suggests that an increased transfer of energy along the external enclosure will be seen around this frequency point.

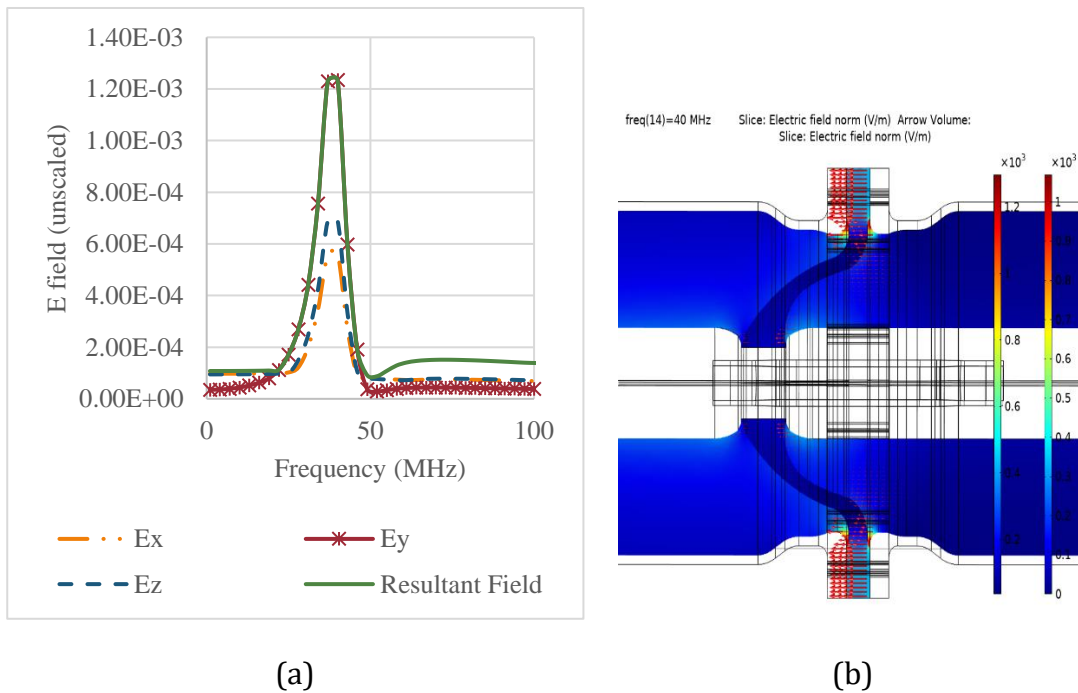


Figure 3.8: Electric field at spacer interface for floating bolt model (a) plot of field components (b) colour and vector field plot.

3.2.1.2 Coupling between internal and external transients – bonded and floating bolts

The extent of coupling between internal and external transients is investigated further. Unshielded spacers are a known coupling location for TEVs. The degree of coupling to the enclosure at the spacer-flange interface appears to be strongly dependent on the bonding around the flange and hence, the shielding effectiveness of the assembly.

The model is expanded to further explore this coupling. External enclosure to ground, domain-PML backed, numeric TEM mode ports are added to evaluate the transmittance/coupling to the external enclosure sections, as highlighted in Figure 3.9. The addition of a numeric port meant that a mode analysis step must be carried out prior

to the main model simulation. As discussed, TEM mode is not dominant throughout the entire VFT/TEV bandwidth and higher order modes can exist, however, to permit the use of S-parameters and allow the quantification of transmission, reflection and coupling to the enclosure, the following models are initialised with the AIB/GIB ports at 1MHz, with an effective mode index of 1 to ensure a quasi-TEM field profile. This is computed, initially, under the assumption that TEM mode field shape is not considered to vary over the frequency range.

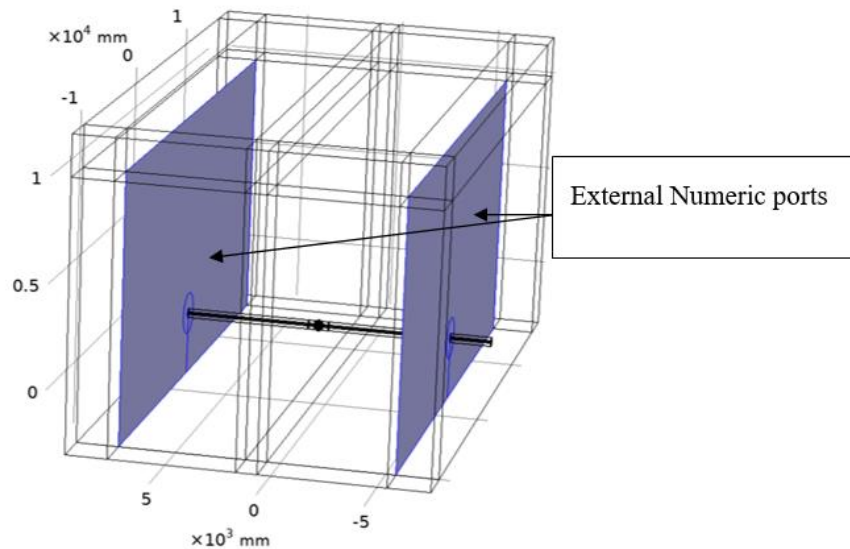


Figure 3.9: Spacer-flange model for TEV coupling.

No additional ground conductor was applied to represent a spacer-flange far from the bushing and GIS hall, and hence, no immediate connection to a grounding system. The extent of the coupling is best demonstrated with S-parameters. S31dB and S41dB are the transmission coefficients describing the transmission between internal and external ports, i.e. the shielding effectiveness of the spacer-flange. S31dB represents the coupling to the external port, located in opposition to the direction of internal incident wave propagation and S41dB represents the coupling to the external port located in the direction of internal incident wave propagation. This computation is inherently looking at the shielding effectiveness of the bolts. It is demonstrated that for the effectively bonded enclosure, the transmitted power is very low over the range. This is not the case for the ungrounded spacer-flange bolt model. The results suggest that coupling externally for the first few tens of MHz is small and builds up to a peak at approximately 40MHz. This also coincides with the peak reflectance for the excitation port, implying a quarter wave resonance. The conclusion that can be drawn from the results is that the highest degree of coupling coincides with the quarter wave resonant

point. A peak transmittance of -11.2dB occurs (or 0.27 p.u. of the VFT) for the floating bolt model, in contrast to a peak of -59dB (or 0.001 p.u of the VFT). The transmittance in both directions is almost identical, however, in reality this would be influenced by the presence of external metallic structures.

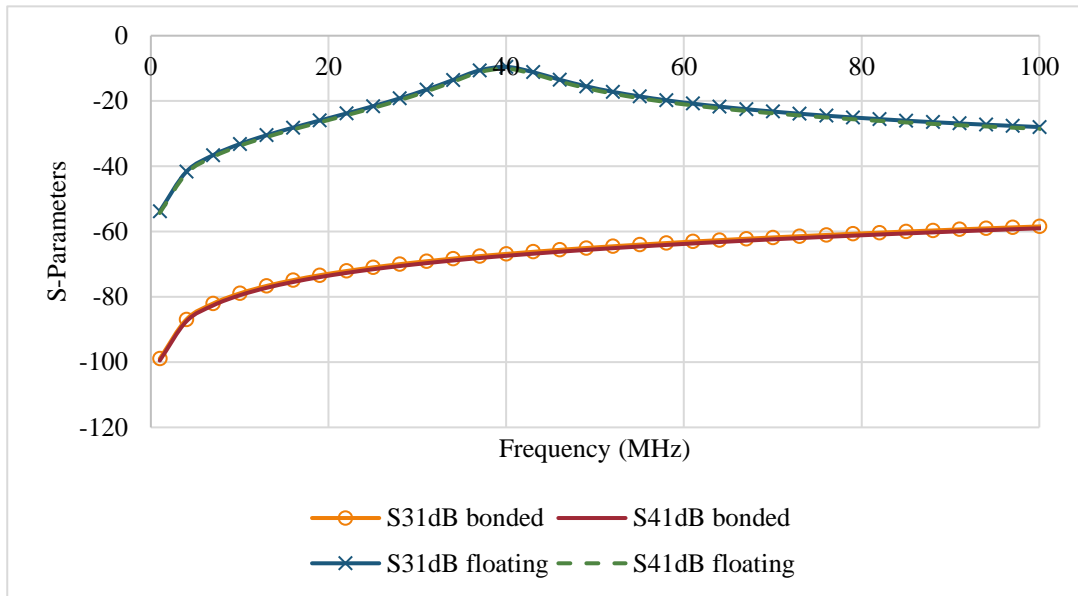


Figure 3.10: S-parameters detailing transmittance from internal excitation port to external enclosure 6m away along a perfect ground.

3.2.1.4 Potential radiation conditions

The electric and magnetic field vector plots in Figure 3.11 appear to demonstrate some radiation. Computed far field plots for a single section of ungrounded bus/enclosure are provided in Figure 3.12, demonstrating the possible radiated field patterns. While it is not the intent of this thesis to study antenna behaviour of the enclosure, the author believes this is noteworthy and should be considered for further investigation, as the impact of a high-power dipole antenna on EMC in and around a substation during disconnector events could be uncertain. Furthermore, multiple spacer-flange apertures could act together as an array, leading to a stronger antenna effect. An effective multiple downlead/ground system along the enclosure could possibly mitigate this effect to some extent, however the downlead height could limit its effectiveness, as discussed in the next section.

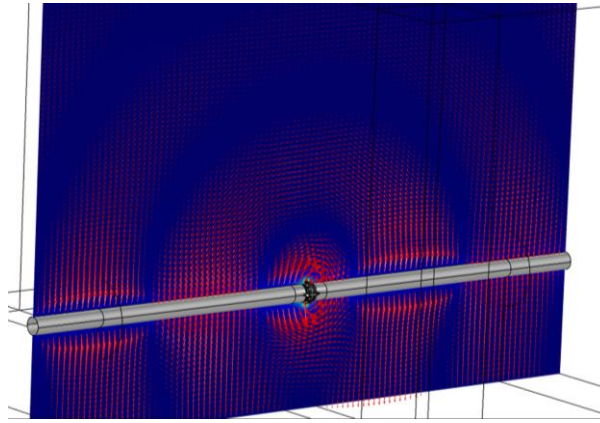


Figure 3.11: Formation of electric dipole across the spacer-flange, appearance of radiating fields.

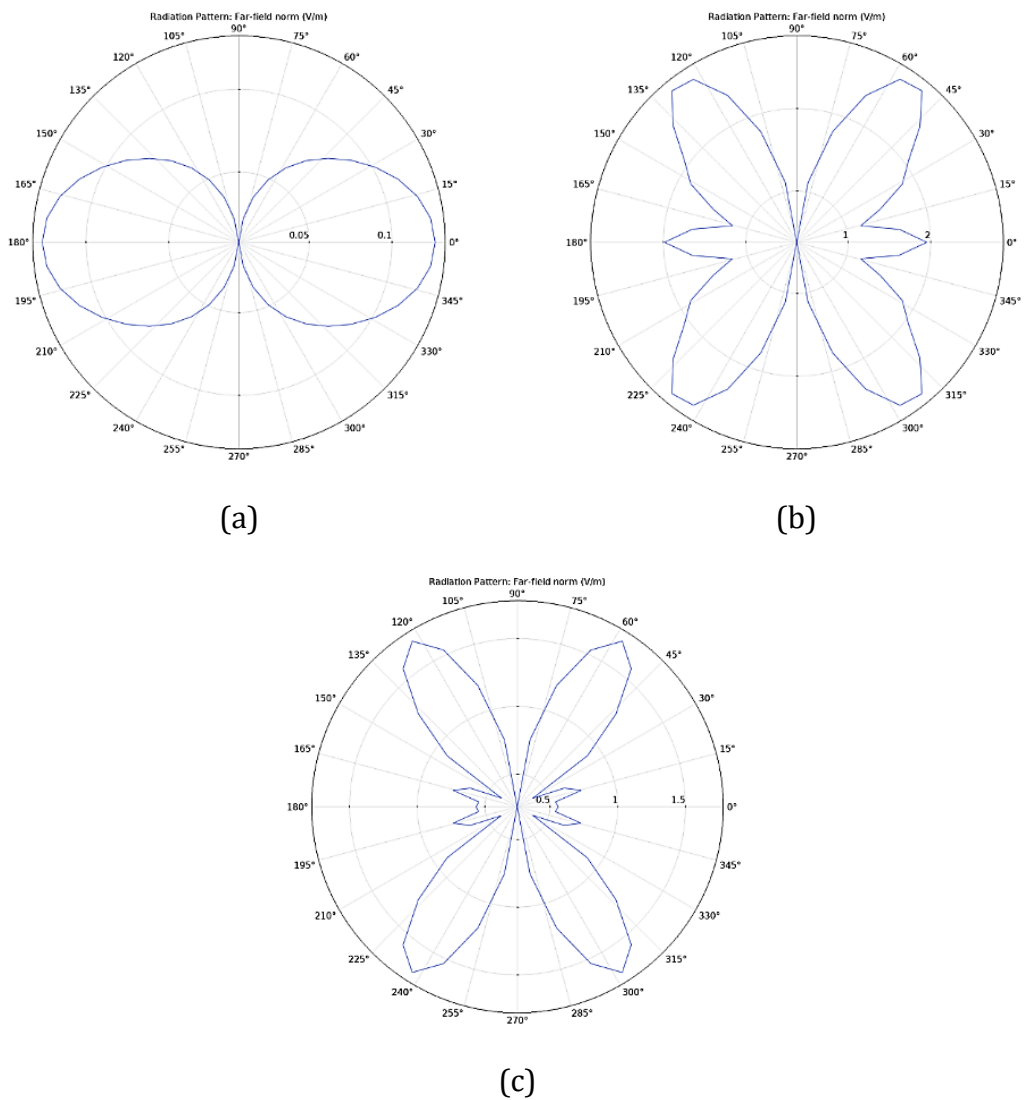


Figure 3.12: Far field plots viewed on horizontal plane (a) 12.5MHz, (b) 50MHz and (c) 75MHz.

3.2.2 Elbow

The 90° elbow is anecdotally considered the ‘weak’ point of the GIS insulation. The sharp bend could encourage resonances and is known to excite higher order modes for frequencies in the PD spectrum [76]. To investigate the transient behaviour of the GIS elbow for the VFT frequency spectrum finite element models were created and followed a similar approach to that used previously to investigate the spacer-flange behaviour. The behaviour of a single elbow was investigated and published as part of the modelling strategy in [77]. The failure at Substation ‘A’ occurred at spacer forming part of a double elbow section, immediately adjacent to the entrance to the GIS hall, therefore it is prudent to investigate a double elbow section further. The finite element model created is shown in Figure 3.13. The section is surrounded by a truncated air domain, above a PEC ground and adjacent to a metallic wall (IBC) representing the steel enclosure of the GIS hall. The model is excited at the point of entrance to the GIS hall and is terminated with a port of matched impedance, backed with a PEC cap to prevent the influence of external fields. Due to the proximity of the spacers at either side of the elbow, it is necessary to include them in the simulation. Furthermore, given the impact of the shielding effectiveness of the flange assembly on results it seems pertinent to also include them.

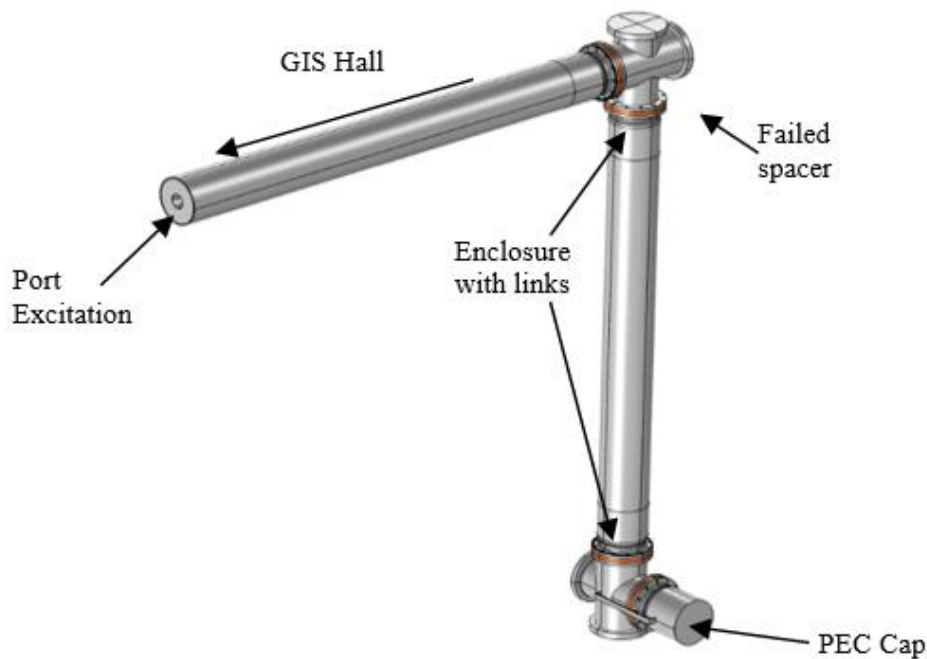


Figure 3.13: 3D representation of the double Elbow for Finite Element Analysis.

3.2.2.1 Elbow Frequency response – bonded and floating bolts

Frequency domain simulations were carried out for 1-100MHz for both an effectively bonded and floating (ungrounded) flange bolt option. The computed S-parameters for the double elbow arrangement are presented in Figure 3.14. The input impedance, derived from the S-parameters is also provided in Figure 3.15 for reference.

In comparison to the spacer-flange model, the double elbow model exhibits many resonant points throughout the spectrum for both the bonded and floating bolt options. Considering transmission lines, resonant points are subsequent periods of highest or lowest reflection; resonances are periodic, occurring at even or odd multiples of the quarter wavelength, depending on the type of termination, being short or open circuit. Given the results for the bonded bolts model and considering the length of the sections (port 5.2m to upper elbow, 5.5m to lower elbow, 0.9m to termination, total port to termination distance is 11.6m), the resonances are not purely multiples of the quarter wave and are distinctly representative of discontinuities. Nevertheless, the input impedance profile varies around the characteristic impedance, with a maximum of 102.6Ω and a minimum of 51.2Ω .

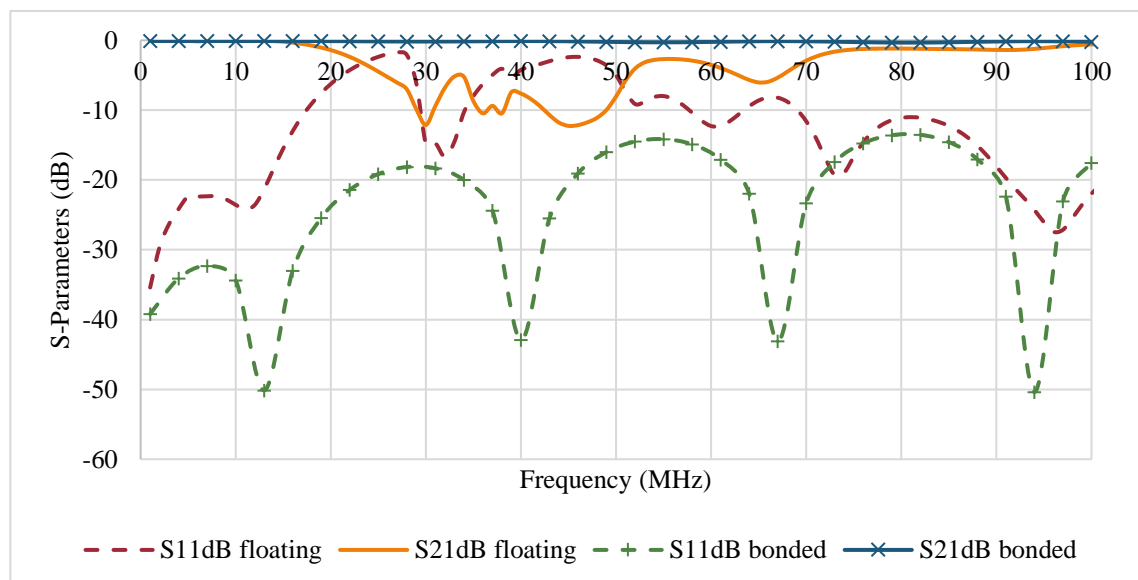


Figure 3.14: S-parameters of double-elbow for bonded and floating bolts arrangements.

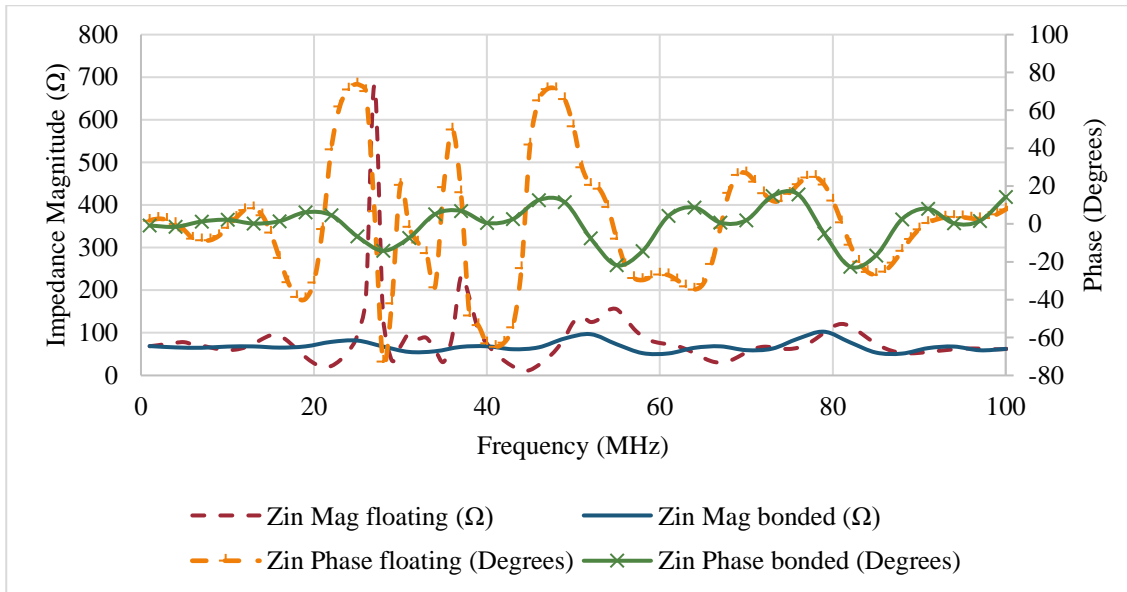


Figure 3.15: Derived impedance of double-elbow models for bonded and floating bolts arrangements.

3.2.2.2 Elbow electric field distribution – bonded and floating bolts

The resonances present for the floating bolt case are similar in quantity but far less subtle. Furthermore, a large cavity-like resonance occurs at approximately 27MHz. Much larger impedance swings occurs, with the maximum coinciding with the sharp cavity-like resonance, at 681.2Ω and the minimum drops to 11.1Ω . This does imply that the voltages and thus, electric fields will vary from the lower frequency, ‘design’ field magnitudes. The computed peak electric field magnitudes between 1-100MHz along the spacer surface (the spacer location identified in Figure 3.13 as location of surface discharge) is shown in Figure 3.16. The peak fields for the bonded and floating models, occurring at 58MHz and 35MHz respectively. The fields are evaluated along a line traversing the spacer from the HV conductor to the enclosure (arc length). A peak field for the bonded model of 3.08 kV/mm occurs at the HV conductor, whereas a peak field for the floating model of 27.62kV/mm occurs near the triple junction, as observed in Figure 3.17.

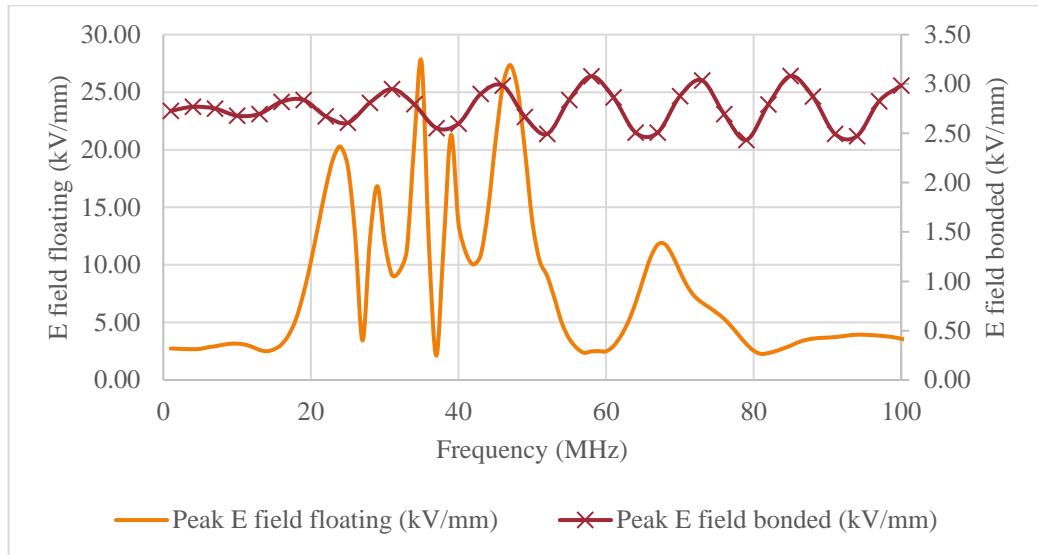


Figure 3.16: Peak E field along spacer surface vs frequency (upper spacer in Figure 3.13).

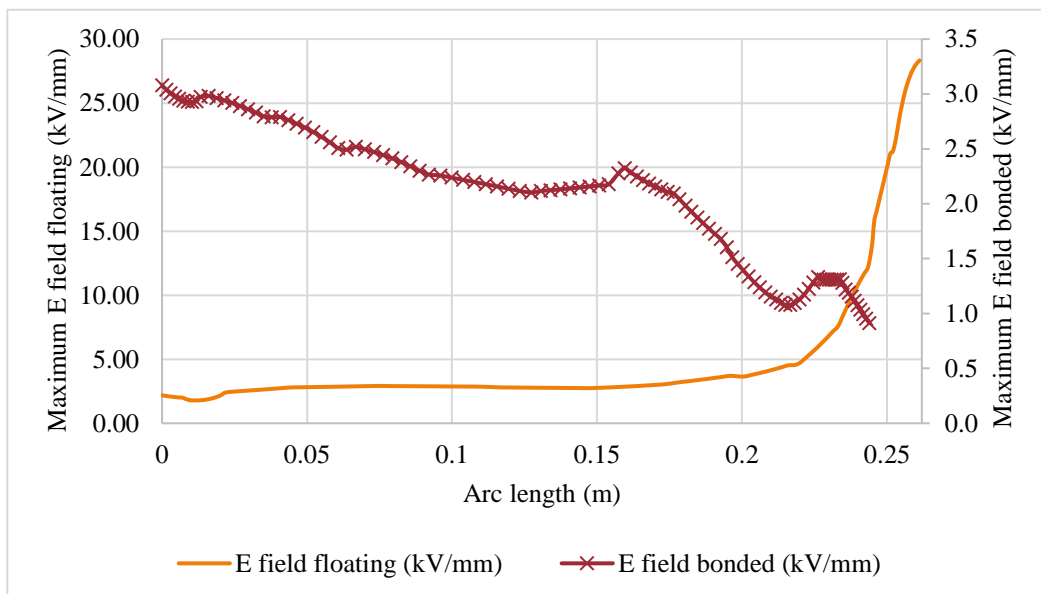


Figure 3.17: E field along spacer surface from HV conductor to enclosure (arc length) (upper spacer in Figure 3.13).

As with horizontal spacer-flange fields assessed in the previous section, the fields presented are based on excitation of the bus from 0 p.u. to 1 p.u. in the frequency range 1-100MHz; a power frequency field component could also be present. The maximum resultant field, occurring for the ungrounded bolts, including calculated steady state field of 2.75kV/mm could reach a peak of 30.37kV/mm. Again, the magnitudes are based on 1p.u peak at each frequency point. Given the behaviour demonstrated for both spacer-flange and elbow models, in addition to the observed arcing at bolts across the

GIS, ineffective shielding may have contributed to the early failure of the spacer at Substation ‘A’.

3.2.2.3 Elbow transient simulation – bonded and floating bolts arrangement

Further to the frequency domain simulations, a transient simulation for the elbow bonding and floating bolt arrangements were carried out in COMSOL to understand the impact of a double elbow arrangement on internal VFTs. The excitation and termination reports were maintained at the same locations, however, a 6ns rise time step voltage at 1V was applied (allowing easy scaling of output variables). A step voltage input of this nature basically replicates a time domain reflectometry (TDR) style approach, allowing the reflected waves to be easily observed, as shown in Figure 3.18. The results demonstrate significantly higher positive reflections, followed by a marginally higher negative reflection for the floating bolt arrangement. The peak constructive reflection of magnitude 1.17p.u. is seen at 89ns for the floating bolt arrangement, while only 1.015p.u. at 92ns for the bonded bolt arrangement. Furthermore, the initial reflections are followed by some ringing, with an oscillation frequency of 29.4MHz. This is likely be associated with the excitation of a resonance.

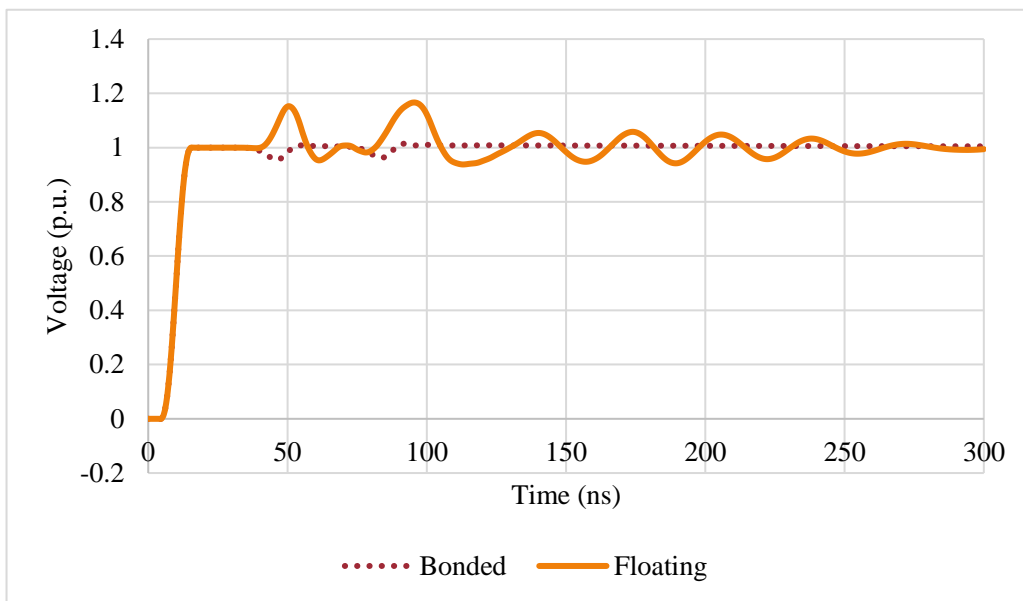
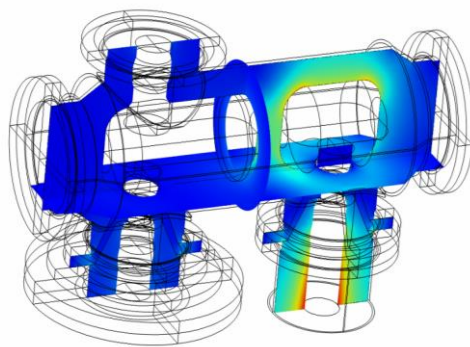


Figure 3.18: Transient double elbow simulation, input voltage step showing reflections.

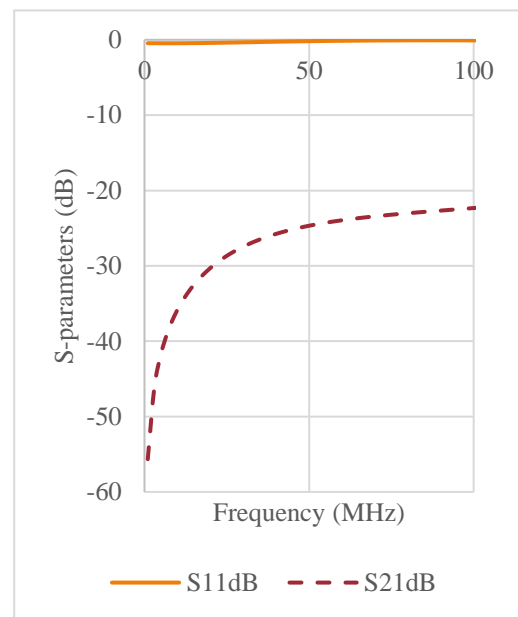
3.2.3 Disconnecter

A disconnecter model was created to initially for the computation of equivalent parameters to be used with a custom disconnecter EMT model. The model and its response is provided in Figure 3.19. The disconnecter model. While basic in its existing

form, it quantifies the magnitudes of surges that can transfer across the gap when in the open position. The transmittance across the open gap increases over the frequency range, reaching a peak of -22.3dB at 100MHz . This means that for 100MHz components a maximum of 0.08p.u. will transfer across the gap. For a 2p.u. VFTO, this suggests that a significant 45.7kV could be present at the outlet port (assuming a matched port input impedance. This could further increase due to reflections at the other isolated This also suggests that work on an assumed ‘dead’ and isolated section of a system should not take place during the switching of other circuits. The model can be further developed to imitate arcing behaviour across the contacts, for the generation of VFTs.



(a)



(b)

Figure 3.19: 3D model of open disconnector and frequency response (a) Electric field distribution (b) S-parameters vs frequency.

3.2.4 Gas to Air Bushing

Aside from the trapped charge magnitude, the most important component in terms of peak VFTO magnitude and waveshape is the gas-air bushing, as it is generally considered the most significant discontinuity to very high frequencies, with characteristic impedance increase from that of the coaxial bus, up to the characteristic impedance of the AIB (calculated approx. 330Ω for 8m bus height). As discussed in Chapter 2, as an approximation the gas to air bushing can be considered as a junction of three impedances; the impedance of the coaxial GIB, the impedance of the AIB and the

impedance of the enclosure. To investigate the coupling mechanisms and quantify the internal reflections and external refractions at the gas to air bushing, the finite element model shown in Figure 3.20 was developed. The bushing assembly does not include the silicone sheds (due to the significant increase in DoF), the model is otherwise a detailed full-scale representation of the actual bushing at Substation ‘A’, built from site detailed drawings, including the internal conductor with shielding, ports and enclosure bonding. All metallic components are unmeshed with a PEC boundary applied. The model is excited internally, in the frequency domain, by a port 1m away from the bushing along the GIB enclosure. Numeric TEM ports, initialised at 1MHz, are assigned between the outer AIB-ground and GIB-ground planes to compute the transmission between internal and external environments. The AIB ports are situated 6m away, while the GIB enclosure port is situated 12m away to avoid the influence of near fields emanating from the bushing interfering with the port fields, therefore, considering only fields that are propagating along each corresponding planes. For a more realistic assessment the grounding connected directly at the bushing is included in a $100\Omega\text{m}$ soil domain.

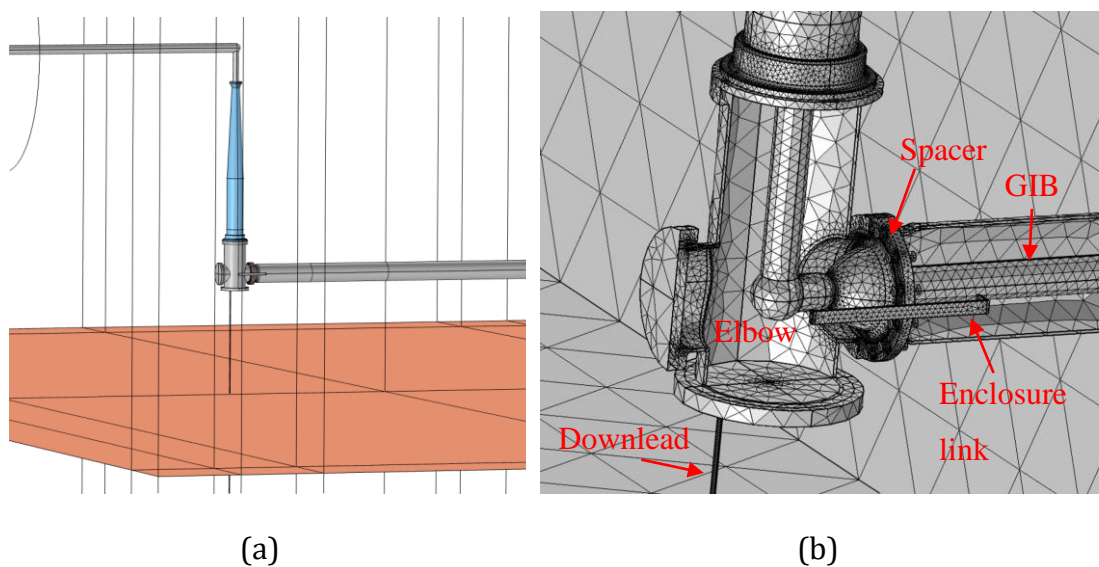


Figure 3.20: 3D bushing model (a) front view (b) magnified view of internal bushing model.

Through modelling, it was found that the extent of the TEVs present on the enclosure is highly dependent on the effectiveness of the grounding at the bushing. An ineffectively grounded bushing will result in greater coupling to and propagation along the enclosure than one that is effectively bonded.

It is well known that the effectiveness of a grounding system at very high frequencies is influenced by the downlead, with the limitation being the height of the enclosure. For the system at Substation ‘A’, the bus is installed a minimum of 3m from the ground. The Z_c gradually reduces to from the top of the downlead down to the Z_c at the surface. A problem that may not be well appreciated is the Z_c magnitude at the top of the downlead, calculated using Equation (3.1) [78], can be very high, leading to a large mismatch of impedances and thus a low transmission, high reflectance behaviour.

$$Z_c = 60 * \ln\left(\frac{2 * height}{radius}\right) \quad (3.1)$$

The calculated Z_c , for the GIB enclosure for the 3m high section of bus at Substation ‘A’ is approximately 196 Ω , while the Z_c for an 8mm radius downlead is approximately 397 Ω . Given Equation (3.1), the fixed variable is clearly the enclosure height. Therefore, the only variable that can be influenced to reduce the characteristic impedance is radius of the conductor. Increasing the downlead radius would reduce the Z_c , but it is an uneconomic and unfeasible solution, and the weight of the cable would quickly become a risk for the enclosures integrity before an effective reduction is witnessed. An option explored through simulation is to include multiple smaller downleads, tapered out from a common connection point to form an equivalent, considerably larger radius. A number of configurations were explored, maintaining a requirement that the combined equivalent diameter is at or below that of the base of the bushing (700mm), so that the additional footprint of the bushing is not increased. Through numerous finite element simulations, the downlead quantity and profile was optimized to produce the smallest peak input impedance in the VFT frequency range, when terminated to a 4.8m vertical rod in a 100 Ω m soil. The size and length of all downleads are identical (8mm radius, 3m height). The resulting multi-downlead profile (which will replace a single downlead at the bushing’s base) along with the electric field pattern confirming an effective increase in radius is provided in Figure 3.21. The electric field inside of the multi-downlead ‘cage’ is very low and would approach zero for higher frequencies as the number of downleads is increased, similar to the electric field behaviour for a single conductor of the same equivalent radius. The single and multi-downlead options are included for the purpose of computing coupling to the enclosure, the specifics on input impedance of the single and multi-downlead to vertical rod combinations are explored further in Chapter 4.

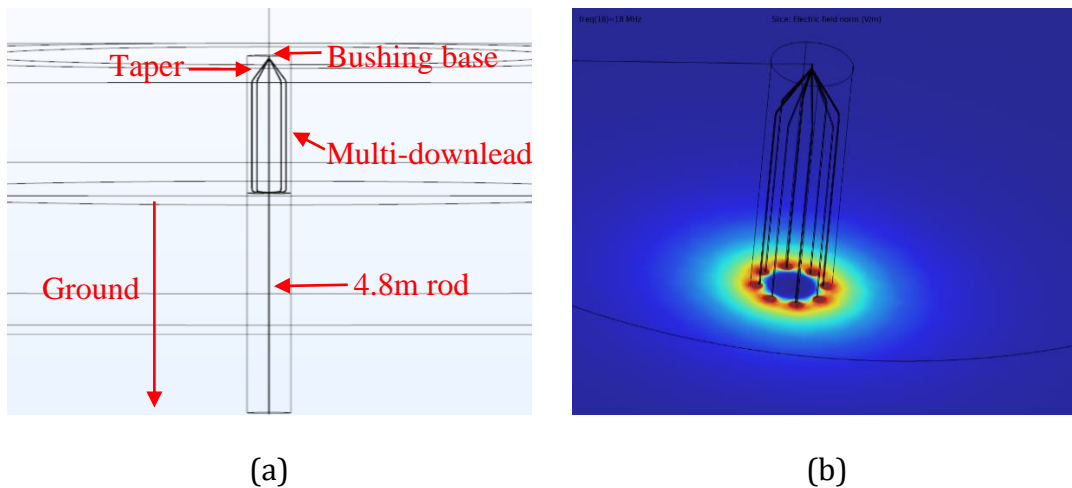


Figure 3.21: Bushing base optimised download arrangement tapered multiple download to 4.8m earth rod (a) multi-download profile (b) electric field pattern.

3.2.4.1 Bushing frequency response and coupling internal to enclosure

The behaviour of the bushing in terms of internal reflection, transmission towards the AIS and coupling to the enclosure leading to the propagation of TEVs is assessed through a frequency domain simulation, for both the standard single download to HF rod and the modified, 8 download to HF rod arrangement, as shown in Figure 3.22 and Figure 3.23.

Due to the inclusion of the soil domain and its additional imposed requirements for meshing, i.e., an even finer mesh is required to meet the number of elements per wavelength requirements under the reduced wavelengths in a $100\Omega\text{m}$ soil, the simulation was limited to a maximum of 50MHz, to maintain a low enough DoF for the available computational resources.

The input impedance, representing the input impedance of the bushing connected to the AIB characteristic impedance 6m from the top of the bushing, is obtained from the S11 parameter. The magnitude and phase of the input impedance is provided in Figure 3.24.

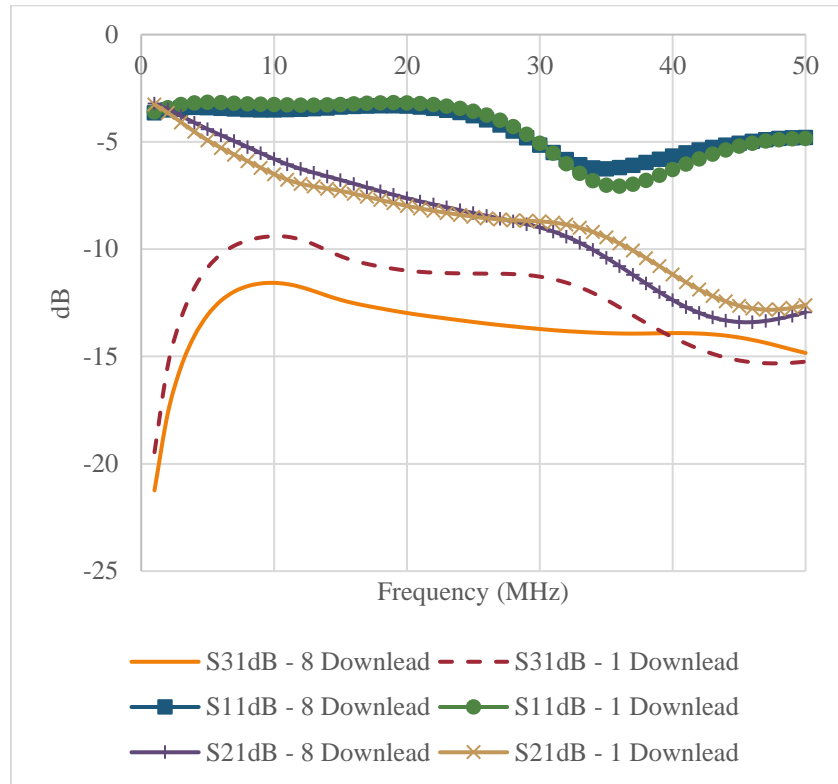


Figure 3.22: Bushing S-parameters for 1 and 8 download arrangements.

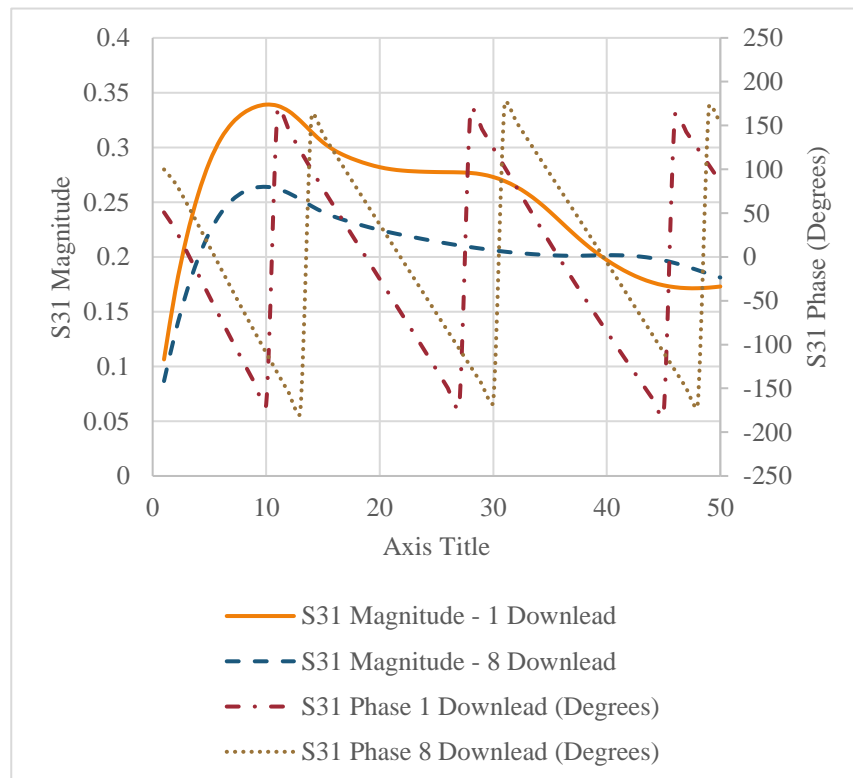


Figure 3.23: Internal port to GIB enclosure port transmission coefficient magnitude and phase for 1 and 8 download models.

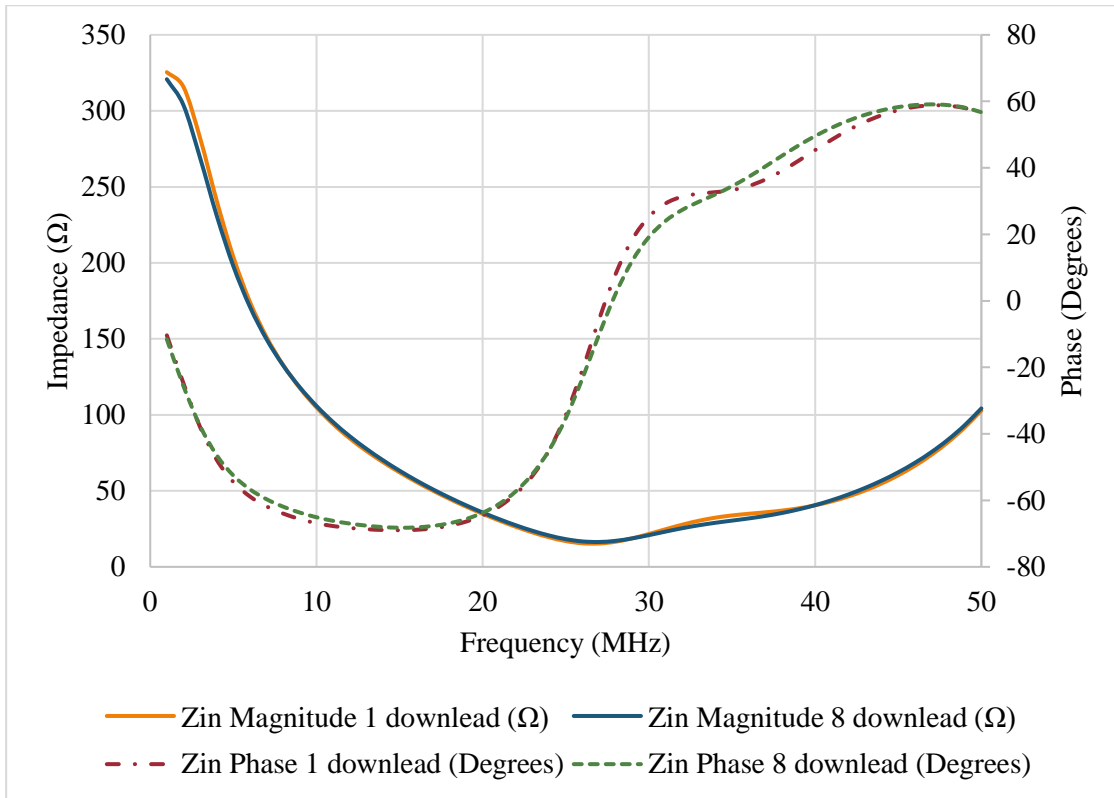


Figure 3.24: Input impedance to the bushing, terminated 6m with the characteristic impedance of the AIB.

3.2.4.2 Bushing power flow for single and multi-download arrangements

In terms of the physical phenomenon of coupling, it is apparent that strong coupling occurs close the bushing, as anticipated, between the vertical section of the HV conductor and the enclosure. It is possible to visualise the direction of propagation of electromagnetic waves through a medium by computing the Poynting vector, as shown in Equation (3.2), from [79].

$$S = \frac{1}{\mu_0} (E \times B) \quad (3.2)$$

The Poynting vector demonstrates the transported directional energy flux density. This is evaluated in COMSOL through the use of the time average Poynting vector [80]. At 1MHz, as shown in Figure 3.25, plotting only the external energy, shows that a significant proportion of power continues in the direction of propagation, upwards towards the air insulated bus; some power also transits the download and earth rod. Internally, a significant proportion of the wave is reflected, however this is not shown for clarity of the TEV power flow. The distribution of power along the enclosure is

relatively uniform circumferentially. The arrow size in all vector plots is logarithmically proportional to the resultant magnitude of power flow.

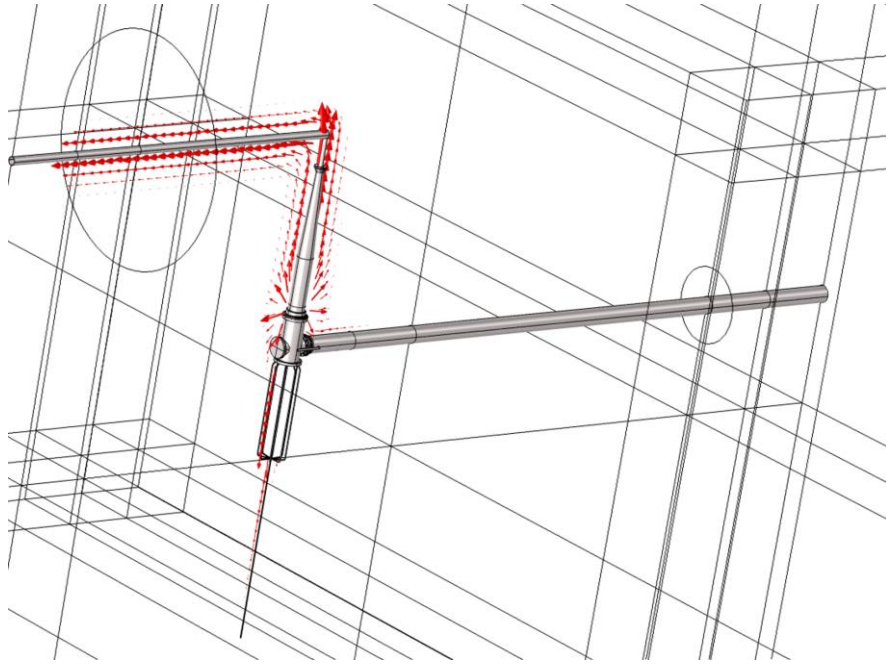


Figure 3.25: 1MHz power flow vector plot from 8 downlead bushing model.

By 10MHz, Figure 3.26 demonstrates a significantly higher proportion of the field is coupled to the enclosure. The ground lead directly beneath the bushing remains quite effective (8 downlead model).

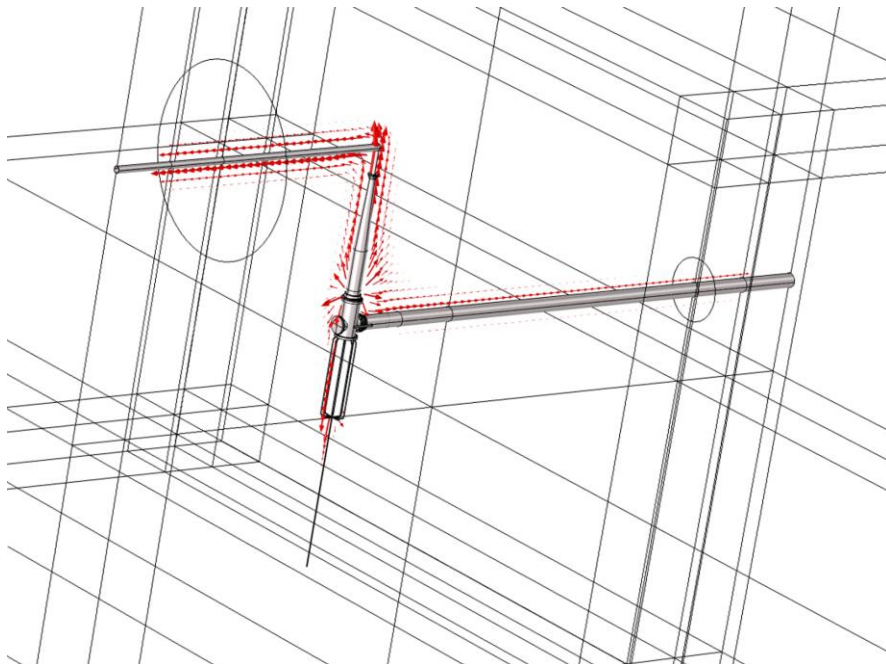


Figure 3.26: 10MHz power flow vector plot from 8 downlead bushing model.

3.3 External Transients

3.3.1 TEVs – above ground propagation

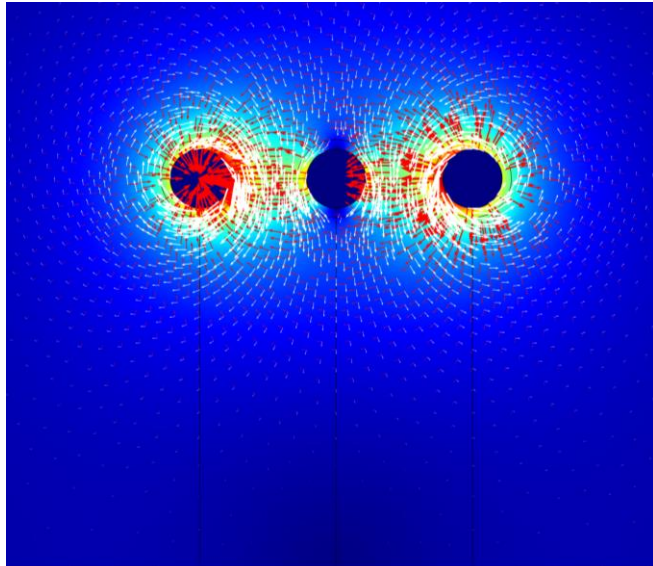
When investigating TEVs, of interest, are the magnitudes and frequency spectrum, the coupling mechanisms and propagation characteristics are of interest. TEVs are quantified by a voltage with respect to a zero potential. The transient current is related to the voltage by the impedance of the enclosure. Standard modelling practices utilise a characteristic impedance is commonly calculated with respect to a perfect ground. This lossless approximation would take the voltage present on the enclosure as the line integral of the electric field between the enclosure and the ground surface, which would be considered to a zero potential reference. When considering a lossy ground, integration must continue below the surface to the point at which the electric field vanishes.

In order to understand the propagation of TEVs, it is essential that we understand the modes of propagation. Ignoring internal propagation and the complex shape along the enclosure, the three enclosures can simply be considered as three cylindrical transmission lines, suspended above a conductive ground plane. When carrying out wave propagation studies, it is useful to decompose the problem in the modal domain, which can be considered similar to the use of symmetrical components for the majority of steady state power system studies. As with transmission lines, aerial mode (propagation between conductors) and ground modes (conductor - ground propagation) exists for multiple enclosure arrangements. These modes are analogous to differential and common mode terminologies used in RF and EMC engineering. Calculation of propagation modes for arbitrary conductors and configurations can be carried out through eigenmode analysis. Eigenmode analysis study solves for the complex propagation constant, with the goal of finding the modes that will propagate for an approximate effective mode index. Propagation modes can be computed by solving a 2D model, including a simplified representation of the enclosures and a suitable air domain.

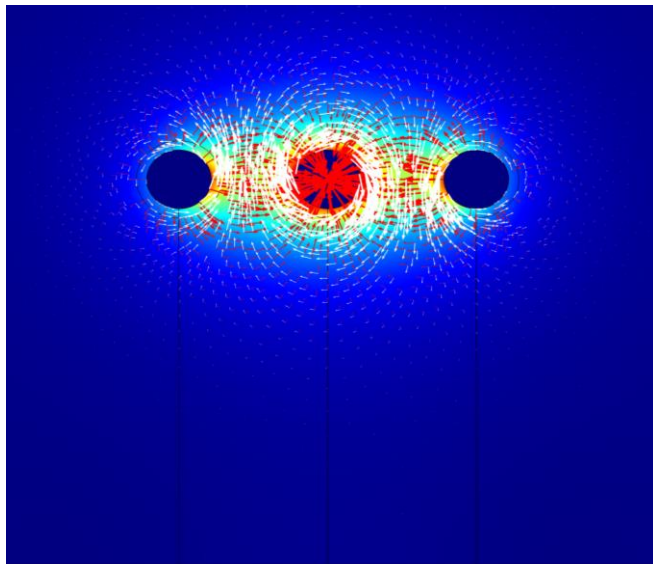
3.3.1.1 2D Eigenmode analysis

It is possible to use 2D mode analysis to establish port characteristics and impedances for both EMT studies and further advanced finite element models. The plots in Figure 3.27 are results from mode computation for three cylindrical conductors at 1MHz enclosed in a large hemispherical air domain, above a perfectly conducting ground.

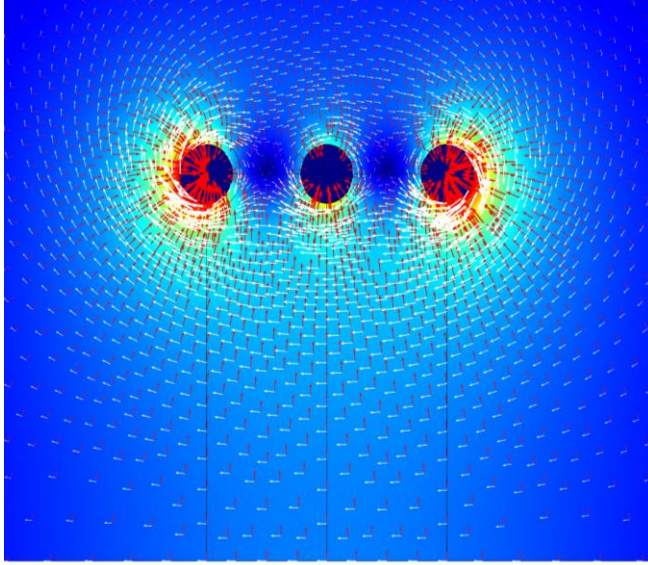
Colours, contours and vectors correspond to the electric field for the first three propagation modes for a mode index search around 1. Two aerial or differential modes are visible, the first being propagation between the center and outer GIBs, shown in Figure 3.27(a). The other visible aerial mode is propagation between the center and an outer and GIB shown in Figure 3.27(b). A ground mode is identified in Figure 3.27(c).



(a) Aerial mode 1



(b) Aerial mode 2



(c) Ground mode

Figure 3.27: GIB Propagation modes – E field vectors (red arrow), B field vectors (white arrow).

In contrast to the internal propagation of VFTs, the external propagation of TEVs is should not be considered lossless. TEVs attenuate at a greater rate through external propagation, when compared with internal VFTs. Increased attenuation of surges that propagate along the enclosure is partially due to the increased effective resistance of the enclosure as discussed in Section 3.2.4. It is also due to the ground, i.e. due to the penetration depth and resulting eddy currents in the soil [37].

3.3.1.2 Penetration depth for external transient propagation

The frequency dependent characteristics of the soil and wave propagation behaviour in lossy media, makes the study of the propagation of TEVs highly complex. For above ground propagation, losses can be considered by dividing the problem into internal and external impedances [81]. Internal losses are predominantly a result of the skin effect while external losses are related to the frequency dependent penetration depth of magnetic fields into the ground, due to finite conductivities and permittivities, and can be calculated using Equation (3.3) [82].

$$\delta_g = \frac{1}{\omega \sqrt{\frac{\mu_0 \epsilon_g}{2} \sqrt{1 + \left(\frac{\sigma_g}{\omega \epsilon_g}\right)^2} - 1}} \quad (3.3)$$

where μ_0 is the permeability of free space ($4\pi \times 10^{-7}$ H/m), σ_g is the soil conductivity, ϵ_g is the soil relative permittivity and ω is the angular frequency (rads/m).

The ground penetration depth, analogous to skin depth, can be considered as the depth at which the current density has reduced to $1/e$ (Euler's number) of the value at the ground surface. This quantity can be used to evaluate the true voltage magnitude that exists between the enclosure and reference earth for each frequency of interest when considering a non-perfect, lossy ground. Furthermore, ground penetration depth may provide indication of the suitability of specific modelling practices used for the study of TEVs. Circuit based software such as EMTP, may not be strictly applicable to calculation of TEV, as they work on the principle of TEM mode propagation and carry out calculations assuming classic transmission line equations. Plotting initially, the skin depth (penetration depth of the ground) against frequency using Equation (3.3) will allow us to observe the effect of soil conditions and frequency on the penetration depth. This is shown in Figure 3.28 for a range of typical (uniform) resistivities of $100\Omega\text{m}$ to $1000\Omega\text{m}$, with the relative permittivity of the ground (ϵ_g) set to 1. The wavelength beyond which other modes of propagation should be considered for a 3m high transmission line is given by Equation (3.4) [81]. Critical frequencies for TEM dominance are also shown in Figure 3.28.

$$\lambda = 2(h + \delta_g) \quad (3.4)$$

where h is the height of the horizontal bus from the ground (m).

The plots demonstrate that TEM mode dominance is greater for higher frequencies with lower resistivity soils when compared with higher resistivity soils. For $100\Omega\text{m}$ soil, standard transmission line approximation behaviour is expected up to around 38.5MHz, whereas for $1000\Omega\text{m}$ soils, this threshold reduces to 16.9MHz. More accurate simulations above these ranges are only possible through a field-based solver.

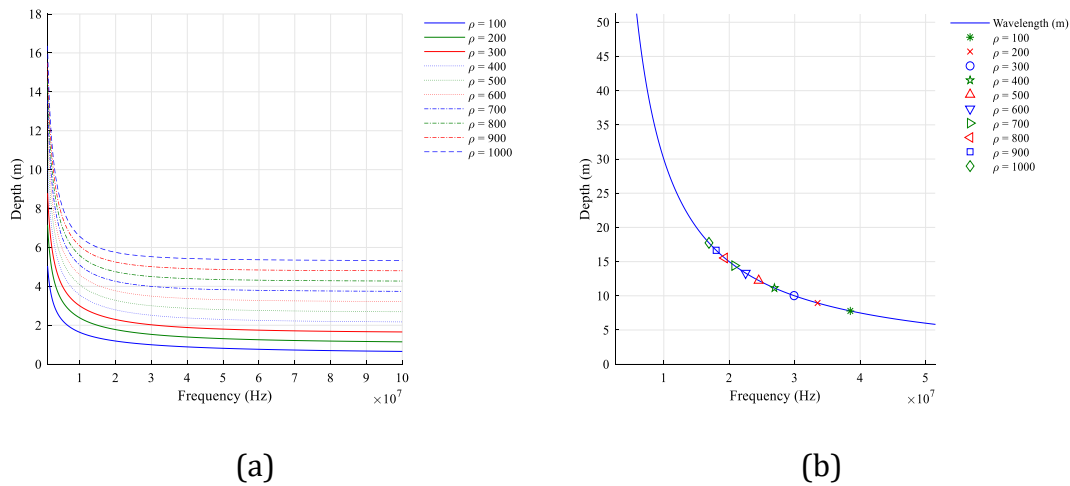


Figure 3.28 – Penetration depth (a) for various uniform soil resistivities (b) Critical frequency for TEM dominant frequencies in uniform soil resistivities.

3.3.1.3 Quasi TEM and higher order mode propagation of TEVs

Where regular EMT line constant modelling approaches rely on a single value for soil resistivity, often with a default value of $100\Omega\text{m}$, eigen mode analysis could permit the calculation of line parameters and identify restrictions on standard modelling practices for any arbitrary soil model. Important wave-related physical quantities, such as velocity, attenuation and phase constant parameters be easily derived. When undertaking 2D lossy eigenmode analysis for a geometry using FEA, the frequency of interest is set and a search for propagating eigenmodes is carried out. A search of modes with an effective index of between 1-1.11 was required to provide best response for a TEM or quasi-TEM propagation mode for the first few tens of MHz. Typically, computation yields any number of possible modes, the majority of which are spurious or evanescent, i.e. will not propagate any significant distance. Manually interrogating the field patterns and propagation constant of the computed modes allows identification of an appropriate quasi-TEM mode. Parameters that aid identification of the correct mode are the characteristic impedance (described above) and the mode velocity, calculated.

In this work, this method was applied to a single GIB enclosure (outer radius 228.6mm) for the purpose of studying TEV propagation and understanding potential limitations of the TLA, for a $100\Omega\text{m}$ soil. It was possible to calculate quasi-TEM modes up to 26.5MHz, after which only spurious modes below an effective mode index of 1 were

found. The velocity and wavelength were extracted from the calculated propagation constant, as shown in Figure 3.29.

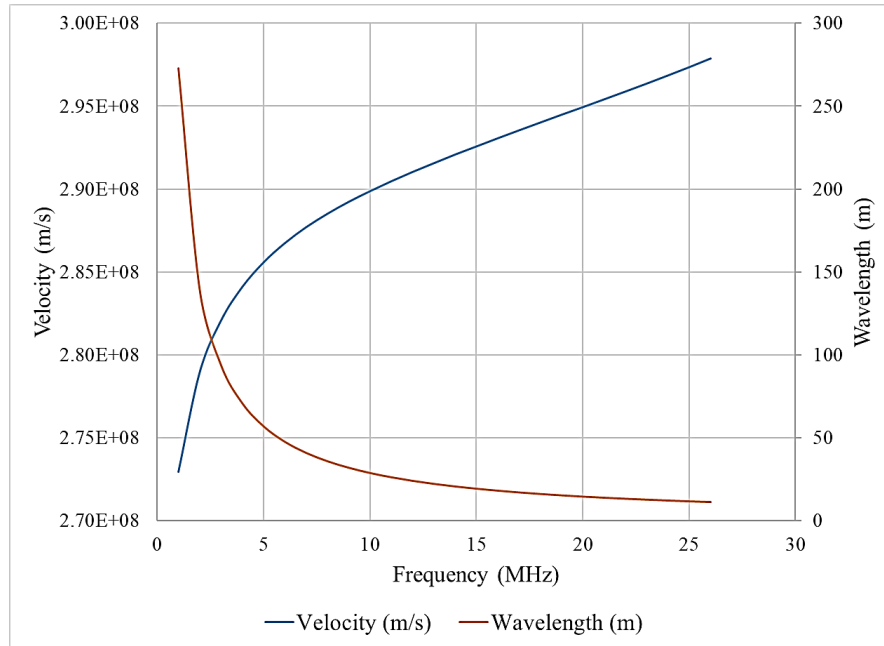


Figure 3.29: Computed wavelength and velocity over frequency.

A comparison of results with the ATP-EMTP line constants program for several soil models and frequencies will demonstrate some of the differences between the TLA and a full wave numerical solution. It is possible to derive characteristic impedances for the identified propagation modes by integrating the port or boundary electric and magnetic field components within the as shown in Equation (3.5). For an ideal TEM mode, integration of the in-plane fields is required.

$$Z_{xy} = \frac{-\int E_{xy}}{\oint H_{xy}} \quad (3.5)$$

A comparison of the EMT and eigenmode calculated characteristic impedances for a 100Ωm soil is required to determine the effective range of use. The impedance for the eigenmode study is initially for calculated by searching for the mode index corresponding to a quasi-TEM mode at each frequency point. The characteristic impedance is also calculated by assuming the field shape is unchanged with frequency, i.e. the mode index is calculated at 1MHz (reference frequency), followed by a frequency sweep against the reference field mode as shown in Figure 3.30. The propagation constant at each frequency point is related to the reference mode by Equation (3.6) [83].

$$\beta^2 = \beta_{ref}^2 + k^2 \left(1 - \left(\frac{f_{ref}}{f}\right)^2\right) \quad (3.6)$$

where β_{ref} is the phase constant at the reference frequency (f_{ref}), f is the frequency of calculation (Hz) and k is the wavenumber.

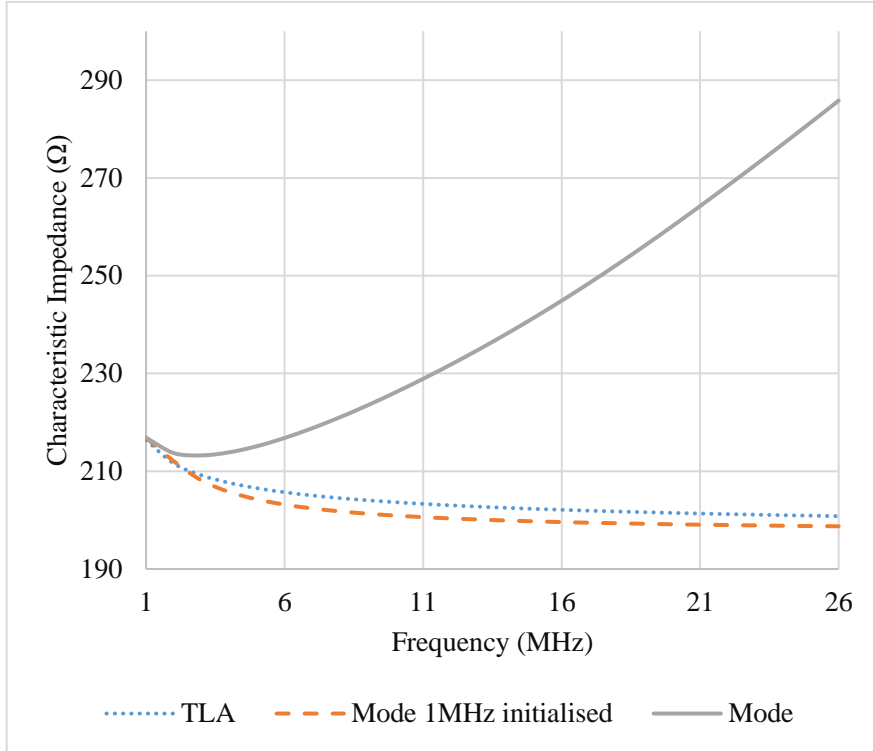


Figure 3.30: Impedance calculated using EMTP LCC routine and eigenmode analysis.

When comparing the calculated characteristic impedances, a reasonable match is seen for the 1MHz referenced eigenmode solutions. Observing the trend of the characteristic impedance calculated using a TLA and the reference mode computation, as the frequency increases, the characteristic impedance tends towards the characteristic impedance for a perfect ground (196Ω). A significant difference is seen after a few MHz for the individually calculated mode impedances. Modes computed at frequency above a few MHz have a significantly higher out of plane electric field, i.e., in the direction of propagation. This demonstrates that higher order modes should be considered, even relatively low in the TEV frequency spectrum. The out of plane electric field component (TM mode) at the ground surface becomes more significant by a few tens of MHz as shown in Figure 3.31 for a $100\Omega\text{m}$ soil.

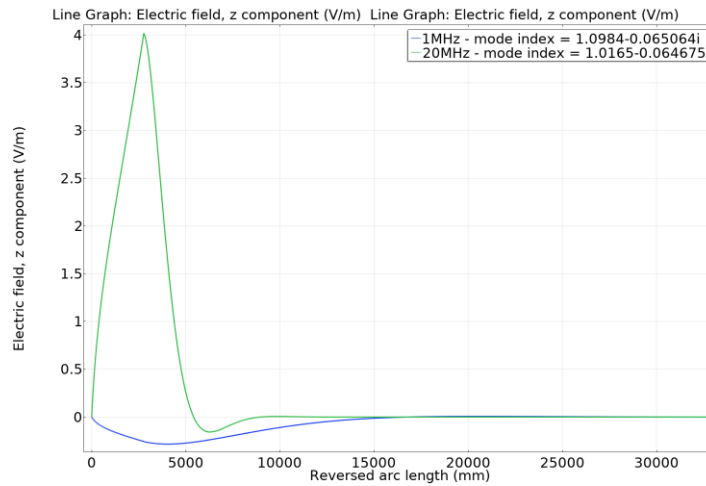


Figure 3.31: Out of plane (Z - direction of propagation) E field at 1 and 20MHz.

To further understand the presence of the out of plane component (Ez component), plotting the Ex and Ey vectors along with a surface plot of the Ez component in Figure 3.32 clearly identifies a TM mode at the ground surface. The field pattern is similar to the findings published by Schaich et al. [84] when investigating a Sommerfeld/Goubau surface wave phenomenon for a circular conductor Planar Goubau Line.

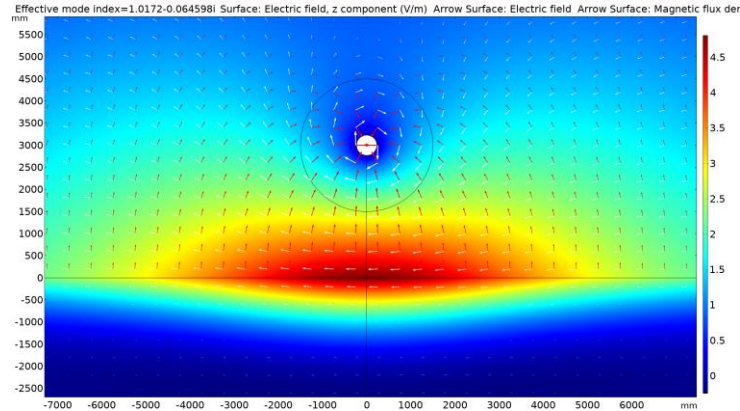


Figure 3.32: Z component contour with X and Y component E field.

3.3.2 Multiple enclosure propagation

After analysing numerous simulations, it was observed that, when externally coupled, TEVs propagate both on the enclosure-ground plane (aerial or differential mode) and the enclosure-enclosure plane (ground or common mode).

Further evidence of all propagation modes and electromagnetic interactions around the external system is provided when looking at the results from a full-scale Substation ‘A’ transient finite element model. With the wider availability of High-Performance

Computing (HPC), full scale, asymmetric models of GIS components can be solved. This bus interaction is computed and visualised for the full-scale outdoor section of a Substation 'A' section of GIB shown in Figure 3.1. The model does have some minor simplifications on the horizontal section, i.e., several spacers are removed, due to the required mesh size and the rapid scaling of RAM requirements with increased mesh and DOFs for wave equation problems. The elbow adjacent to the GIS hall is fully modelled, assuming a floating bolt (worst case) arrangement, however, power frequency enclosure continuity links are still present. The centre GIB bushing, as with the model used in the previous section, does not include the silicone sheds, again due to excess mesh requirements. The other two bushings are neglected, one bus has a PEC cap at the bushing, while the other is left open to assess the presence of any enclosure to GIB coupling occurs. The enclosure grounding arrangements (above ground conductors) are included as per the actual system, however below ground electrode and the remainder of the very large earthing system is neglected as it is not required with a perfect ground assumption. All other substation equipment, with the exception of the AIB which terminates via a PML is not included, as even the available resources accessed by a supercomputer cluster would be insufficient to include all equipment at present. For the transient simulation, with a 0.8ns timestep, the centre GIB, is excited at the GIS hall entrance with a 6ns, 1p.u. step voltage, to observe wave reflections from that point, in a TDR style approach.

From the Finite Element transient simulation results, the voltage seen at the input port (initial step applied at 10ns), internally close to the bushing and present between the enclosure-ground and the centre (yellow phase) to outer (blue phase) at the midpoint of the GIB, are plotted in Figure 3.33.

Field colour and vector plots are provided in Figure 3.34. The plots are rescaled at each timestep to aid the visualisation. The plots, showing the propagation, coupling and general undulatory behaviour of the electric field over times corresponding to (a) the initial TEV at start of the horizontal GIB (generated by the double elbow assembly), (b) the initial TEV peak (double elbow coupled) at the midpoint of the bus, (c) the peak internal VFT at the bushing and (d) the peak TEV at mid-point (coupled mostly from the bushing). While non-TEM propagation modes are avoided due to the lack of lossy ground, propagation is clearly multi-modal, including ground modes (common modes) and aerial modes (differential modes).

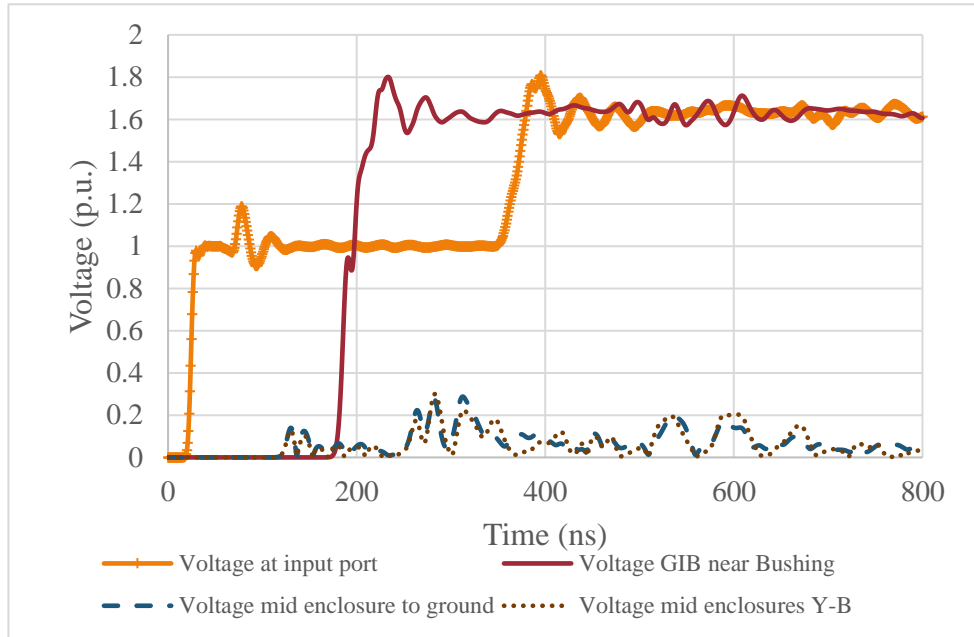
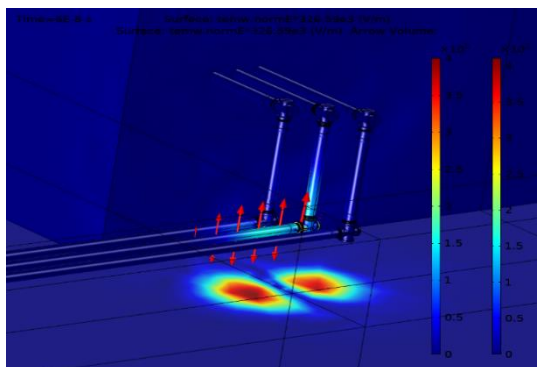
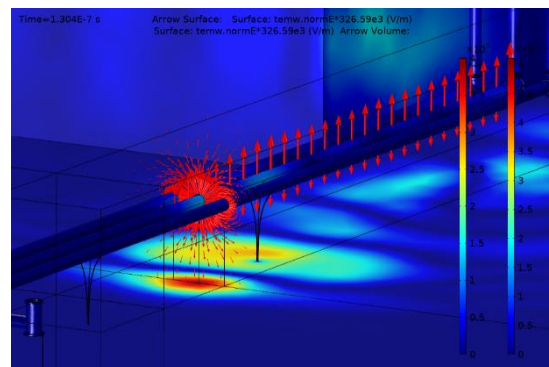


Figure 3.33: Substation ‘A’ GIB/AIB complete model calculated voltages for internal 6ns step voltage excitation.

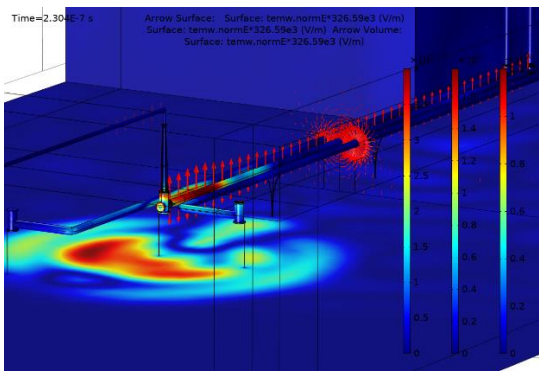
Observing the voltages developed across all enclosure modes in Figure 3.35, it is apparent that the enclosure-ground and enclosure to enclosure voltages are similar in magnitude, with the dominance of one mode over another varying over the duration of the transient. Surprisingly, the highest magnitude is actually developed between yellow (Y) and blue (B) phases.



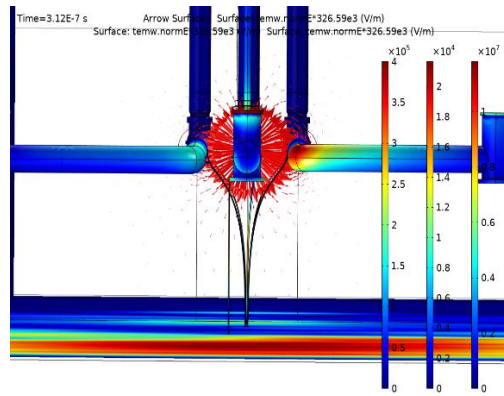
(a)



(b)



(c)



(d)

Figure 3.34: Full-scale Substation ‘A’ circuit 1 finite element model, external field propagation at (a) initial TEV generated at elbow-spacer-flange, (b) at first peak mid bus, (c) at peak VFT near bushing and (d) at peak mid bus TEV.

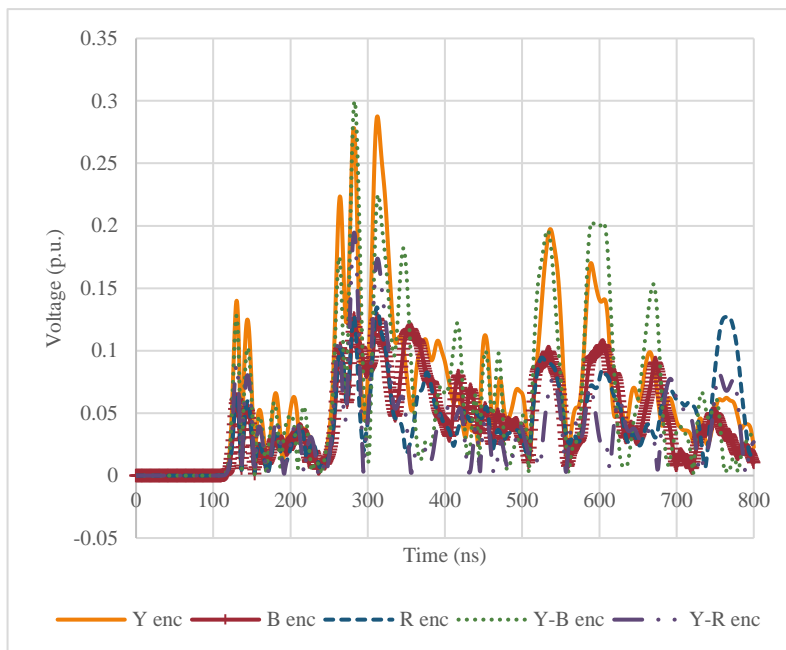


Figure 3.35: Substation ‘A’ GIB/AIB complete model enclosure modal voltages for 1p.u. internal excitation.

A further point to note is the apparent mode conversion on the ‘non excited’ bus enclosures, with an enclosure to ground, common mode voltage present. The fairly high magnitudes could be a consequence of the high field density around the centre enclosure; the quasi-TEM nature of that field means that the line integration of the field

possibly incorporated components of the centre enclosure common mode fields. However, generating a streamline electric field plot considering only the outer enclosure (red and blue phase) boundaries, proves that there are some common mode fields on the outer enclosures, as demonstrated by the red streamlines in Figure 3.36. While this observation is based on a perfect ground plane and the behaviour may differ above a lossy ground, these findings complement the high degree of coupling observed through measurements, as presented in Chapter 7.

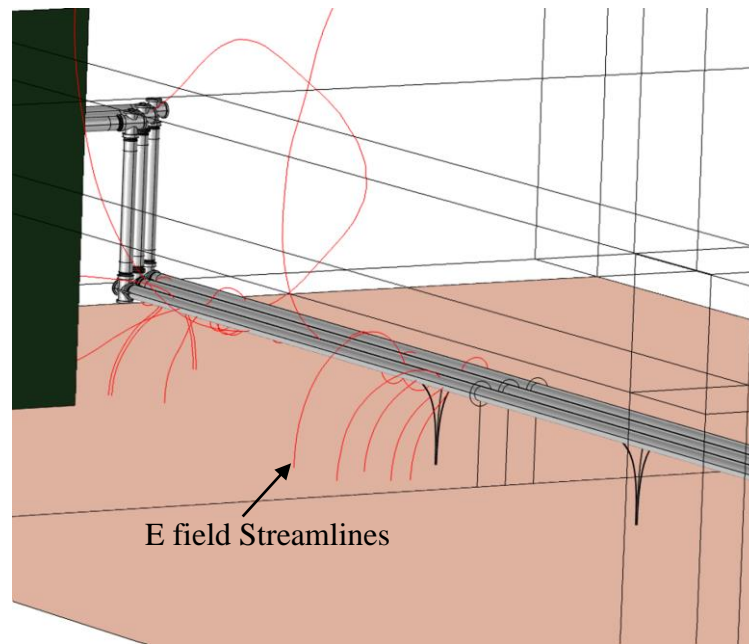


Figure 3.36: Outer enclosure electric field streamlines at 300ns.

3.4 Conclusion

In this Chapter, concepts from high voltage engineering and RF/EMC engineering were utilised for the investigation of VFT and TEV behaviour. These concepts were explored through advanced numerical modelling technique, namely finite element modelling. The applications of FEM for the study VFTs and TEVs in GIS are abundant. Providing careful consideration of boundary conditions, material characteristics and frequency dependent mesh requirements when solving electromagnetic wave equation problems, numerical models such as those presented are only limited at present by computational resources. As technology progresses and is coming more available, larger models can be built and more complete models including the interactions of other, seemingly noncritical factors can be included. Numerical modelling could eventually reduce the reliance on estimated characteristics for circuit-based models.

Modelling in this chapter has focused on several of the key equipment types installed as part of the GIS at Substation 'A'. Data obtained from Network Operator in the form of installation drawings and plans was used to build full scale, realistic models. The high computational requirements that scale rapidly with the number of DOF for wave problems meant that some models had to undergo minor simplifications, such as the gas to air bushing model which does not include silicone sheds. As it was not intended to investigate the performance of this material/profile and the compact profile of this dielectric material will have minimal effect on the coupling behaviour to be investigated, this compromise was deemed acceptable.

The spacer-flange and double elbow models have highlighted an important consideration with regards to the shielding effectiveness of the spacer-flange assembly. The results compliment previously reported arcing at bolts throughout the system and internal imperfections aside, and ineffectively shielded spacer through poor flange bolt contact is possibly the best explanation for the occurrence of the flashover. Computations were based on the extremes of all-bonded and all-floating bolts to quantify best and worst-case voltage and field conditions. It is possible that the actual system will lay somewhere in between; there may be an imperfect connection to the flange on one or many bolts. Following the initially reported arcing events, serrated washers are believed to be fitted to some or all of the bolts around the system. This may have in-fact to some extent rectified the issue. However, a later investigation by a third party produced evidence that arcing is still occurring at bolts, therefore it is recommended that bolts are inspected. Continuity measurements may be enough to determine the effectiveness, however, more elaborate shielding effectiveness measurements should be investigated in the future.

The generation, coupling and propagation of TEVs has been explored extensively for spacer-flange, double elbow and the gas to air bushing models. The bushing model quantifies the highest magnitude of TEVs for a uniform $100\Omega\text{m}$ soil. Site specific magnitudes, utilising measured, frequency-dependent soil characteristics may provide further accuracy, however, would also add further DoF and further non-linearity to the problem.

4 THE RESPONSE OF EARTHING SYSTEMS TO TRANSIENT ENCLOSURE VOLTAGES

4.1 Introduction

Earthing system design for GIS is generally more complex than for an AIS, even at power frequency. A very high proportion of return current is induced in the enclosure, carrying approximately 95%, this forces the designer to consider current through earthing conductors forming a loop under normal conditions. An ad-hoc measurement using a current clamp at Substation 'A' indicated approximately 90A present at a bushing downlead alone. A universal earthing arrangement for GIS is therefore, highly unlikely. There are numerous factors to consider, including GIS topology, ground characteristics and even the available area. Whilst earthing systems are generally designed for its behaviour under power frequency faults and often supplemented with high frequency rods for extra protection in the event of an external lightning strike, it is necessary to evaluate a range of earthing configurations and assess the impact on harmonic impedance in the TEV frequency spectrum, 100kHz-100MHz.

From the results presented in this Chapter, there are several observations for very high frequency behaviour of earthing system elements and the actual bus/earthing arrangement of circuit 1 at Substation 'A'. According to literature, the optimum scenario for the arrangement would be a negative reflection from ground that destructively interferes with the incident surge. This is possible where the return

propagation time is less than the rise time of the incident wave. In practice, this suggestion would require a perfect ground plane and a short downlead. Also, the ground reflected surge could still divide at the enclosure, which is a junction of three impedances, continuing propagation as a TEV.

The earthing systems are evaluated using CDEGS and where further detail is required finite element models are also evaluated. For CDEGS models, a 1A current injection is assigned to a segment representing the required energisation point. Using a combination of CDEGS SEStTransient, which combines the HIFREQ and FFTSES modules, numerous frequencies are swept to build the impedance profile over the desired range.

Propagation characteristics of the soil were discussed in the previous Chapter, in reference to the above ground propagation. While the response of an earthing system to TEVs is investigated, it is not within the scope of this thesis to further explore below ground propagation. This, however, could be investigated using the techniques explored within this Chapter and Chapter 3. Nevertheless, it is important to consider the impact of soil conditions on the wavelengths and as such the segmentation required for earthing system models.

4.2 Modelling of earth electrodes for very high frequencies

Designed originally for antenna modelling, the method of moments (MoM) is an integral equation based NEA technique [64], based on a thin wire approximation, i.e. the solution loses accuracy as the size of the segment approaches the radius of the conductor.

For analysis of transients in a grounding system, to compute accurate current and potential distributions and fields at any point over any frequency range while obeying Maxwell's equations, CDEGS HIFREQ can be used. The method utilised by the CDEGS HIFREQ software module was originally developed and published by Grcev and Dawalibi [85]. The method, based on MoM and numerical integration of the Sommerfeld integral. A system is initially solved in the frequency domain, while the transient response can be achieved through an inverse FFT.

As the HIFREQ computation method utilises the Method of Moments, the accuracy of the solution depends to a great degree on segmentation. As the number of segments is increased, the solution converges towards a final calculated value. This is demonstrated for a 4.8m vertical rod energised at 50MHz with a uniform 100Ωm soil in Figure 4.1.

The plot shows that the resistance and reactance seen at the energisation point appears to converge to a constant value at around 20 segments. A general rule of thumb when it comes to segmentation of conductors is to ensure there are at least 10 segments for a given wavelength. As CDEGS utilises MoM, as pointed out, there are limitations on the segmentation.

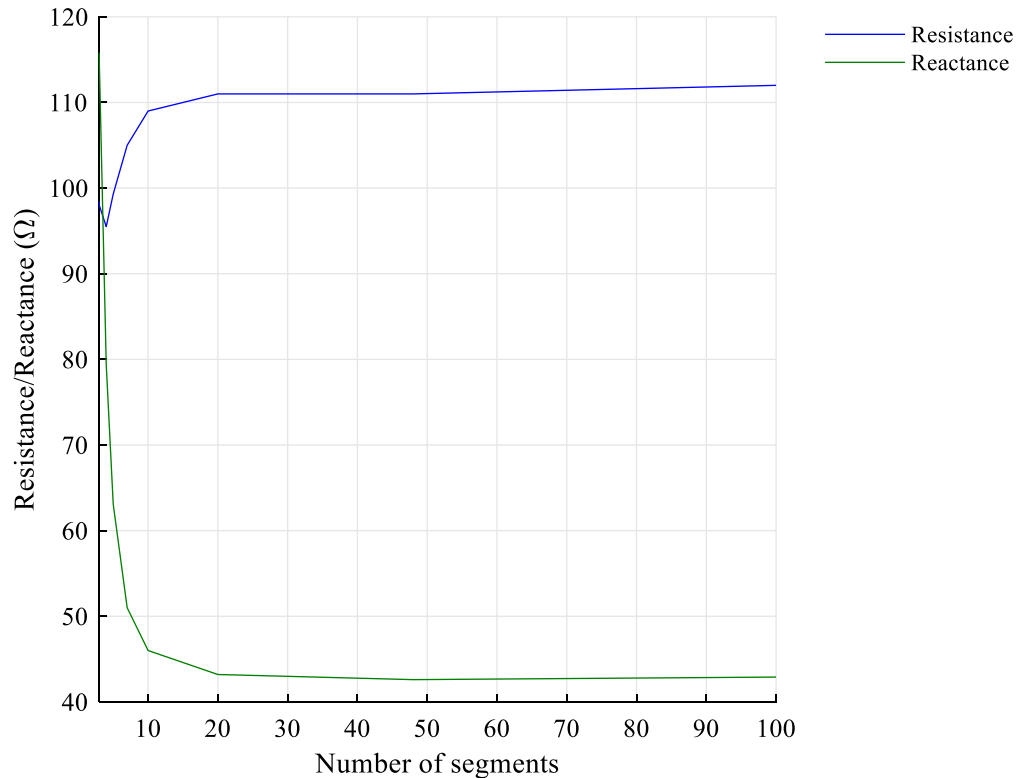


Figure 4.1: Segmentation required for a 4.8m vertical rod in 100Ωm soil at 50MHz.

4.3 Modelling the very high frequency response of earthing system elements

4.3.1 High frequency rods

High frequency rods are normally associated with the earthing arrangements for surge arresters, as they provide a short, reasonably low inductance path to ground for lightning and switching surges. The rods installed are usually longer than standard earthing rods at 4.8m or greater [86], in an attempt to penetrate any lower resistivity layers that may reside beneath the immediate surface.

In this investigation, the effectiveness of a high frequency earth rod in isolation (ignoring download) has been simulated for a range of ground characteristics. The adopted model shown in Figure 4.2, is connected to a 16mm diameter, 4.8m long

copper rod. For the vertical rod, a number of ground characteristics and lengths were analysed.

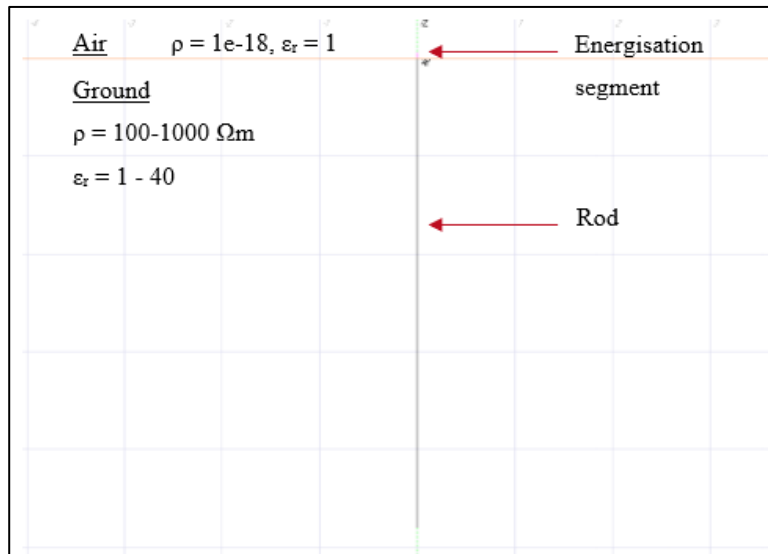


Figure 4.2: HF rod CDEGS model.

Figure 4.3 demonstrates the changes in impedance of a 4.8m vertical rod for varying uniform soil conditions. The results demonstrate that the maximum impedance across the frequency range increases with resistivity as expected. At $400\Omega m$ and above, the response becomes more oscillatory as capacitive and inductive effects start to dominate interchangeably over the range. The sweep of rod length for a $100\Omega m$ soil, in 1.2m steps (standard rod lengths), demonstrates an asymptote at around 3.6m. Any further increase in length does not appear to improve the response in a uniform soil. This clearly demonstrates the effects of penetration depth at very high frequencies for low resistivity soils. Figure 4.3(d) shows that impedance of a vertical rod varies significantly with the soil permittivity, as shown in. Changes in permittivity have a large impact on the below ground wavelength and hence transmission line resonances are more easily observed for relatively modest increases in permittivity. This could indicate that soils with high permittivities, such as in areas with high water content or high-water tables, could transfer high frequency transients with reduced attenuation. Given the significant reduction in wavelength associated with an increase in permittivity (electromagnetic waves transit materials with higher dielectric with a reduced velocity due to polarisation delays, the frequency is fixed so the impact is the apparent compression of the

wavelength) and therefore the increased segmentation requirements, which start to approach the thin wire approximation limits, the accuracy of the higher relative permittivity responses is uncertain.

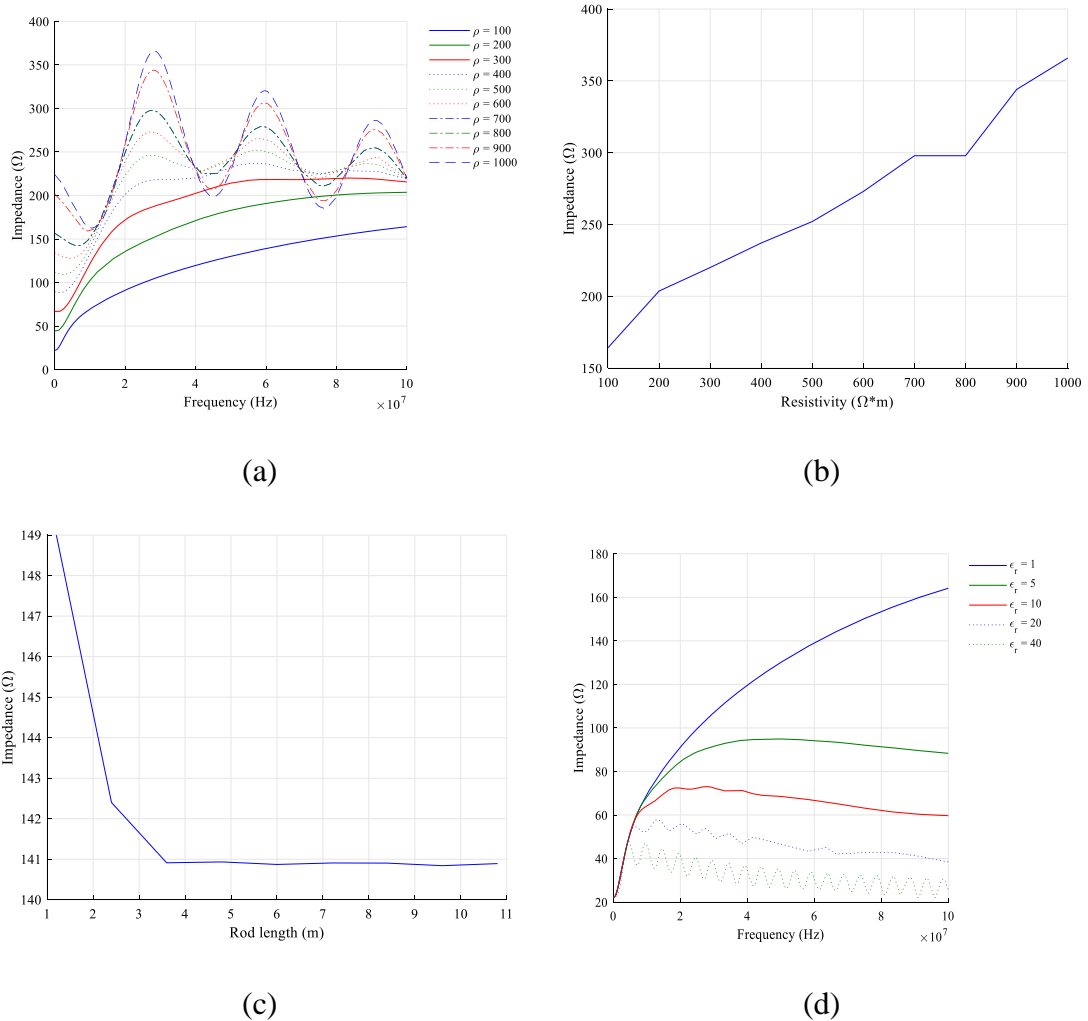


Figure 4.3: HF rod impedance (a) DC to 100MHz for uniform soil resistivities $\epsilon_r = 1$, (b) swept over resistivity range $\epsilon_r = 1$, (c) swept rod length $\rho = 100\Omega\cdot\text{m}$ $\epsilon_r = 1$ (d) DC to 100MHz $100\Omega\cdot\text{m}$ soil swept permittivities $\rho = 100\Omega\cdot\text{m}$.

4.3.2 Download and rod

Outdoor GIS enclosure heights are based on clearance and safety issues. The surge impedance of the enclosure and the effectiveness of an earthing system during TEVs, is highly dependent on the download arrangement. This observation is equally applicable to surge arrester downloads, as the base of the surge arrester at Substation ‘A’ is installed on a platform 2.6m high and the performance of a standard download to high frequency rod combination will be limited for very high frequencies.

The input impedance of a rod when viewed from the top of a 3m downlead (horizontal bus height) exhibits a completely different response to that of a below ground vertical rod alone. The large difference between the intrinsic impedance of air and soil means that the response is complex, reflection will occur continuously over the height of the downlead, however, the most significant difference will be at the surface. Therefore, the assessment of earthing systems at ground level only for TEV studies (VHF and above) is only a partial assessment. Figure 4.4 shows the CDEGS calculated input impedance for a range of uniform soil resistivities viewed from the top of a 3m downlead, connected at the surface to a 4.8m vertical rod. Segmentation is applied based on the 10 segments per wavelength minimum requirement.

It is apparent that the highest input impedance at the top of a 3m downlead occurs for lower soil resistivities. This appears to be a consequence of the reduced penetration depth. The peak magnitude occurs at the apparent quarter wavelength of the downlead/rod combination (approximately 19.5MHz). For comparison, a downlead over a perfect ground would have a quarter wave frequency of a 3m downlead would be approximately 25MHz.

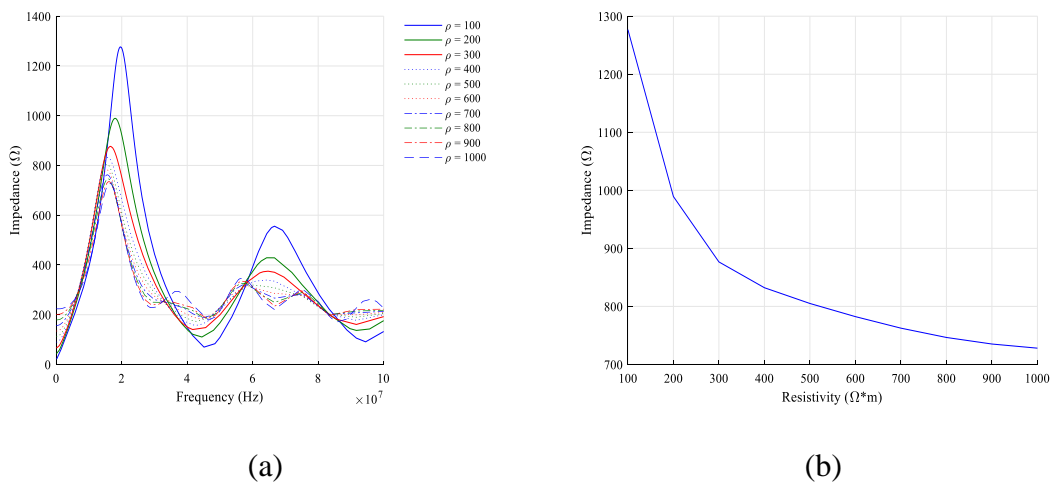
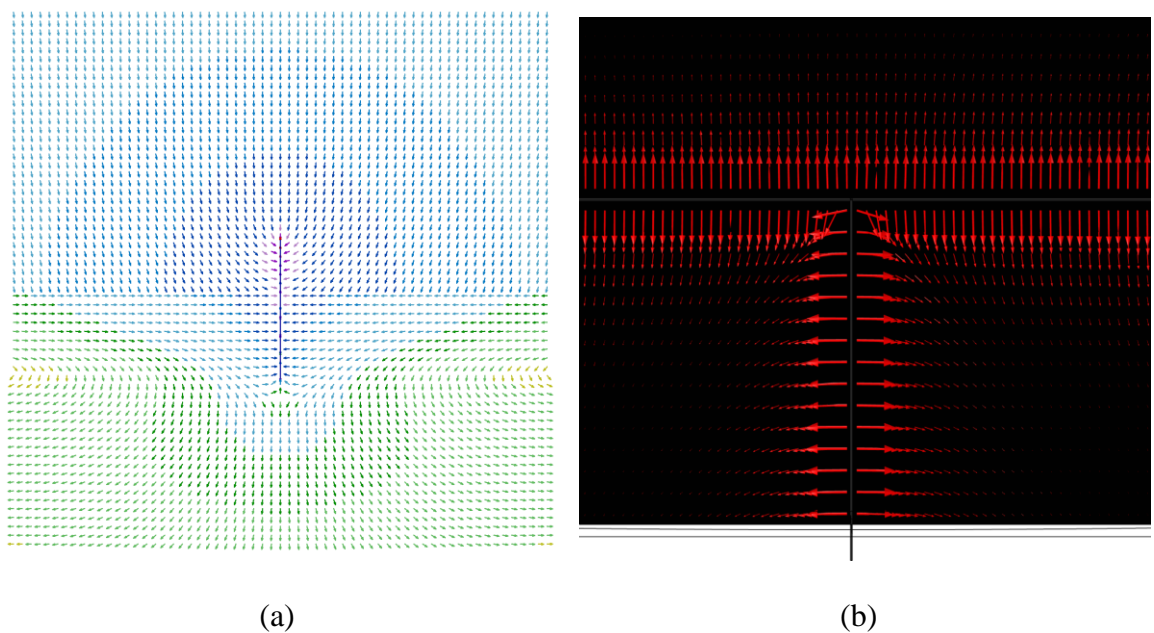


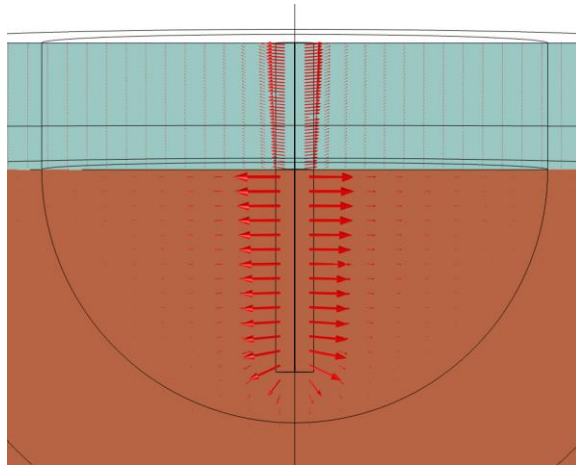
Figure 4.4 – input impedance of 3m downlead to 4.8m rod for uniform soils (a) impedance magnitude DC to 100MHz for various uniform soils, $\epsilon_r = 1$ (b) the peak impedance of various uniform soils $\epsilon_r = 1$.

Further evaluation of the input impedance of the downlead-rod combination was carried out using COMSOL. While the model shown in Figure 4.5 may appear to be basic, selecting an appropriate excitation method and the appropriate modelling domain and outer boundary conditions for very high frequencies is quite a challenging concept. Finite element models were initially created to study the field propagation along a

download. Initially, rather than excite the download at the top, to observe a more realistic field pattern of an ‘illuminated’ download, the download was connected to a horizontal conductor, and excited with a TEM wave several meters away. A comparison of the electric field vector plots show no ‘upwards directed’ fields for the illuminated download model in Figure 4.5(b), the fields appear to have only a minor tilt. The CDEGS vector plot in Figure 4.5(a) demonstrates fields referenced to a remote earth as the computation method demands; as a result a TM mode appears to be encouraged from the top of the download, progressing to TEM mode closer to the ground. This comparison isn’t strictly justified as the CDEGS plot includes a 100Ωm soil, whereas the COMSOL model includes a scattering boundary immediately surrounding the base of the download. However, it is presented as a suggestion that the excitation method at the top could be a closer to a pure TEM mode. Options for excitation include the use of the previously computed solution at the base of the download to excite a new download in a separate, previously non-computed domain below (a layered multi-domain modelling approach), or an arbitrary field pattern could even be set as excitation at the top of the download through a background field or scattering boundary condition. A far simpler approach would be to utilise a port boundary. A coaxial port can be configured to generate the ‘pure’ TEM excitation described above. The port could be dimensioned according to the characteristic impedance at the top of the download according to Equation (4.1).

$$Port\ radius = rod\ radius * e^{\frac{Z_c}{60}} \quad (4.1)$$





(c)

Figure 4.5 – Vertical downlead excitation electric field vectors (a) CDEGS dipole excitation referenced to remote ground (b) COMSOL vertical downlead ‘illumination’ (c) COMSOL coaxial port vertical excitation.

A comparison of the absolute, real and imaginary impedances computed in CDEGS and COMSOL is provided in Figure 4.6. The results demonstrate close agreement at the lower range of frequencies, but a higher peak impedance is observed in the COMSOL model results. This is possibly because the calculated impedance within the COMSOL model has a higher proportion of axial electric field.

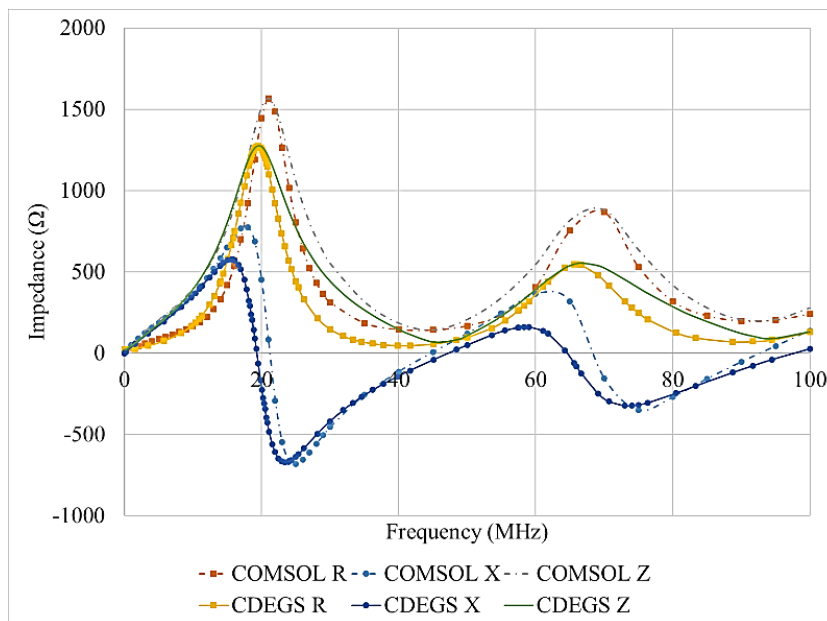


Figure 4.6 – Comparison of downlead-rod impedance calculated using CDEGS and COMSOL.

Utilising Equation (4.2) [55], the reduction of the incident wave can be estimated for the peaks attributed to both CDEGS and COMSOL downlead-rod models. For a 100Ωm uniform soil, the minimum reduction, coinciding with peak impedances of 1274Ω and 1568Ω respectively, are 0.92 and 0.94. This means that at best, a single downlead-rod will reduce an oncoming TEV by up to 8% when considering only the peak impedances.

$$s = \frac{-2Z_G}{2Z_G + Z_{enc}} \quad (4.2)$$

where Z_G is the ground surge impedance (Ω), Z_{enc} is the horizontal enclosure surge impedance (Ω).

The magnitude of impedance seen for a single downlead-rod arrangement instigated the investigation for a better solution. As briefly discussed in Chapter 3, the downlead is the major limitation to an earthing system's response under TEVs. Part of the reason for this is the high Z_c . A Z_c much higher than that of the enclosure will not be effective in dividing an oncoming surge. It was found that this characteristic impedance and ultimately the input impedance seen from the top of the downlead, can be dramatically reduced by incorporating multiple downleads, creating a much larger 'effective radius'. Numerous iterations of the design were explored. The number of downleads, 'effective' radius, taper angles at the top and bottom of the multi-downlead assembly (above the 4.8m rod connection), all impact the peak magnitude of input impedance. The input impedance for an 8 downlead arrangement is provided in Figure 4.7. The input impedance of a single downlead is also repeated for comparison, both models assume a uniform 100Ωm soil. The response shown is for the multi-downlead model shown in Figure 4.7(a). The downlead is tapered from the energisation point, out at an angle of 55° to an 'effective' radius of 700mm, close to the surface, a steep taper of 86° brings the downleads to a common point just above the rod. The peak impedance for the multi-downlead reduces significantly to 275Ω. The reduction factor at the peak now drops to 0.73, meaning a more significant proportion of a surge will divide at the downlead. It should be noted that the equivalent COMSOL model generated a peak input impedance of 530Ω. While significantly higher, it is clear that a significant division of the surge will occur. A further reduction in impedance is possible with increased number of conductors and 'effective' radius. No discernable reduction was evident through inclusion of a 'central' downlead in addition to the 'circumferential' downleads. Furthermore, multiple downleads, terminated on multiple individual rods, while better than a single downlead, did not seem to perform as well as the proposed multi-downlead

to single rod solution. This technique could be further developed to create site specific impedance matched downloads.

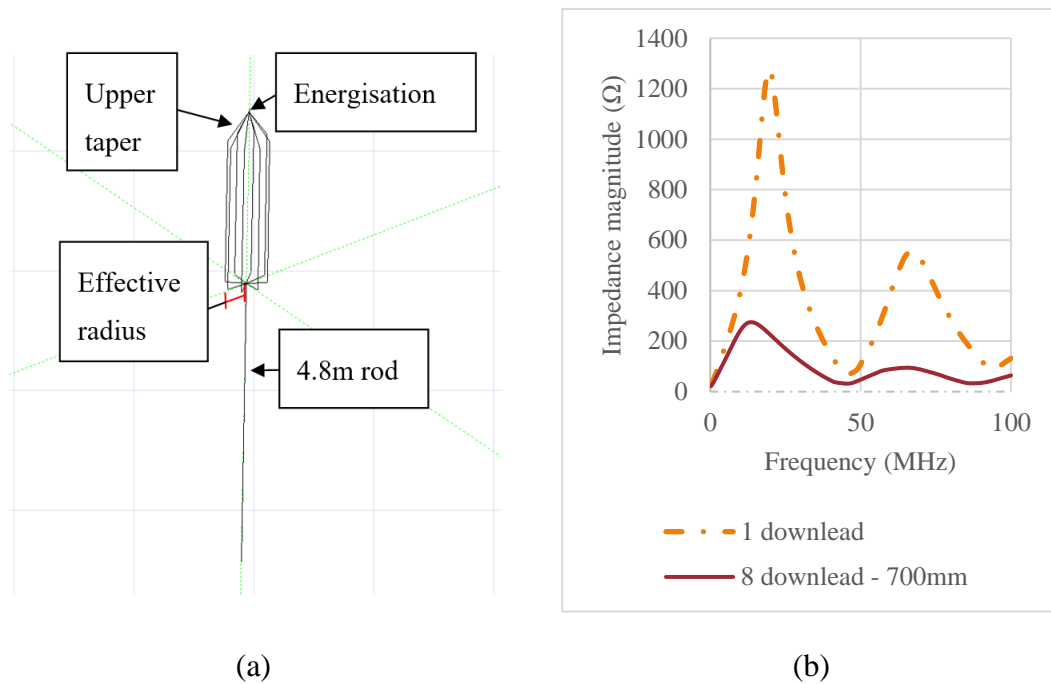


Figure 4.7 – Tapered multi-download (a) CDEGS model and (b) impedance response.

4.3.3 Impact of a download-meshed grid

A ‘standard’ earthing system arrangement used in many substations, comprises a horizontal meshed grid system. Multiple connections between the GIS enclosure and the main earthing system are often recommended, although these requirements must consider the impact of large power frequency return currents. Meshed systems and in particular meshed systems that cover a large area, provide a low impedance grounding system. A high mesh density is often used to control touch and step voltages around the substation. While power frequency earthing requirements will take priority over an earthing system’s high frequency performance, the impact of meshed systems in GIS should be assessed for very high frequencies.

Initially, a 5m x 5m meshed grid with download was investigated for varying uniform soil resistivities. The grid comprises 50x4mm copper tape, with a two additional crossmembers which cross the centre to make a 4-sector grid.

The results shown in Figure 4.8 demonstrate a significant increase in peak impedance across the range of resistivities when compared with that of a simple download-rod arrangement. Furthermore, for the meshed arrangement the input impedance is

increasing with soil resistivity, in contrast to the behaviour of the downlead-rod combination. The behaviour is likely to be occurring at least partly due to a decreased penetration depth.

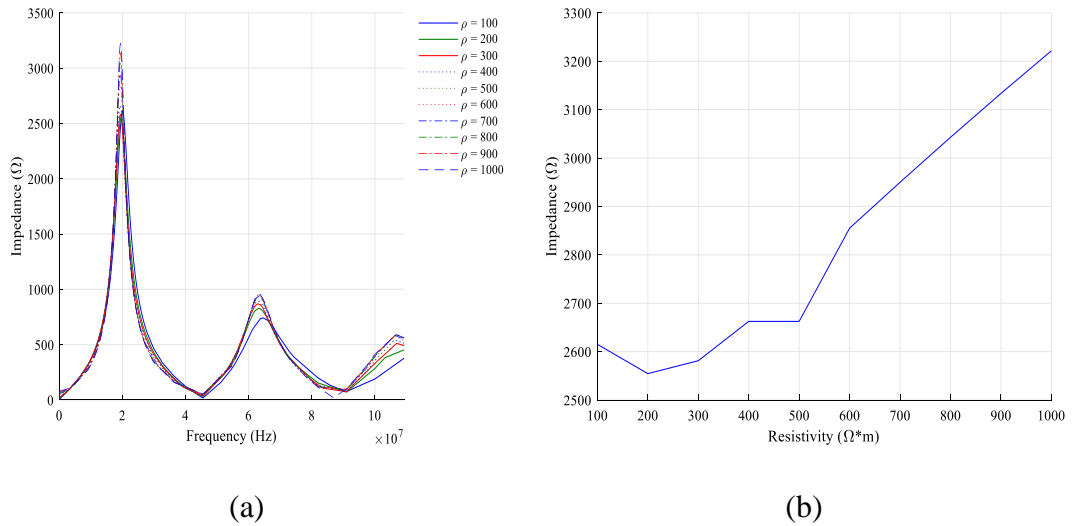


Figure 4.8 – Input impedance downlead to 5m grid (a) impedance vs frequency for $\epsilon_r = 1$ (b) peak impedance vs resistivity for $\epsilon_r = 1$.

With low frequency earthing systems, the impedance is proportional to the area of the grid. To assess the effects of an increased mesh area and density, further models of 10x10m, 15x15m and 20x20m grids, each with one horizontal and one vertical cross member through the centre of the grid were studied. Additionally, the mesh density of each grid size was increased, adding two vertical and two horizontal cross members, creating a sixteen-sector grid. Based on the results provided in Figure 4.9, with the exception of a 5m dense mesh, the mesh density appears to provide only a minor reduction in input impedance. Also, in general the size of grid appears to have minimal impact on grids larger than 10m. A 5m dense grid, exhibits significantly higher impedance compared to the 5m coarse grid and all other grid arrangements.

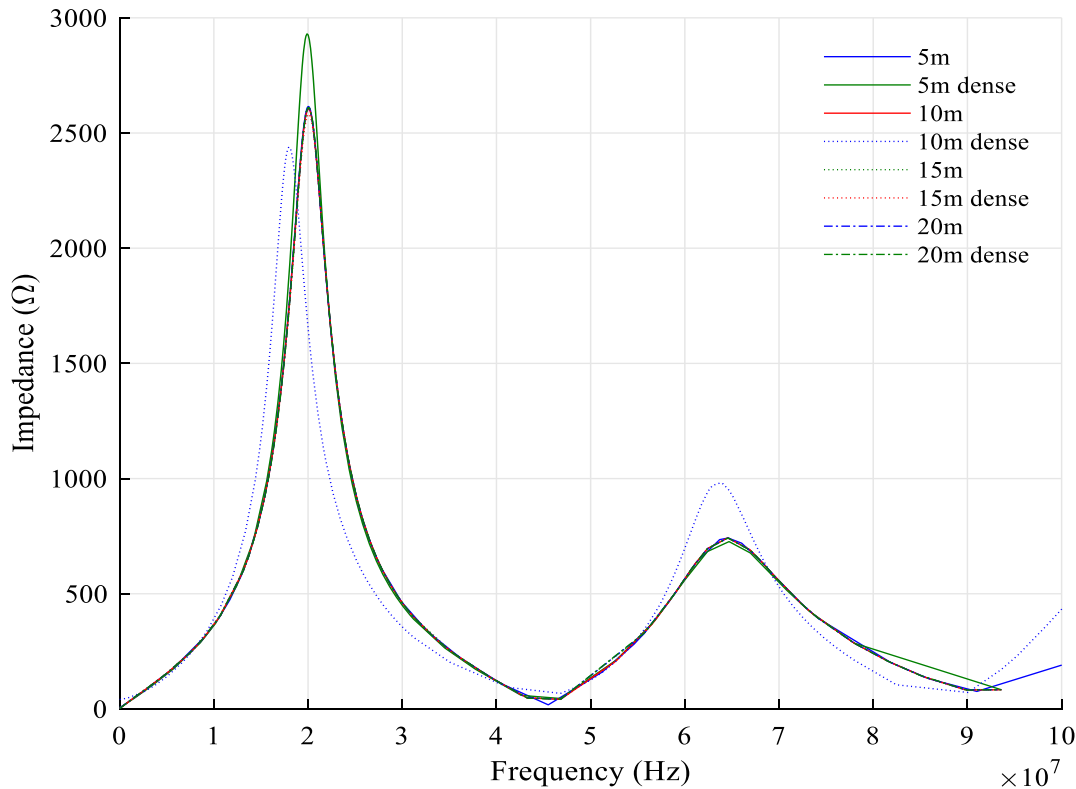


Figure 4.9: download-grid impedance for various grid dimensions and densities.

4.3.4 Response of GIS model with substation earthing system

Simulations were also carried out for a section of external bus (Substation ‘A’ circuit 1 Red Phase), as shown by the wireframe representation of the enclosure including flanges and links in Figure 4.10. The computation time for such a configuration was of the order of several days. It was possible to simplify representation of the GIS by implementing a coaxial cable type, specifying conductor and enclosure dimensions and material characteristics. For a 1A, 50Hz energisation at the flange directly beneath the gas-air bushing location on the red phase, including only contribution from the two high frequency rods, results for wireframe and simplified representations were in good agreement (less than 1% error at 50Hz). Therefore, to reduce computation time for further simulations, a cable type single line representation was used, as shown in Figure 4.11.

While simulations were carried out for the simplified GIS with the entire earthing system representation, to solve the model for up to 100MHz, with the segmentation requirements failures in computation were consistently met. This was due to the extremely large matrix size, even utilising the simplified GIS geometry. To solve the

entire system the segmentation had to be reduced, therefore accuracy would be affected and for that reason, the quantifiable results will not be presented. Nevertheless, the undulatory behaviour observed was useful as shown in Figure 4.12. The observed behaviour suggests the maximum GPR associated with TEVs is confined around the enclosures and given the spatial variation of the fields in that region, high touch and step voltages are inevitable.

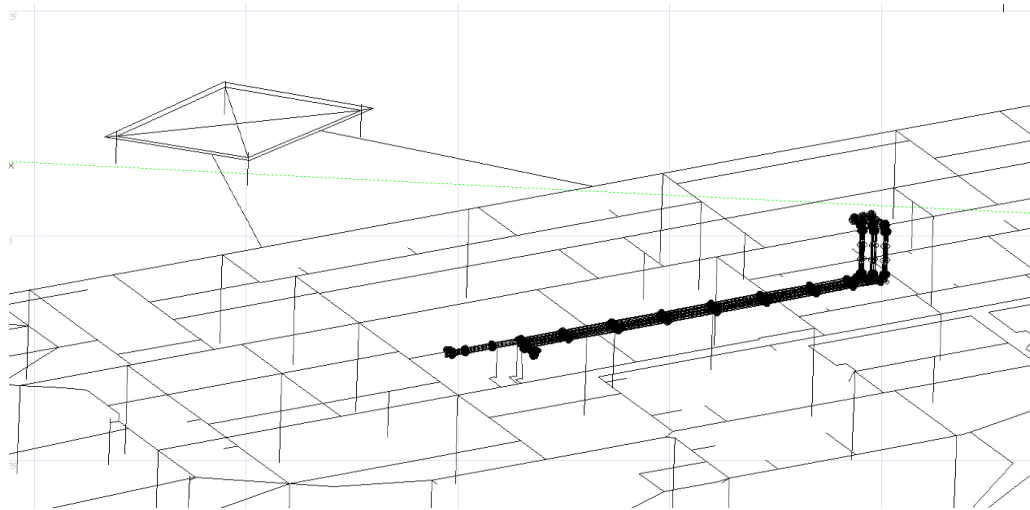


Figure 4.10: CDEGS wireframe representation of GIS enclosure.

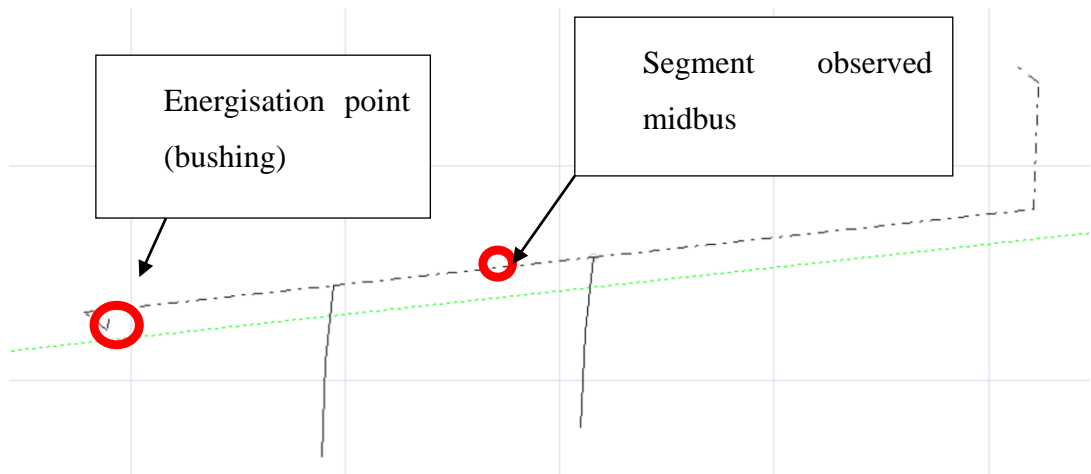


Figure 4.11: Simplified 'coaxial cable' representation of GIS enclosure.

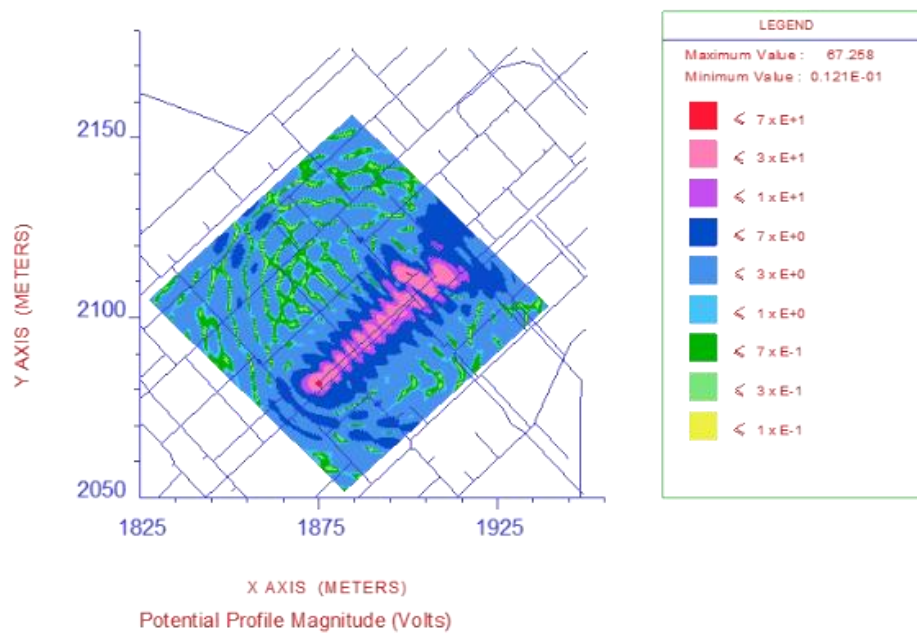


Figure 4.12: Substation 'A' high frequency earthing model with simplified GIS at 40MHz.

As solving the entire earthing system model proved to be challenging, simulations were carried out for the simplified GIS model subjected to various discrete earthing system elements.

By energising the enclosure (1A multiple frequencies) immediately adjacent to the location of the bushing, as identified in Figure 4.11, it is possible to observe the impact of various grounding and soil arrangements of circuit 1. The impedance and mid-bus enclosure GPR are provided in Figure 4.13 and Figure 4.14. Computations were carried out for the following options of configuration:

- Standard – design consisting of 2 rods and original soil model with no surface layer (or chippings), representing the model shown in Figure 4.11.
- Additional rods - Installation of 2 additional rods, equally spaced either side of base arrangement.
- Additional rods @ bushing - Installation of 2 additional rods close to the bushing/energisation point.
- Top layer $\rho = 10 \Omega\text{m}$ - A low resistivity 100mm top layer (10 Ωm)
- Top layer $\rho = 10000 \Omega\text{m}$ -A high resistivity 100mm top layer (10000 Ωm)

Results in Figure 4.13 confirm the lowest impedance and hence, the lowest TEV, is achieved where additional downlead-rods are included at the bushing. This compliments the multi-downlead findings in Section 3.

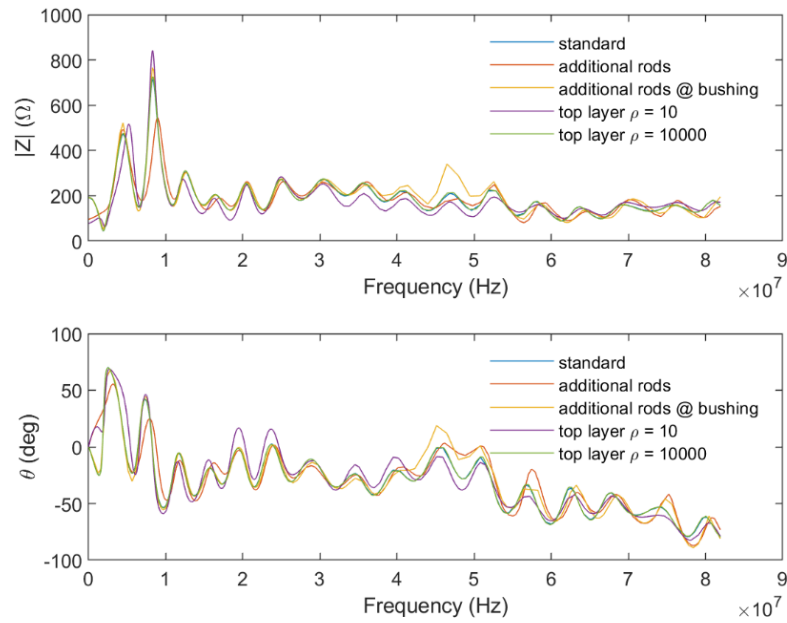


Figure 4.13: Impedance-frequency plot - various grounding configurations for simplified GIS enclosure model.

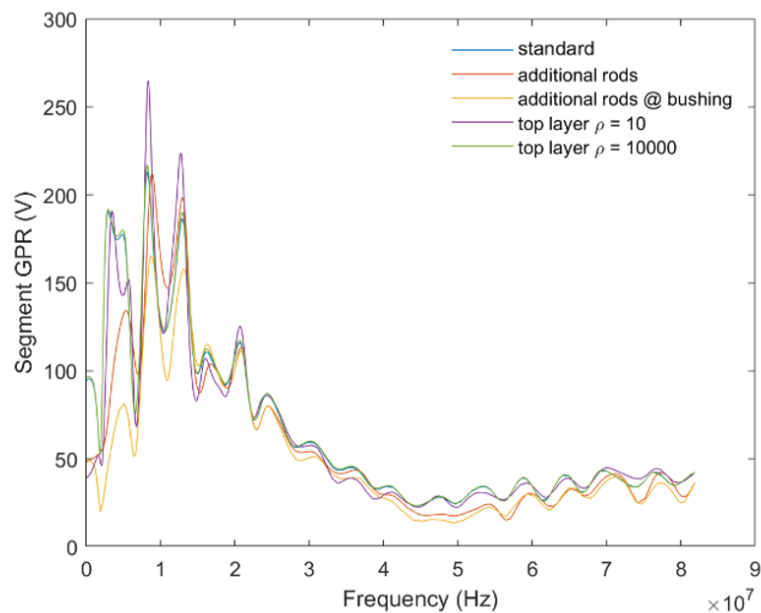


Figure 4.14: Segment GPR midbus various grounding configurations for simplified GIS enclosure model.

4.4 Soil ionisation for very high frequency modelling of earthing systems

Soil ionisation will influence the transient impedance of an earthing electrode and the distribution of fields. However, it is unconfirmed in the literature whether or not this phenomenon occurs under TEV. Existing studies have focused on soil ionisation under lightning where a dynamic impedance is evident, and two conduction mechanisms are considered, the first being electrolytic and the second related to the generation of a plasma channel [59]. Soil ionisation will effectively increase the area of the ground electrode, resulting in a reduction of impedance [87]. The majority of research related to this topic is carried out with respect to high amplitude lightning current impulse. At present, it is unclear if this occurs with TEVs. The critical field for ionisation is reported by many researchers, with a wide variation in results. Fields present on the ground leads as shown in Figure 4.15 for a 1p.u. VFTO, could easily exceed the 3kV/cm suggested in [59], with an implied magnitude of 32kV/cm in a 100Ωm soil, even without any power frequency return current effects. While this significantly exceeds the suggested threshold, soil ionisation is subject to a statistical and formative time lag, which could be characterised by a voltage-time curve for a set of soil characteristics; where a TEV event falls on this curve for further investigation. Due to the uncertainty of the presence of the success of the phenomenon when considering TEVs, soil ionisation is not considered in all any of the simulations presented in this thesis.

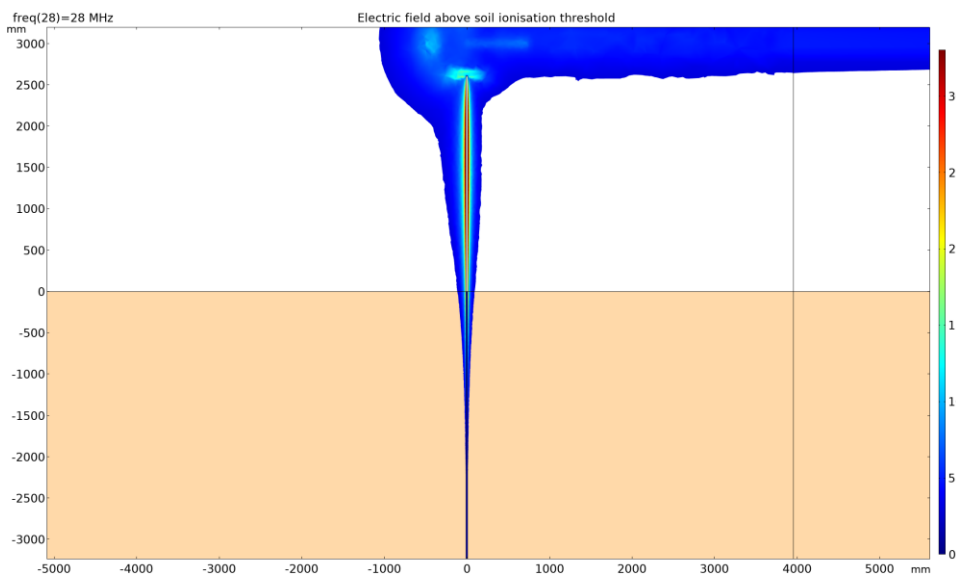


Figure 4.15: Electric field above soil ionisation threshold.

4.5 Conclusion

This chapter has investigated the response of earthing system elements under very high frequencies. Grounding studies in this frequency range appear to lead to results that are unpredictable in some cases. The air-ground interface adds a great deal of complexity to what appears from the outset appears to be a straightforward problem. Further complexity is added due to the ever-present concern of appropriate segmentation and the extent of the system that needs to be modelled.

Through the detailed modelling of earthing system elements for various soil conditions, including the vertical rod, downlead-rod, downlead-grid, and GIS enclosure with various ground terminations was evaluated. Given the results presented, the necessity for the consideration of the impact of the downlead on the response of the earthing system is clear; the downlead is a major limitation to the reduction of TEVs. Of the standard earthing designs assessed, the downlead-rod appeared to produce the best very high frequency response, particularly at high soil resistivities. Furthermore, when considering the simplified GIS model, multiple downleads at the bushing appeared to be most effective at reducing the TEV.

In exploration for a solution to the downlead issue, a multi-downlead approach was found to be a viable solution, essentially providing an increased 'effective' radius. The downlead profile was optimised through modification of the taper angles, number of downleads and effective radius to provide the lowest peak impedance for the proposed design constraints (a total diameter not exceeding the diameter of the base of the bushing). A reduction of up to 27% was observed with a multi-downlead configuration for a single high frequency rod termination. This multi-downlead approach could be applied to any GIS, GIL or other above ground conductor configuration. Furthermore, subject to further research and confirmation, the method could be adopted for the improvements to the performance of HV cables/cable screens at joint bay locations when subject to high and very high frequencies.

Finally, through finite element modelling, computed electric fields below the ground were demonstrated to be significantly higher than soil ionisation thresholds considered for fast transients. Nevertheless, further research is required to establish the volt-time characteristics of soil in the TEV frequency range, and to identify whether or not inclusion of the phenomenon would improve model accuracy.

5 A CIRCUIT BASED MODEL FOR THE STUDY OF VFTS AND TEVS

5.1 Introduction

While detailed numerical modelling has been presented in the previous chapters, there will always be the need for a circuit-based modelling approach. Providing component parameters are accurately determined, or a reasonable estimation is assumed, a good understanding of circuit behaviour can be achieved. Nevertheless, options for improvements in model accuracy should always be sought.

The improvements in custom models were apparent in Chapters 3 and 4, with detailed models created using finite element and MoM packages. Finite Element packages such as COMSOL, used in Chapters 3 and 4, have a SPICE based interface that allows the inclusion of simple circuit equivalent models with the intention of enabling a discrete model behaviour to interact with a wider circuit. These interfaces, however, are at present very limited and do not permit the complexity and flexibility that EMTs permit.

In this Chapter, the waveforms around Substation ‘A’ are calculated through a mixture of standard circuit-based modelling and an enhanced circuit-based modelling approach. Enhancements are brought about through the use of NEA in a co-simulation style arrangement.

Two circuit-model enhancement techniques are developed, both utilising outputs from the finite element and MoM models developed in Chapters 3 and 4. The first technique essentially relying on the direct conversion of S-parameters, while the second proposes a vector fit blackbox modelling approach, along with a unique algorithm that generates

efficient and stable transient equivalent circuit models. An enhancement on the standard modelling approach is introduced through the development of a customisable disconnecter, suitable for triggering potentially several tens to hundreds of breakdowns over a complete DS cycle of operation.

Finally, a detailed circuit model for Substation 'A' is developed, with the aim of determining the scenarios that can lead to the highest overvoltages and their impact on system insulation levels. The impact of the switching arrangement and bus capacitance is explored, along with the identification of the coupling mechanisms of MOSA currents at Substation 'A'. For extra clarity of explanations throughout, the final circuit model is shown in Figure 5.1 and Figure 5.2.

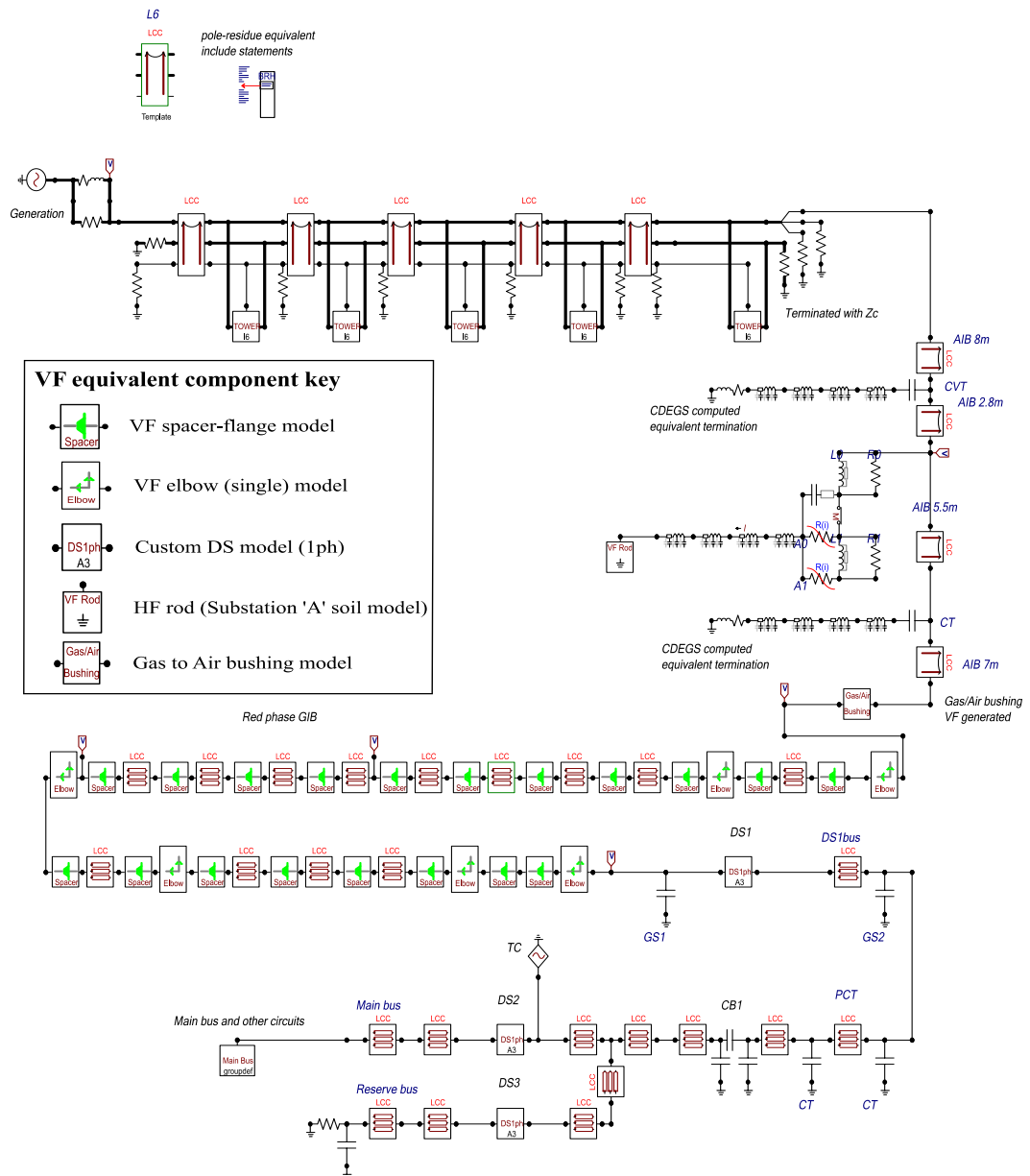


Figure 5.1: Section of developed Substation 'A' ATP-EMTP red phase GIB model.

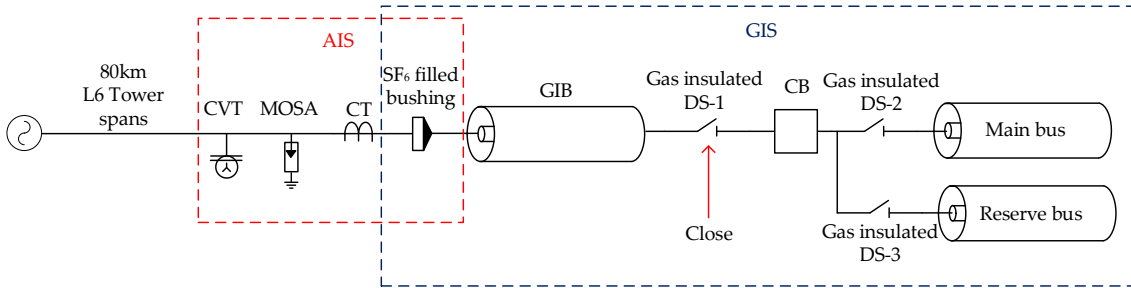


Figure 5.2: SLD detailing generation source to Substation ‘A’ main and reserve bus.

5.2 Circuit model elements

A brief description of the requirements for modelling of individual components, based on the model requirements for Substation ‘A’ 400kV GIS, are provided in the Appendix C. Components that have been incorporated into the main circuit model that have been enhanced through the finite element modelling or through the creation of custom/tuneable model interfaces are presented in this Chapter.

5.2.1 Gas/Air Bushing

The impact of the external enclosure and earthing arrangement is very difficult to incorporate with a simplified bushing model and standard modelling practices, owing mainly to the complex coupling and behaviour of TEVs as discussed in Chapter 3. A VF derived blackbox bushing model, incorporating the external AIB, enclosure and grounding arrangement at the bushing is presented in Chapter 5.3.2.

5.2.2 Metal Oxide Surge Arresters

ZNO Surge arresters have a complex non-linear behaviour. At high frequencies, this behaviour is even more complex, with the intergranular capacitance and the inductance of the grains, connectors and ground leads. There are several published models which attempt to capture the high frequency ZNO surge arrester behaviour, including the IEEE model, CIGRE model, Fernandez’s model, Haddad’s model and Pinceti model. For Substation ‘A’, the IEEE model was implemented, as shown in

Figure 5.3. The IEEE model A0 and A1 non-linear characteristics for the Substation ‘A’ surge arrester are replicated in Figure 5.5.

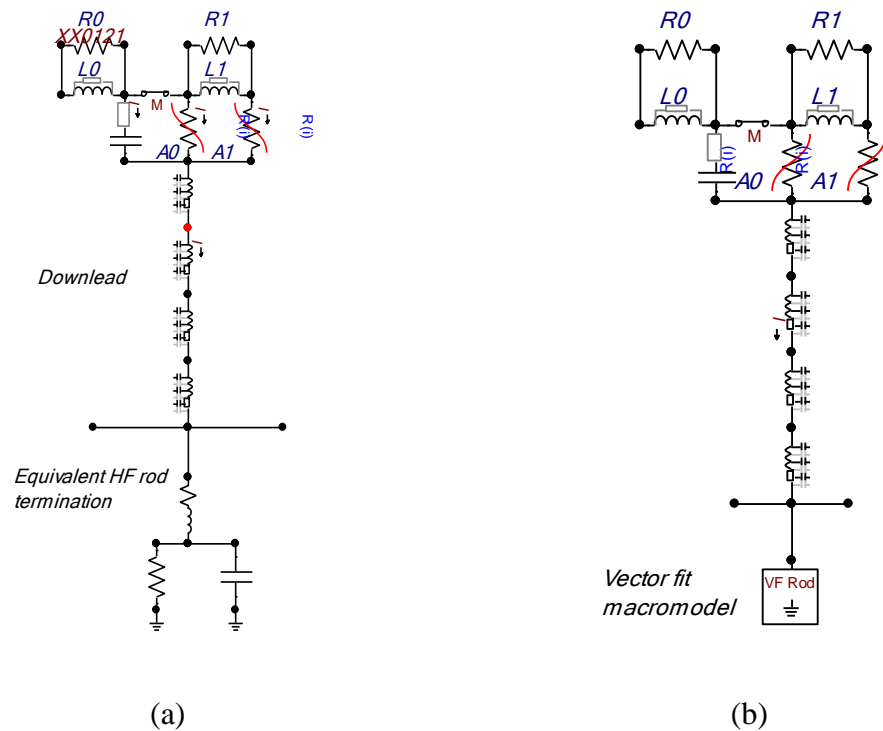


Figure 5.3: MOSA – IEEE Model with download and equivalent rod termination options (a) HF rod circuit equivalent (b) Vector fit macromodel.

For high frequencies, the MOSA grounding characteristics are essential for evaluating the MOSA’s high frequency response. The IEEE MOSA model is supplemented with a vertical download representation (varying characteristic impedance based on height). The surge arrester mounting at Substation ‘A’ is shown in Figure 5.4.

The download is terminated with the equivalent vertical HF rod impedance, calculated using a frequency sweep in CDEGS HIFREQ. For the lumped circuit equivalent HF rod model, the parameters are extracted at the measured dominant frequency. To incorporate a full frequency dependent HF rod, vector fitting can be used to create an admittance parameter based macromodel; methods for macromodel generation are discussed in Section 3. The frequency response of the MOSA HF rod for the macromodel in the Substation ‘A’ soil model (3 layer - top 448Ωm-1.1m, central - 1213Ωm-4.1m, bottom - 125Ωm-∞) is shown in Figure 5.6.

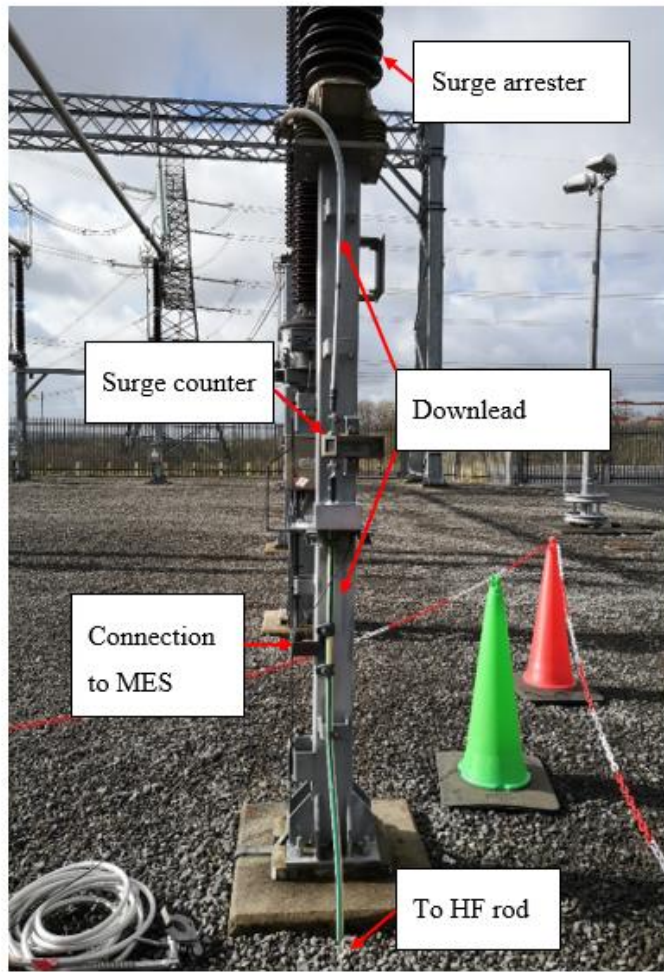
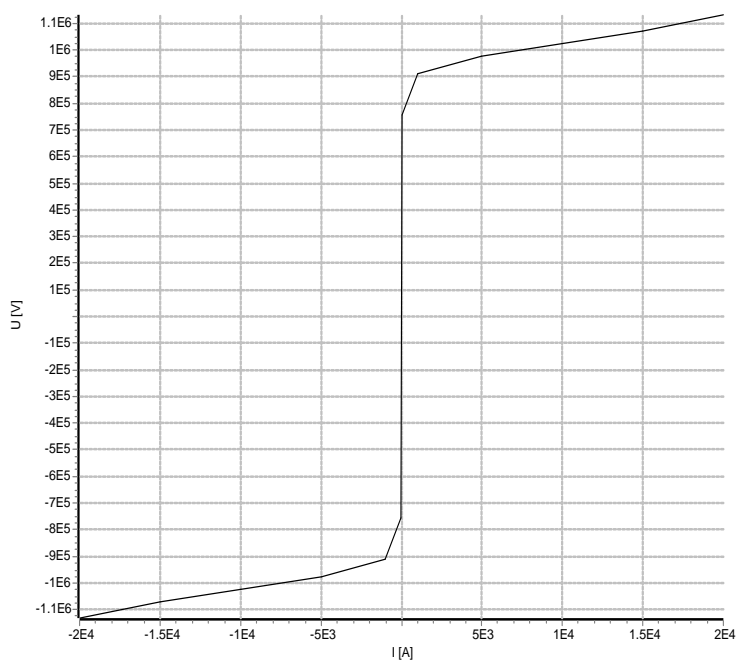
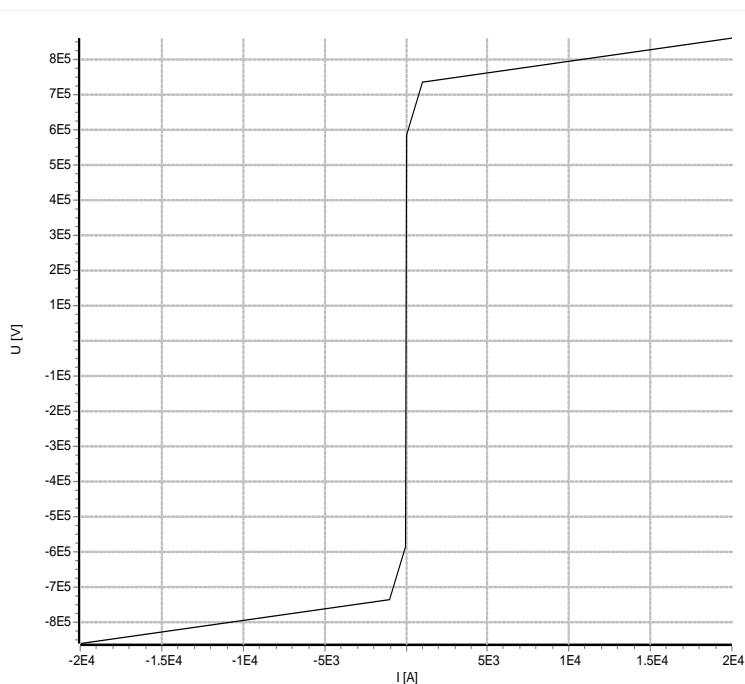


Figure 5.4: MOSA installation at Substation 'A'.

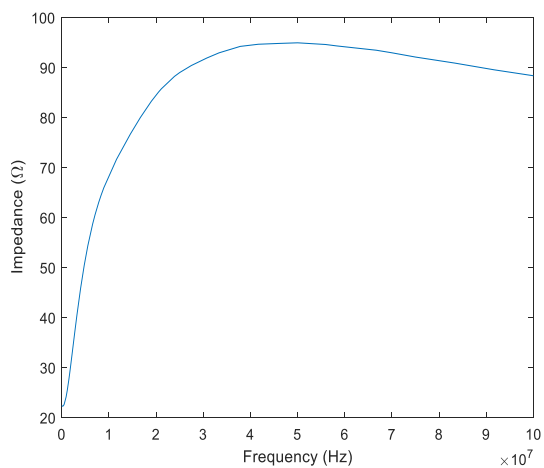


(a)

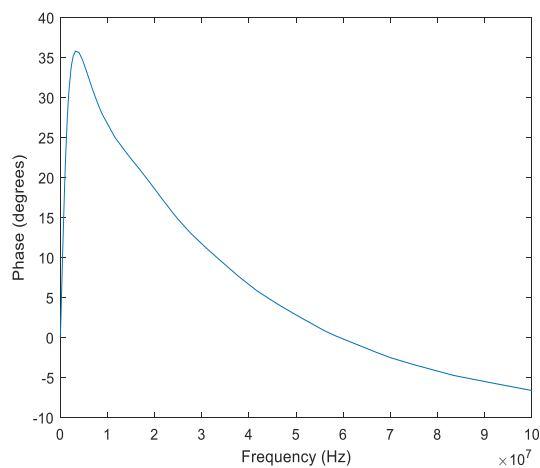


(b)

Figure 5.5: MOSA – IEEE model nonlinear characteristics (a) A0 (b) A1.



(a)



(b)

Figure 5.6: MOSA HF rod at Substation 'A' blackbox model computed frequency response (a) magnitude (b) phase.

5.2.3 Disconnecter model

In order to generate VFTs with frequency components and amplitude that match with transients produced by the actual system, an accurate disconnecter model is required. Disconnectors are commonly represented in very basic forms by a decaying exponential resistance, accompanied by a capacitance in parallel (representing the capacitance between the contacts of the switch [8]). This representation may be adequate for reproducing a single set of transients for a basic study. However, it is important for an in-depth study to develop a more comprehensive model. Disconnector geometries, contact speeds, pressures etc. can vary from one system to another, so a customisable model, allowing the sensitivity of each input parameter to be varied is required to calculate the maximum overvoltage and the number of transients in each operation.

A key consideration for a disconnecter model is the rise time of the VFTs it produces. The actual rise time of the VFTs is strongly related to the formative time of the arc, which is a function of gas pressure and field inhomogeneity, as described by Toepler's equation. The arc model, in its simplest form is represented by exponentially decaying resistance, using Equation (5.1) [20].

$$R = R_a + R_0 e^{-t/\tau} \quad (5.1)$$

where R_a is the arc resistance (Ω), R_0 is the resistance of the gap (Ω) and τ is the time constant for spark duration in SF₆.

Further advanced models allowing the implementation of a tailored dynamic model to include multiple restrikes or even the magnetohydrodynamic properties of an arc. Dynamic arc models such the Mayr model, the Cassie model or the Mayr-Cassie model are often used to represent circuit breaker arcing phenomenon [88]. The Mayr arc model is considered to be more suited to lower arc currents [89], such as that of the low capacitive currents in disconnecter switching; although good agreement on VFTO magnitude and frequency was found for a number of arc models including those previously mentioned in [90]. Contrary to this, these dynamic models are seldom used for VFTO studies due to difficulty of the estimating the correct input parameters (arc power etc.). Of greater importance is the non-linear resistance and multi-strike phenomenon.

As the full operating characteristics and design for the actual disconnecter (DS1) were not available, as is the case for many equipment types, it was deemed necessary to produce a customisable disconnecter design, with parameters that could be subsequently

adjusted, either if the actual disconnector characteristics became available or for a parametric study. The disconnector parameters that can be adjusted are as follows:

- Schwaiger breakdown equation (Equation (5.2)) or breakdown table.
- Open/close operation.
- Timed start of operation.
- Electrode field uniformity and curvature factor.
- Pressure.
- Gap distance.
- SF₆ reduced critical field strength.
- Operating speed.
- Breakdown time – specific or from statistical distribution.
- Gap recovery time - specific or from statistical distribution.

A disconnector model was created using EMTP MODELS language. The MODELS code is provided in Appendix D. The model inputs are the voltage at each side of the switch and the output is the time varying resistance, representing the arc. The disconnector can be simulated in single or three phase modes as presented in Figure 5.7 to Figure 5.9. The configurations shown are applicable to both open and close operations as the switching function is carried out via the TACS resistor, which is controlled by the disconnector MODELS block. Selection of opening or closing and variation of all other parameters listed above is achieved through the MODELS group definition data box. The three phase model is not electromagnetically coupled, phases operate independently.

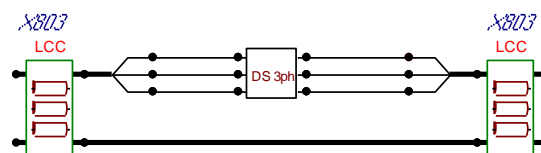


Figure 5.7: Three Phase disconnector model – grouped.

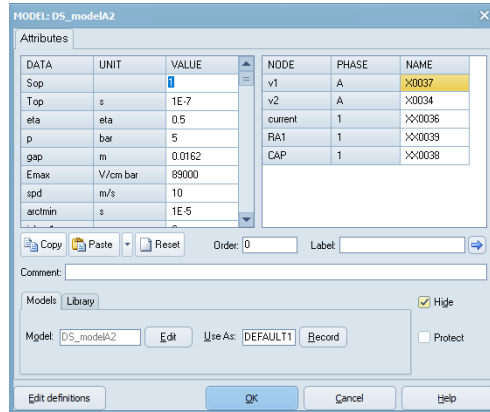


Figure 5.8: Custom disconnector model parameterisation.

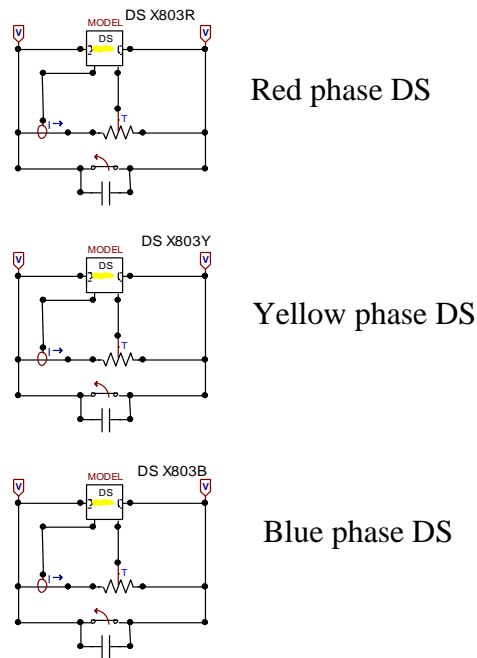


Figure 5.9: 3 Phase (R/Y/B) disconnector model – internal decoupled group.

Using the input variables listed above and Schwaiger's equations shown in Equation (5.2) from [5], it is possible to calculate the breakdown voltage of the gap according to the distance in which the moving contact has travelled. The field uniformity factor for various electrode arrangements can be estimated using Schwaiger's curves, shown in Figure 5.10.

$$V_b(t) = E_i \times \eta \times e_{max} \times \rho \times d(t) \quad (5.2)$$

where E_i is the intrinsic strength (kv/cm bar), η is the field uniformity factor, e_{max} is the curvature factor, ρ is the pressure (bar) and $d(t)$ is the gap distance over time (m).

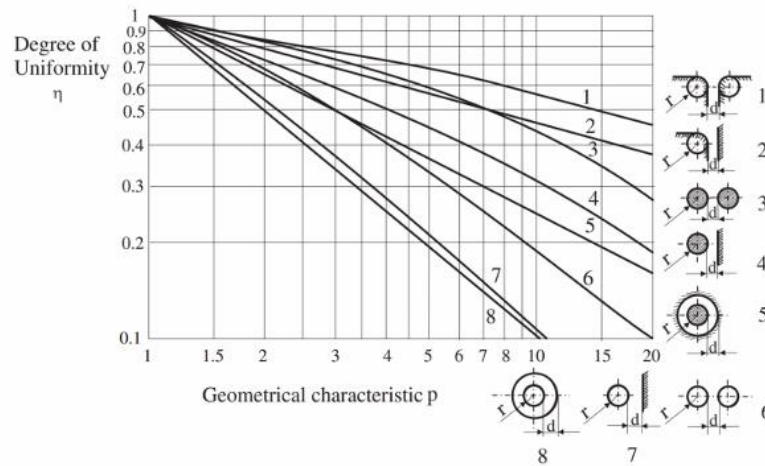


Figure 5.10: Schwaiger uniformity curves [5].

In practical arrangements, the inherent relative strength and linear form is not often completely accurate and the actual breakdown curve when measured can follow the trend identified by curve 1 in Figure 5.11 [5]. Assessing Equation (5.2), based on a coaxial arrangement, for a range of field uniformity factors, for a pressure of 5 bar provides the results shown in Figure 5.12.

At each time step, the distance of the moving contact is calculated, along with the corresponding time dependent cold withstand voltage curve. When the measured voltage between the contacts exceeds the calculated withstand voltage, a breakdown occurs, represented by an exponentially decaying resistance. Trapped charge is implemented using a current source. The disconnecter model has the option to be used as single and three phase modes, therefore allowing the generation of VFTs in all phases to be realised. The model allows the full movement and each breakdown to be calculated, as shown with the characteristic stepwise pattern on the disconnected section of bus in Figure 5.13. The breakdown events over the entire duration of operation can be extracted for a given set of parameters. As a small timestep and relatively long simulation time can be apparent (particularly for slow speed disconnectors with operating times up to three seconds), the total simulation may need to be split into smaller segments, utilising the ATP ‘START AGAIN’ function. Model parameters can even be modified systematically to undertake a statistical analysis. Alternatively, the individual transient and step wise breakdown patterns could be recreated from measured data by ‘tuning’ any of the estimated parameters used.

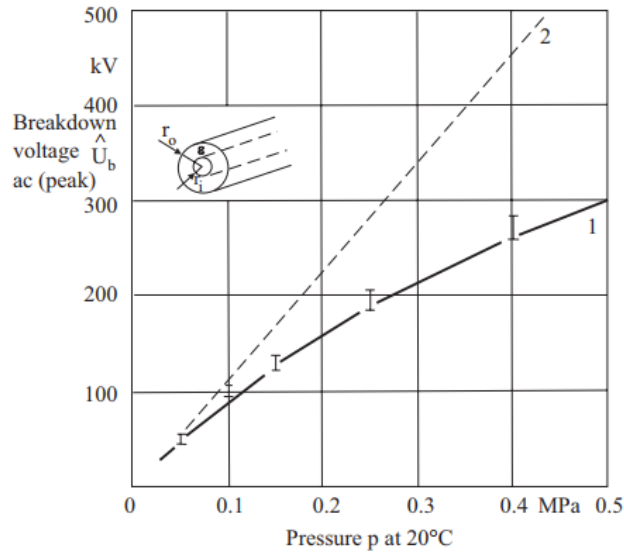


Figure 5.11: Inherent breakdown strength (curve 2) and measured breakdown strength of coaxial arrangement [5].

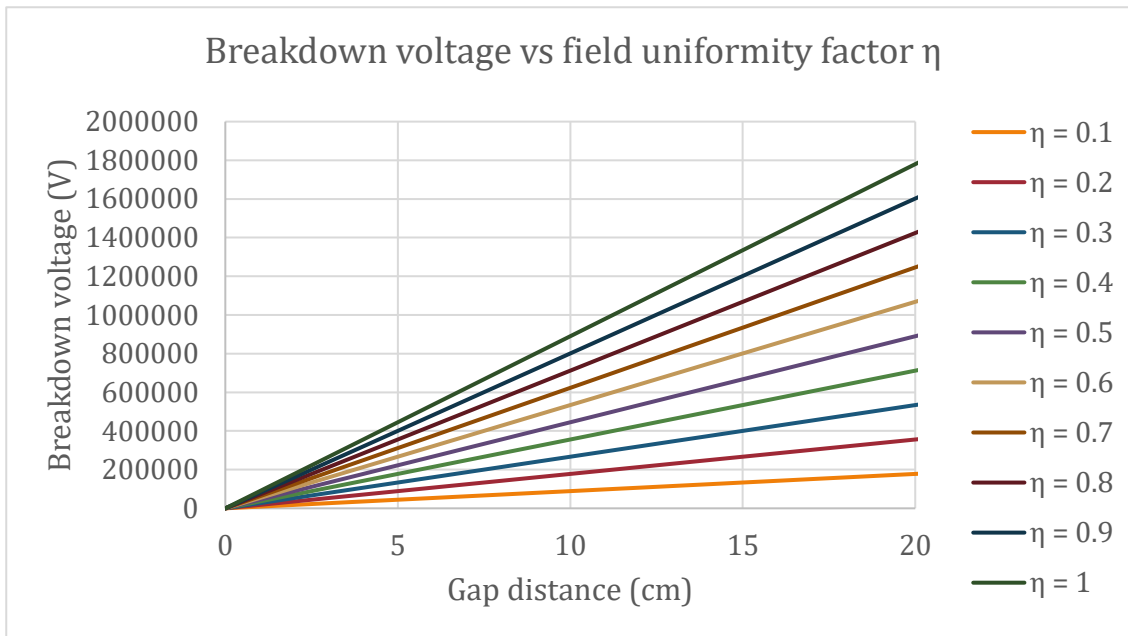


Figure 5.12: Linear breakdown voltage vs gap distance for a range of field uniformities.

Arc interruption behaviour is predominantly dependent on the current slope and the Rate of Rise of Recovery Voltage, while restrike behaviour is dominated by thermal processes [91]. However, it is more complex for very high frequency, low magnitude capacitive currents in which arc duration is highly dependent on the connected network (particularly load and source side capacitances). The model described simplifies arc interruption as a function of time.

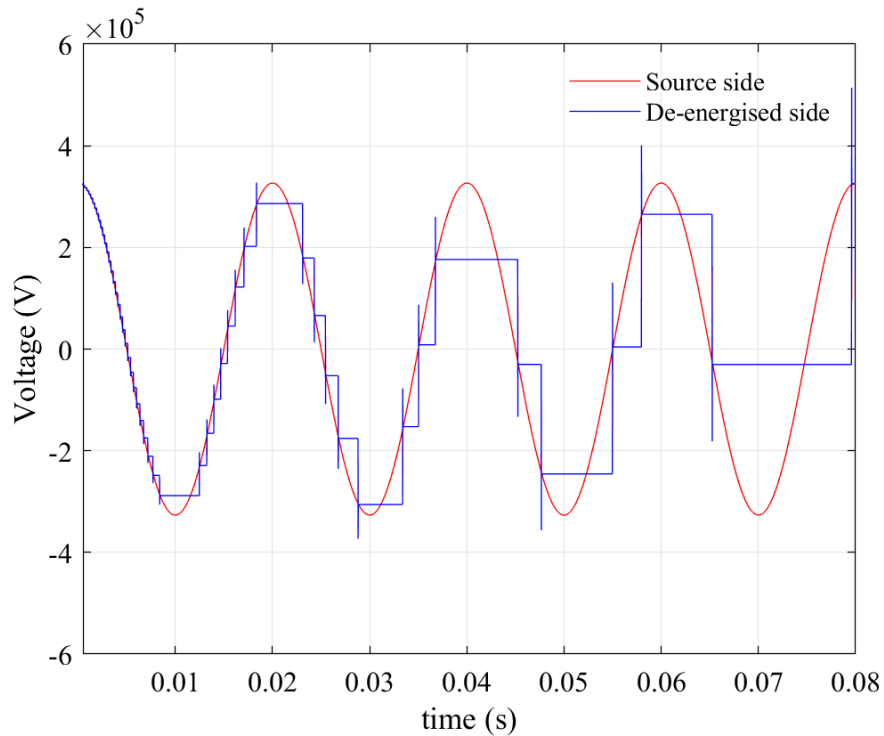


Figure 5.13: Stepwise breakdown pattern generated using custom disconnector model.

5.2.4 Disconnector – breakdown curves from measurements

The modelling results in Chapter 3 and 4, demonstrates that the coupling between phases is high; the degree of interphase coupling makes identification of the phase responsible for the initiation of the transients extremely difficult. Signal post-processing may allow for the separation of transients into their respective phase of origin, however, some assumptions have to be made. The separation of transients according to the phase of origin could also aid identification of the breakdown curves for each disconnector, allowing both more accurate modelling and a potential source of information for condition monitoring, e.g., if measurements are taken frequently, a gradual change in the breakdown curve may indicate potential issues with disconnector contacts; wearing/damage to the contacts could result in a change in field uniformity, altering the breakdown curve.

As an approximation, it was assumed that the circuit arrangements, HV equipment and measurement equipment exhibit the same frequency response and it is also assumed that the phase disconnector initiating the transient will be subject to the highest amplitude, then a method for separation of data can be developed. The developed method, normalises the data from each channel according to largest peak present in each signal,

allowing a better comparison of magnitudes present in each channel. Then, using a peak detection algorithm, the peaks detected in each normalised sample are localised, subject to a minimum amplitude and period between successive peaks. The positive and negative peaks in each sample are then be compared against the other samples. Following the logic that the highest peak originates on the phase responsible for the transient initiation, then a direct comparison of the normalised amplitudes yields the phase responsible for the transient, allowing the other samples for the transient period under evaluation to be nullified. The resulting peaks are separated into phases as shown in Figure 5.14 and Figure 5.15. Patterns or clusters of data are visible but the straightforward comparison of absolute magnitudes between signals does yield a number of outlier data points. These outliers can be excluded from subsequent fit processes.

The process and algorithm developed is provided in Figure 5.16. The method is relatively basic and relies on some user interaction. The process will not produce accurate results for flawed or missing data. Furthermore, the curve fitting process may be skewed by inaccurate declipping action (missing higher frequency superimposed transients due to exceedance of set oscilloscope vertical resolution). With a larger dataset of measurements, it may be possible to further automate the process through cluster recognition or machine learning, although requires further research. The process applied to a disconnecter DS2 close operation (measurement data described in Section 5) provides the breakdown curves shown in Figure 5.15. The resulting linear approximation can be used within the custom disconnecter model documented in Appendix D via a POINTLIST function.

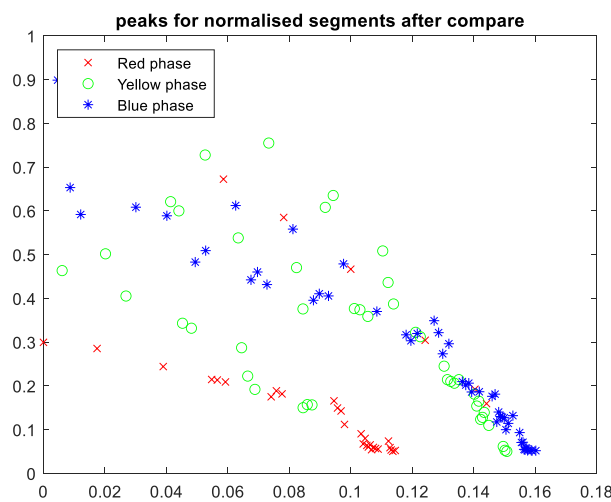


Figure 5.14: Normalised peaks – DS2 close 4 21/10/20.

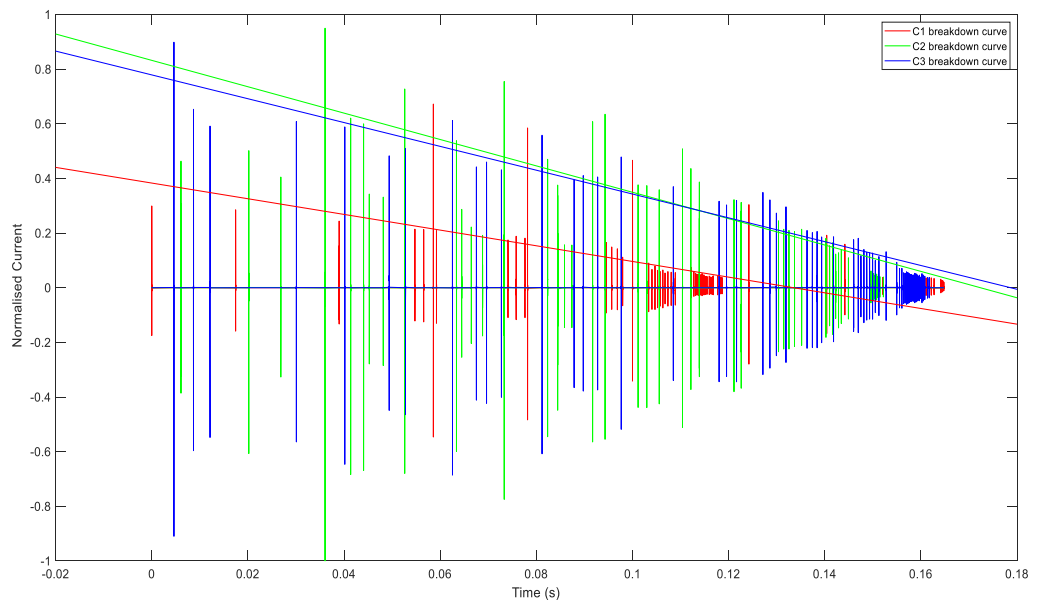


Figure 5.15: Example of measured (original-normalised) waveforms with fitted breakdown curves – DS close operation.

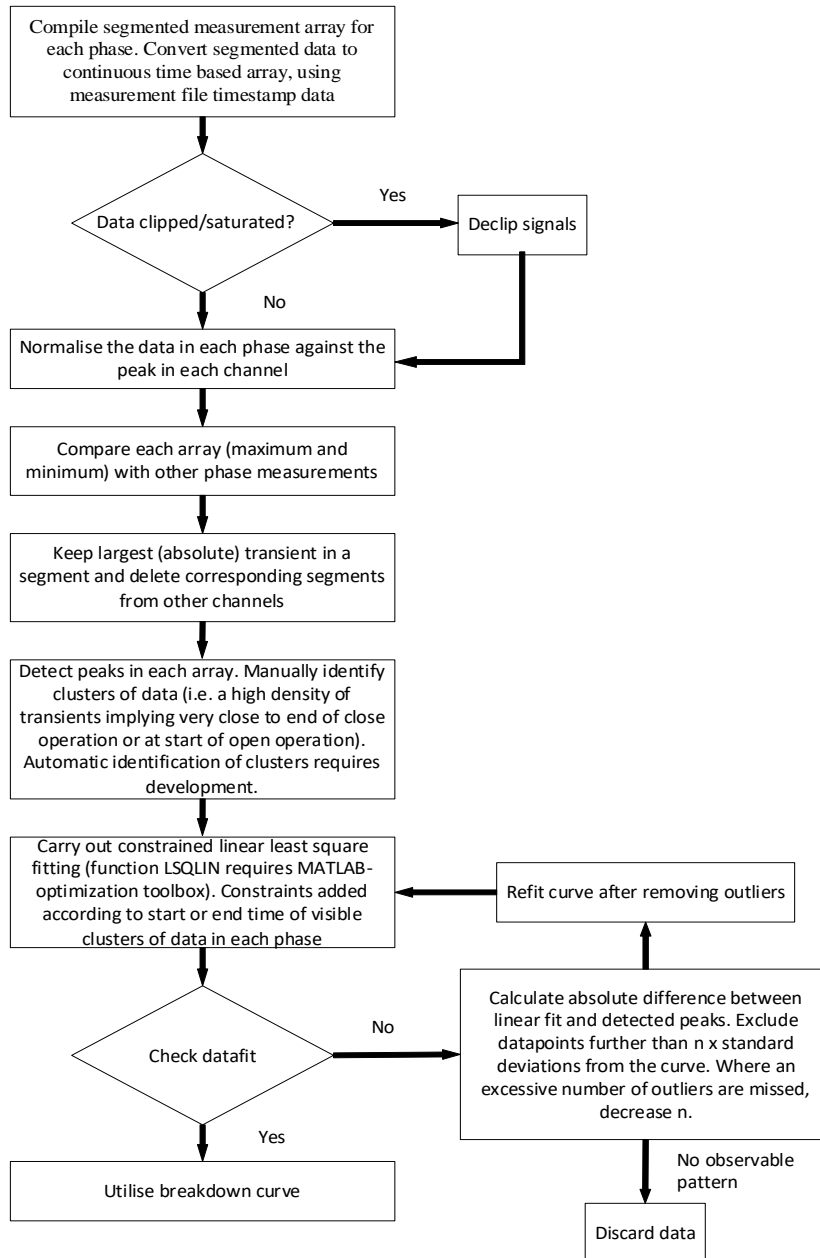


Figure 5.16: Transient initiating phase identification and generation of Linear approximation breakdown curve.

5.3 Equivalent model generation

5.3.1 RLCG equivalent extraction

RLCG (Resistance, Inductance, Capacitance and Conductance) extraction techniques from spacer-flange finite element model computed S-parameters were developed. The method relies on the conversion of S-parameters into transmission line ABCD parameters. RLCG parameters can subsequently be obtained from ABCD parameters following calculation of the complex propagation constant and characteristic impedance

using Equations (5.3) to (5.8) as described in [92] and [93]. Due to minor numerical errors in the computed response, the extracted S-parameters are occasionally non-passive, therefore it is often necessary to enforce passivity using the MATLAB RF toolbox [94].

$$\gamma = 1/l \cosh^{-1} \left(\frac{(1 - S_{11}^2 + S_{21}^2)}{2S_{21}} \right) \quad (5.3)$$

$$Z = \sqrt{\frac{L}{C}} \quad (5.4)$$

$$R = \text{Real}(\gamma Z) \quad (5.5)$$

$$L = \frac{\text{Imag}(\gamma Z)}{\omega} \quad (5.6)$$

$$C = \frac{\text{Imag}\left(\frac{\gamma}{Z}\right)}{\omega} \quad (5.7)$$

$$G = \text{Real}\left(\frac{\gamma}{Z}\right) \quad (5.8)$$

Using this approach, an equivalent frequency dependent RLCG model is extracted. The frequency dependent parameters extracted for a 1m section of bus, with a spacer flange at the centre is shown in Figure 5.17 [95]. The plots show that results start to diverge after the quarter wave resonant frequency and the results therefore suggest this method is only suitable at frequencies below this threshold.

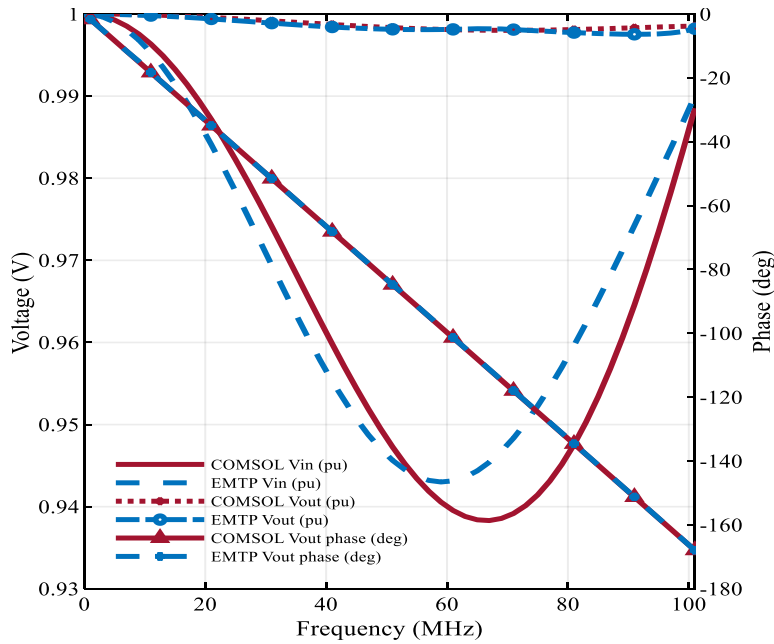


Figure 5.17: Extracted circuit parameters.

5.3.2 Generation of finite element derived blackbox models for ATP-EMTP

EMT models built for the purpose of studying VFTs, typically include a mixture of lumped and distributed components. The issues associated with LCC TLAs are described in Appendix C.

An enhanced circuit model concept was developed in this project to aid circuit-based modelling and avoid the use of possibly inaccurate and unstable TLAs. The method, which can be applied to any physical component (limited only by computation resources), is based on taking the frequency response from a computed full-wave finite element model. The major benefit is that by solving a wave equation, we inherently account for all return paths through appropriate boundary conditions and detailed material parameters.

The computed finite element model's frequency response is best extracted in the form of S-parameters. For the components studied, Y-parameters formed the best basis for fitting the relevant finite element model results, therefore S-parameters were converted to Y-parameters as an initial step. When fitting admittance matrices, error magnification is possible if care isn't taken of the boundary conditions, due to the large spread of eigenvalues across a wide frequency response. It was found that so long as the connected circuit termination was not an open or short circuit, the model remained stable with high accuracy.

Following conversion, vector fitting is applied to the admittance matrix (input, output and transfer elements). Vector fitting is a robust fitting technique, allowing a broadband frequency responses to be expressed in pole-residue form or expanded to the state space form as given in Equations (5.9) and (5.10) respectively [96]. The vector fitting technique is further discussed in the Appendix E.

$$f(s) \approx \sum_{n=1}^N \frac{c_n}{s - a_n} + d + se \quad (5.9)$$

$$f(s) \approx C(sI - A)^{-1}B + D + sE \quad (5.10)$$

where a_n and c_n are the poles and residues either in real or complex conjugate pairs, d and e are the constant and proportional terms, A , B , C , D and E are the state space matrices.

The accuracy and stability of the fit in both the frequency and time domain is also a function of the choice of the model's order of approximation. As a first pass, a suitable model can be chosen to equal the number of resonance peaks present in the response, however on some occasions, instability in the transient response still occurs, ranging from overshoot/undershoot to full divergence of the solution. Even considering the low number of resonance peaks input data, a high order approximation, in many cases, provides reasonable results, albeit at the expense of a more computationally demanding output models that had the potential to exceed ATP table limits (even considering the higher limits permitted through use of the TPGIG solver). Nevertheless, with seemingly high model orders, bands of instability were occasionally observed. This would suggest that as a minimum, a trial and error assessment is required to test for a stable time domain model, however this can be quite time consuming, as each combination of order, weighting and treatment of the constant and proportional terms must be assessed systematically.

A method was developed in this work to locate the lowest possible order of approximation for a stable transient model, following the observed convergence of the RMS error of pre and post fit matrices. Transient model stability was seen for model order RMS errors that approach the RMS error at the asymptote (seen at very large model orders) as described by Equation (5.11).

$$Y_{err} \cong \lim_{n \rightarrow \infty} (Y_{err}(n)) \quad (5.11)$$

Table 5.1: Pole residue equivalent model extraction terms.

Constant and proportional branches	$C_0 = e$ $R_0 = \frac{1}{d}$
Real poles	$R = -\frac{a}{c}$ $L = 1/c$
Complex conjugate pairs	$\frac{c' + jc''}{s - (a' + ja'')} + \frac{c' - jc''}{s - (a' - ja'')}$
Resulting branch terms	$R = (-2a' + 2(c' + a' + c''a'')L)L$ $L = \frac{1}{2c'}$ $\frac{1}{C} = (a'^2 + a''^2 + 2(c'a' + c''a'')R)L$ $G = -2(c'a' + c''a'')CL$

The method developed is summarised by the algorithm in Figure 5.20. The concept was initially assessed for some of the models described in Chapter 3, the spacer-flange and elbow (single). The finite element models utilised assume the flange bolts are effectively bonded.

Results show very good agreement with both frequency domain and transient responses. The transient response, as shown in Figure 5.21 produced a maximum error of below 1% for the VF derived pole-residue equivalent circuit model compared to the impedance profile of the finite element model. The maximum errors for a selection of termination types are presented in Table 5.2. The VF derived models were produced using a 13th and 15th order approximations for the spacer-flange and elbow respectively. The circuit-based (standard) model demonstrated a good match only up to 10MHz. The spacer-flange model section was represented by two 0.5 m distributed transmission lines (Bergeron lines initialised at 5 MHz) and a spacer at the center (modelled as a 10pF capacitance to ground). The 90° elbow was represented by a 0.5 m Bergeron line at each end, and two spacers. The transient response was evaluated in both ATP-EMTP and ADS (using the ADS S-parameter to macromodel generator).

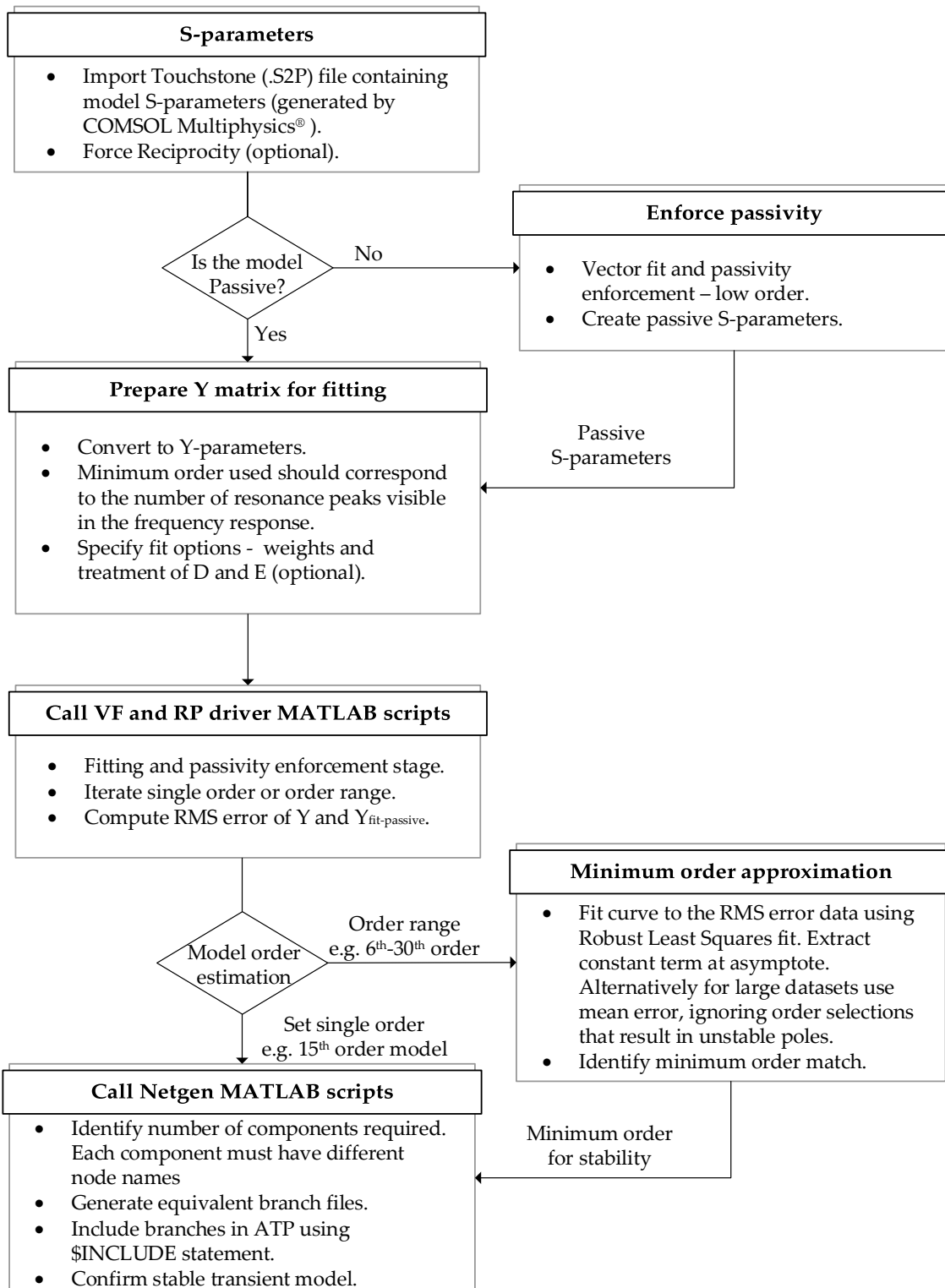


Figure 5.20: GIS Blackbox Macromodel generation at minimum order for stability algorithm.

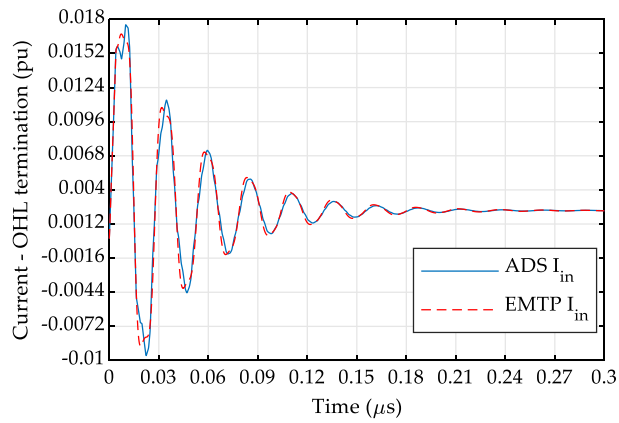


Figure 5.21: 90° elbow - EMTP vs. ADS transient response comparison for model with OHL termination.

Table 5.2: Computed spacer-flange and elbow model performance for range of terminations.

Termination method	RMS Error					
	Spacer-flange			90° Elbow		
	V_{out}	I_{in}	I_{out}	V_{out}	I_{in}	I_{out}
Matched	0.002	4.7×10^{-6}	2.2×10^{-5}	0.002	1.6×10^{-5}	2.6×10^{-5}
Short Circuit	0	0.35	0.35	0	0.04	0.04
Open Circuit	0.205	0.003	1.0×10^{-8}	0.20	0.003	1.0×10^{-8}
Resistive 1 Ω	0.003	0.003	0.003	0.002	0.002	0.002
OHL Z_0 434 Ω	0.003	3.8×10^{-5}	6.8×10^{-6}	0.009	1.3×10^{-4}	2.0×10^{-5}
Capacitive-Resistive	0.019	3.1×10^{-4}	4.5×10^{-5}	0.092	0.001	1.2×10^{-4}

When spacer-flange and elbow pole-residue equivalent models were included in the larger GIS system model shown in Figure 5.1 (with the model configured for a worst case VFTO, energised line side, closing line side disconnector onto a 1.1p.u. trapped charge with the circuit breaker 1 open), a slight reduction in VFT magnitude was seen overall as observed in Figure 5.22 and Figure 5.23. Peak magnitudes of 650kV and

628kV were calculated for the circuit-based approach and the enhanced pole-residue approach respectively. The peak magnitudes did occur at different times, significantly earlier for the pole-residue model. Furthermore, the transient appeared to decay significantly quicker in the pole-residue model.

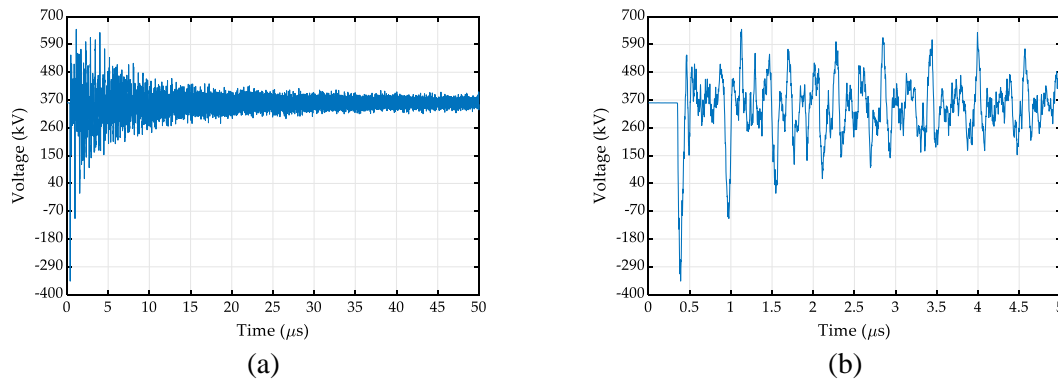


Figure 5.22: Voltage at gas-air bushing for circuit-based model: (a) 50µs duration, (b) magnified 5µs.

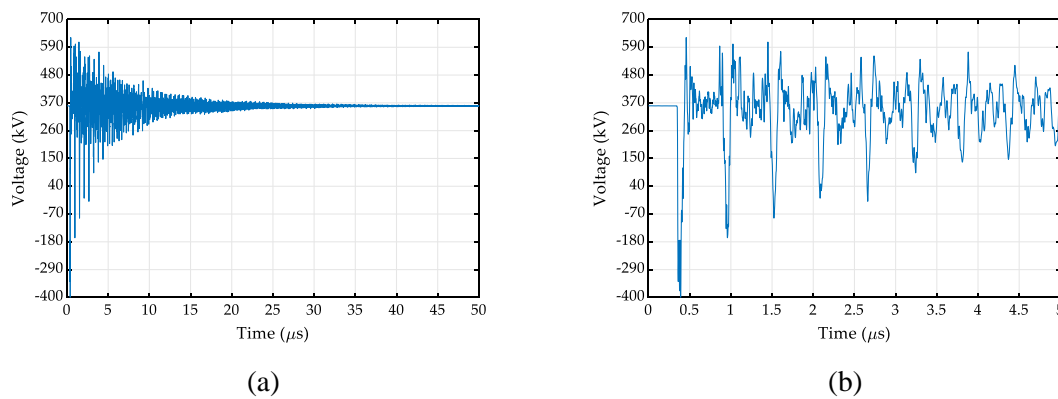


Figure 5.23: Voltage at gas-air bushing for pole-residue model: (a) 50µs duration, (b) magnified 5µs.

Further pole-residue equivalent models have also been produced for the Gas to Air Bushing. The finite element model included AIB, enclosures and downlead/rod arrangements; further model specifics and details of the electromagnetic phenomenon were discussed in Chapter 3. A one port, pole-residue equivalent was created from the finite element model's S11 parameter and imported into ATP-EMTP. A comparison of the magnitude and frequency response of the pole-residue equivalent and the finite element model, as shown Figure 5.24, reveals a near perfect match across the range. Applying a 1 p.u. step voltage to the pole-residue equivalent circuit, with a rise time of 6ns and an impedance equal to the bus Z_c , gives the response shown in Figure 5.25. The

maximum transient overvoltage seen for the circuit was 1.72 p.u. This is based on a reflection purely at the bushing only and not considering other reflections from elsewhere in the system, which could superimpose constructively to a higher magnitude. Carrying out the same simulation for the bushing with the 8 downlead configuration confirms a slight reduction internally to 1.70 p.u. This suggests that the grounding system, while having a major impact on TEVs, has a smaller impact on the internal VFTs.

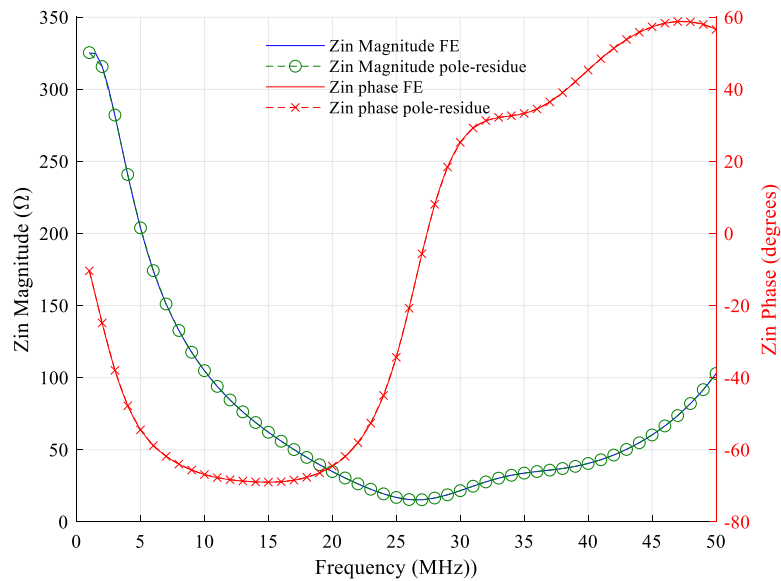


Figure 5.24: Finite Element model and pole-residue equivalent impedance comparison.

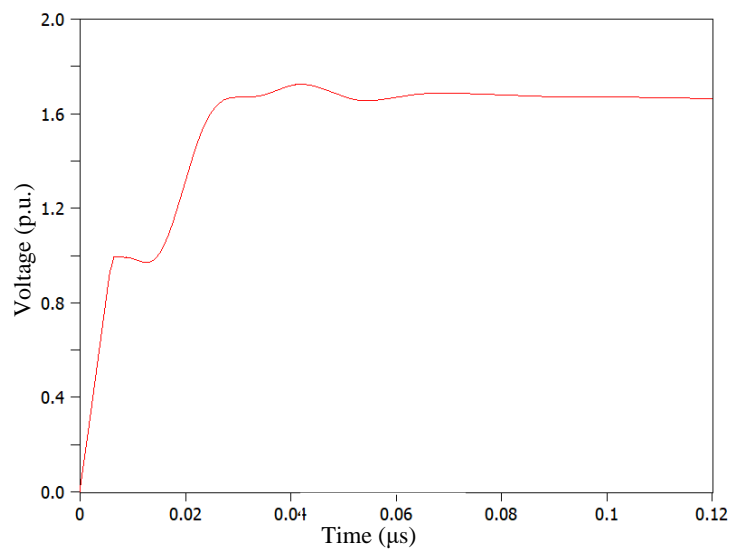


Figure 5.25: Transient overvoltage at Bushing pole-residue model for a 1p.u. 6ns step input voltage.

5.4 Substation ‘A’ 400kV GIS EMT model

The ATP-EMTP model shown in Figure 5.1 highlights the relevant section of the extended ATP-EMTP model created for Substation ‘A’. A section of the Substation’s single line diagram is provided in Figure 5.26.

The OHL section is modelled with the full 3 phase line models, with the first four short spans modelled as Bergeron lines initialised at 12.5MHz; the long span is modelled as a Pi line. The Substation ‘A’ circuit section is modelled at the discontinuities (spacer and elbows) as vector fit macromodels as described in Chapter 3. The sections of bus in between these discontinuities are modelled as coaxial ‘Bergeron’ cables using the LCC routine, initialised at 12.5MHz.

The main bus and outgoing circuits are simply modelled as distributed lines, defined by a surge impedance, velocity and resistance. With the exception of the SGT, all other outgoing circuits are modelled by surge impedances and are matched remotely to prevent reflections. There was sufficient detail available to construct detailed models of the entire system. The circuit model shown is configured to generate transients for an DS2 (bus side DS) operation. The 50Hz source is supplied from the main bus, while the Substation ‘A’ circuit is de-energised. Both the circuit breaker (CB1) and the line side disconnecter (DS1) are open, represented as a 5pF inter-contact capacitance and two 52pF capacitances to ground (both extracted from DS Finite Element model). There was sufficient detail to model the disconnecter in COMSOL, making it possible to extract the capacitance matrix with full frequency dependence. The computed capacitance was used in the EMTP model. There was insufficient design detail available for a circuit breaker model, therefore, an estimated gap (50pF) and ground capacitance (200pF) was used; it is assumed that there are no grading capacitors installed.

Figure 5.27 shows a single transient for an DS2 (bus side DS) close operation, in particular the first transient initiated during a close operation. Subsequent transients will initiate according to the trapped charge that remains after the arc has extinguished and the 50Hz AC voltage. Each transient decays rapidly within 5-6 μ s, however minor oscillations persist for some time. The transients in Figure 5.27 and Figure 5.28 show a forced arc extinction 50 μ s after the transient is initiated. The arc extinction results in further small oscillations on the line side. Further calculated single transient segments for DS2 operation while DS1 is closed are shown in Figure 5.29 and Figure 5.30. It is

evident that the current at the download is significantly larger for DS2 operations where DS1 is closed.

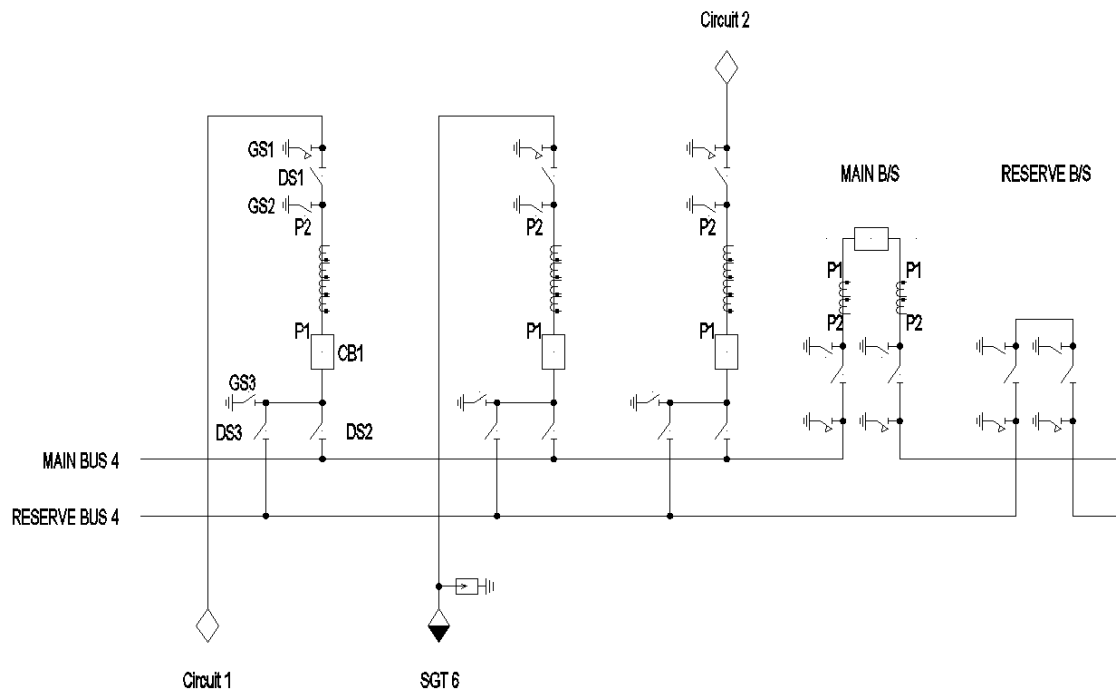


Figure 5.26: Section of Substation 'A' SLD.

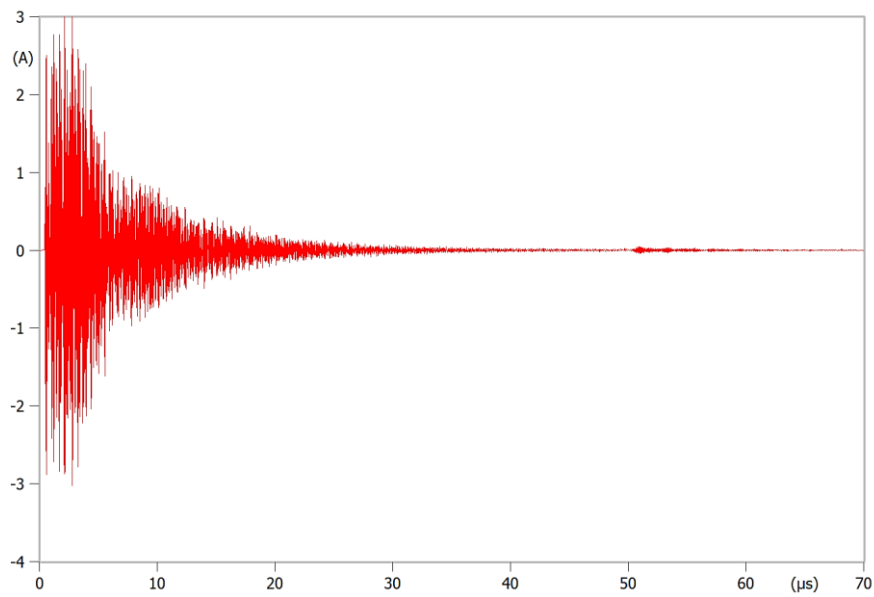


Figure 5.27: Computed DS2 close single transient at MOSA download – CB1 open, DS1 open, DS3 open.

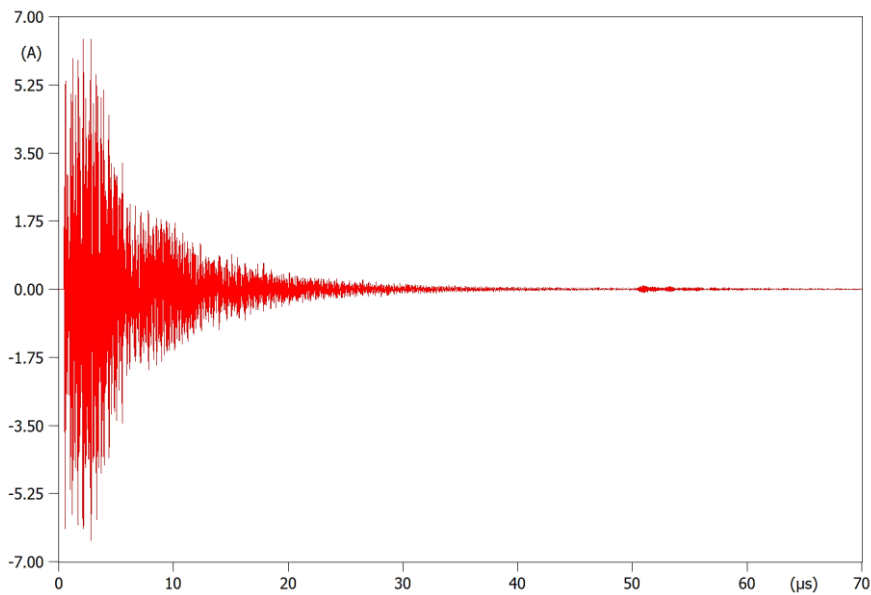


Figure 5.28: Computed DS2 close single transient (with -1p.u. trapped charge) at MOSA download– CB1 open, DS1 open, DS3 open.

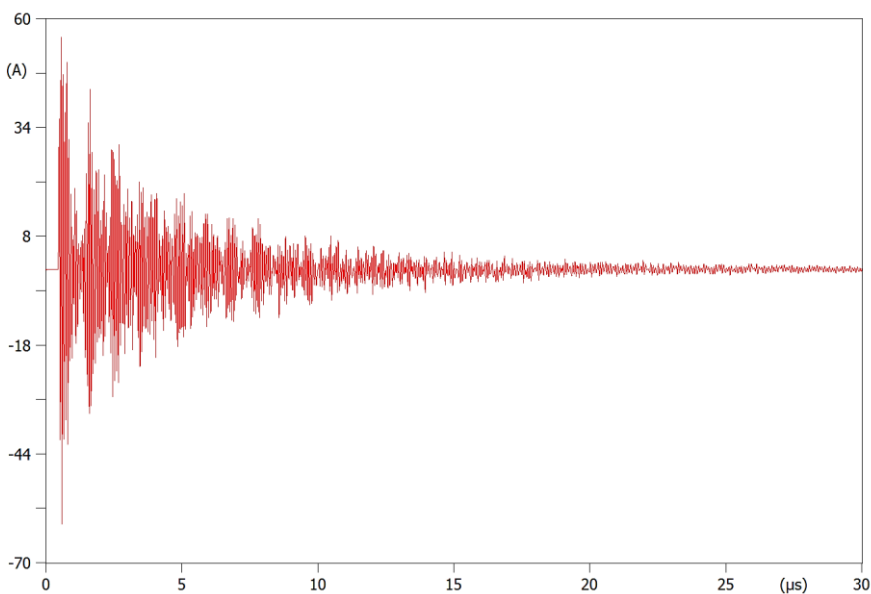


Figure 5.29: Computed DS2 close single transient at MOSA download first transient – CB1 open, DS1 closed, DS3 open.

The maximum amplitude calculated in the line side bus for an DS2 close operation, with DS1 closed, is 296kV, as seen in Figure 5.31. While the attenuation inside the GIB is low, by the time the initial wavefront reaches the bushing, it has dampened due to the effects at the spacers and elbows. Figure 5.32 shows that by the time the wave front reaches the bushing, the magnitude reduces to 229kV and the front time has increased from the initial 5ns to 25ns.

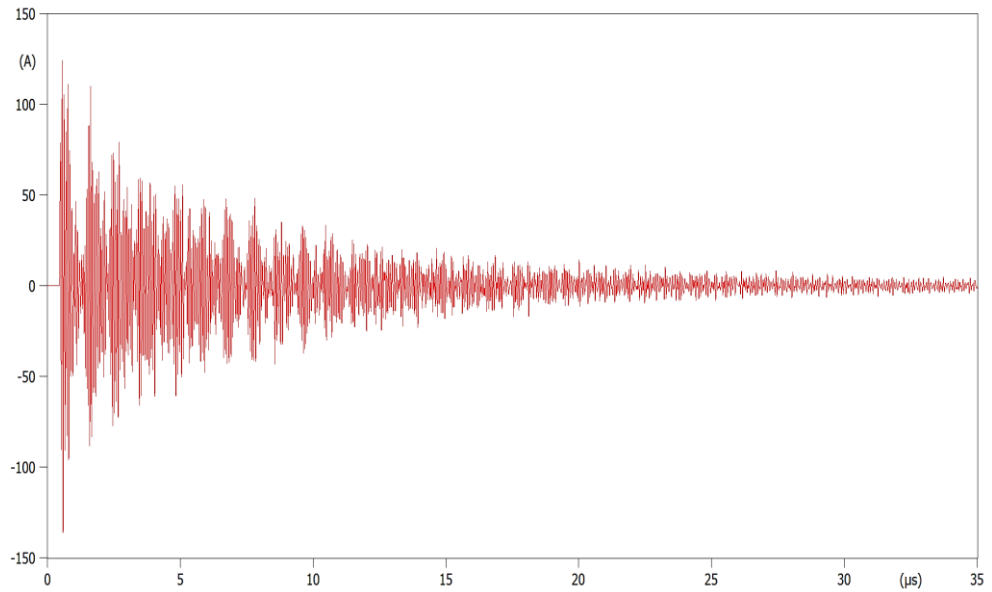


Figure 5.30: Computed DS2 close single transient (with -1p.u. trapped charge) at MOSA download – CB1 open, DS1 closed, DS3 open.

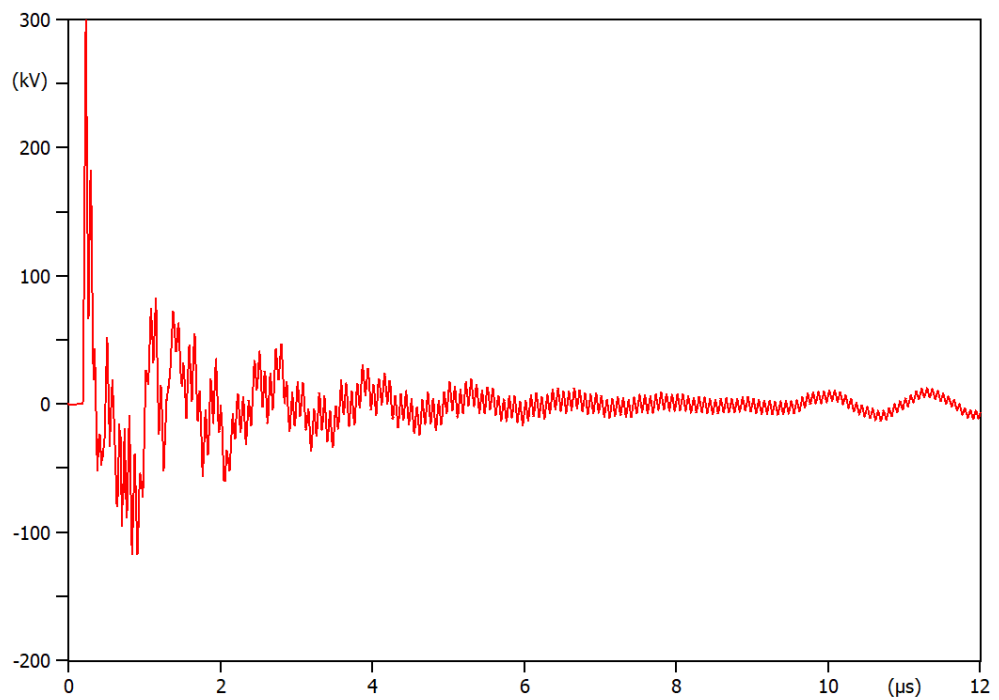


Figure 5.31: Computed line side voltage at elbow - DS2 close, DS1 closed, CB1 open, DS3 open.

The maximum amplitude on main bus is larger than the line side for bus side disconnector switching. Depending on the configuration of the other circuits off the main bus, it is possible to see larger transients, initiated by Substation ‘A’ Circuit 1 disconnectors, on other circuits. Figure 5.33 shows an DS2 generated transient on an

adjacent circuit, with a magnitude of 540kV, in comparison with the Substation 'A' Circuit 1 bus 296kV.

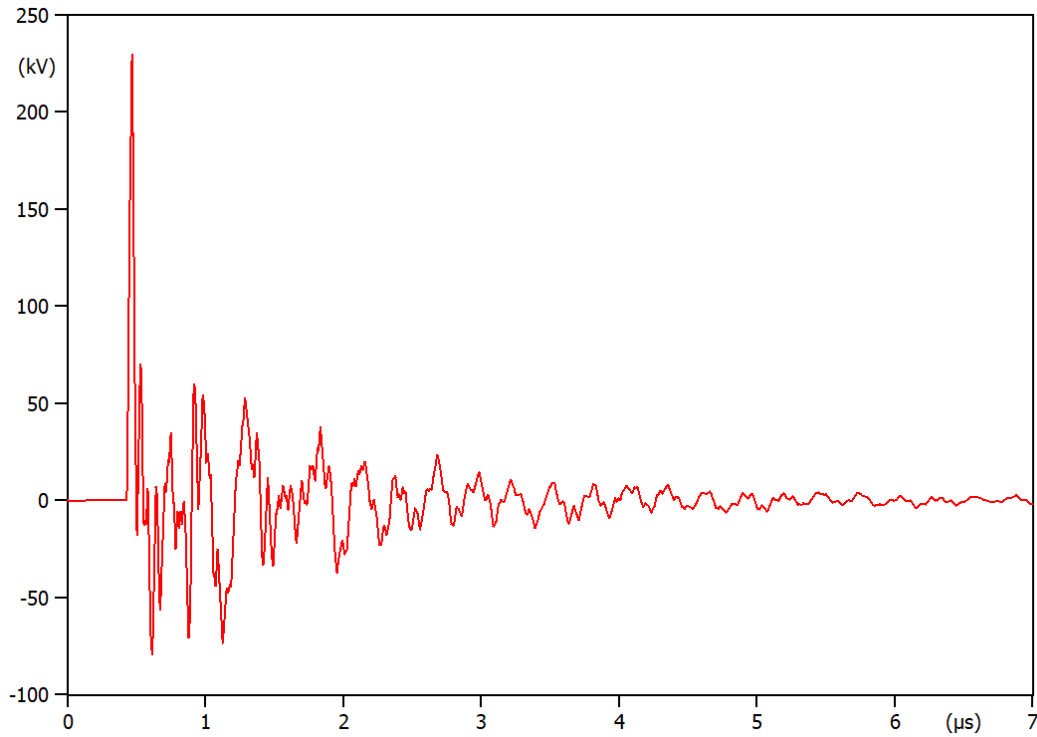


Figure 5.32: Computed voltage waveform at bushing – DS2 close, DS1 closed, CB1 open, DS3 open.

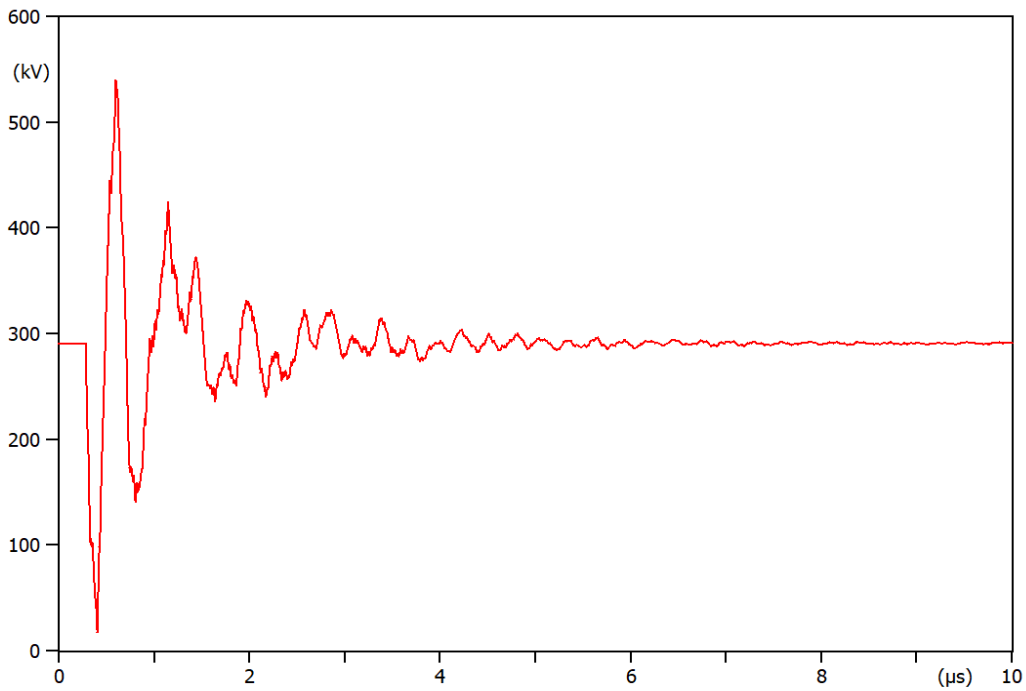


Figure 5.33: Computed DS2 close single transient (with -1p.u. trapped charge) at adjacent circuit – CB1 open, DS1 closed, DS3 open,

5.4.1 Switching regime

The network operators common switching regime involves energisation from the main bus out to the line, load or generation. As discussed further in Section 6, this practice avoids the excessive line side GIB transients that are commonly reported in literature. There may be occasions where the line is energised from remote generation and the line side disconnector may be required to operate before closing the circuit breaker onto the main bus. It is this scenario in which the largest transients will be seen on the line side GIB. For this switching scenario, the highest GIB VFTO is 707kV at the bushing as shown in Figure 5.34. While this is still unlikely to cause a flashover in a defect free system, it is still considerably higher than the other switching regimes and should be avoided where possible.

5.4.2 Simulated Coupling at MOSA

A significant unknown when considering surge counter incrementation for VFT events is the propagation/coupling mechanism. Due to the frequencies and magnitudes involved, propagation/coupling could occur through MOSA conduction, capacitive coupling (near field), coupling via the grounding system, or even radiated coupling. It is very difficult to prove the coupling method using measurements alone. Figure 5.35 shows the current magnitudes delivered to the MOSA downlead through the equivalent MOV block capacitance and the nonlinear resistance. It is clear that the magnitudes detected at the MOSA downlead during DS switching are a result of coupling through the MOV block capacitance. The ‘displacement’ current through the capacitance is approximately 130 times larger than the resistive ‘leakage’ current. The plot in Figure 5.36 shows only the resistive currents. The waveforms clearly have the same frequency content, but a slightly different waveshape, as the magnitude dependence is more evident.

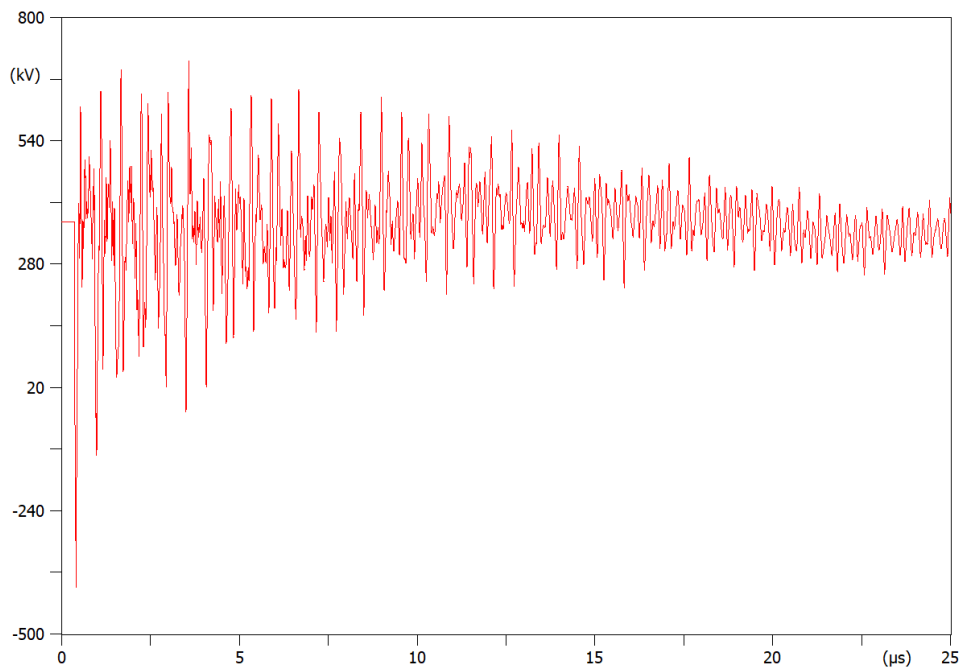


Figure 5.34: Computed line side energisation, DS1 close, CB1 open, DS2 open, DS3 open.

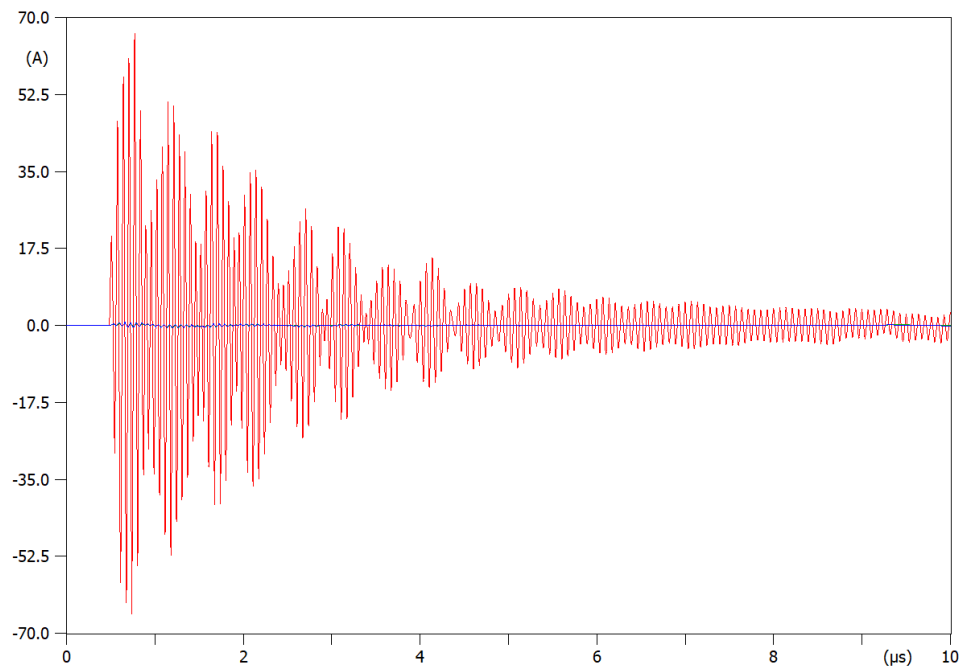


Figure 5.35: Computed DS2 close current coupling mechanism through MOSA – CB1 open, DS1 closed – Capacitive current (red), A0 resistive current (green) and A1 resistive current (blue).

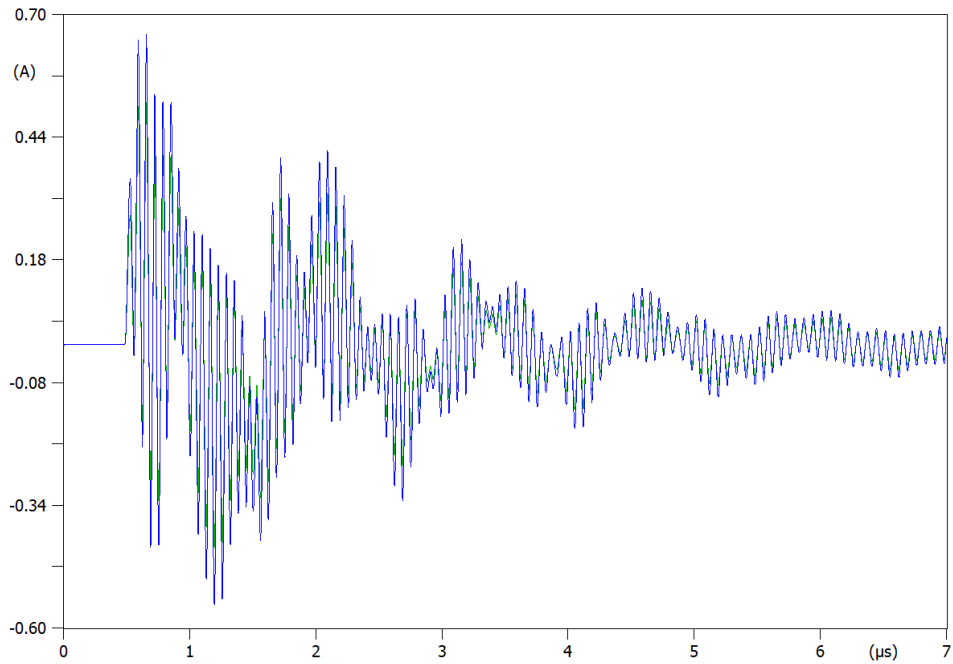


Figure 5.36: Computed DS2 close current coupling mechanism through MOSA – CB1 open, DS1 closed, resistive currents only - A0 resistive current (green) and A1 resistive current (blue).

5.4.3 Effect of Bus Capacitance

The initial wavefront magnitude does have some dependency on the ratio of bus capacitances. Looking at the initial voltage collapse either side of the switching disconnector in Figure 5.37 to Figure 5.39 it is evident that increasing the isolated bus side capacitance, results in a larger initial voltage collapse and hence, a larger peak transient.

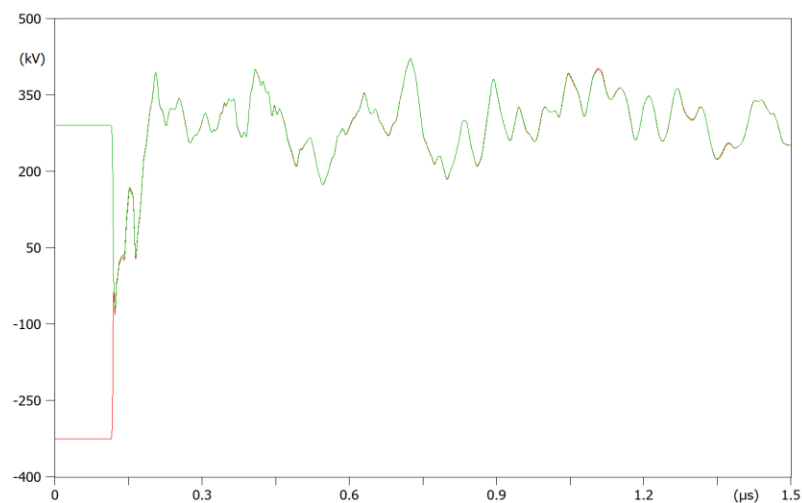


Figure 5.37: Computed voltage collapse at either side of DS2 for actual model – red isolated bus, green energised bus.

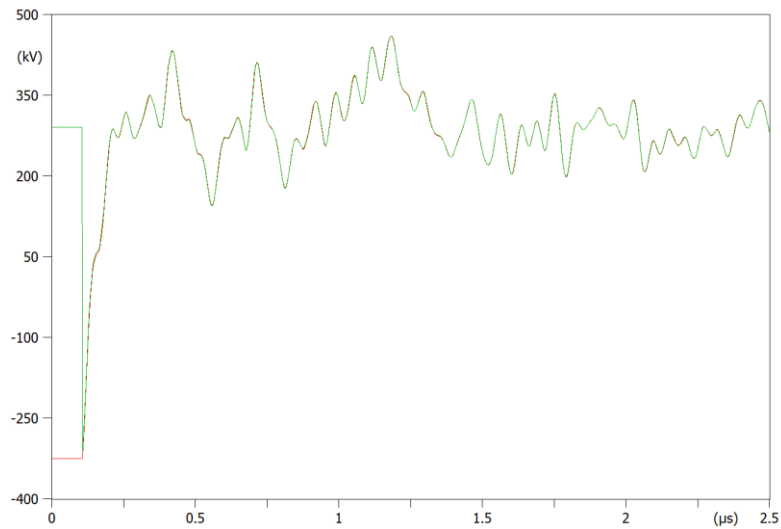


Figure 5.38: Computed voltage collapse at either side of DS2 for model with additional 1nF capacitance on isolated bus– red isolated bus, green energised bus.

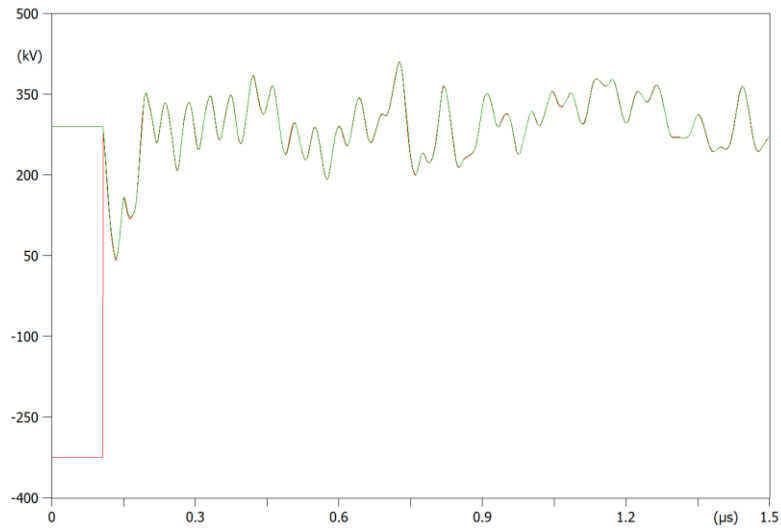


Figure 5.39: Computed voltage collapse at either side of DS2 for model with additional 1nF capacitance on isolated bus– red isolated bus, green energised bus.

5.5 Conclusion

Using recommended modelling practices, enhanced with a custom disconnector model and finite element/MoM derived blackbox models, this chapter has quantified the electromagnetic transient behaviour of Substation ‘A’ GIS, during disconnector switching operations.

The approach used is intended as a co-simulation style approach to modelling for this class of transients, for increased accuracy. With further modelling efforts, particularly

with regards to the voltage dependent non-linear behaviour of surge arresters, the entirety of the model could be replaced with discrete blackbox models, originating from numerical modelling or even measured S, Y or Z parameters. The advantage over existing ATP-EMTP modelling approaches (and other EMTs) based on TLAs is apparent.

The vector-fitting method has been adopted for the extraction of highly accurate, finite element derived models. The method has been enhanced by a simple but seemingly robust method of identifying which model orders of approximation will be stable in a transient simulation, along with the minimum order of approximation for a stable solution. A useful workflow diagram is provided in Appendix E. Although untested, it is likely the process will also work for measured S-parameter data.

Through detailed circuit modelling, with the enhancements brought about by the equivalent circuit extraction methods developed, the worst-case magnitudes were computed around the system for various DS operations.

From the computed results, assuming a full bonded spacer-flange interface and the given switching regime implemented by the network operator (energisation from the main bus towards generation), the magnitudes presented should not threaten insulation levels of an ideal system (uncompromised insulation).

The main bus to source energisation method results in lower magnitudes on the line side of the circuit being switched. This is apparent for two reasons, firstly, when switching the bus side DS, the power frequency voltage on one side, with the trapped charge on the other, will produce high magnitude VFTOs, however, observing from the line side (e.g. at the bushing), these transients are significantly lower, attenuated by the open state of CB1. Secondly, as the line side of the circuit is not yet energised at power frequency, switching of the line side disconnecter (DS1) is subject only to the switching of trapped charges. Trapped charge may exist on the floating section of bus between DS1 and CB1, however, on the line side, charges dissipate quickly through the AIS equipment and OHL, meaning line side DS switching should see much lower magnitudes than bus side switching for the circuit.

High surge counts are a concern for the network operator as the condition of the surge arresters under fast and very fast transients can deteriorate after numerous exposures. From a lightning perspective just two 65kA surges can increase the leakage current of the MOSA by 50% [4]. The VFT associated currents are of course significantly lower,

but their effects on ageing require further research. Nevertheless, it was necessary to evaluate the currents present on the downlead during DS switching to quantify the magnitudes. Furthermore, given the debate over the nature of the currents through MOSA during VFT events, it was necessary to confirm whether capacitive, resistive, inductive or even radiated coupling is dominant. From modelling, for Substation 'A' circuit 1 it is clear that the currents seen are mostly capacitive and of reasonably low magnitude. It is unlikely that these currents will exceed the voltage-time thresholds implemented by surge counter devices and therefore register as a count. This observation is again a factor of the switching regime used by the network operator and not conclusive in the general sense. Energising from generation towards the main bus will generate higher magnitude VFTs and the nature of the MOSA current could change.

Further observations have been made on the magnitude of isolated bus capacitances. increasing the isolated bus capacitance and therefore, charge, results in a larger initial voltage collapse and hence, a larger peak transient.

6 DEVELOPMENT OF MEASUREMENT SYSTEMS FOR FIELD BASED MEASUREMENTS

6.1 Introduction

Modelling techniques using Finite Element Modelling or circuit-based platforms can provide an invaluable insight to the behaviour of Gas Insulated Substations (GIS) during switching operations. However, modelling is often subject to many assumptions and simplifications. Unrealistic boundary conditions are often imposed in order to achieve model convergence with the available data and computational resources. Large, complex geometries must be simplified where possible to reduce the number of degrees of freedom without impacting the results. It is therefore essential that models are validated by an appropriate means. Arguably the best validation of models is achieved through measurement, although it must be ensured that the measurement system does not have a significant effect on the transients under measurement, observing the concepts of measurement uncertainty. Several measurement techniques are explored and developed for the measurement of both internal and external transients. Promising results were achieved from initial site-based testing and have prompted further revisions to the designs and calibration procedures. Initial measurements were also extremely useful for establishing triggering thresholds for data acquisition equipment, permitting a higher number of successful captures in subsequent visits.

The development of external, or externally accessible temporary sensors for the measurement of internal transients will minimise the inconvenience and additional cost

brought about some existing VFT measurement systems, allowing the system operator to have a good understanding of the risks posed to a system during switching and helping to identify the need for mitigation techniques or even a change in procedures.

An intriguing consequence of disconnector switching in GIS is the incrementation of the surge counters associated with the main air insulated surge arresters. While it is a well-known phenomenon, only limited investigations into the causes behind its occurrence have been carried out and therefore the true effects on the surge arrester cannot be determined. Installation of high frequency measurement equipment at the surge arresters will provide a much-needed insight into both surge counter and surge arrester behaviour during VFT events, while also providing some validation to the observations made on MOSA currents during DS switching in Chapter 5.

6.2 Calibration vessel

A more realistic test set-up using an approximate half scale aluminium vessel (with the exception of the spacer-flange width for which dimensions were maintained to test shielding arrangements), shown in Figure 6.1 was designed and built in-house. The device was used to test and calibrate sensors. Calibration and testing can be carried out using both a VNA and low voltage impulse generator.

The device was subsequently installed inside an EMI chamber, as it was picking up radiated emissions when installed in the large open space laboratory. The vessel has a 75Ω characteristic impedance, close to that of the GIB at approximately 68Ω . An epoxy spacer has been machined from Epoxy tooling board. The constant impedance internal and external tapers ensure that the 75Ω impedance is maintained as the dimensions are scaled up from that of the N type connector. When simulated in HFSS, the model has good transmittance and a usable bandwidth beyond the 120MHz simulation limit when mounted over a perfect ground plane at 1m height. To confirm the vessel's frequency response, S-Parameter measurements were carried out using a VNA. After re-normalising the S-parameters from the 50Ω port impedance to 75Ω , the results show a bandwidth greater than 200MHz as shown in Figure 6.2.

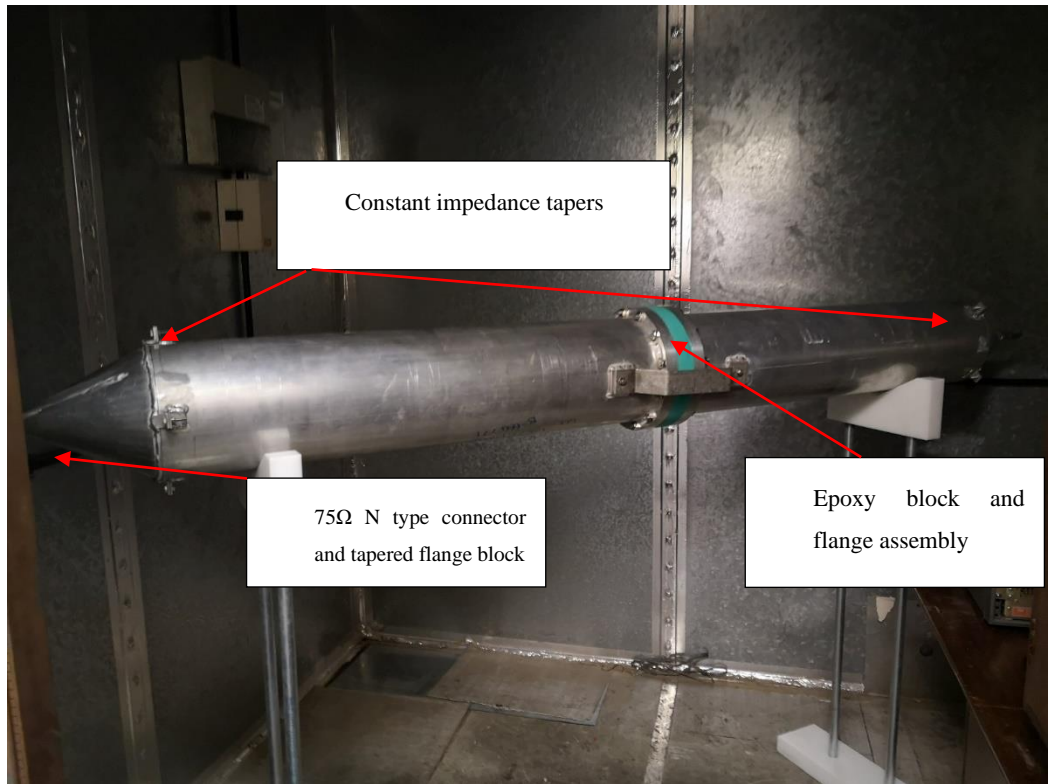


Figure 6.1: Calibration vessel installed in EMI Chamber.

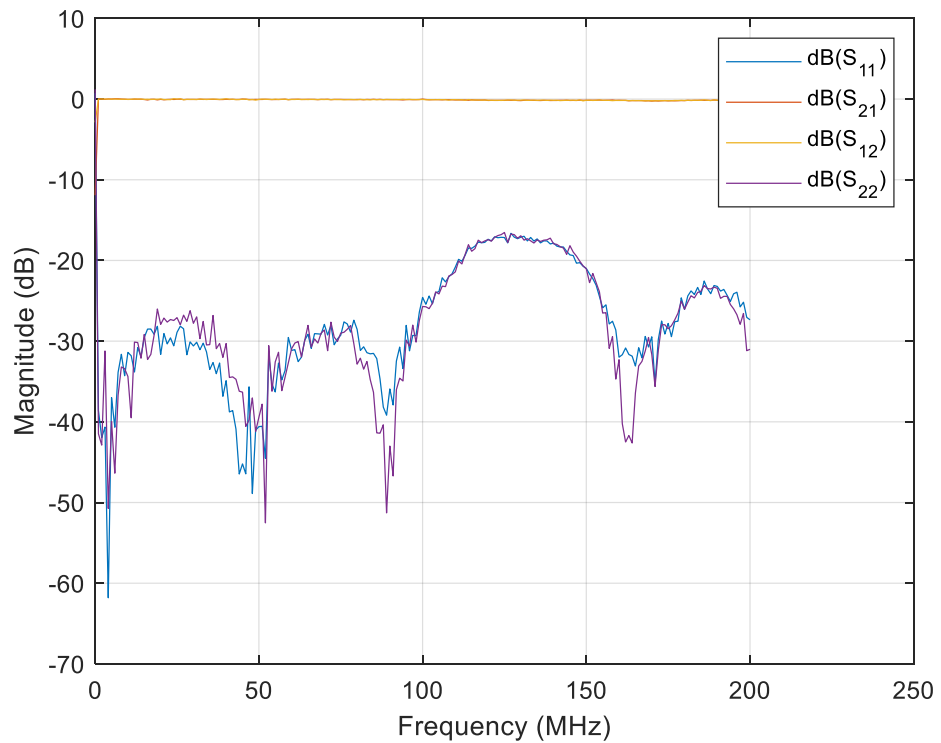


Figure 6.2: Vessel measured S-Parameters.

6.3 High Frequency Current Transformers

As discussed, a reported consequence of switching operations in GIS is the incrementation of the surge counters. The surge counters installed at Substation 'A' GIS are the ABB EXCOUNT – I model. The model is more sensitive than others in the range with a trigger threshold of 10A for 8/20 μ s waveforms [97]. The trigger threshold generally increases for shorter rise/fall times although the thresholds for VFT waveforms (decaying sinusoidal waveform with wide spectrum of frequencies) are unknown. Experiments conducted by ABB suggest that even small amplitudes in the mA range at higher frequencies can cause triggering of the counter [98]. Only the basic operation of the surge counter model is known. The counter detects surges via an integrated CT (of unknown bandwidth) [99]. The output from the CT (following rectification) charges a capacitor circuit, which subsequently registers a surge when the capacitor's voltage reaches a pre-determined magnitude. Through measurement of the current propagating via the surge arrester downlead, it may be possible to deduce not only the magnitude of surges that result in counter incrementation but also the mechanism of propagation/coupling.

Internal VFTs can reach voltage magnitudes up to 3p.u. [8], with the associated current reaching several kA, the voltage and current related by the surge impedance of the bus. At the gas to air bushing these transients are partially reflected into the bus; partially refracted externally, continuing propagation as TEVs; and partially transmitted towards the air insulated bus. The magnitude of the transmitted surge is determined by the surge impedances of these propagation routes. Although not confirmed and highly debated, the response time of a surge arrester's ZnO blocks subjected to VFTs should be sufficiently quick, with a response time better than 3ns. The inductance of the internal and external connections and the magnitude of the transients will be the main factors for its behaviour during VFTs. It is possible that VFTs occasionally appear at magnitudes higher than the rated voltage of the surge arrester, forcing the surge arrester into higher conduction and exceeding the threshold for the counter through conducted current. Further propagation/coupling mechanisms that could account for surge counters incrementation are surges that couple through the arrester's capacitance. When a surge arrester is in its low-conduction state, it presents as a large capacitance to the surge, which is a result of the large inter-granular layer capacitances [100]. This layer depletes as the surge arrester goes further into conduction. The propagation mechanisms and direction at present are unknown, the possibilities are summarised below:

- Propagation via the surge arrester in mid to high conduction, either directed from the overhead line towards the ground or upwards from the ground/earthing system. Possible with a high magnitude VFT event.
- Coupling via the surge arrester's capacitance in low conduction, directed from the overhead line or grounding system.
- Radiated coupling via ground/surface wave, illuminating the high frequency rod and downlead.

In order to capture the high frequency currents present on the downlead, High Frequency Current Transformers (HFCT) were suggested for installation at Substation 'A' circuit 1 surge arrester downleads. High bandwidth HFCTs with large apertures were purchased for this purpose. The HFCTs were not well suited for outdoor use, therefore it was necessary to construct a weatherproof enclosure for protection. A metallic enclosure was chosen to shield the CT from external EMI and moisture ingress, as shown in Figure 6.3. The enclosure is grounded via the fabricated scaffold attached to the surge arrester mounting post. Apertures cut on both sides of the box allow the downlead to pass through with minimal disturbance. The CT is supported by a 3D printed Polylactic Acid block and the box is sealed and made watertight with a 3D printed gland and a sealant solution. The CT is not grounded internally to avoid conductive interference and the creation of induction loops with the acquisition system cables. Therefore, the CT is terminated inside the box with an insulated BNC connector. The aluminium box shields the CTs reasonably well from external EMI.

To ensure the CT/enclosure wouldn't detract from the performance of the downlead and also to aid the design process, a basic CT finite element model was built (as number of windings, termination resistor and layout etc. of the actual CT was unknown), housed in the enclosure as shown in Figure 6.4. The CT case dimensions were measured, and dimensions for the core, case slit dimensions, number of turns and material characteristics were all approximated. It was not necessary to replicate exactly the performance of the HFCT from a modelling perspective as laboratory based measurements were possible, therefore the exact construction of the CT was not important. For the simulated domain, the downlead and surrounding cylindrical air domain was extended up to 2.6m from the ground level to to represent the distance to the base of the surge arrester from ground level.

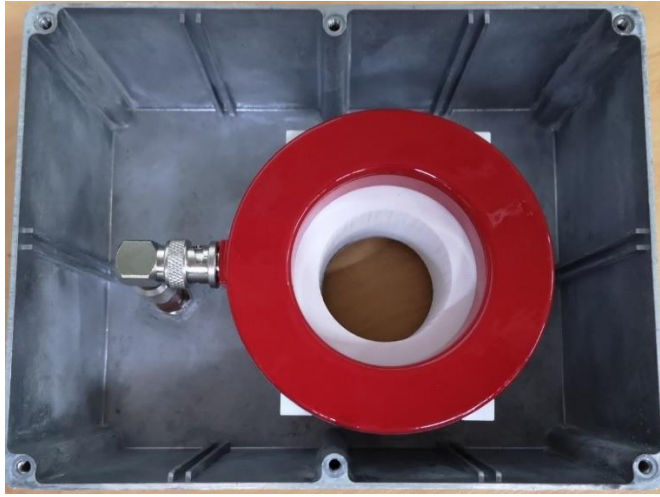


Figure 6.3: HFCT mounted inside IP rated Aluminium enclosure.

Assessing the model with and without the CT box at 12.5MHz, shows that by introducing the CT box, the absolute reflectance at 12.5MHz when viewed from the top of the download is actually decreased by 0.206%, which means there is marginally positive effect on propagation, even for very high frequencies. This may be because the introduction of a CT has a minor flux cancelling effect on the primary circuit, therefore reducing the inductance of the download.

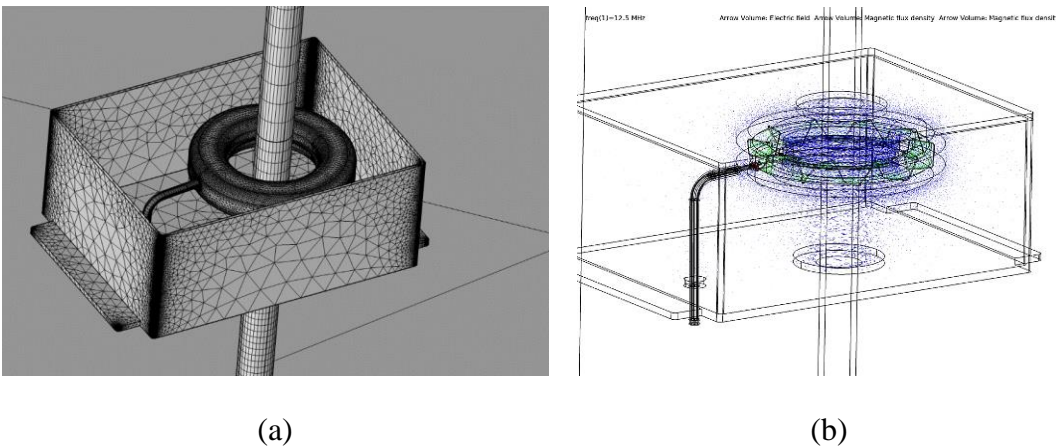


Figure 6.4: Developed HFCT and enclosure finite element model components (a) geometry and mesh (lid removed) (b) computed fields within enclosure, download propagating magnetic flux density (blue arrows) and induced magnetic flux density (green arrows).

A basic test rig was constructed to measure the frequency response of the unit and to ensure the 3dB bandwidth remained high enough with the CT mounted in its enclosure. A coaxial constant impedance taper was created using a 3D printed PLA and covered

with copper foil. This enabled a constant 50Ω connection to a Vector Network Analyser (VNA), scaling up the pin/body size of the SMA connector via a constant impedance taper and preventing excessive reflections, thus maintaining a reasonably low Voltage Standing Waveform Ratio (VSWR). Impedance matching of the internal shaft that passes through the CT inside the box.

The bottom of the rod extending through the CT aperture was terminated via a low inductance 50Ω resistor to the enclosure. The measurement setup including the CT box connected to a VNA is shown in Figure 6.5.

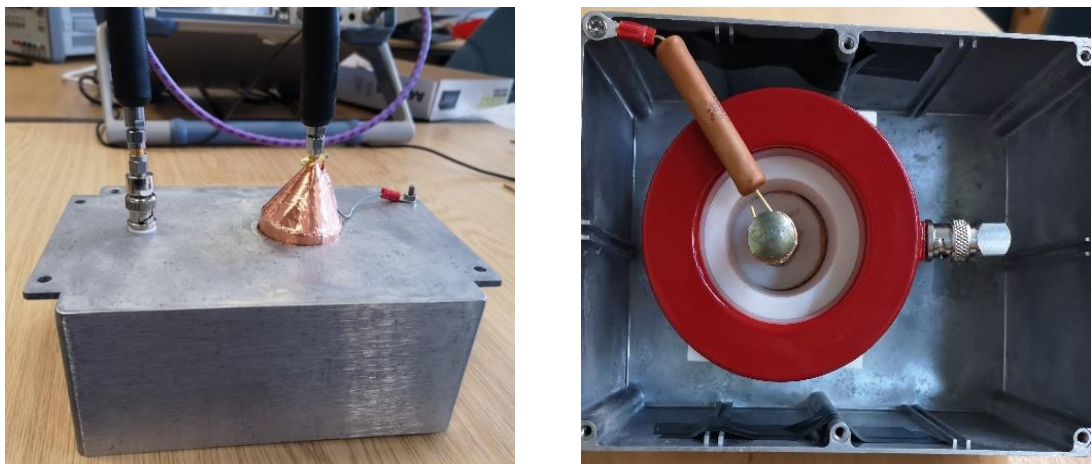


Figure 6.5: VNA frequency response measurement setup.

The expected S_{21} dB for a 0.5V/A CT into a 50Ω port is -40dB . For the measured configuration above, the measured data from the VNA shows less than 3dB variation over the required bandwidth, as observed in Figure 6.6.

It is evident that the enclosure arrangement reduces the upper bandwidth limit, however, the 3dB bandwidth is maintained up to 130MHz , which meets the requirements for these measurements. While this bandwidth is evaluated at 50Ω , the actual impedance of the download varies with height. The installed setup at Substation 'A' is shown in Figure 6.7.

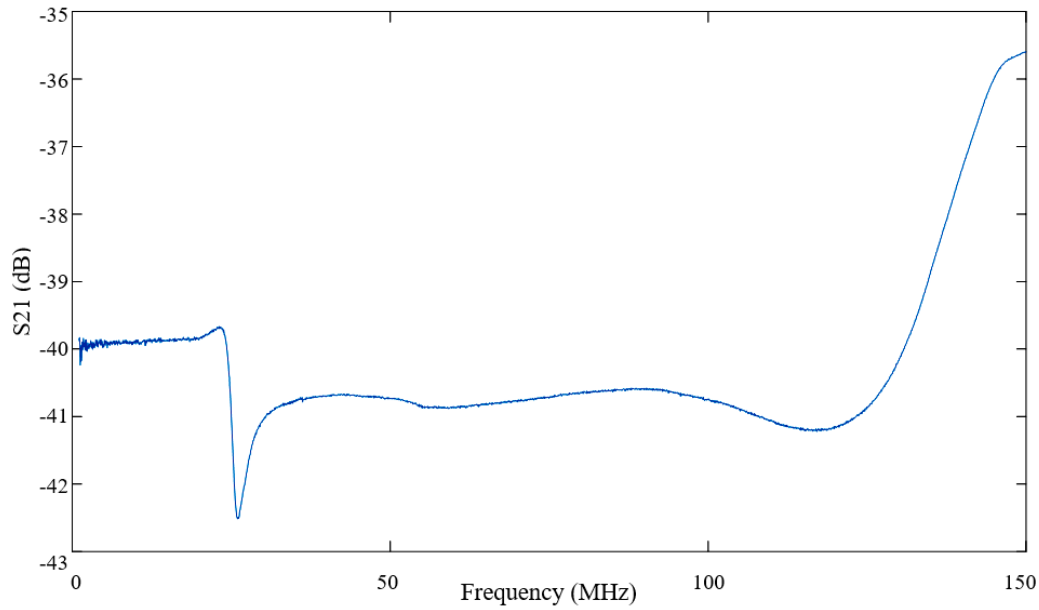


Figure 6.6: VNA measured HFCT with enclosure response.

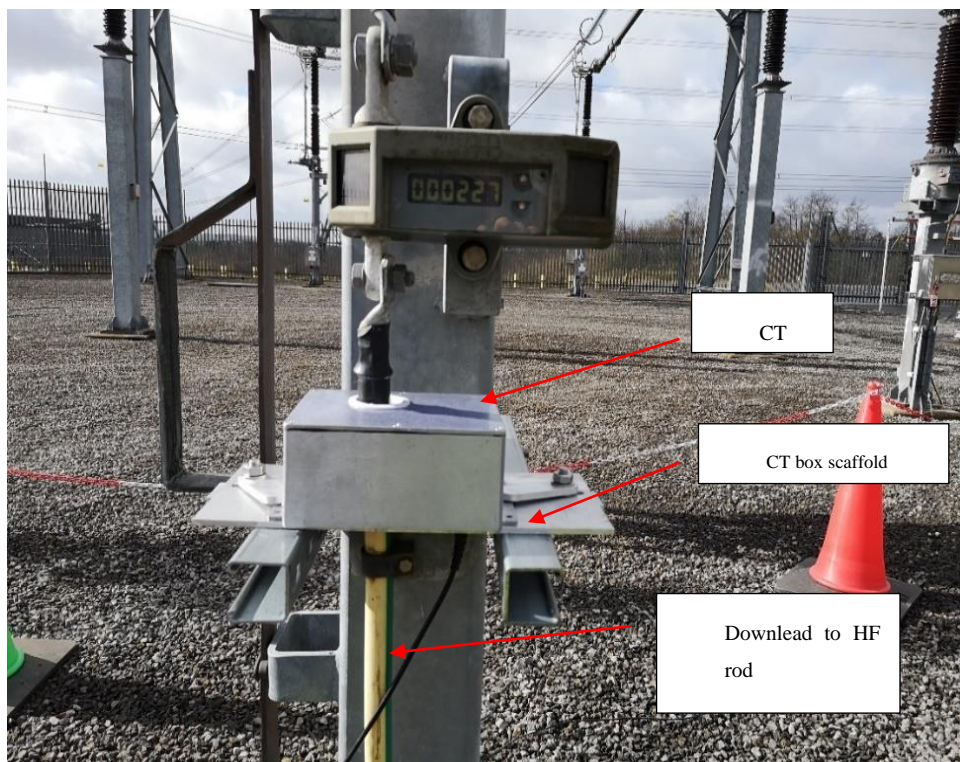


Figure 6.7: HFCT enclosure installation at Substation 'A'.

6.4 Ultra-High Frequency sensor coupler unit

It is observed from Chapter 2 that internal VFTs in operational systems are most commonly captured by an internal measurement device, oftentimes through the post-commissioning installation of an internal capacitive divider which is a complex and time-consuming process. A better solution would be to make use of existing sensors

installed as part of the system monitoring. The Partial Discharge UHF sensors that are installed as standard on most GIS sites, appears to be the obvious choice. The UHF sensor is an internal antenna, which detects the low magnitude, electromagnetic waves that are excited during a PD event, with frequencies in the UHF range. This antenna couples capacitively to the high voltage conductor, allowing its exploitation as a capacitive divider. In order to test this concept, the 3D finite element model in Figure 6.8 was created using available 2D plan view drawings [101]. As capacitance is almost entirely a function of geometry and material characteristics, the capacitance matrix is easily through a sweep of energisation ports, as shown in Table 6.1.

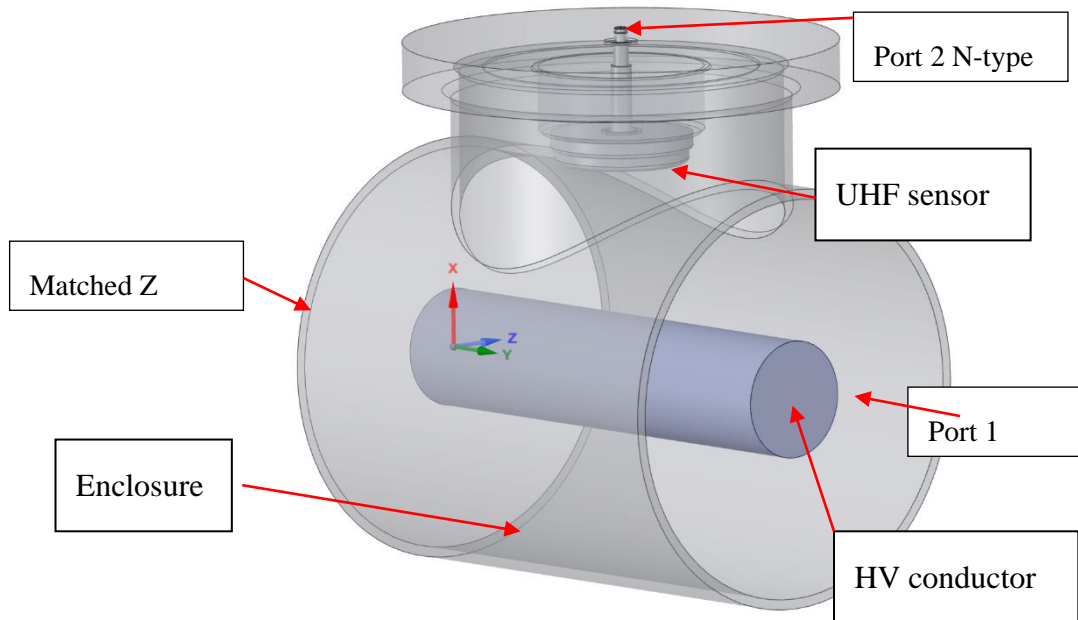


Figure 6.8: UHF sensor and bus section Finite Element Model.

Table 6.1: Calculated mutual capacitance matrix.

	HV conductor	UHF sensor
HV conductor	33.08 pF	0.94 pF
UHF sensor	0.94 pF	61.30 pF

Further solving of the wave equation allows full characterisation of a device over a required frequency range using S-parameters. Terminating the output N type connector with 50Ω port assigned (port 2) gives the transmitted S-parameters as shown in Figure 6.9. The increasing transmission trend with frequency is representative of capacitive coupling.

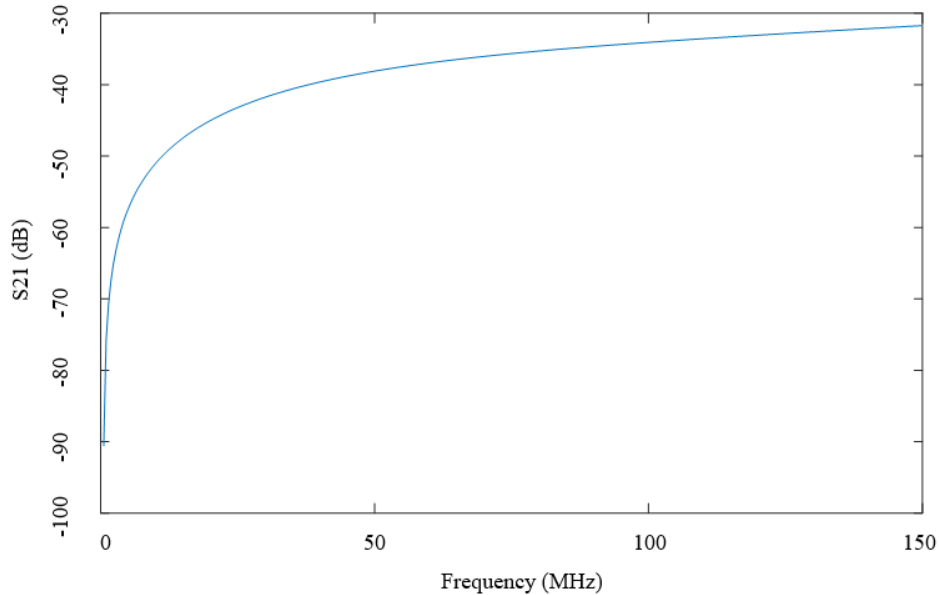


Figure 6.9: Transmission characteristics between HV conductor and UHF coupler.

6.4.1 Termination of the UHF sensor

Considering only the PD sensor and based on the capacitance matrix in Table 6.1, a division ratio of approximately 66 is calculated, based on self and mutual capacitances. At the anticipated voltage levels this division ratio would result in an output that significantly exceed allowable limits for any connected components, therefore further voltage division is required, so that a more appropriate ratio can be realised with an externally connected low voltage arm. A low voltage arm can be achieved using discrete components, forming a circuit on a substrate. Exporting the three port S-parameter model into ADS, enabled development of a tailored low voltage arm which would form part of the divider. Design of a low voltage arm for a capacitive divider within the VHF range is extremely challenging as component parasitics become a major design consideration. For example, a simple capacitor behaves capacitively until its First Series Resonance (FSR), following which it behaves inductively. This behaviour repeats at multiples of the FSR. This FSR is determined by the capacitors Equivalent Series Inductance (ESL) which is not negligible at high frequencies. To ensure the low voltage

arm behaves appropriately throughout the frequency range, capacitors were selected so that their individual FSR were outside of this range. Many capacitor types (film, electrolytic etc.) exhibit high ESL and are therefore not suitable for use in the VHF range and above. One of the most common capacitor types used in this range are surface mount (SMD) multilayer ceramic capacitors, which exhibit a very low ESL and Equivalent Series Resistance (ESR).

ADS [102], is commonly used for RF and microwave circuit design. Utilising ADS most component parasitics can be accounted for, giving a more realistic approximation of circuit behaviour. The low voltage arm circuit was initially designed using imported models from the Modelithics library [103]. Modelithics models, developed from strictly controlled measurements, account for the full parasitic behaviour and results are even scaled for the type of substrate selected and pad dimensions. FR4 substrates are commonly used for PCB development due to their low cost, however, FR4 performs poorly at high frequencies due to a comparatively high real and imaginary permittivities. Ceramic boards provide the best performance at very high frequencies. For this reason, a 30 mil, double sided, copper coated board was chosen as the substrate. A suitable division ratio was achieved by paralleling multiple SMD capacitors with some additional impedance matching at both the input and output of the board. At the VFT frequency range, even short sections of microstrip between components will have a bandwidth reducing effect, therefore these were included using the ADS-momentum software [102], which combines circuit simulation with finite element simulation through its co-simulation option. Co-simulation utilises a FEM solver for all distributed elements in the circuit, such as the microstrip traces, coupled with the circuit solver for discrete components to produce highly accurate results. Following co-simulation the parasitic effects of the microstrip connections between components was evident, hence further circuit tuning was required. ADS allows the optimisation of component values and microstrip trace widths to achieve a 3dB response over the required bandwidth. The co-simulation model, comprising circuit components, microstrip components, pads and vias, is shown in Figure 6.10.

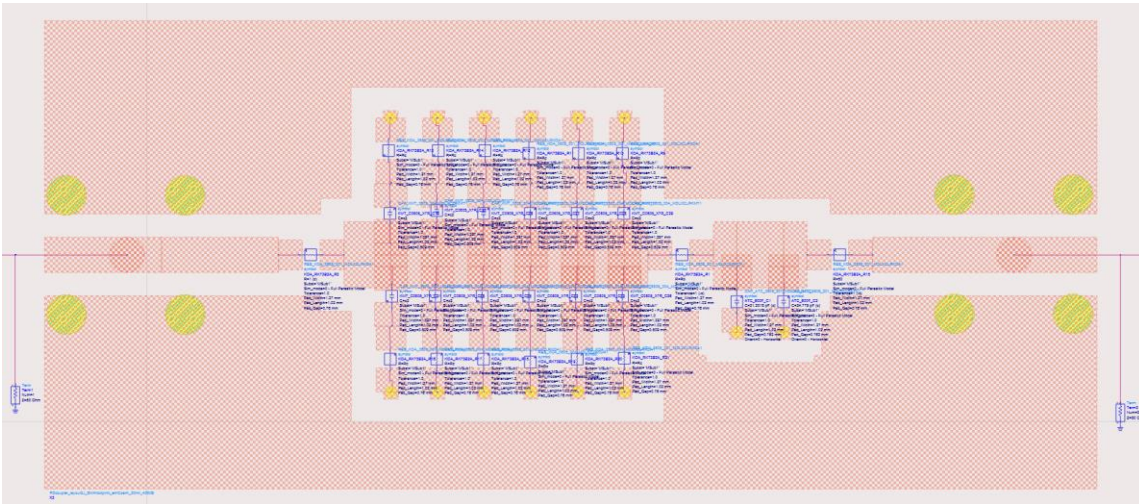


Figure 6.10: ADS circuit with EM model view.

6.4.2 Bandwidth test of the UHF sensor coupler unit

After evaluation of the circuit's frequency domain response, the circuit consisting of the UHF sensor, PCB, output cable and oscilloscope was then simulated to ensure appropriate impulse response. A double exponential impulse was simulated at the Gas Insulated Bus (GIB), at port 1 (UHF model) and absorbed at port 3. The resulting coupled impulse at port 2 is provided in Figure 6.11. Undershoot is visible towards the end of the impulse as the system approaches its lower frequency limit. However, a good high frequency response is achieved.

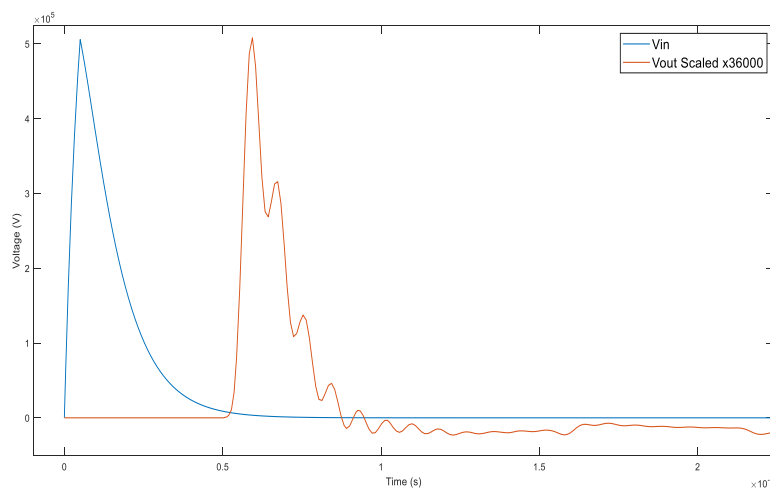


Figure 6.11: Double exponential (5ns/50ns) response.

While ADS/momentum utilises a full wave, method of moments computation approach, the visualisation and interaction of fields with the enclosure and the additional parasitics of the connectors is not easily accounted for. The PCB was therefore reconstructed as a

finite element model in ANSYS HFSS, as shown in Figure 6.12(a). This also provided an additional method of validation. The fabricated coupler box is shown in Figure 6.12 (b).

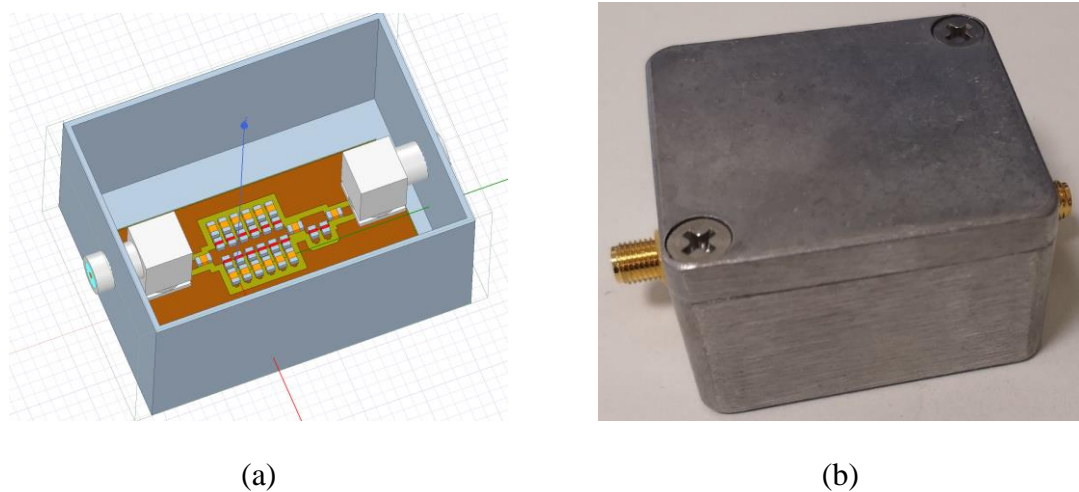


Figure 6.12: UHF sensor coupler (a) Ansys HFSS finite element model with right angle SMA connectors and metallic case (b) manufacturer coupler.

The S_{21} dB results given in Figure 6.13, compare results from the various simulation strategies with the results of actual device, measured using a VNA. All two port S-parameter results are very close to the measured values, with the HFSS results being the most accurate, as it also includes a representation of the SMA connectors and the metallic case. The ADS/momentum full wave model results are almost identical to the HFSS results. Both the HFSS and ADS momentum results are very close to the measured response, with a maximum difference of 1.15dB and 1.18dB respectively. The use of ideal components within ADS still produces a reasonable match, with a maximum difference of 2.76dB. Due to the coupling ratio, it was not possible to measure the transient response of the unit in the laboratory, therefore additional software validation and frequency measurement steps were conducted to prove the use and bandwidth of the device.

Unfortunately, prior to testing this device at Substation 'A', a simple resistance measurement of the GIS UHF sensor produced unexpectedly a low resistance signal to ground, as opposed to the previously anticipated high resistance/open circuit. Further protective elements causing this behaviour were not visible. Therefore, the device was not connected to the antenna for operational measurements. Further clarification of the UHF sensor characteristics is required before the coupling unit is connected to the

system. Nevertheless, measurements by VNA and simulations suggest the device will be usable and would be the potentially the most reliable method of internal transient measurement.

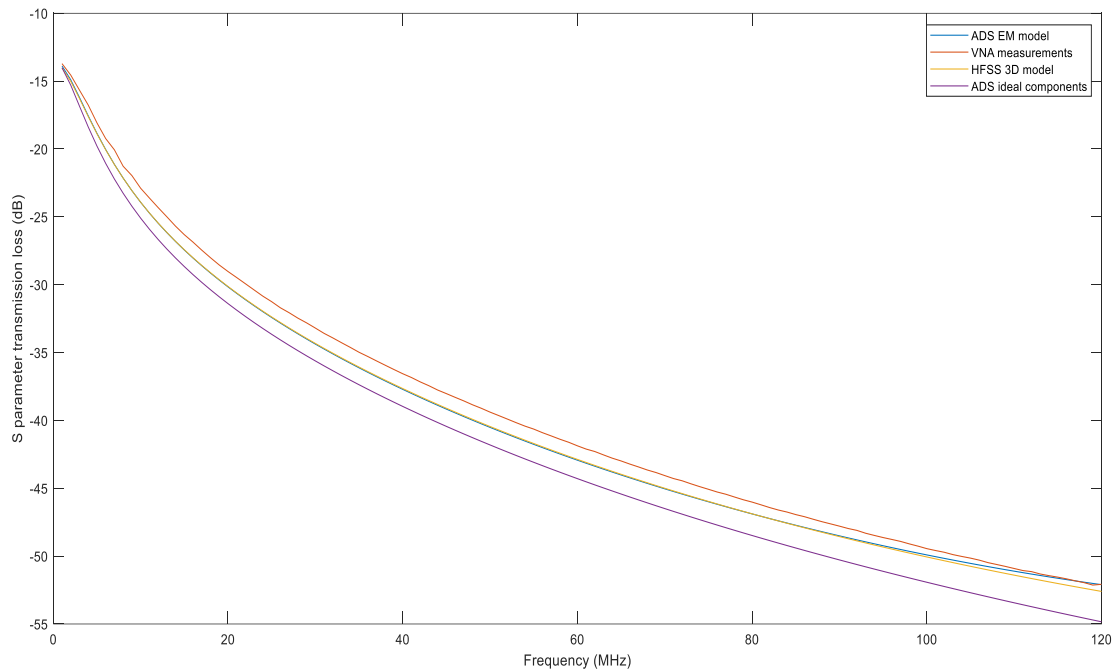


Figure 6.13: Transmission loss comparison modelled and measured results.

6.5 Development of a D-dot sensor for GIB measurements

It is known that VFTs propagate internally, between the outer surface of the HV conductor and inner surface of the enclosure, remaining internal due to the skin effect. Electromagnetic fields can emerge at apertures, such as the insulating spacer (unshielded spacers without embedded electrode only). This allows the possibility of sampling the internal transients via what is effectively a dielectric window. This is confirmed through simulation, as shown in Figure 6.14, the fields emanate through the space between the bolts (assuming an effectively bonded system).

An option for measuring this electric field is via a D-dot probe. The D-dot sensor is a non-contact field measurement probe measuring time varying electric displacement fields. In this section, a concept for a D-dot sensor for measurement of internal VFTs is developed. The sensor is designed to be wrapped around the spacer's circumference, as shown in Figure 6.15. The sensor is designed to be easily installed/removed, with a flat, non-adhesive copper surface so that the spacer surface is not contaminated in any way. The sensor is secured using around the spacer using Velcro, allowing good contact to be made.

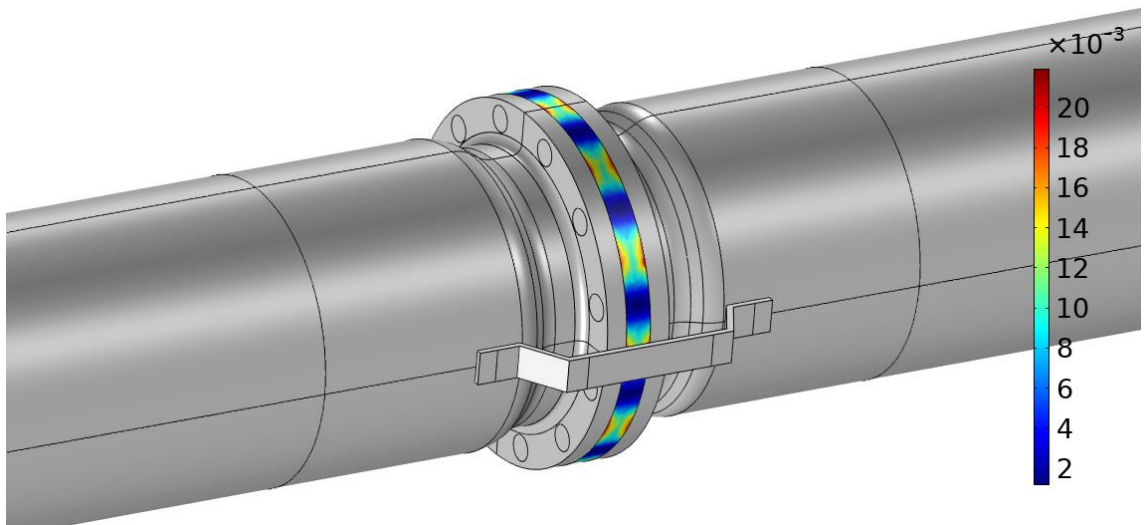


Figure 6.14: Electric field (kV/mm) profile at spacer surface for 400kV internal bus excitation.

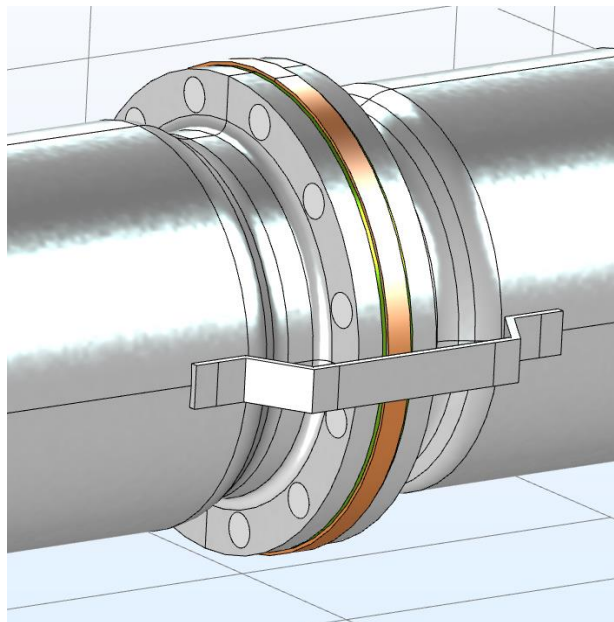


Figure 6.15: D-dot sensor design installed around spacer dielectric.

The mode of operation of a D-dot sensor is highly dependent on the sensor's capacitance, termination impedance and frequency. The mode of operation can be determined by its transfer function as shown in Equation (6.1) [104].

$$(C_s + C_m)R_m\omega < 1 \tag{6.1}$$

where C_s is the self-capacitance of the sensor, C_m is the mutual capacitance between the sensor and the HV electrode, R_m is the termination resistance and ω is the angular frequency.

When the operation mode value is less than 1, the D-dot will operate as a derivative sensor. This condition is satisfied when the sensor is terminated by a low impedance e.g. matched with the characteristic impedance in a low frequency range, where the sensor will operate as a true D-dot probe and the voltage measured is proportional to the rate of change of the displacement field, as shown in Equation (6.2) [105]. When operating in a derivative regime, the output requires integration, achieved using a passive or active integrator circuit or alternatively the output can be integrated numerically. When the operation mode is greater than 1 the sensor will operate as a charge meter or capacitive divider, and the voltage output can be calculated using Equation (6.3) [105].

$$V_{out}(t) = R_s A_{eq} \frac{\partial D}{\partial t} \quad (6.2)$$

$$V_{out}(t) = \frac{A_{eq} D(t)}{C_s} \quad (6.3)$$

where A_{eq} is the equivalent area of the sensor, R_s is the sensor output resistance and D is the displacement field vector.

It is possible to produce a sensor based on the above principles for measurement of VFTs. If the sensor functions as suggested, it will have significant advantages over other capacitive divider types, most of which require minor modifications to the system and internal installation, incurring a significant disruption to service.

There are several design considerations including materials, profile, LV arm arrangement and grounding, response and calibration measurements, field control, susceptibility to interference and measurement uncertainty. From an initial design perspective, to measure fields via the spacer, the sensor must follow the spacer's cylindrical profile and be easy to fit and remove. A degree of flexibility is required to achieve this; therefore, a flexible insulation is required. As the sensor is effectively a loop, consideration of magnetically induced currents is required. Having a non-continuous loop should limit the effect of induced and circulating eddy currents.

A large capacitance between the sensing electrode and the ground electrode of field sensors is commonly used to increase measurement sensitivity. There are several ways this could be achieved while giving consideration to the bandwidth of the sensor. An inexpensive, narrow strip of flexible dielectric, such as silicone rubber separating two copper electrodes, along with a separate parallel capacitor bank arrangement using SMD ceramic capacitors, analogous to that described in Section 3 could be used. While unavoidable for the UHF sensor, an issue with this external LV arm arrangement is that any significant length of cable or microstrip trace between the sensing electrode and this secondary capacitance will significantly limit the bandwidth of the sensor by decreasing the first SRF. A better approach would be to distribute the capacitors circumferentially around the sensor. A similar approach was used by Wang et al [106] recently for pulsed voltage measurement in a transmission line, with SMD capacitors mounted on a circular substrate. The capacitors were mounted on a double layer substrate, orientated in opposition to instigate a flux cancelling effect.

A further approach is to achieve a large capacitance using only the electrode and dielectric materials by utilising a high permittivity dielectric, such as Rutile (Titanium dioxide), which has relative permittivity's in the range 80-1000. This material would have to be cast in house, which, due to the length of the sensor and wide range of permittivity, may prove difficult to achieve an appropriate division ratio.

For the development of a high capacitance, flexible sensor, a better and more simplistic approach would be the use of a comparatively low permittivity thin film insulation material. Based on Equation (6.4), the smaller the gap between the electrodes, the higher the capacitance. A smaller gap between electrodes reduces the loop area and should, therefore, also reduce the inductance of the electrode arrangement.

$$C = \frac{\epsilon A}{D} \quad (6.4)$$

Initial prototypes were based on a 1µm thick Kapton film; a Copper foil tape (with adhesive backing) was carefully applied to the Kapton film. One of the issues associated with a flexible sensor is the risk of delamination of the conductive electrodes. A very thin layer of conductive material protected with a conformal coating may limit the risk of delamination occurring.

The method of termination of the sensor requires a significant amount of consideration. The sensor will be temporarily installed in a high EMI environment, being exposed to

internal VFTs, external TEVs and possibly radiated fields. The first prototype consisted of a single shield that was not bonded to the enclosure, therefore, this shield also acted as the reference for a differential measurement, via a floating oscilloscope arrangement. This approach was used because of the possibility that TEVs could propagate between enclosures, risking coupling from other enclosures, as implied by Figure 6.16. Following initial testing at Substation ‘A’ and the difficulty interpreting the source of the transients (internal or external) it became apparent that the sensor required an external shield, allowing greater directivity of the sensed fields and differentiation of source of the coupled field. To function as an electrostatic shield, this external shield will need to be bonded to the enclosure, but not the sensor. To explore this design brief, the simplified 2D axisymmetric model was created, including 2D axisymmetric representations of the internal bus, enclosure, gas and sensor/air domain. Figure 6.17 shows the computed electric potential for a stationary source sweep with the bus energised and sensor ground/enclosure set to 0V. Two scales are provided in the plot due to the A 2D model was necessary in this case due to the contrasting scale of geometries, ranging from micrometres to metres, and the extensive meshing requirements required for a full 3D model.

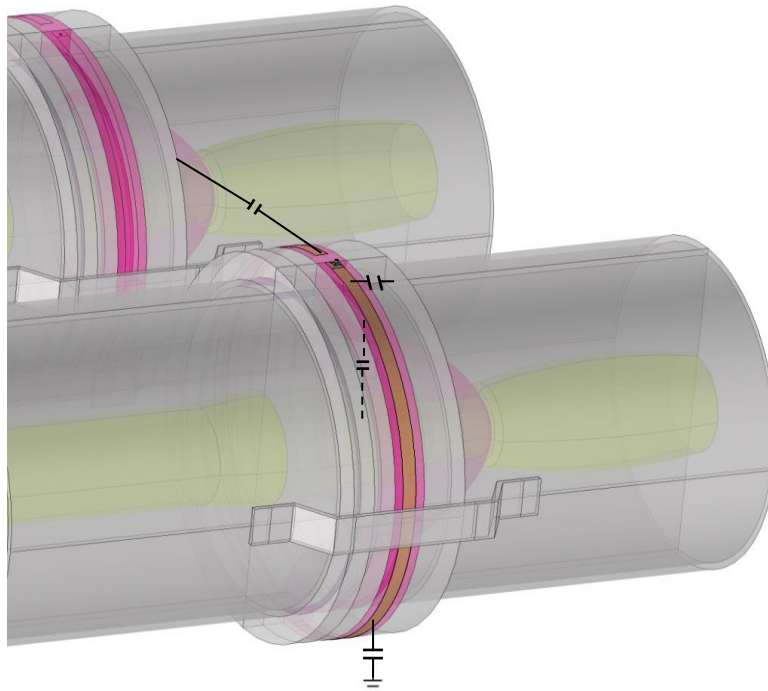


Figure 6.16: D-dot capacitances (floating ground)

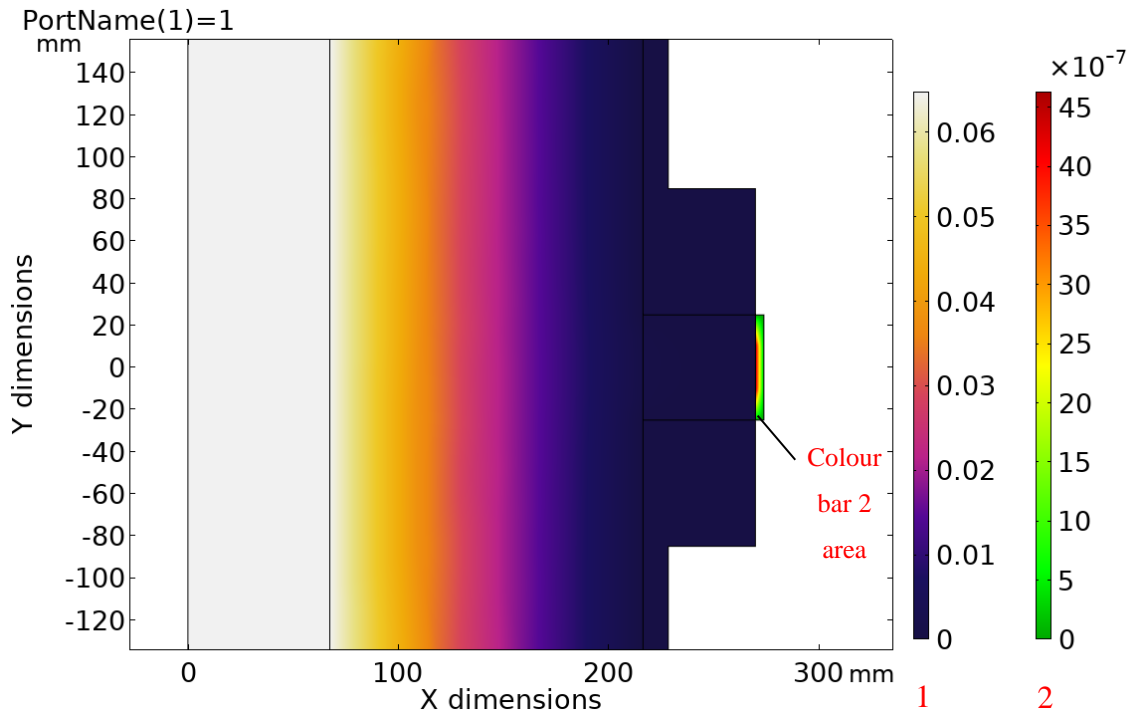


Figure 6.17: Simplified 2D axisymmetric model of GIB with sensor attached to spacer outer surface. Colour bar 1 electric potential (V) - bus, enclosure and internal SF₆ space. Colour bar 2 electric potential (V) – sensor and air space around sensor.

The capacitance matrix is given in Table 6.2, where the self-capacitances (to ground) of the HV conductor, inner sensing electrode and reference electrodes, along with the mutual capacitances are given. For this electrostatic model, the enclosure and external shield are considered as grounded. When compared to the results without a shield, the computed matrix suggests that the external shield has a negligible effect on the inner sensing electrode and a moderate effect on the reference electrode. However, a good division ratio is still maintained. To connect to this sensor, a triaxial cable arrangement was used, with the secondary shield terminated to the outer shield of the sensor/enclosure.

Table 6.2: D-dot calculated mutual capacitance matrix.

	HV	Sensing electrode	Reference electrode
HV	95.372 pF	0.0831 pF	0.0068 pF
Sensing electrode	0.0831 pF	152.10 pF	45.28 nF
Reference electrode	0.0068 pF	45.28 nF	1.132 nF

The latest D-dot prototype adopts an approach used for modern flexible PCBs, with the D-dot fabricated from Pyralux[®], which is essentially a polyimide film coated with copper on both sides (rolled-annealed or electrodeposited). Using strips of Pyralux[®] cut to size and following PCB chemical etching processes, it was possible to produce a sensor/flexible PCB, as shown in Figure 6.18. The new method minimises the risk of delamination and provides a better surface finish. Furthermore, as opposed to providing an external matching circuit, it was possible to etch the microstrip traces and component pads directly onto the substrate.



Figure 6.18: D-dot section chemically etched onto Pyralux[®] flexible substrate (a) etched Shield side with SMA connector (b) etched electrode side.

As suggested, the termination impedance is highly important. When connected to a recording device via a cable, the frequency response of the sensor will be affected regardless of the mode of operation (differentiating or integrating). A suitable termination method should be considered in order to prevent reflections and maintain a flat frequency response over the required bandwidth, with consideration of the effect the termination will have on the mode of operation, a matched resistance to the output of the sensor with the cable impedance was used for the measurements, was chosen for its simplicity and minimal impact on the measured signal.

Based on the capacitances calculated and Equation (6.3), it is possible to calculate the frequency range for operation strictly as a derivative sensor and the transition frequency to self-integration behaviour. As seen in Figure 6.19, the proposed sensor, terminated at 50Ω , behaves as a self-integrating sensor above 100kHz . The same calculation was made for a termination resistance of $1\text{M}\Omega$, which concluded that the sensor would behave as self-integrating all the way down to 4Hz . For the frequency range under investigation, it is therefore more appropriate to use the sensor in self-integrating mode.

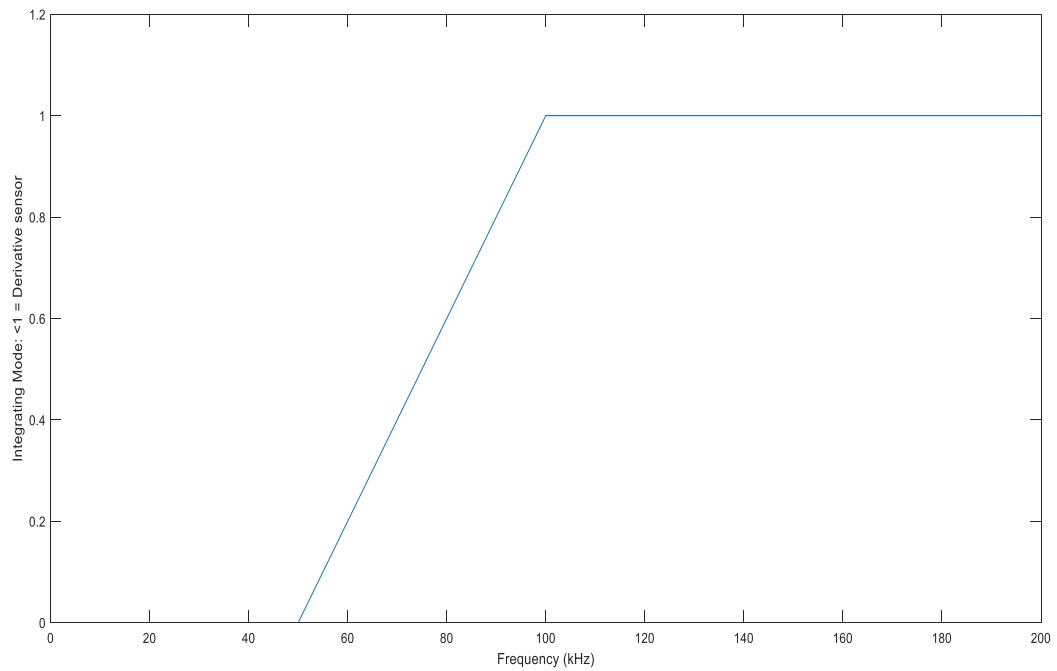
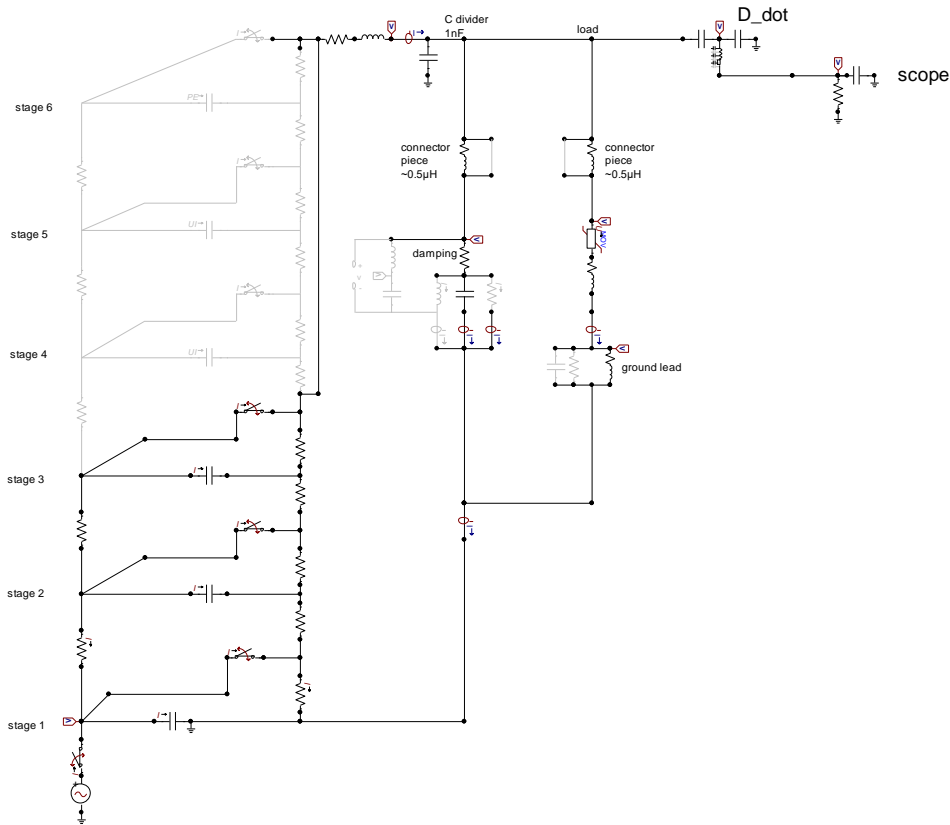


Figure 6.19: D-dot integration mode vs frequency.

Initial impulse measurements were carried out, with the double exponential output ($1.2/50\mu\text{s}$) of a Marx generator (3 stages connected, approximately 8kV per stage), connected to a braided conductor, dropped through the centre of a spacer mounted horizontally on a bench and terminated on an 12kV surge arrester. The measurement setup and equivalent circuit is shown in Figure 6.20.



(a)



(b)

Figure 6.20: D-dot impulse measurement setup (a) spacer with d-dot installed around outer circumference (b) D-dot with 3 stage Marx measurement circuit diagram.

The measured lightning impulse response is shown in Figure 6.21. While oscillations on the rising edge are apparent for both the capacitive divider and D-dot, these oscillations are more exaggerated for the D-dot measurement and were likely due to the relatively high inductance of the impulse circuit and grounding.

Further measurement accuracy and higher frequency resolution measurements were required, due to the limited rise time of the Marx generator and the observed oscillations. VNA measurements of the D-dot were undertaken to determine its frequency response and division ratio through S-parameters. A VNA is connected to one of the tapered input ports of the vessel to injected a swept frequency, the other side of the vessel is matched; the measurement setup is shown in Figure 6.22. The calculated S21dB is shown in Figure 6.23. The results show a reasonably flat response, with a flat 3dB response between 12MHz and 101.5MHz. The response at the below 12MHz drops

outside out this flat response region, however, the response is within 8dB across the required 1-100MHz range. The minimum division ratio in the range is 12.65e3:1.

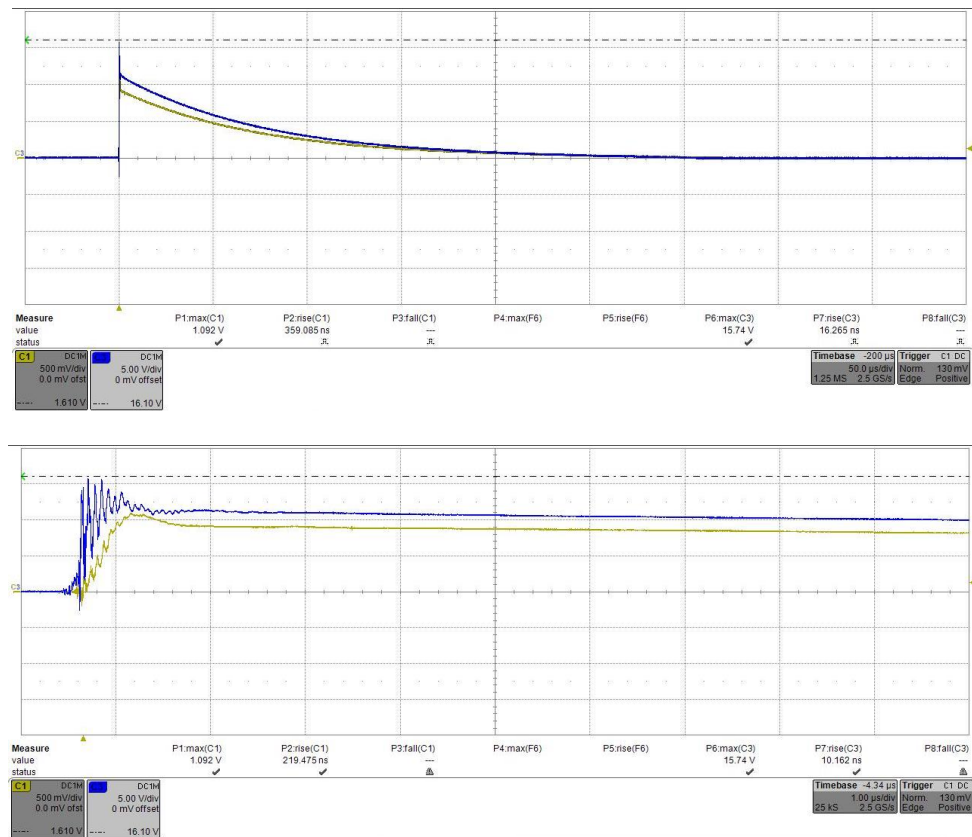


Figure 6.21: D-dot impulse measurements – divider measurement (yellow trace) and D-dot measurement (blue trace).

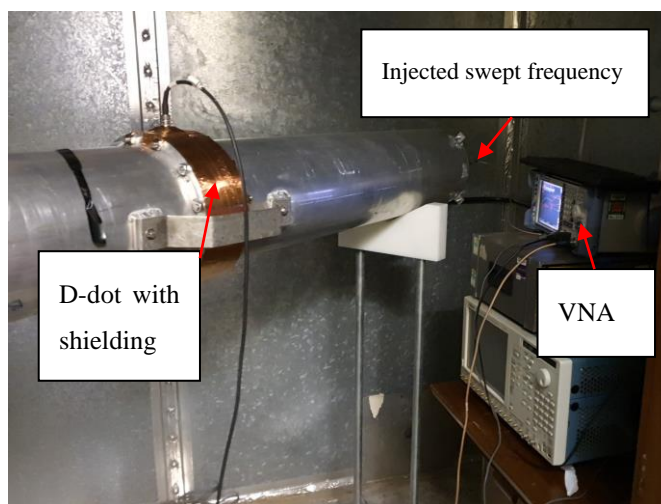
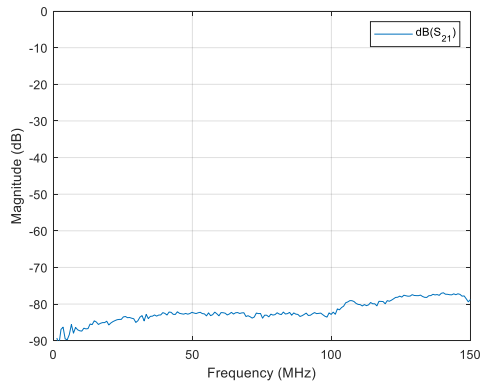
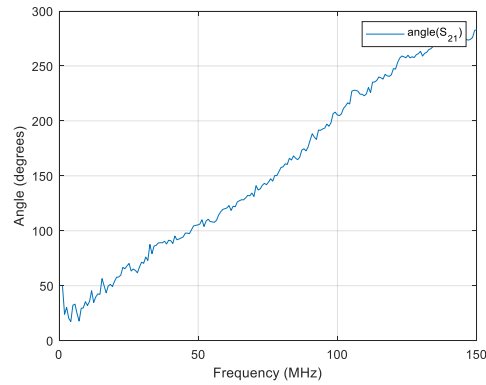


Figure 6.22: D-dot laboratory frequency response measurements.



(a)



(b)

Figure 6.23: D-dot S-parameters (a) magnitude (dB) (b) phase (degrees).

6.6 Development of a high bandwidth analogue Fibre Optic link

The susceptibility of cable systems to EMI is well known and particularly important when measuring VFTs in GIS. Steps can be taken to minimise unwanted coupling to a cable system, including appropriate bonding, using twist cancellation or ferrite cores, a better acquisition system would be to utilise a fibre optic transmitter/receiver system to transfer a representation of the captured waveforms. For this work, a low cost, wideband analogue system was developed based on the concerns of EMI following initial measurements.

At frequencies above a few MHz the response time of standard LEDs becomes insufficient, and a laser diode is often utilised, however, with the correct selection of components and appropriate circuitry a quicker response was achieved. A summary of the high frequency PCB design philosophy appropriate to the design of this fibre optic link follows:

Amplifiers:

- Gain bandwidth – amplifier quoted bandwidth is dependent on the gain. High gains reduce bandwidth considerably. The amplifiers were configured with relatively low gain and cascaded to achieve the desired gains.
- Slew rate - for fast rise times a high slew rate is required. A smaller voltage swing was utilised for a higher slew rate.
- Input and output impedance matching was critical for a distortion free output signal.

- Input and output voltage. Operation in the small signal range provides a significantly higher bandwidth.

LED transmitted and photodiode receiver:

LEDs have limitations on their on/off times. The HFBR 1527 transmitter was prebiased in the linear region of operation (linear forward current vs forward voltage). When prebiased, the LED is capable of optical rise times as low as 3ns. The basic concept used was to modulate above and below this bias, replicating the input signal without the need for analogue to digital conversion. The HFBR 2526 photodiode receiver used has a built in transimpedance amplifier to convert the light directly to a voltage.

Passive components:

All electrical components have parasitics, causing them to behave in a non-ideal manner. For very high frequencies and above, consideration of component parasitics was essential to avoid resonances and changes in behaviour over a wide frequency range. This non ideal behaviour was considered using ADS for specific components when importing equivalent SPICE or measured component S-parameter models using add on programs such as MODELTHICS.

Substrate:

While FR4 is generally known to perform less effectively than the high-speed ceramic type boards due to a comparatively high real and imaginary permittivities, the cost is low and availability high. This effects of the low-quality board were factored into simulations.

Power supply:

As the device is required to be portable, a built-in power supply was required. An LT3032 LDO voltage regulator was used to provide a stable power supply to the driver circuits. Additional input and output capacitances were required to improve the transient response. When dealing with fast rising edges, to avoid unwanted reflections, microstrip trace widths, lengths and routing were optimised for the required frequency response. Components and traces were terminated appropriately to avoid reflections. Multistage filters were required at the receiver output to achieve a flatter frequency response. Initially an ADS model was built, incorporating all component parasitics. The circuit models are shown in Figure 6.24 and Figure 6.25. The design/co-simulation process is illustrated in Figure 6.26.

The second step was layout optimisation, which consisted of a co-simulation approach. Co-simulation combines the electrical circuit simulation of the components with a method of moments solver for the traces and PCB. Component values and trace parameters are set up for optimisation against a desired frequency bandwidth. Gradient optimisation algorithms are then used to finely tune the circuits to minimise the error against the design 3dB bandwidth. Using this method, it was possible to design a circuit with a flat response. The latest prototype fibre optic link is shown in Figure 6.27 and Figure 6.28.

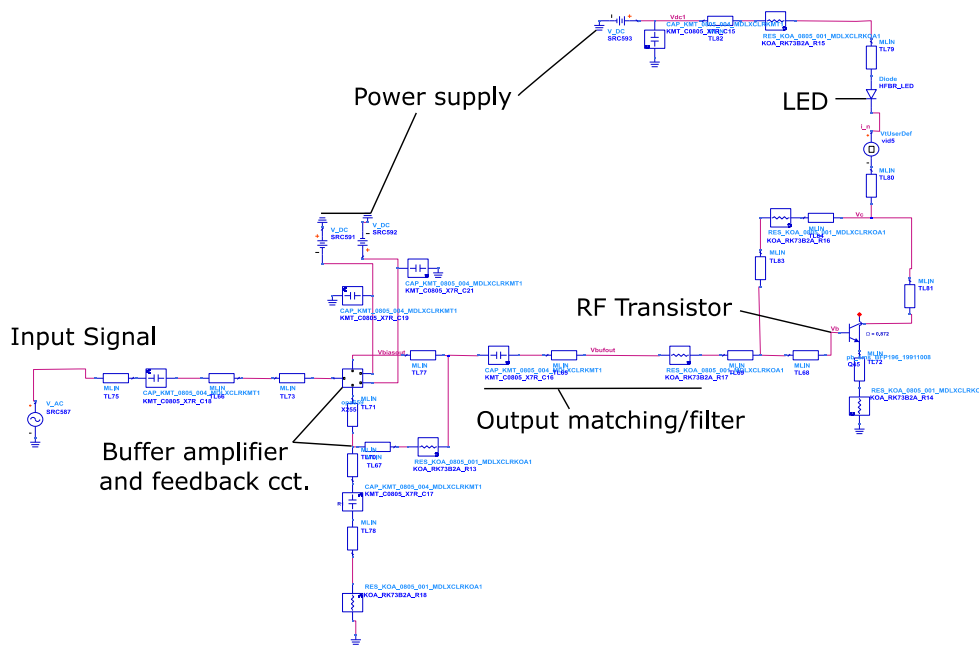


Figure 6.24: Fibre optic link – transmitter circuit.

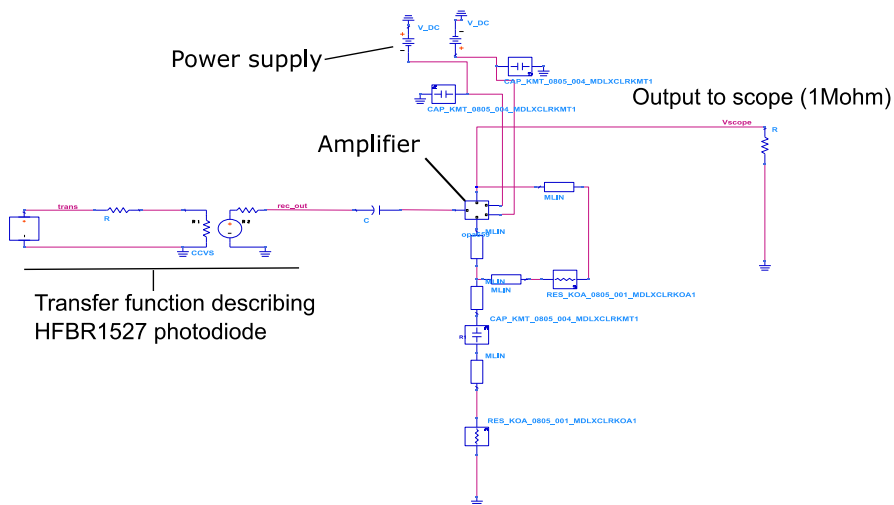


Figure 6.25: Fibre optic link – receiver circuit.

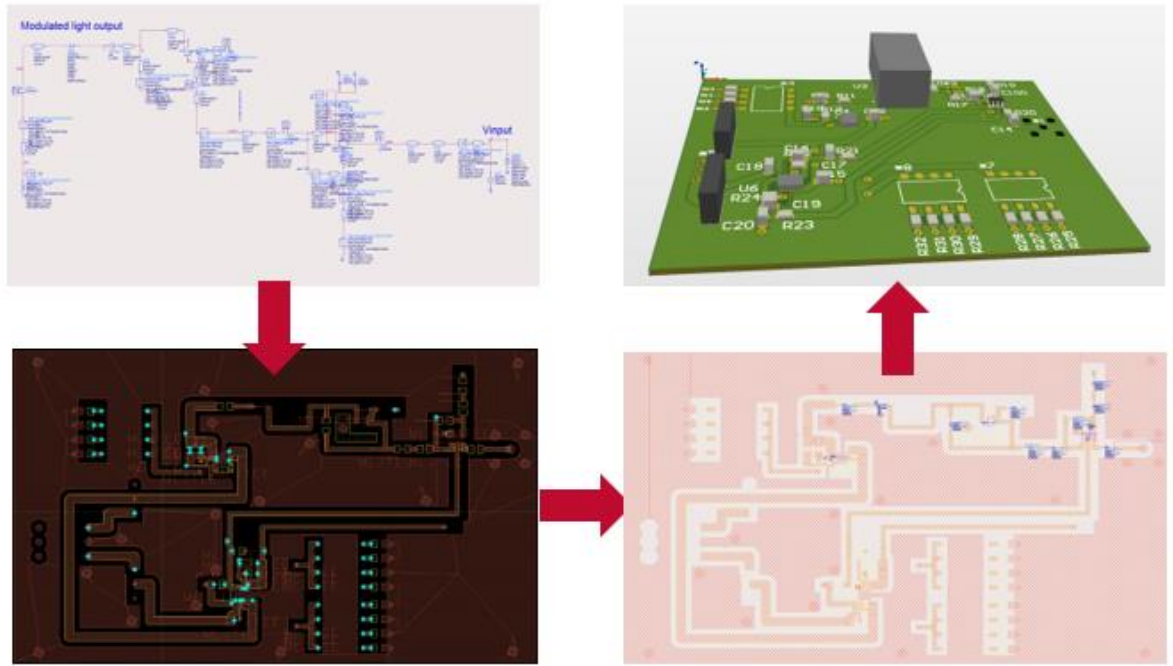


Figure 6.26: Fibre optic link circuit design process (showing prototype).

The fibre optic link was designed to have a small signal bandwidth of just over 100MHz and a gain of 1 across the range. To test the link, a square wave input with steep rising and falling edges were created using a signal generator, connected at the input to the optical link transmitter, as shown in Figure 6.29.

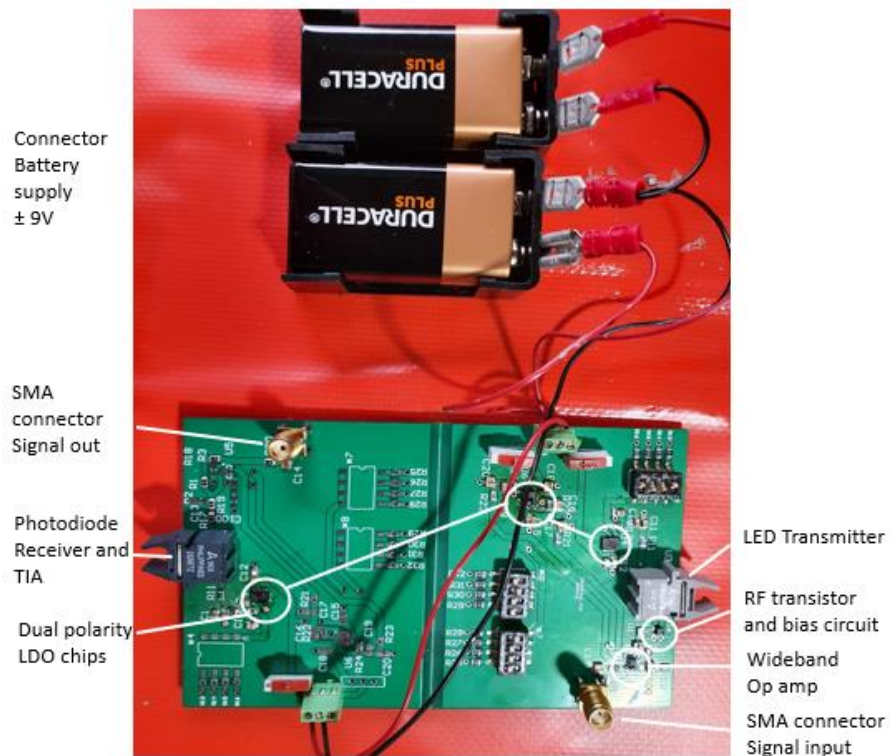


Figure 6.27: Fibre optic link prototype (as built).



Figure 6.28: Fibre optic transmitter in cast aluminium case.

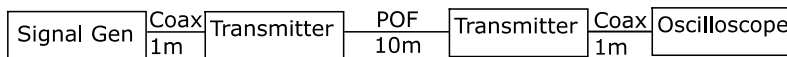


Figure 6.29: Optical link test arrangement.

Figure 6.30 demonstrates the response of the link via a 10m 1mm plastic optical fibre (POF). The rise time of the link was $<6.5\text{ns}$, implying a 53.84MHz small signal bandwidth. Deviations from simulation results are expected as all components are subject to tolerances. Further optimisation may lead to higher bandwidths. However, the dominant frequencies present in the VFT waveform at Substation ‘A’ are estimated to be below this limit and the superimposed higher frequencies have limited effect on the overall fundamental waveshape.

To illustrate the requirements for an optical link while also demonstrating the potential EMI and acquisition concerns, the D-dot sensor developed in section 6.4 was installed on the calibration vessel. A short duration 10MHz signal was applied using a signal generator with RF amplifier, as shown by the measurement setup in Figure 6.31.

Figure 6.32 shows the prototype D-dot sensor’s response to the injected waveform. For this measurement, the applied oscillations were artificially extended for the coaxial cable routed along the enclosure case.

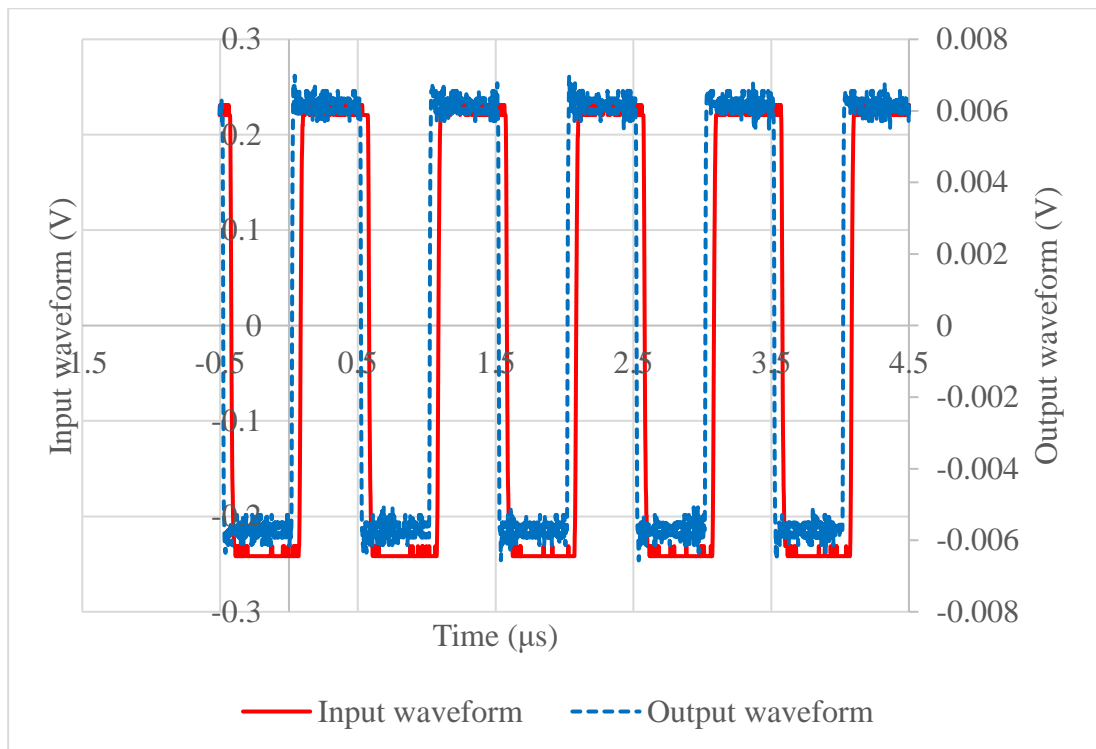
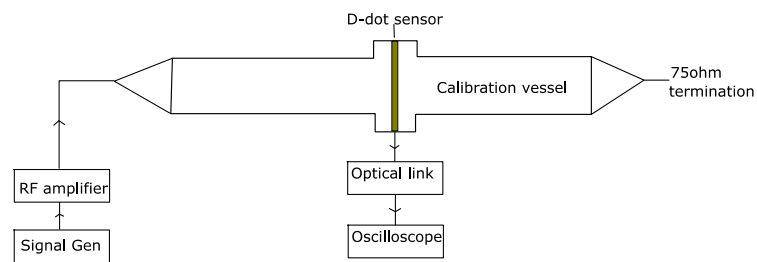
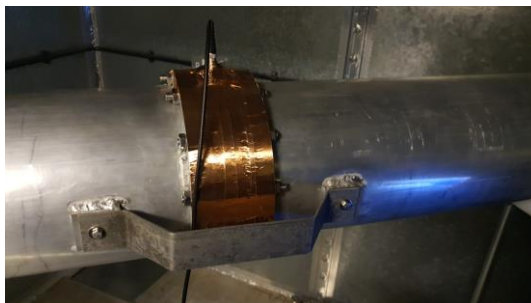


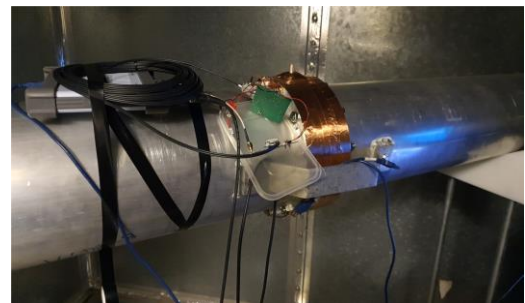
Figure 6.30: Input waveform (red), fibre optic output waveform (blue).



(a)



(b)



(c)

Figure 6.31: D-dot and cable/optical link measurement setup (a) measurement setup diagram (b) coaxial cable measurement (c) fibre optic link measurement.

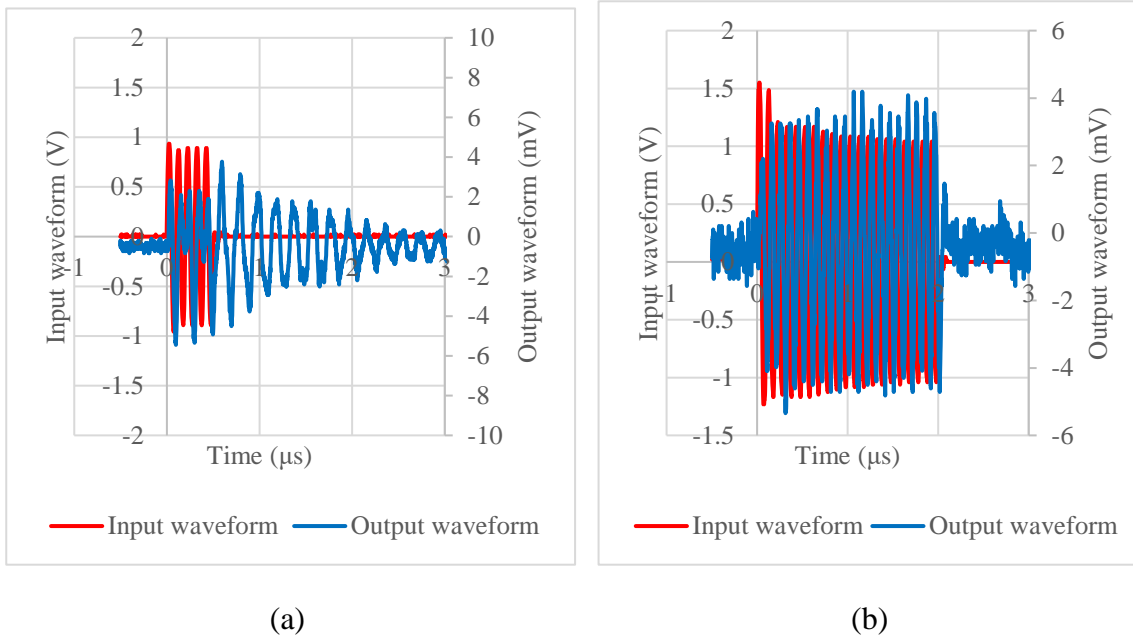


Figure 6.32: D-dot sinusoidal response (blue) for 10MHz input (red) – (a) coaxial cable (b) fibre-optic link.

6.7 Conclusion

High voltage measurements at the VFT range of frequencies are extremely challenging. Limited switching capabilities of live assets restricts the development of sensors in realistic environments, hence extensive lab-based development and advanced simulations are required. A contradiction of this statement is that both require validation through site-based measurement, therefore all methods become equally important. Calibration of devices for the measurement of VFTs and measurement uncertainties are important topics of consideration at present, with the focus of ongoing CIGRE working groups investigating this issue [107]. Until findings are published, engineers and researchers must take extreme care when considering the design and calibration of devices for measurement of VFTs.

In this work, specialist measurement techniques were developed to quantify the transient impulses developed on the GIS and connected surge arresters during VFT/TEV events. All sensing techniques have a designed bandwidth of 1-100 MHz; however, it is quite possible that the frequency content can even exceed these limits, therefore ongoing development is required. One of the main design specifications adhered to throughout the measurement system design process is limited interruption to

assets. Installation of the sensors described throughout this thesis have aimed to meet this design requirement.

Customised HFCT units were designed to be installed at Substation 'A' circuit 1 surge arrester downleads, to capture any transient currents present on the downlead. The units afford minimal disruption to the circuit and can even be installed while the substation is live, through the application of temporary earths. The bandwidth of the unit was measured, and simulations prove that no adverse impact on the downlead transient response occurs.

VFT/TEV measurements were made possible through two unique methods, the UHF sensor coupler unit and the flexible spacer-flange D-dot sensor. The UHF sensor coupler unit was designed to connect to the N-type connector of the existing GIS UHF PD antenna. These antennas are installed at multiple locations around the system, therefore many choices of measurement location are possible. The sensor could not be tested during operational switching due to the unforeseen characteristic of the actual sensor installed at Substation 'A'. Further clarification of the Substation 'A' UHF PD antenna output impedance is required, however, through simulation efforts and laboratory measurements, it is likely that after minor design modifications, the sensor will work as expected.

A high capacitance self-integrating D-dot sensor produced using Pyralux[®] flexible substrate prototype was designed and built for the purpose of measuring internal VFTs through the spacer dielectric. This is possible for spacer-flange assemblies like those at Substation 'A' that do not employ a completely shielded design. The sensor is shown to have a good response across the required frequency range, an ideal response is within the range 12MHz to 101.5MHz and will provide a minimum division ratio of 12.65e3:1, providing the necessary isolation from the high voltages generated during disconnector operation.

Finally, a high bandwidth, analogue fibre optic link system was developed, allowing measurements to be conducted in high EMI environments without the concerns of external coupling or artificially extended oscillations. Both the transmitter and receiver were designed to be portable with the lowest possible power consumption. The devices could operate on a single 9V battery for several hours, without deterioration of performance.

7 MEASUREMENTS OF TRANSIENTS GENERATED BY GIS SWITCHING OPERATIONS

7.1 Introduction

Site measurements were carried out during a number of scheduled outages. All site measurements were based on the switching of Substation ‘A’ circuit 1 disconnectors and the circuit breaker, all identified in Figure 7.1.

The first outage in March 2019 provided the opportunity for the installation of three HFCTs at the Substation ‘A’ circuit 1 surge arresters and the temporary installation of a prototype D-dot sensor at a spacer-flange interface. Sensors were connected to an oscilloscope via short lengths of coaxial cable. The oscilloscope was housed inside an aluminium box to provide a reasonable degree of immunity to interference. Additionally, because of the possible presence of EMI and to avoid inaccurate measurements due to the presence of transients on the grounding system, the oscilloscope was operated in an ungrounded arrangement, powered by a 12V battery and an inverter. A diagram of the arrangement is given in Figure 7.2. The switching schedule followed for the largest set of measurements is given in Table 7.1, plots in this chapter are related to a specific switching sequence number.

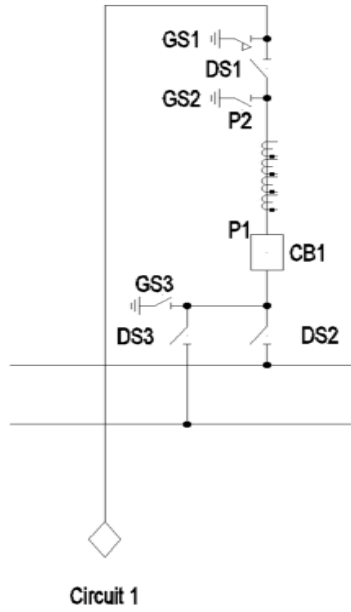


Figure 7.1: Substation 'A' Circuit 1 SLD.

Table 7.1 21st October 2020 Switching schedule.

Switching operation sequence	Switch operated
1	DS2 close
2	DS2 open
3	DS2 close2
4	DS2 open2
5	DS3 close
6	DS3 open
7	DS1 close
8	DS2 close3
9	DS2 open3
10	DS2 close4
11	DS2 open4
12	CB1 close
13	CB1 open
14	DS3 close 2

15	DS3 open 2
16	DS2 close 5
17	CB1 close

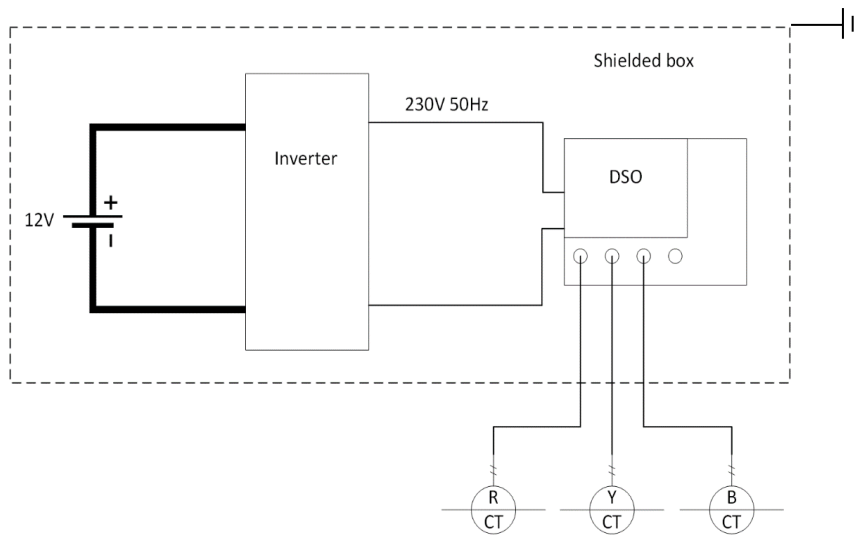


Figure 7.2: Data acquisition system.

7.2 HFCT measurements

It was the intention to capture all transients over the disconnector operation to monitor the variation in magnitudes and density of transients at the start and end of open and close operations respectively, ideally capturing the characteristic open/close VFT patterns. Due to the 50MS buffer of the Lecroy HDO6104 oscilloscope used and the high sample rate required to capture the transients in detail, the scope had to be operated in sequencing mode. After the initial trigger and segment capture according to the set duration, the scope re-arms awaiting the next trigger event. The segments can then be reconstructed using the associated timestamp data. Figure 7.3 shows an example of the reconstructed waveform for a disconnector open operation. The characteristic pattern for a disconnector open operation is initially small magnitude, high density, becoming larger and more infrequent as the gap between the contacts increases. A magnified view of a single transient is shown in Figure 7.4 and the frequency content of the transient is shown in Figure 7.5.

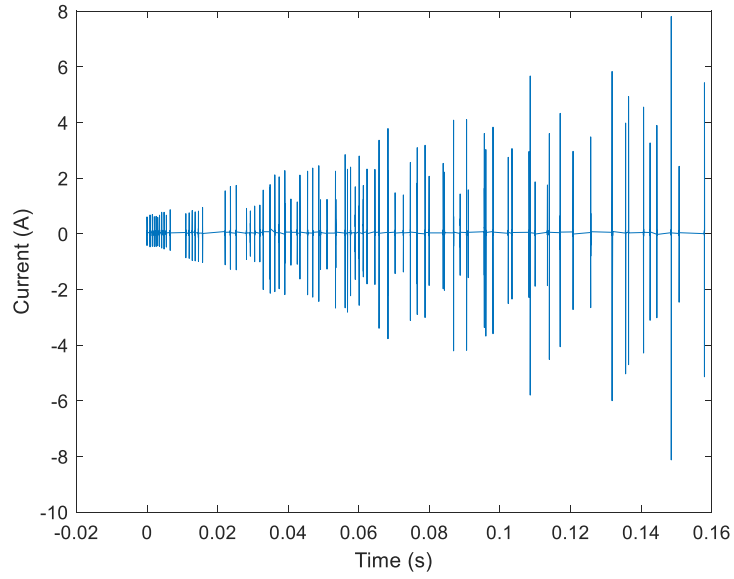


Figure 7.3: DS3 open transients – switching sequence 6.

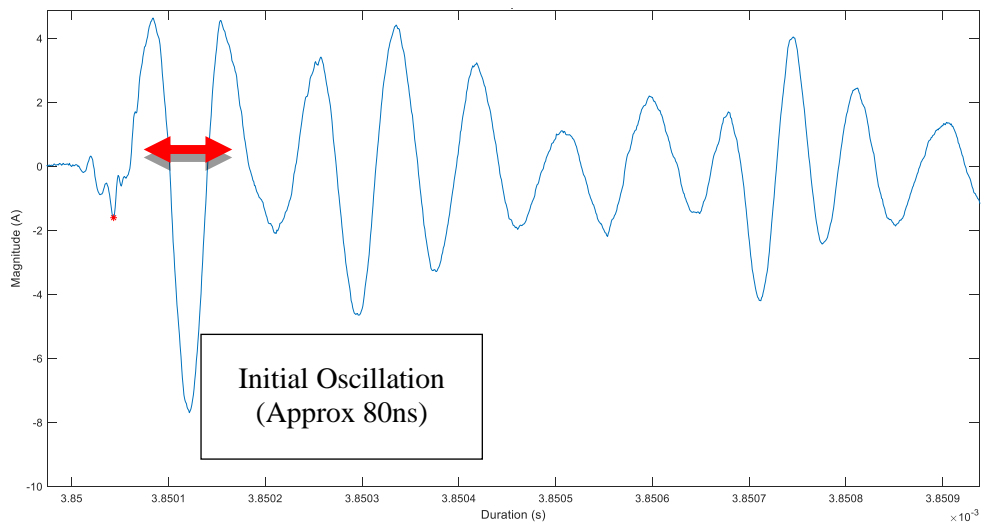


Figure 7.4: Single transient magnified, 1 μ s capture – switching sequence 6.

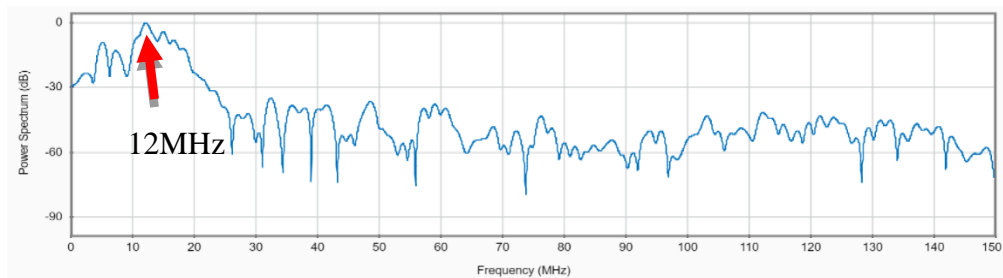


Figure 7.5: Frequency spectrum single transient – switching sequence 6.

The results recorded from numerous switching events on 21/10/20 are provided below. Further measurement results are provided in Appendix G. An extensive switching schedule was established following a major maintenance event on the Substation 'A' circuit. Given the range of switching operations, it was difficult at first to predict the magnitude of currents at the MOSA download and selection of attenuators was difficult. This resulted in a few poor captures, although the majority of measurements were successful. Due to the range of measurements, clipping of signals at the scales set on the oscilloscope was apparent. Clipping is unavoidable when measuring VFTs as magnitudes have many dependencies and a very large magnitude range over a single disconnecter operation. Attenuators protect equipment to an extent but, sometimes there is a compromise between attenuation and the capture of the smaller transients during the event. Measurements that have been limited by clipping have been declipped using a modified MATLAB function. Clipped regions are detected examining each data point and calculating the derivative. Where signals are sinusoidal, a derivative of 1 is indicative of a clipped region. The clipped regions are fitted with an n^{th} order polynomial. A declipped transient measured at the yellow phase CT on Substation 'A' circuit 1 is shown in Figure 7.6. As the declipping process cannot account for superimposed higher frequencies within the saturation interval, the process can result in amplitudes that are slightly higher or lower than the actual, the resultant amplitude is, therefore, an estimation.

The frequency spectrum has been assessed using STFT and a Kaiser window. The amplitudes, along with the three highest dominant frequencies listed according to their power spectra for the entire switching schedule are provided in Table 7.2. As the data was captured by the oscilloscope in sequence mode, the data had to be reconstructed based on segment and timestamp data. The timestamp data had limited precision down to 100ns, meaning that the start time of segment when reconstructed had the potential to be up to 100ns out. The number of transients and total duration of the reconstructed signals is given in Table 7.3. The number of transients detected during each switching operation was based on detection of peaks over a minimum amplitude, within a minimum delay time between peaks of 20 μ s, across the entire measured signal (including the effects of interphase coupling). This allows enough time for the decay of the transient and avoids false detections. The reconstructed, declipped DS3 open profile is shown in Figure 7.7. The frequency persistence spectrum in Figure 7.9 details the history of the transient frequency spectrum over the full signal. Repeated frequency

content increases the spectral density, allowing dominant frequencies to be more easily identified for a long repetitive signal.

The results suggest relatively low magnitude currents are present on the download throughout disconnector operations, with a peak detected magnitude of 273.4A. The highest magnitudes are apparent immediately after the circuit breaker switching, implying the presence of higher trapped charge magnitudes.

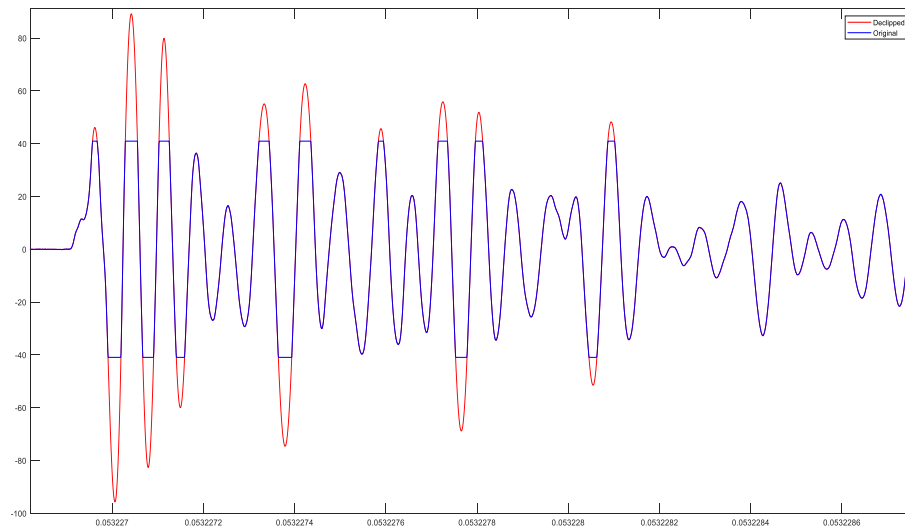


Figure 7.6: Clipped waveform and de-clipping action.

Table 7.2: 21/10/2020 HFCT measured values – amplitude and frequency content.

Switching operation	C1		C2		C3	
	Max Amplitude (A)	Frequencies (MHz)	Max Amplitude (A)	Frequencies (MHz)	Max Amplitude (A)	Frequencies (MHz)
DS2 close	Poor capture	Poor capture	5.4	12.9, 10.4, 7.3	5.06	12.9,10.4,7.3
DS2 open	Poor capture	Poor capture	5.74	12.9, 10.4, 7.4	5.3	12.9, 10.5, 7.4
DS2 close2	Poor capture	Poor capture	6.15	13.0, 10.3, 7.4	5.4	12.9, 10.4, 7.3
DS2 open2	5.1	13.3, 10.4, 36.5	6.6	13.0, 10.4, 7.4	5.9	12.9, 10.4, 7.3
DS3 close	5.1	35.9, 11.5, 29.0	6.5	11.5, 8.2, 18.2	5.0	11.6, 9.4, 18.3

DS3 open	5.7	11.6, 36.0, 29.0	7.8	11.5, 8.1, 14.2	5.9	11.6, 8.4, 14.7
DS1 close *	19.4	10.5, 39.7, 37.8	60.1	11.7, 9.2, 7.5	31.6	11.6, 8.4, 14.9
DS2 close3*	41.9	10.5, 39.7, 37.8	106.9	13.3, 10.5, 7.7	67.2	13.1, 10.3, 8.0
DS2 open3*	31.9	10.5, 23.6, 29.0	88.2	13.3, 10.5, 7.6	68.1	13.0, 10.3, 7.9
DS2 close4*	41.0	10.4, 25.5, 29.0	88.8	13.2, 10.5, 7.7	72.4	13.0, 10.3, 8.0
DS2 open4*	26.9	10.4, 25.6, 34.6	110.6	13.3, 10.5, 7.8	63.3	12.9, 10.3, 8.0
CB1 close *	9.2	12.3, 25.4, 17.4	52.4	14.0, 5.0, 6.8	17.1	14.1, 9.2, 7.9
CB1 open	No capture	No capture	No capture	No capture	No capture	No capture
DS3 close 2*	55.1	26.4, 11.9, 35.7	273.4	11.9, 13.9, 8.2	Poor capture	Poor capture
DS3 open 2*	137.4	26.4, 35.6, 11.9	Poor capture	Poor capture	179.8	12.2, 8.5, 18.2
DS2 close 5*	65.9	25.6, 23.5, 34.6	89.1	13.3, 10.5, 7.7	77.0	13.0, 10.3, 8.1
CB1 close	No capture	No capture	No capture	No capture	No capture	No capture
<p>Note</p> <p>* waveform clipped due to scope range and scale (40V peak). Clipped signals have been corrected with and 4th order polynomial fit.</p>						

Table 7.3: 21/10/2020 HFCT measured values – number of transients and duration.

Switching operation	Max No of transients (all phases)	Total duration (ms)	Surge counter incrementation					
			R _{pre}	R _{post}	Y _{pre}	Y _{post}	B _{pre}	B _{post}
DS2 close	99	181	41	41	235	235	142	142
DS2 open	101	163	41	41	235	235	142	142
DS2 close2	106	161	41	41	235	235	142	142
DS2 open2	90	151	41	41	235	235	142	142
DS3 close	110	208	41	41	235	235	142	142
DS3 open	87	158	41	41	235	235	142	142
DS1 close	15	61	41	41	235	235	142	142
DS2 close3	282	172	41	41	235	235	142	142
DS2 open3	242	183	41	41	235	235	142	142
DS2 close4	282	165	41	41	235	235	142	142
DS2 open4	231	163	41	41	235	235	142	142
CB1 close	4	1.1	41	41	235	235	142	142
CB1 open	No capture	No capture	41	41	235	235	142	142
DS3 close 2	446	217	41	41	235	235	142	142
DS3 open 2	344	174	41	41	235	235	142	142
DS2 close 5	265	187	41	41	235	235	142	142
CB1 close 2	No capture	No capture	41	41	235	236	142	143

Observed throughout all measurements was high degree of coupling of transients across all phases, as demonstrated by the overlapping plots of red, yellow and blue phase measurements in Figure 7.10 and Figure 7.11. This coupling was also observed through simulation and was discussed in Chapter 3. The coupling does inflate the apparent number of transients in each switching operation; the number of transients reported in Table 7.3 is based on the maximum number of apparent peaks across all phases. This does provoke the question of the number of transients reported to be generated in each disconnector operation across literature, which may be skewed by single phase measurement data.

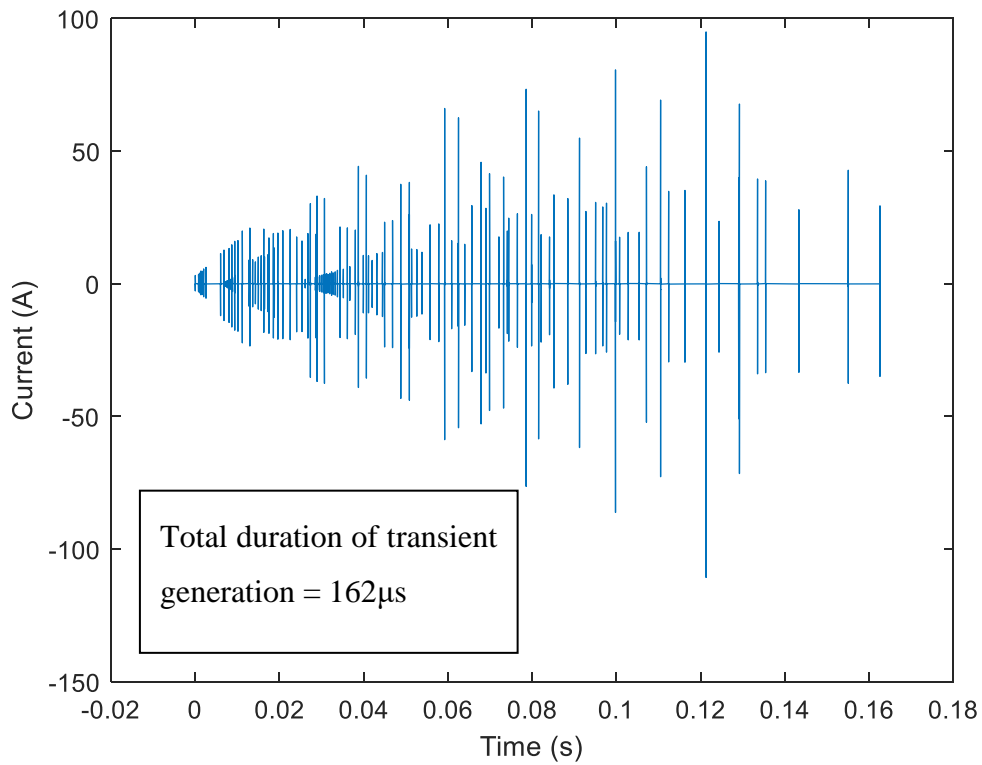


Figure 7.7: Transients measured throughout DS2 open 4 – DS1 closed position - switching sequence 11.

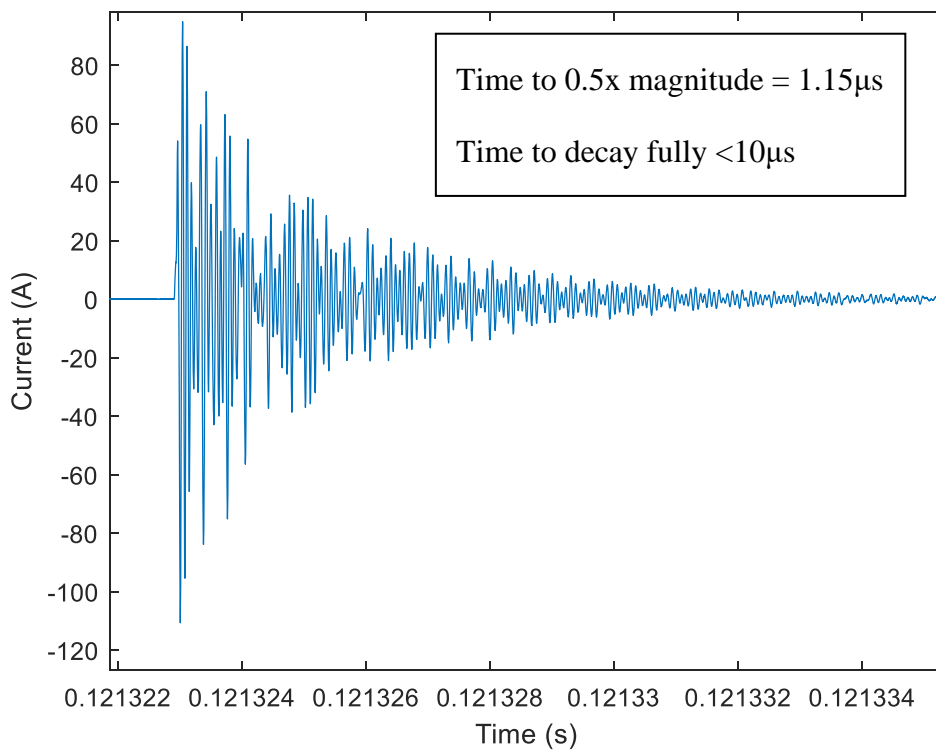


Figure 7.8: Single transient magnified (highest amplitude) DS2 open 4 – DS1 closed position - switching sequence 11.

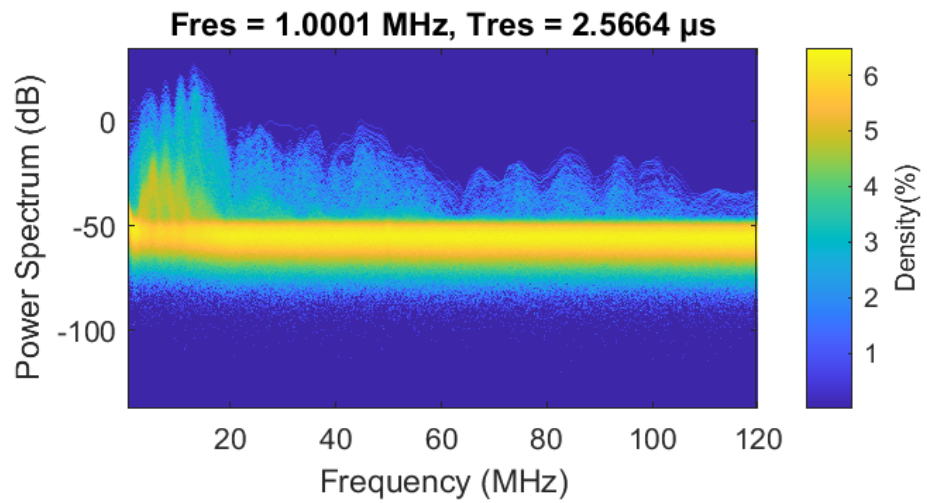


Figure 7.9: Frequency persistence spectrum DS2 open 4 – DS1 closed position - switching sequence 11.

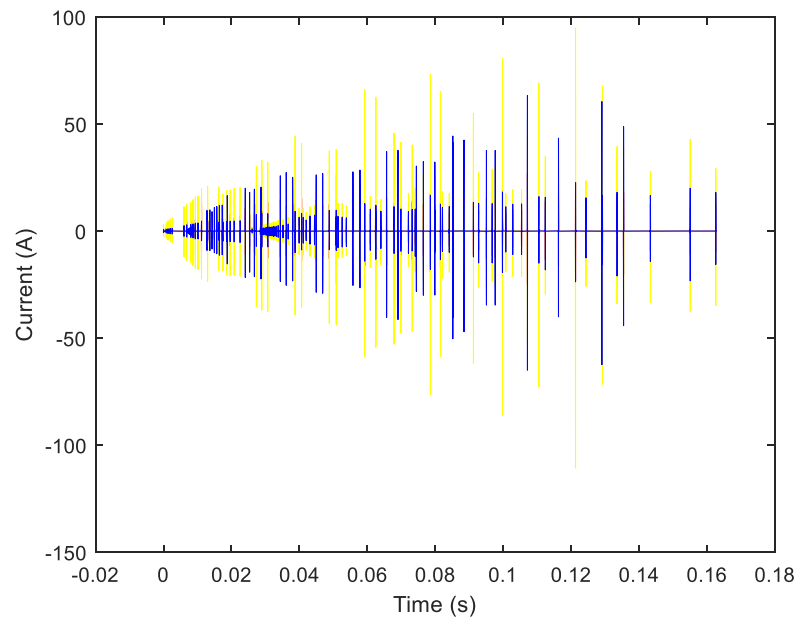


Figure 7.10: Observed coupling of transients to all phases - switching sequence 11.

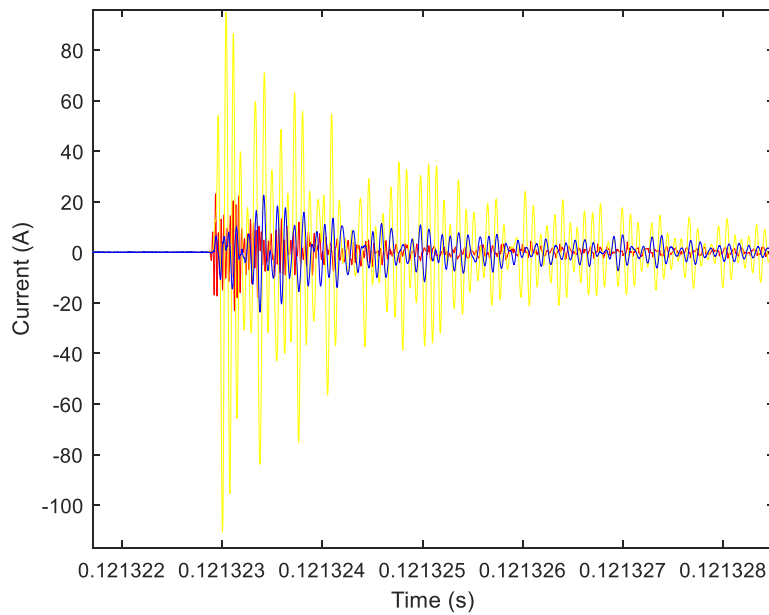


Figure 7.11: Observed coupling of transients to all phases (magnified) - switching sequence 11.

7.3 Surge counter incrementation

Surge counter incrementation was only witnessed in section 7.2 (and further measurement results in Appendix G) for some circuit breaker operations, particularly circuit breaker operations that were closing or opening line volts. Transients generated by a complete CB1 operation are shown in Figure 7.12. A single circuit breaker close transient is shown in Figure 7.13 and the frequency spectrum is shown in Figure 7.14. For comparison, the complete cycle DS2 disconnecter close transients are shown in Figure 7.15, a single transient is shown in Figure 7.16 with its spectrum in Figure 7.17. While there are measured transients for both circuit breaker and disconnecter operations with higher peak currents, these transients, were selected for evaluation as the operations were sequential and the circuit breaker operation did in fact result in surge counter incrementation.

While the same dominant frequency is present in both signals, for the circuit breaker, the dominant frequency is more pronounced, and the spectrum appears to be narrower. It is likely that some of the expected higher frequencies which are a result of minor reflections at the internal GIB discontinuities are present. However, the density of these components is significantly lower and masked by the dominant frequency. One possibility is that this higher spectral density lower down in the expected VFT range,

makes the surge counter more prone to incrementation during circuit breaker transients than disconnector transients.

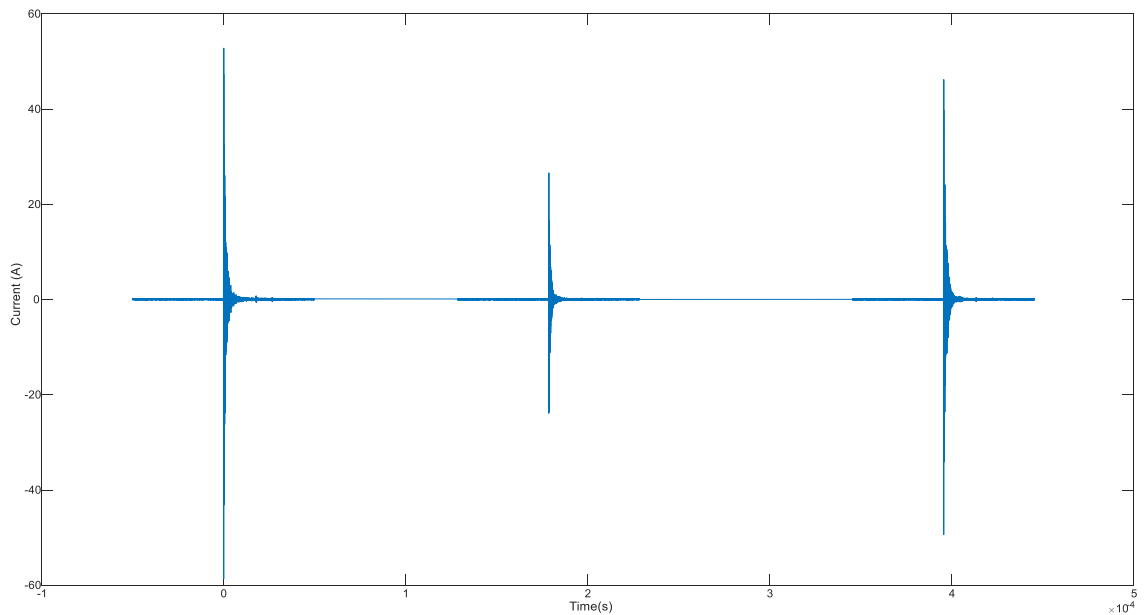


Figure 7.12: CB1 close transients - switching sequence 12.

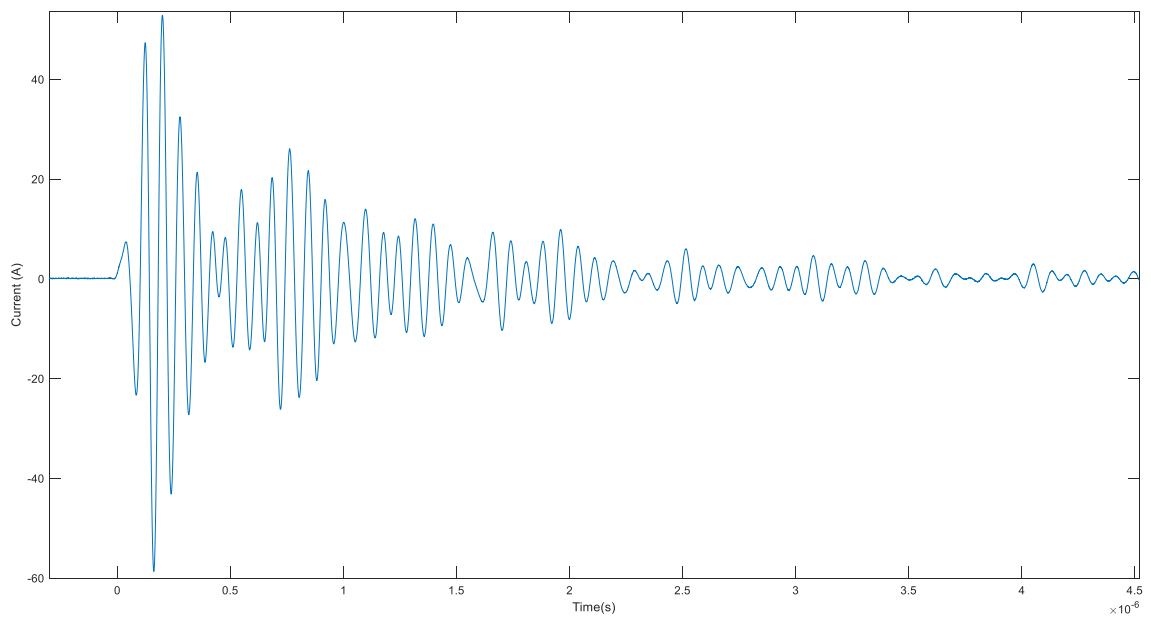


Figure 7.13: CB1 close line volts single transient - switching sequence 12.

Further comparison of the switching transients is undertaken by evaluating the charge for each event, by integrating the current over the entire transient signal. Prior to integrating the current waveforms, denoising and reconstructing the data using wavelets and removing the dead time between transients (removes any background noise not removed by the wavelet decomposition using MATLAB's Wavelet signal denoiser application). The charge over CB1/DS2 close operations is shown in Figure 7.18 and

Figure 7.19 respectively. Directly comparing the total charge for a complete circuit breaker operation against a complete disconnecter operation, it is clear that the disconnecter operation actually delivers more total charge. However, this total charge is delivered over a significantly longer period, in some cases over 200ms longer. A shorter, but more significant injection of charge delivered by the circuit breaker transients may explain incrementation in circuit breaker operation. A final possible explanation for the surge counter incrementation during circuit breaker switching is the presence of temporary overvoltages. The HFCTs have a lower bandwidth of 200Hz and could miss lower frequency oscillations.

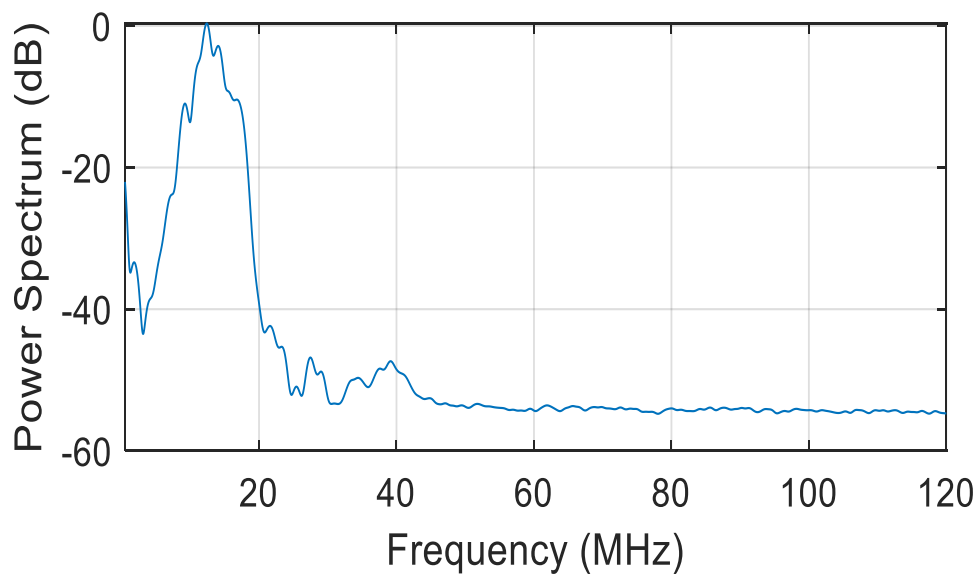


Figure 7.14: CB1 close transient frequency spectrum - switching sequence 12.

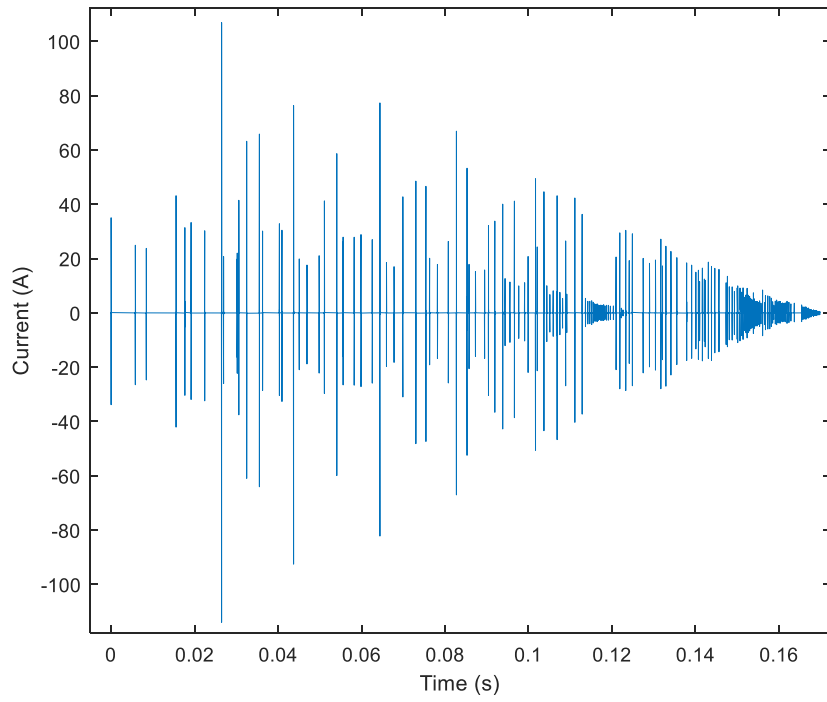


Figure 7.15: DS2 close transients - switching sequence 8.

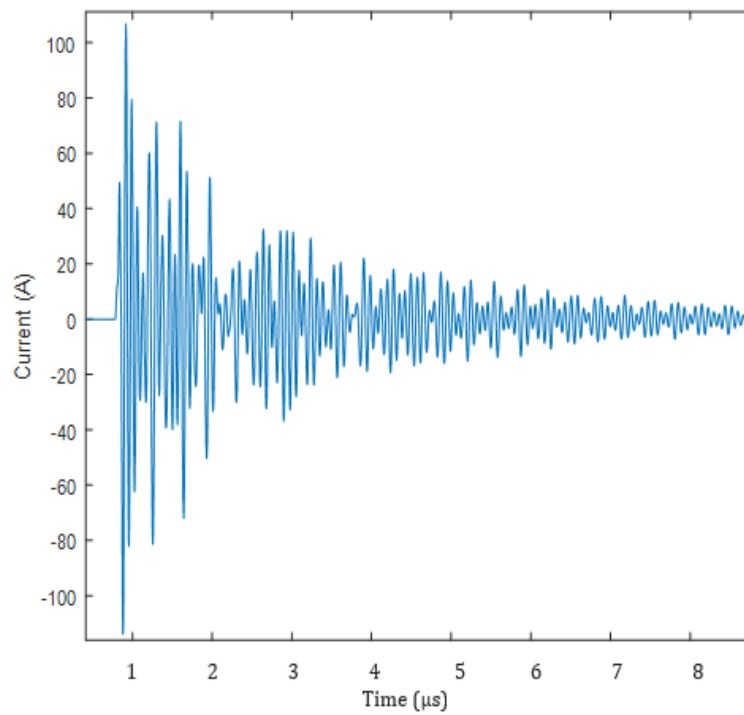


Figure 7.16: DS2 close magnified single transient - switching sequence 8.

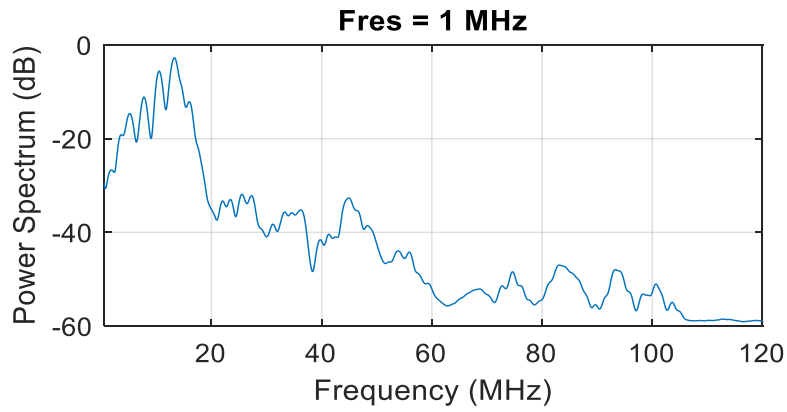


Figure 7.17: DS2 close transient frequency spectrum - switching sequence 10.

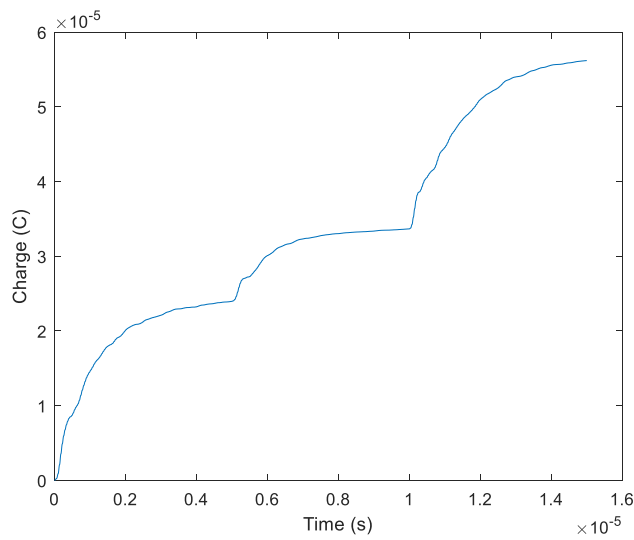


Figure 7.18: CB close CB1 transient – total charge over CB operation.

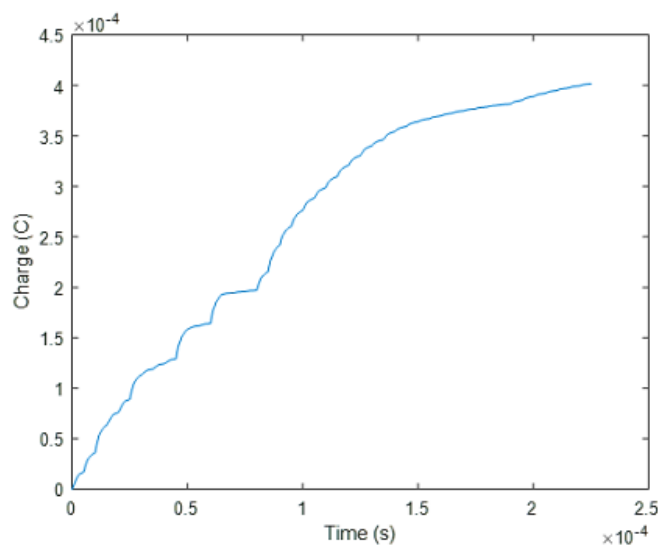


Figure 7.19: DS2 close transient – total charge over DS operation - switching sequence 10.

7.4 D-dot installation and measurements

The D-dot was temporarily installed around the outer surface of a spacer on Substation ‘A’ circuit 1 Red phase as shown in Figure 7.20. This probe was the initial prototype D-dot sensor and as discussed in Section 4, a differential measurement was performed, with the reference electrode not bonded to the enclosure due to the presence of TEVs. The SMA output of the sensor was connected to the data acquisition system via a coaxial cable into a $1\text{M}\Omega$ input of a Picoscope 5244B. Due to the relatively large buffer of the Picoscope, it was configured to capture the entire transient event at 500MS/s at 12bit resolution.

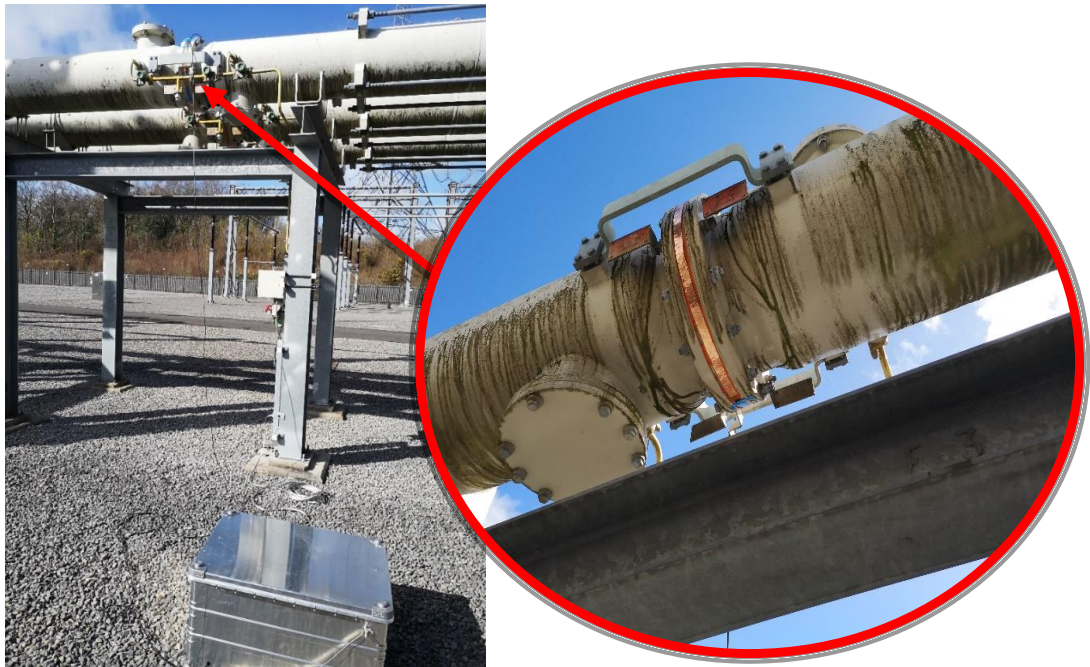


Figure 7.20: Installation of the D-dot probe (without shield).

The full transient event, captured over 200ms during a full DS2 operation is shown in Figure 7.21. Over 100 individual transient events are visible. The characteristic pattern of closing operation is more easily viewed, although coupling between phases is still apparent.

A single transient, subject to an exponential decay, has completely attenuated by $5\text{-}6\mu\text{s}$, as seen in Figure 7.22. Fitting an exponential curve to the data provides the exponential decay rate. Using a Kaiser window applied over the entire signal, the frequency

spectrum and time-frequency spectrogram in Figure 7.23 provides useful information on the frequency content of the transient. There are many frequencies present in the waveform with the five most dominant frequencies at 36.5MHz, 29MHz, 13.8MHz, 4.6MHz, 44.5MHz in order of the relative power density. Higher frequencies at 99MHz and above appear in the spectrum, although based on the 500MS/s sampling rate of the oscilloscope anything higher than 100MHz should be considered with caution.

While the results appear promising, it became apparent that the D-dot sensor was actually detecting predominantly external TEVs, due to the difficulty in achieving effective shielding on operational assets due to the various indentations (not completely smooth curve externally) and painted finish of the enclosure. It is anticipated that the D-dot method of measurement at an unshielded spacer outer surface could provide quick an accurate measurements of internal VFTs, however, shielding effectiveness of the installation proved to be more challenging and requires further research.

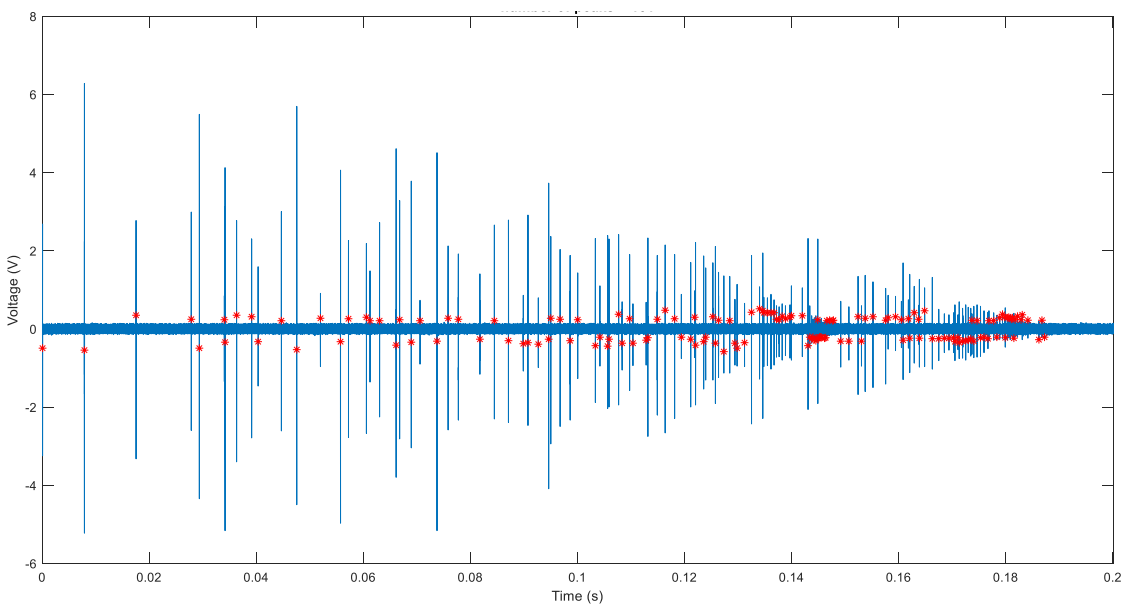


Figure 7.21: 200ms capture during close operation – switching sequence 7.

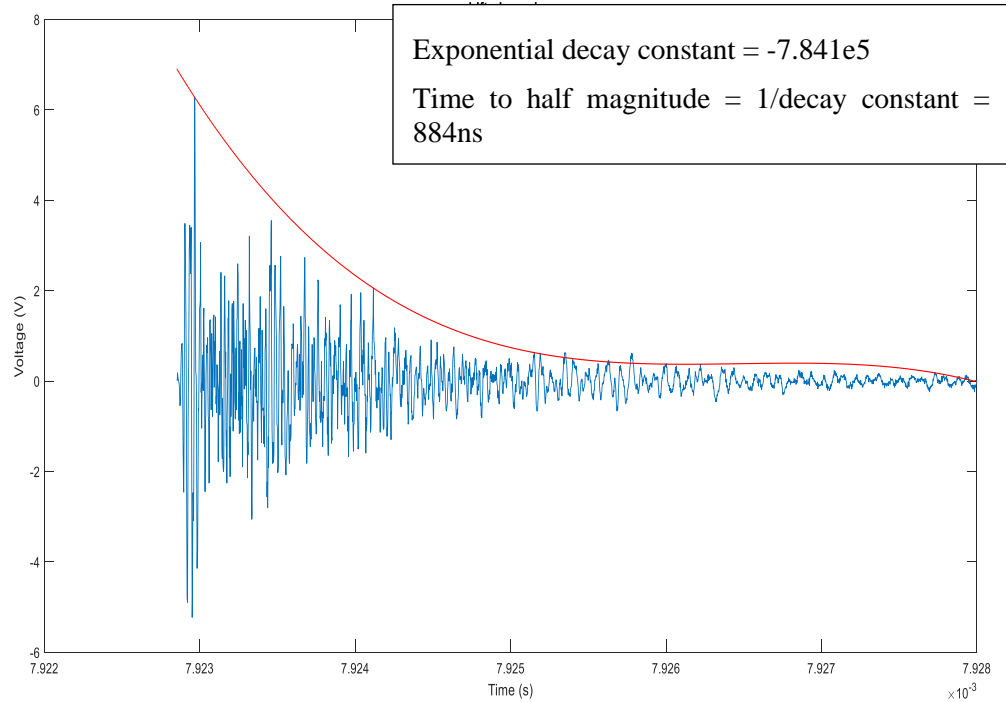


Figure 7.22: Single transient magnified – 10µs capture – switching sequence 7.

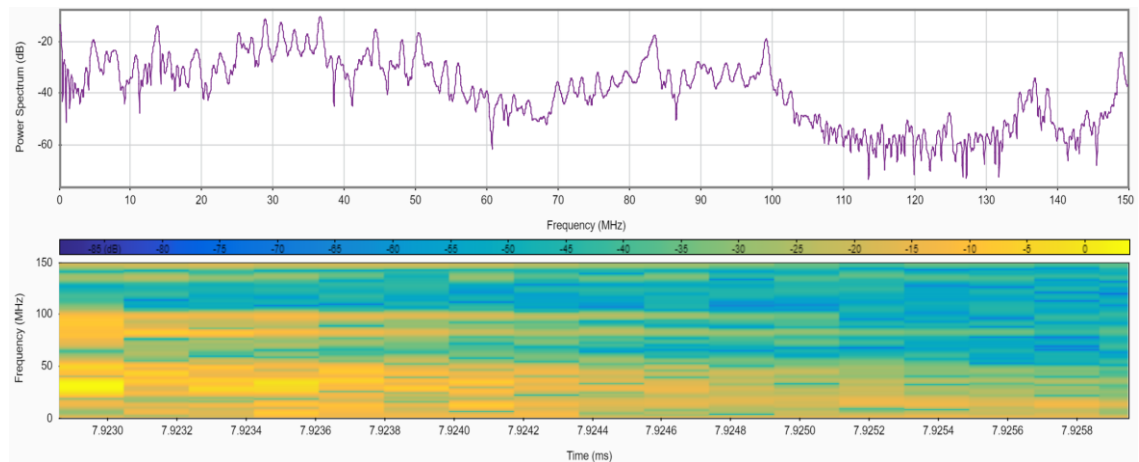


Figure 7.23: Frequency spectrum and time-frequency spectrogram – switching sequence.

7.5 High Frequency Earthing Measurements

High frequency earthing measurements were carried out at Substation ‘A’ on 20/10/20 using the equipment setup shown in Figure 7.24 and Figure 7.25. Measurements were acquired via external CTs and a differential probe at the red phase MOSA download using two systems, the IMS (Impedance Measurement System) and a signal generator/RF amplifier combination. A reference earth electrode was extended outside of the substation in a direction to avoid the influence of the overhead lines. The IMS

system developed by Cardiff University consists of two lock-in amplifiers cable of measuring the voltage and current input from the differential probe and CT and provides valuable phase information. The RF system consists of a Marconi 2019A signal generator providing a clean high frequency sinusoidal excitation and an Amplifier Research 25A250 25W amplifier with a 250MHz bandwidth.



Figure 7.24: Earthing measurement setup at Substation ‘A’.

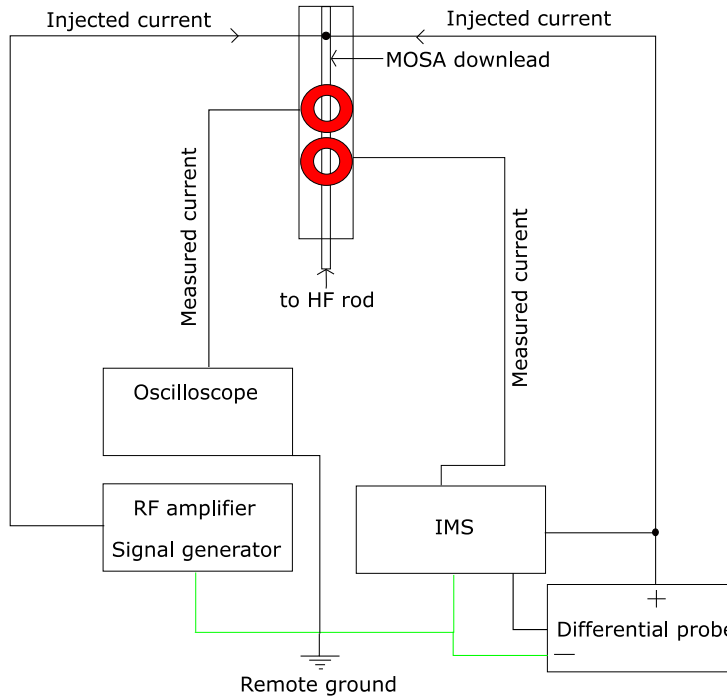


Figure 7.25: Earthing measurement at download arrangement diagram.

The IMS has an upper bandwidth of 100kHz, while the RF systems performs better in the higher frequency range. A collaborative measurement was carried with support from

colleagues from another project to help with the extensive efforts required for the test and to cover a range from low frequency up to 10MHz. It is evident from trials carried out at Llanrumney for a basic vertical rod arrangement that for frequencies over a few MHz, the signals start to become severely distorted, owing to the ground reflections, imperfect connections and difficulty incorporating impedance matching at rod connections. The measurement impedance magnitude and phase are shown in Figure 7.26 and Figure 7.27.

The results demonstrate an increasing impedance as the inductive effects dominate up to approximately 150kHz. At 150kHz, the phase angle decreases as the capacitive effects begin to dominate. Between 200-300kHz, inductive effects begin to dominate again. There appear to be multiple resonant effects throughout the range, the most prominent appears at 1MHz. The sharp resonance indicated in the measurements at 1MHz may be a result of measurement error, otherwise, a sharp resonant response at this frequency has potential implications for the rod's performance under lightning impulse, as the impulse could potentially see a maximum impedance.

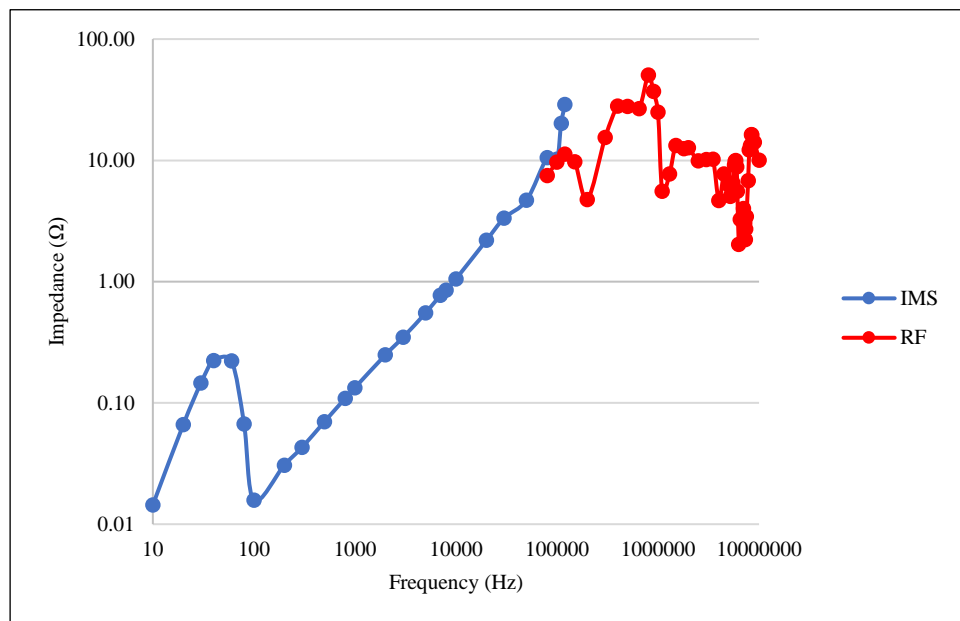


Figure 7.26: Measured impedance magnitude.

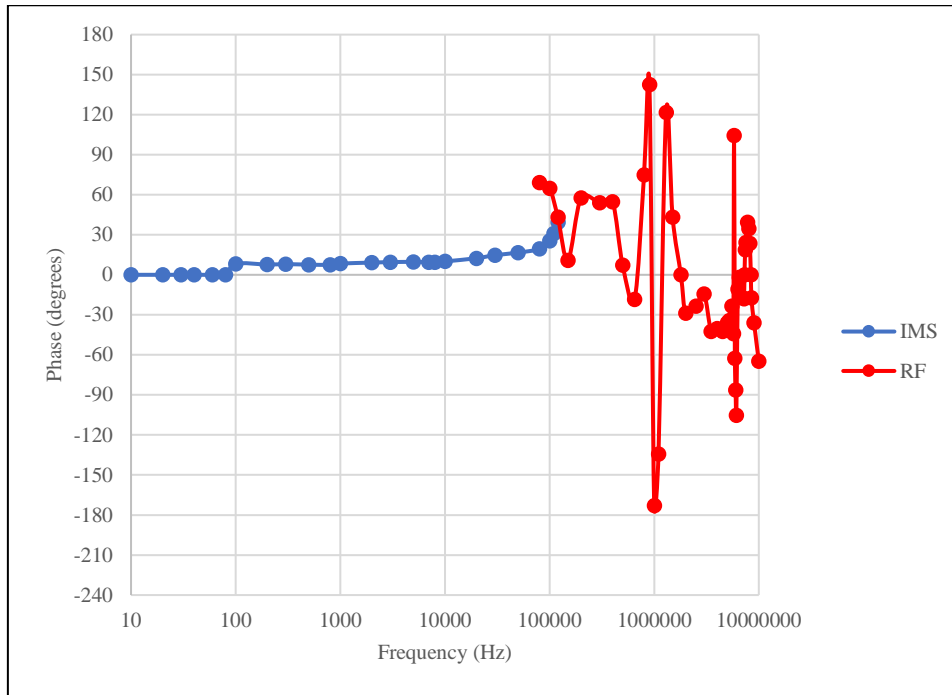


Figure 7.27: Measured impedance phase.

For the top layer resistivity of the original Substation ‘A’ soil model ($448\Omega\text{m}$), a relative permittivity of 1 and a relative permeability of 1, the wavelength at 1MHz is calculated to be approximately 66m, far too large to be a transmission line resonance for the HF rod alone. The multiple resonances suggests that the rod was connected to the main earthing system, the appearance of an apparent above ground bonding connection is further evidence that the rod is connected to the main earthing system, therefore making the measurements of the high frequency rod in isolation almost impossible.

7.6 Measurement observations

From the series of measurements carried out at Substation ‘A’, the following observations are made:

- Results provide some validation of EMT models. Magnitudes and durations are similar and overall frequency content is similar.
- Coupling between phases is present for every transient detected, implying (along with observed simulated coupling) that when the transients exit the GIB at the bushing, they continue propagation towards the AIS via multiple propagation modes. Extracting the exact phase responsible for initiating each transient is difficult. Firstly,

each phase has a very slightly different arrangement, with minor variations in bus lengths, differences in routing and position of grounding elements and phase equipment such as surge arresters, CTs and CVTs, all of which will not be completely identical in its high frequency response to the others. Secondly, the measurement and acquisition circuit will likely have minor differences in frequency/amplitude response. Further unknowns are the disconnecter operation time, contact velocity and the field uniformity of the contacts, meaning that each disconnecter could begin restriking/prestriking at different times, or even at times outside of the acquisition window.

- With the previous point in mind, given the number of transients (datapoints) generated over one disconnecter operation and the variation of dominant magnitudes across the three phases, breakdown curves can be extracted from measured data, providing the transients could be attributed to specific phases. This was explored in Chapter 5.
- The first transient for a DS2 close operation should be subject to a smaller or no trapped charge and will therefore not be the largest over the disconnecter operation. This is witnessed for both the modelled and measured cases as shown in Figure 7.28. The maximum MOSA download current is approximately 80A for this scenario.

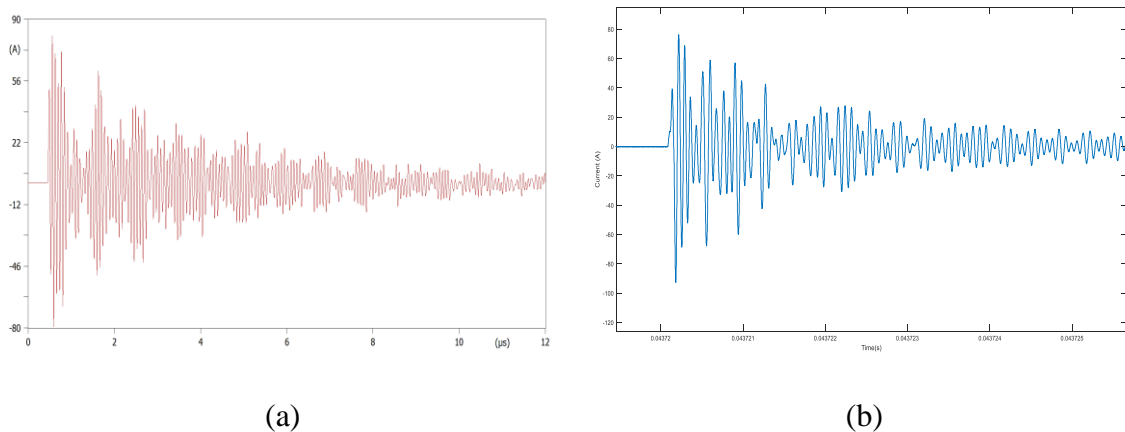


Figure 7.28: DS2 close maximum transient (DS1 closed – 1p.u. trapped charge), (a) simulated (b) measured.

- The characteristic patterns of transients are easily observed, i.e. during close operation the initial transients are large in magnitude but sparse, becoming smaller in magnitude and more frequent as the disconnecter contact approaches the closed position. The opposite is true for open operations. This is due to the variation of withstand voltage with gap distance.

- Surge counter incrementation was observed only with circuit breaker operation not disconnectors.
- Circuit breaker transients (prestrikes/restrikes) have a narrower band of dominant frequencies; this may contribute to the surge counter operation.
- Bus side disconnector operations will result in smaller transients on the line side bus. Based on EMT models and validation provided by measurements, the transients generated on the bus side will be significantly larger.
- The larger VFT magnitudes reported in literature (2p.u. and above) are often based on the switching of line side disconnectors with energised lines. The practice most commonly used by the network operator, i.e. the re-energisation of circuits from the main bus, out to the load/generation will avoid these large VFTs on the line side (although not avoided bus side). For systems in which the line side GIB has reduced dimensions in comparison with the main bus, operating the line side disconnector with an energised line should be avoided.
- After closure of DS1, transients generated by DS2 and DS3 are up to 35 times larger on the line side. The disconnector gap provides significant attenuation.
- The frequency spectra for open and close operations are identical.
- From extensive modelling and validation through measurements, it is apparent that internal and external transients have similar frequency spectra, however the dominant frequencies for external transients appear to be dependent on the external equipment and earthing system, while dominant internal frequency components appear to be more dependent on the GIB configuration. This implies that the waveforms captured at any point in the system as a result of disconnector operations are standing wave patterns which result from the superposition of travelling waves, as opposed to lumped system oscillations.
- The fibre optic link developed and used for final measurements produced similar results for the smaller transients but some higher dominant frequency components (25MHz). The 25MHz component appears to be present in the other phases also, but at a lower spectral density. This effect also appears to be less pronounced at lower amplitudes. It is highly likely that for the larger signals, the fibre optic link is exceeding its small signal bandwidth. Resulting in non-linear amplification over the frequency range.
- Repeated measurements have resulted in both a larger dataset and model validation for various switching operations. As switching operations are limited on live

assets there was previously a risk of missing captures due to the choice of attenuator or oscilloscope scales. It is now far more straightforward to select appropriate attenuators and oscilloscope settings to capture more detail.

- While it appears as though the number of transients detected increases significantly when the line side disconnecter (DS1) is closed. It is likely that the number of transients generated before closure of the line side disconnecter are actually similar, but the attenuation of the transients by the open gap means that the smaller transients are possibly too low to be detected.
- CB transients have narrow band transient in comparison to DS transients.
- From the model, for DS2 and DS3 close operation, it appears the disconnected section of bus is actually at floating potential for the initial transient, not strictly a trapped charge. The floating is unipolar (due to capacitive coupling), oscillating at 50Hz and in phase with the main bus voltage. The initial transient can be reduced due to this floating potential.
- From modelling, the peak magnitudes are dependent on the ratio of capacitances either side of the disconnecter. Increasing the isolated bus side capacitance, will result in a larger voltage collapse and therefore, a larger peak transient.
- The decay rate of single transient events reported are more closely aligned with the enhanced circuit model (with VF elements) than the circuit model that followed a standard approach.

7.7 Conclusion

This chapter has presented several new measurement techniques for measuring both internal and external transients. The measurement techniques have been designed with the aid of finite element analysis and various RF engineering software packages. The response of built prototypes has been verified, both through models and measurements, utilising the custom designed and fabricated half scale GIB, which itself provides an excellent frequency response over the required range. While possibly the most troublesome on site, the D-dot sensor shows promise in the laboratory environment with a good, self-integrating frequency response; further work on producing an effective shield will guarantee its use.

The developed UHF coupler unit shows the most promise for the measurement of internal VFTs. The device can be installed at multiple locations around the GIS, Substation 'A' incorporates UHF sensor at most elbow locations throughout the system.

Due to the discussed measurement issues on site, the operational use of the UHF coupler unit could not be proven, however, detail model and laboratory based validation measures were carried out and all suggest the device will function as intended.

A high frequency fibre optic link was designed to further enhance measurements on site. The link provided a good response as confirmed within the laboratory tests, however, the components used could only operate at the required bandwidth in the small-signal region, given the significant variation in magnitudes, it proved difficult to maintain this while ensuring a trigger operation on the oscilloscope. The main limitation of the design was the use of an LED. Future designs should focus on laser technologies and components that have the required bandwidth for small and large signals.

Aside from a number of successful measurements at Substation 'A', one of the key points to note is the difficulty faced in predicting the magnitudes that would be generated for subsequent events, which did appear to vary significantly. This had an impact on the selection of appropriate attenuators and oscilloscope trigger thresholds and did limit the number of successful captures, through either a missed capture or severe waveform clipping. After the experiences to date, the author suggests obtaining a coarse set of 'base' measurements for each switching operation, prior to refining and calibrating measurement equipment for a finer measurement. Given the network security concerns when large substations or circuits like those at Substation 'A' are offline for maintenance, obtaining this 'base' set of measurements may be difficult to achieve logistically. Any opportunity to take these measurements, such as following quick routine maintenance, should be exploited. A further measurement issue that requires further work is the decoupling of signals. Some efforts have been made to decouple signals but mainly for the purpose of creating measurement based custom disconnecter models.

The measurements overall provided validation and clarification for the developed models. The HFCTs installed at the surge arrester download, appeared to be the most consistent and helped provide the necessary evidence to conclude that the transients seen at the surge arresters during disconnector operations were capacitively coupled, as opposed to the surge arresters going into 'high conduction'. The measurements also clarified that operation of the surge counters did not occur for disconnector operations, the transients were too low in magnitude. They did however operate multiple times for circuit breaker open and close transients.

The impedance of the circuit 1 red phase surge arrester downlead was measured using two separate measurement systems. A good response was obtained from the IMS system up to approximately 100kHz. For the higher frequencies, the RF system produced a clear response up to approximately 1MHz, at which point many system resonances started to appear, as identified by the sharp oscillations in the impedance plots. Significant enhancements to earthing system measurements are possible through appropriate matching of connection impedances, however, further research is required.

8 CONCLUSION AND FUTURE WORK

8.1 Conclusion

The main aim of this thesis was the investigation of transient events associated with disconnector operations. The GIS substation at Substation ‘A’ was used as a basis for the research, as it was subject to what was believed to be a VFT related failure at a spacer located in a double elbow section of the outdoor GIB. Through extensive modelling and measurement, the possible causes of failure could be attributed to one or more of the following:

- Internal contamination or material defect.
- External, unrecorded transient.
- VFT caused degradation and/or subsequent early failure.
- Inefficient bonding of the spacer-flange.

Given that previous reports described arcing at bolt locations around the GIS, it is quite possible that, as suggested by the modelling results in Chapter 3, inadequate shielding of the spacer-flange due to poor bolt to flange conductivity is fully or partially to blame for excessive overvoltages and high fields. This may be a further explanation for the apparently high degree of coupling of TEVs between the enclosures. While the extremes in magnitude provided are unlikely, as the likelihood of all bolts securing a spacer flange have poor electrical contact, the results are presented as a worst case to highlight the risk of poor bonding practices at this location. The author postulates that a completely shielded design, i.e. an appropriated rated metallic shield should be installed circumferentially around the spacer as this would alleviate the majority of issues

associated with this design of GIS. This is evidenced by simulations that utilise a perfect bolt connection and other models (internal only propagation models) that have assumed a perfect electrical conductor is present at the spacer surface.

Given this information, all flange bolts should at the very least be checked for continuity. If this phenomenon was responsible for the flashover that occurred at Substation 'A', the addition of serrated washers to improve the electrical connection of the bolts to the flange may have partially or fully resolved this issue, in which case it is unlikely that another flashover would occur for ideal internal conditions. While this recommendation may appear to suggest the prevention of external arcs directly, the enhancements to the shielding effectiveness are crucial for reduced magnitude internal transients.

Several modelling approaches have been adopted in order to obtain a broad perspective of the phenomenon. No single modelling technique used is sufficient alone to investigate VFTs and TEVs, therefore a multiple platform or co-simulation type approach is the best option. To aid with modelling and the general understanding of very high frequency transients, many of the concepts used more traditionally by RF/EMC disciplines have been used. This thesis has highlighted some of the many issues of looking at these transients with a low frequency 'mindset'. Even utilising fairly sophisticated EMTPs, modelling inaccuracies, errors or numerical instability is possible. A key point to note on modelling using EMTPs, as demonstrated in this thesis is the use of TLAs for the study of TEVs will not be appropriate over the entire frequency range, if at all. To partially combat this issue and to enhance circuit-based models in general, two techniques have been developed for the extraction of equivalent circuits. The vector-fitting method is by far the most accurate and versatile, utilising data from finite element models to produce accurate and stable transient equivalent circuit models, at the lowest possible order of approximation. The methods developed, could be used to create a complete replica of a GIS.

The coupling and transference of transients from the internal bus to the external enclosure was explored with the bushing models. The models are internally excited near the base of the bushing and terminated several metres away on the AIB-ground and GIB enclosure-ground with numeric ports. Peak magnitudes of 0.34 p.u. are computed. TEVs generated at the bushing appear to have a high dependence on the grounding arrangement directly at the bushing. This observation initiated the investigation of an improved downlead arrangement.

Further propagation characteristics of TEVs are studied through eigenmode analysis and ultimately a full-scale Substation 'A' circuit replica model. The models utilising eigenmode analysis the limitations of a quasi-TEM dominant assumption for the propagation of TEVs. The full-scale transient model, shows in detail the propagation and reflection at the various discontinuities within the system, utilising a TDR style approach. The peak enclosure voltage when excited by an internal step voltage matches reasonably well at 0.3p.u. with that computed by the bushing only model. The minor difference could be attributed to the presence of the adjacent enclosures and a slight difference in distance of the enclosure voltage calculation point. The propagation of the transient showed both aerial and ground modes, in addition to the apparent mode conversion on the outer 'non-excited' enclosures.

Further numerical modelling concepts were applied to the assessment of elements of the grounding system. Large scale models were initially assessed, but due to the additional segmentation requirements at the TEV frequency range, matrix limits appeared to be exceeded and numerous failed simulations occurred. The modelling instead took the form of an assessment of the frequency response several discrete elements. The known limited response due to length of downleads, connecting the enclosure to the grounding system was corroborated and quantified for various uniform soils and earthing terminations. The downlead-rod combination provided the best transient response however, a single downlead-rod is still quite ineffective at dividing a surge. An optimised multi-downlead solution was proposed, providing a much lower input impedance, closer to the characteristic impedance of the enclosure-ground by increasing the 'effective' radius. The arrangements, after some minor optimisation could be applied to any GIS height and there is a potential to 'impedance match' the enclosure to an earthing system for an optimal division of a surge.

Several new fast current and voltage measurement systems, composed of transducers, high frequency circuit boards, signal transmission and recording devices were developed for use at Substation 'A', during operational switching programmes. The techniques are equally applicable for many other systems. The systems allow the safe measurement of transients of expected magnitudes up to 3p.u. The measurement systems were tested during development using a specially design half scale GIS model. On-site measurements provided quantitative results while achieving a good degree of validation of the modelling techniques used. Likewise, the measurement systems were designed and optimised using the modelling techniques described. Due to the switching

practice implemented by the network operator, it was verified through measurements and modelling that the highest possible VFTs are mostly avoided (on the line side of the circuit being switched).

High frequency CTs were installed at the downleads of the circuit 1 surge arresters to quantify the magnitudes present during switching and to elaborate on the nature of coupling. Through both measurement and simulation through the enhanced circuit models, it was possible to deduce that the surge arresters at Substation 'A' were not reaching high conduction thresholds and the currents present on the downlead were predominantly due to capacitive coupling from the AIB. Further discussions on the thresholds required to register a count on the surge counters were held. The surge counter incrementation witnessed throughout testing occurred only during operation of the circuit breaker. Given the comparisons of frequency content and charge transferred during both circuit breaker and disconnecter operations, it is likely that the lower range of dominant frequencies present in the circuit breaker when compared to the disconnectors (causing V-t characteristic above the threshold of the counter), may be the cause of surge counter incrementation. Alternatively, lower frequency transients if present, below the lower range of the HFCTs could be responsible.

The measurements from the HFCTs installed at the base of the surge arresters, along with the results from the results from the blackbox model enhanced ATP-EMTP model, also provided strong evidence that the waveforms present on the surge arrester downlead, were capacitive coupling from the AIB, and were below the threshold to register a count on the surge counters. The surge counter incrementation witnessed throughout testing occurred during operation of the circuit breaker.

A D-dot sensor was installed at a spacer location close to the gas to air bushing, with the aim of measuring the internal VFTs present inside the GIB. While validated under laboratory conditions, difficulties in achieving an effective shielding of the inner and outer electrodes meant that coupling of external TEVs occurred, evidenced by the apparent interphase coupling. Further efforts in developing enhanced shielding arrangements will make the D-dot suitable for internal VFT measurements.

A further UHF coupler unit was developed to exploit the pre-installed internal UHF sensors as a transducer for voltage measurements. While site-based measurements using the units could not be carried out, extensive modelling and laboratory measurements confirm its suitability.

A high frequency fibre optic link was also designed and built to aid measurements and avoid the influence of external EMI and distortion of signals.

8.2 Future work

This thesis has highlighted several issues in current modelling practices for the study of VFTs and TEVs. Further enhancements to circuit-based models should be sought, building on the methods established. One such enhancement would be the addition of frequency dependent soils to the finite element models. There may be a trade-off with the inclusion of frequency-dependent soils at present, as even utilising the University's supercomputer, RAM requirements are quickly exceeded. Furthermore, finite element models could include a greater extent of an earthing system, as opposed to discrete elements. Models of external AIB connected components, in particular, a surge arrester model, incorporating the non-linear, voltage dependent behaviour of the ZNO disks. Further essential models include VT and CTs. These external elements could introduce large additional reflections from outside of the GIS. It may be possible to produce finite element and enhanced circuit models of each component within a substation, which could lead to significant improvements in accuracy.

In terms of the propagation of TEVs, further research in the topic of surface waves (TM mode). Using Eigenmode analysis, it may be possible to identify the cutoff frequencies of higher order modes within the VFT/TEV range.

For measurements, further improvements of the D-dot sensor shielding are required for it to be functional as a strictly VFT measurement device. The Pyrolux based D-dot prototypes appears to be the most versatile substrate, exhibiting a large capacitance and small inductance, with the additional ability to create flexible matching networks directly on the substrate.

The UHF sensor coupler shows the greatest promise as a portable device that is suitable for internal measurements. Further assessment of the input characteristics at the UHF sensor's N type connector will enable identification of any minor modifications for use on the Substation 'A' system.

Significant work in the measurement of earthing systems at the very high frequency range is required. More specifically, a method of matching, and exciting the top of a downlead is required. The use of bulk current injection probes and CTs should also be explored.

To enable high quality measurements in these harsh, high EMI environments, further modifications to the design of the fibre optic link are recommended. Improvement of the frequency response for large signal inputs should be sought in the first instance. Due to the bandwidth of the selected components, the prototype could only perform as intended in the small-signal region, as proven by laboratory tests. The highly irregular magnitudes attributed to successive switching operations meant it was extremely difficult to predict the measured magnitude and select an attenuator to maintain the small signal levels, while still ensuring a capture. Further to this, the careful selection of external attenuators for the anticipated magnitude of transient (determined through modelling or following a baseline measurement).

A further measurement improvement would be on the decoupling of signals from all three buses. The method produced in this thesis is relatively simple, more advanced methods rely on cluster recognition or artificial intelligence.

Finally, given the progress made in identifying a potential cause of or contributor to failure of the spacer at Substation 'A', further measurements to evaluate the shielding effectiveness of spacer-flange should be developed. If further quantified through measurement, the conclusion of spacer failure would be apparent. Furthermore, if this measurement technique was to show promise, it could become part of commissioning and periodic maintenance to ensure safety and security of the substation equipment and its operators.

9 REFERENCES

- [1] H. Koch, Gas Insulated Substations. Wiley Blackwell, 2014.
- [2] A. Ametani, N. Nagaoka, Y. Baba, T. Ohno, and K. Yamabuki, Power system transients : theory and applications, 2nd ed. 2016.
- [3] D. Povh, H. Schmitt, O. Völcker, and R. Witzmann, “Modelling and analysis guidelines for very fast transients,” IEEE Trans. Power Deliv., vol. 11, no. 4, pp. 2028–2035, 1996, doi: [10.1109/61.544291](https://doi.org/10.1109/61.544291).
- [4] A. Haddad, D. F. Warne, and Institution of Engineering and Technology., Advances in high voltage engineering. Institution of Engineering and Technology, 2004.
- [5] R. Arora and W. Mosch, High Voltage and Electrical Insulation Engineering. Wiley, 2011.
- [6] A. Janssen, R. P. P. Smeets, M. Kapetanovic, D. F. Peelo, and L. Van der Sluis, Switching in electrical transmission and distribution systems. Wiley, 2014.
- [7] IEEE Power and Energy Society, “Substations Committee GIS Subcommittee K0 Working Group K2 - Module GIS Theory,” in Transmission and Distribution Conference and Exposition, 2008, p. PN04.
- [8] J. A. Martinez, P. Chowdhuri, R. Iravani, A. Keri, and D. Povh, “Modeling Guidelines for Very Fast Transients in Gas Insulated Substations,” in PES-TR7

of IEEE Working Group on Modeling and Analysis of System Transients, 1998, pp. 6-1-6–24.

- [9] M. Stosur, M. Szewczyk, W. Piasecki, M. Florkowski, and M. Fulczyk, “GIS disconnector switching operation VFTO study,” Proc. - Int. Symp. Mod. Electr. Power Syst. MEPS’10s, 2010, [Online]. Available: <https://www.engineeringvillage.com/>
- [10] C. Neumann, D. Konig, and G. Imgrund, “Transient current and voltage behaviour during interruption of small capacitive currents with GIS-Disconnectors,” in Gaseous Dielectrics VI, 1990, pp. 497–502.
- [11] S. Carsimamovic, Z. Bajramovic, M. Ljevak, and M. Veledar, “Very fast electromagnetic transients in air insulated substations and gas insulated substations due to disconnector switching,” in IEEE International Symposium on Electromagnetic Compatibility, 2005, vol. 2, pp. 382–387, doi: [10.1109/ISEMC.2005.1513544](https://doi.org/10.1109/ISEMC.2005.1513544).
- [12] S. A. Boggs, F. Y. Chu, N. Fujimoto, A. Krenicky, A. Plessl, and D. Schlicht, “Disconnect switch induced transients and trapped charge in gas-insulated substations,” IEEE Trans. Power Appar. Syst., vol. PAS-101, no. 10, pp. 3593–3602, 1982, doi: [10.1109/TPAS.1982.317032](https://doi.org/10.1109/TPAS.1982.317032).
- [13] IEEE, “C37.122.1-2014 - IEEE Guide for Gas-Insulated Substations Rated Above 52 kV,” 2014.
- [14] U. Riechert, M. Bösch, M. Szewczyk, W. Piasecki, and a B. B. Poland, “Mitigation of Very Fast Transient Overvoltages in Gas Insulated UHV Substations,” Cigré Sess., 2012.
- [15] M. Babaei, M. Babaei, and G. Nourirad, “Analysis of influential factors in determining Very Fast Transient Overvoltages of GIS substations,” in Proceedings of the 2014 IEEE 8th International Power Engineering and Optimization Conference, PEOCO 2014, 2014, pp. 79–84, doi: [10.1109/PEOCO.2014.6814403](https://doi.org/10.1109/PEOCO.2014.6814403).
- [16] T. Lu and B. Zhang, “Calculation of Very Fast Transient Overvoltages in GIS,” in 2005 IEEE/PES Transmission & Distribution Conference & Exposition: Asia and Pacific, 2005, pp. 1–5, doi: [10.1109/TDC.2005.1546760](https://doi.org/10.1109/TDC.2005.1546760).

- [17] L. L. Grigsby, *The electric power engineering handbook. Power systems*, 3rd ed. CRC Press, 2012.
- [18] British Standards Institute, “BS EN 62271-102:2002+A2:2013 - High-voltage switchgear and controlgear. Alternating current disconnectors and earthing switches.” 2002, Accessed: Jan. 03, 2017. [Online]. Available: <http://shop.bsigroup.com/>
- [19] J. C. Das, *Transients in electrical systems : analysis, recognition, and mitigation*, 1st ed. McGraw-Hill, 2010.
- [20] M. Szewczyk, M. Stosur, W. Piasecki, M. Fulczyk, M. Steiger, and J. Kostovic, “New disconnector model for Very Fast Transient studies in High Voltage Gas Insulated Substations,” *EEUG Conf. Pap.*, vol. 1, no. 1, 2010.
- [21] Working Group 33/13-09, “Very fast transient phenomena associated with Gas Insulated Substations,” in *CIGRE Session, Paper No. 33-13*, 1988, Accessed: Jan. 03, 2017. [Online]. Available: <http://www.e-cigre.org/>
- [22] J. A. Martinez-Velasco, *Transient analysis of power systems : solution techniques, tools, and applications*. Wiley, 2015.
- [23] IEC, “IEC 62271-203:2011 High-Voltage switchgear and controlgear - Part 203:Gas-insulated metal-enclosed switchgear for rated voltages above 52 kV,” 2011.
- [24] CIGRE working group A2-A3-B3.21, “Electrical Environment of Transformers – Impact of Fast Transients,” *Electra* No 218, pp. 25–37, 2005, Accessed: Jun. 17, 2017. [Online]. Available: <http://ipstconf.org/papers/>
- [25] S. Haifeng, L. Guishu, Z. Xile, and C. Xiang, “Analysis of resonance in transformer windings under very fast transient overvoltages,” *Electromagn. Compat. 2006. EMC-Zurich 2006. 17th Int. Zurich Symp.*, no. 1, pp. 432–435, 2006, doi: [10.1109/EMCZUR.2006.214964](https://doi.org/10.1109/EMCZUR.2006.214964).
- [26] G. Luxa et al., “Recent research activity on the dielectric performance of SF6, with special reference to very fast transients,” in *International Conference on Large High Voltage Electric Systems*, 1988, Accessed: Jan. 03, 2017. [Online]. Available: <http://www.e-cigre.org/>
- [27] Lu Zhang et al., “Insulation characteristics of 1100 kV GIS under very fast transient overvoltage and lightning impulse,” *IEEE Trans. Dielectr. Electr.*

- Insul., vol. 19, no. 3, pp. 1029–1036, Jun. 2012, doi: [10.1109/TDEI.2012.6215109](https://doi.org/10.1109/TDEI.2012.6215109).
- [28] T. Flohr, W. Pfeiffer, C. Zender, and V. Zimmer, “Dielectric Strength of SF₆ in Nonuniform Gaps Stressed by Very Fast Transient Voltages,” in *Gaseous Dielectrics VII*, Boston, MA: Springer US, 1994, pp. 267–273.
- [29] M. S. Naidu, *Gas insulated substations*. I.K. International Pub. House, 2008.
- [30] K. D. Srivastava and J. Zhou, “Surface charging and flashover of spacers in SF/sub 6/ under impulse voltages,” *IEEE Trans. Electr. Insul.*, vol. 26, no. 3, pp. 428–442, Jun. 1991, doi: [10.1109/14.85114](https://doi.org/10.1109/14.85114).
- [31] T. Kuczek and M. Florkowski, “Modelling of overvoltages in gas insulated substations,” *PRZEGLĄD ELEKTROTECHNICZNY (Electrical Rev.)*, vol. 4a, 2012.
- [32] TC 112, “IEC TR 60505:1975 Guide for the evaluation and identification of insulation systems of electrical equipment (withdrawn),” 1975.
- [33] A. C. Gjerde, “Multifactor ageing models - origin and similarities,” *IEEE Electr. Insul. Mag.*, vol. 13, no. 1, pp. 6–13, Jan. 1997, doi: [10.1109/57.567392](https://doi.org/10.1109/57.567392).
- [34] P. Cygan and J. R. Laghari, “Models for insulation aging under electrical and thermal multistress,” *IEEE Trans. Electr. Insul.*, vol. 25, no. 5, pp. 923–934, 1990, doi: [10.1109/14.59867](https://doi.org/10.1109/14.59867).
- [35] Q. Xie, X. Liu, C. Zhang, R. Wang, Z. Rao, and T. Shao, “Aging Characteristics on Epoxy Resin Surface Under Repetitive Microsecond Pulses in Air at Atmospheric Pressure,” *Plasma Sci. Technol.*, vol. 18, no. 3, pp. 325–330, Mar. 2016, doi: [10.1088/1009-0630/18/3/18](https://doi.org/10.1088/1009-0630/18/3/18).
- [36] J. V. G. Rama Rao, J. Amarnath, and S. Kamakshaiah, “Accurate modelling of very fast transient overvoltages in a 245kV GIS and research on protection measures,” in *2010 Annual Report Conference on Electrical Insulation and Dielectric Phenomena*, Oct. 2010, pp. 1–4, doi: [10.1109/CEIDP.2010.5723980](https://doi.org/10.1109/CEIDP.2010.5723980).
- [37] E. P. Dick, N. Fujimoto, G. L. Ford, and S. Harvey, “Transient Ground Potential Rise in Gas-Insulated Substations - Problem Identification and Mitigation,” *IEEE Trans. Power Appar. Syst.*, vol. PAS-101, no. 10, pp. 3610–3619, Oct. 1982, doi: [10.1109/TPAS.1982.317046](https://doi.org/10.1109/TPAS.1982.317046).

- [38] H. Muto, M. Yoshimura, C. Nishida, S. Okabe, and S. Yuasa, "Simulation of propagation characteristics of higher order mode electromagnetic waves in GIS," in Proceedings of the 7th International Conference on Properties and Applications of Dielectric Materials (Cat. No.03CH37417), vol. 1, pp. 227–231, doi: [10.1109/ICPADM.2003.1218394](https://doi.org/10.1109/ICPADM.2003.1218394).
- [39] S. W. Rowe, "G.I.S. disconnectors: A physical model for ground faulting," in Conference on Electrical Insulation & Dielectric Phenomena? Annual Report 1986, Nov. 1986, pp. 564–572, doi: [10.1109/CEIDP.1986.7726501](https://doi.org/10.1109/CEIDP.1986.7726501).
- [40] J. Chen et al., "Behavior Comparison of Metal Oxide Arrester Blocks When Excited by VFTO and Lightning," IEEE Trans. Electromagn. Compat., vol. 57, no. 6, pp. 1608–1615, Dec. 2015, doi: [10.1109/TEMC.2015.2450221](https://doi.org/10.1109/TEMC.2015.2450221).
- [41] P. Valsalal, S. Usa, and K. Udayakumar, "Response of metal oxide arrester in gas-insulated substation and methods to improve its dynamic characteristics," IET Sci. Meas. Technol., vol. 6, no. 4, p. 222, 2012, doi: [10.1049/iet-smt.2011.0051](https://doi.org/10.1049/iet-smt.2011.0051).
- [42] A. Tavakoli, A. Gholami, H. Nouri, and M. Negnevitsky, "Comparison Between Suppressing Approaches of Very Fast Transients in Gas-Insulated Substations (GIS)," IEEE Trans. Power Deliv., vol. 28, no. 1, pp. 303–310, Jan. 2013, doi: [10.1109/TPWRD.2012.2221748](https://doi.org/10.1109/TPWRD.2012.2221748).
- [43] J. V. G. Rama Rao, J. Amarnath, and S. Kamakshaiyah, "Simulation and experimental method for the suppressing of very fast transient over voltages in a 245kv gis using ferrite rings," in 2010 International Conference on High Voltage Engineering and Application, Oct. 2010, pp. 128–131, doi: [10.1109/ICHVE.2010.5640847](https://doi.org/10.1109/ICHVE.2010.5640847).
- [44] J. Smajic, W. Halaus, A. Troeger, S. Burow, R. Brandl, and S. Tenbohlen, "HF Resonators for Damping of VFTs in GIS," in International Conference on Power Systems Transients, 2011.
- [45] J. Smajic, A. Shoory, S. Burow, W. Halaus, U. Riechert, and S. Tenbohlen, "Simulation-based design of HF resonators for damping very fast transients in GIS," IEEE Trans. Power Deliv., vol. 29, no. 6, pp. 2528–2533, 2014, doi: [10.1109/TPWRD.2014.2330757](https://doi.org/10.1109/TPWRD.2014.2330757).

- [46] IEEE Power and Energy Society, "IEEE Guide for Safety in AC Substation Grounding," IEEE Std 80-2013 (Revision IEEE Std 80-2000/ Inc. IEEE Std 80-2013/Cor 1-2015), no. February, pp. 1–226, 2013, doi: [10.1109/IEEESTD.2015.7109078](https://doi.org/10.1109/IEEESTD.2015.7109078).
- [47] G. L. Ford and L. A. Geddes, "Transient Ground Potential Rise in Gas Insulated Substation - Assessment of Shock Hazard," IEEE Power Eng. Rev., vol. PER-2, no. 10, pp. 23–24, Oct. 1982, doi: [10.1109/MPER.1982.5519875](https://doi.org/10.1109/MPER.1982.5519875).
- [48] N. Fujimoto, E. P. Dick, S. A. Boggs, and G. L. Ford, "Transient Ground Potential Rise in Gas Insulated Substations - Experimental Studies," IEEE Power Eng. Rev., vol. PER-2, no. 10, pp. 21–22, Oct. 1982, doi: [10.1109/MPER.1982.5519873](https://doi.org/10.1109/MPER.1982.5519873).
- [49] M. M. Rao, M. J. Thomas, and B. P. Singh, "Electromagnetic field emission from gas-to-air bushing in a GIS during switching operations," IEEE Trans. Electromagn. Compat., vol. 49, no. 2, pp. 313–321, 2007, doi: [10.1109/TEMC.2007.8933334](https://doi.org/10.1109/TEMC.2007.8933334).
- [50] W. Ruan, F. P. Dawalabi, and J. Ma, "Study of Transient Ground Potential Rise in Gas-Insulated Substations During Fault Conditions Using Electromagnetic Field and Circuit Theory Approaches," in Proceedings of the Third IASTED International Conference on Power and Energy System, 2000.
- [51] Safe Engineering Services & Technologies ltd., "CDEGS - Current Distribution, Electromagnetic Fields, Grounding and Soil Structure Analysis." Canada.
- [52] Y. Cai, Y. Guan, and W. Liu, "Measurement of transient enclosure voltage in a 220kV gas insulated substation," in 2015 IEEE International Instrumentation and Measurement Technology Conference (I2MTC) Proceedings, May 2015, pp. 115–120, doi: [10.1109/I2MTC.2015.7151250](https://doi.org/10.1109/I2MTC.2015.7151250).
- [53] S. Okabe, J. Takami, and K. Nojima, "Phenomena of leaking electromagnetic waves and high frequency surges from isolated joint of gas insulated switchgear," IEEE Trans. Dielectr. Electr. Insul., vol. 15, no. 4, pp. 1006–1014, Aug. 2008, doi: [10.1109/TDEI.2008.4591221](https://doi.org/10.1109/TDEI.2008.4591221).
- [54] K. Chandrakar and R. S. Gorayan, "Analysis and control of transient enclosure voltages in GIS (EMTP simulation studies)," in 2013 Annual IEEE India

- Conference (INDICON), Dec. 2013, pp. 1–6, doi: [10.1109/INDCON.2013.6726041](https://doi.org/10.1109/INDCON.2013.6726041).
- [55] J. Lewis, *Earthing of GIS - An Application Guide*. CIGRE, 1993.
- [56] C. F. Dalziel, “A Study of the Hazards of Impulse Currents,” *Trans. Am. Inst. Electr. Eng. Part III Power Appar. Syst.*, vol. 72, no. 2, Jan. 1953, doi: [10.1109/AIEEPAS.1953.4498738](https://doi.org/10.1109/AIEEPAS.1953.4498738).
- [57] E. P. Dick, A. Naderian, and E. Petrache, “Transient earth potential rise in gas insulated substations,” in *2016 Down to Earth Conference (DTEC)*, Sep. 2016, pp. 1–9, doi: [10.1109/DTEC.2016.7731290](https://doi.org/10.1109/DTEC.2016.7731290).
- [58] CIGRE, “Monograph on GIS Very Fast Transients,” WG 33/13-09, 1988.
- [59] J. He, R. Zeng, and B. Zhang, *Methodology and Technology for Power System Grounding*. 2012.
- [60] P. J. Coetzee, “A technique to determine the electromagnetic properties of soil using moisture content,” *S. Afr. J. Sci.*, vol. 110, no. 5/6, pp. 1–4, May 2014, doi: [10.1590/sajs.2014/20130225](https://doi.org/10.1590/sajs.2014/20130225).
- [61] R. Morrison, *Grounding and shielding : circuits and interference*, 6th ed. Wiley, 2016.
- [62] K. Chandrakar and R. S. Gorayan, “Analysis of Transient Enclosure Voltages in GIS (EMTP Simulation Studies),” *Int. J. Res. Eng. Technol.*, vol. 02, no. 02, pp. 120–125, 2013, doi: [10.15623/ijret.2013.0202006](https://doi.org/10.15623/ijret.2013.0202006).
- [63] C. M. Wiggins and S. E. Wright, “Switching transient fields in substations,” *IEEE Trans. Power Deliv.*, vol. 6, no. 2, pp. 591–600, Apr. 1991, doi: [10.1109/61.131116](https://doi.org/10.1109/61.131116).
- [64] CIGRE WG C4.501, “TB 543: Guide for Numerical Electromagnetic Analysis methods: Application to surge phenomena and comparison with circuit theory-based approach,” 2013.
- [65] H. Dommel, “EMTP - ElectroMagnetic Transients Program.” Bonneville Power Administration, Portland, Oregon, 1984.
- [66] Bin Liu, Yue Tong, Xiao-pin Deng, and Xiang-xiang Feng, “Measuring of very fast transient overvoltage and very fast transient current generated by disconnector operating,” in *2014 International Conference on Power System*

- Technology, Oct. 2014, pp. 1349–1354, doi: [10.1109/POWERCON.2014.6993660](https://doi.org/10.1109/POWERCON.2014.6993660).
- [67] Y. Gongchang, L. Weidong, C. Weijiang, G. Yonggang, and L. Zhibing, “Development of Full Frequency Bandwidth Measurement of VFTO in UHV GIS,” *IEEE Trans. Power Deliv.*, vol. 28, no. 4, pp. 2550–2557, Oct. 2013, doi: [10.1109/TPWRD.2013.2267781](https://doi.org/10.1109/TPWRD.2013.2267781).
- [68] J. Wang et al., “Laboratory and on-site measurements of TEV generated by disconnecter switching in 362 kV GIS,” *Conf. Rec. IEEE Int. Symp. Electr. Insul.*, vol. 2, pp. 681–684, 1998, [Online]. Available: <https://www.engineeringvillage.com/>
- [69] J. Meppelink, K. Diederich, K. Feser, and W. Pfaff, “Very fast transients in GIS,” *IEEE Trans. Power Deliv.*, vol. 4, no. 1, pp. 223–233, 1989.
- [70] W. Hauschild and E. Lemke, *High-Voltage Test and Measuring Techniques*. Berlin, Heidelberg: Springer Berlin Heidelberg, 2014.
- [71] C. Hewson and W. R. Ray, “The effect of electrostatic screening of Rogowski coils designed for wide-bandwidth current measurement in power electronic applications,” in *2004 IEEE 35th Annual Power Electronics Specialists Conference (IEEE Cat. No.04CH37551)*, pp. 1143–1148, doi: [10.1109/PESC.2004.1355583](https://doi.org/10.1109/PESC.2004.1355583).
- [72] S. Ogawa, E. Haginomori, S. Nishiwaki, T. Yoshida, and K. Terasaka, “Estimation of Restriking Transient Overvoltage on Disconnecting Switch for GIS,” *IEEE Trans. Power Deliv.*, vol. 1, no. 2, pp. 95–102, 1986, doi: [10.1109/TPWRD.1986.4307939](https://doi.org/10.1109/TPWRD.1986.4307939).
- [73] M. Szewczyk, K. Kutorasinski, M. Wronski, and M. Florkowski, “Full-Maxwell Simulations of Very Fast Transients in GIS: Case Study to Compare 3D and 2D-Axisymmetric Models of 1100 kV Test Set-Up,” *IEEE Trans. Power Deliv.*, pp. 1–1, 2016, doi: [10.1109/TPWRD.2016.2527823](https://doi.org/10.1109/TPWRD.2016.2527823).
- [74] H. Xue, A. Ametani, J. Mahseredjian, Y. Baba, F. Rachidi, and I. Kocar, “Transient Responses of Overhead Cables Due to Mode Transition in High Frequencies,” *IEEE Trans. Electromagn. Compat.*, vol. 60, no. 3, pp. 785–794, Jun. 2018, doi: [10.1109/TEMC.2017.2737439](https://doi.org/10.1109/TEMC.2017.2737439).

- [75] W. Boeck, J. Gorablenkow, G. F. Luxa, L. Menten, and W. Taschner, Insulating behaviour of SF6 with and without insulation in case of fast transients. Cigre, 1986.
- [76] S. Okabe et al., “Simulation of propagation characteristics of higher order mode electromagnetic waves in GIS,” *IEEE Trans. Dielectr. Electr. Insul.*, vol. 13, no. 4, pp. 855–861, Aug. 2006, doi: [10.1109/TDEI.2006.1667746](https://doi.org/10.1109/TDEI.2006.1667746).
- [77] J. James, M. Albano, D. Clark, D. Guo, and A. M. Haddad, “Analysis of Very Fast Transients Using Black Box Macromodels in ATP-EMTP,” doi: [10.3390/en13030698](https://doi.org/10.3390/en13030698).
- [78] E. F. Vance, “Electromagnetic-Pulse Handbook for Electric Power Systems,” United States, 1975.
- [79] D. J. Griffiths, *Introduction to electrodynamics*, 3rd ed. Prentice Hall, 1999.
- [80] COMSOL inc, “RF Module User’s Guide, Version 5.5.” 2019.
- [81] F. Rachidi and S. Tkachenki, *Electromagnetic Field Interaction with Transmission Lines*. Magdeburg: WIT Press, 2008.
- [82] N. Theethayi, R. Thottappillil, Y. Liu, and R. Montano, “Important parameters that influence crosstalk in multiconductor transmission lines,” *Electr. Power Syst. Res.*, vol. 77, no. 8, pp. 896–909, Jun. 2007, doi: [10.1016/J.EPSR.2006.06.014](https://doi.org/10.1016/J.EPSR.2006.06.014).
- [83] “COMSOL Multiphysics® v. 5.6.” <https://www.comsol.com/release/5.6>.
- [84] T. Schaich, D. Molnar, A. Al Rawi, and M. Payne, “Analytic modelling of a planar Goubau line with circular conductor,” *Sci. Reports* 2020 101, vol. 10, no. 1, pp. 1–10, Nov. 2020, doi: [10.1038/s41598-020-77703-w](https://doi.org/10.1038/s41598-020-77703-w).
- [85] L. Grcev and F. Dawalibi, “An electromagnetic model for transients in grounding systems,” *IEEE Trans. Power Deliv.*, vol. 5, no. 4, pp. 1773–1781, 1990, doi: 10.1109/61.103673.
- [86] “Technical Specification - TS 3.01.02,” 2014.
- [87] A. Ametani, *Numerical Analysis of Power System Transients and Dynamics*, vol. 1. The Institution of Engineering and Technology, 2015.
- [88] J. A. Martinez-Velasco, *Power system transients : parameter determination*. CRC Press/Taylor & Francis Group, 2010.

- [89] E. Haginomori, T. Koshiduka, J. Arai, and H. Ikeda, Power system transient analysis : theory and practice using simulation programs (ATP-EMTP). Wiley, 2016.
- [90] D. Hang, L. Xiaofan, and Z. Weidong, “Simulation of VFTO by ATP/EMTP with Various Arc Models,” doi: [10.4028/www.scientific.net/AMM.602-605.245](https://doi.org/10.4028/www.scientific.net/AMM.602-605.245).
- [91] L. G. Christophorou and I. Sauers, Eds., Gaseous Dielectrics VI. Boston, MA: Springer US, 1991.
- [92] R. Papazyan, P. Pettersson, H. Edin, R. Eriksson, and U. Gafvert, “Extraction of high frequency power cable characteristics from S-parameter measurements,” IEEE Trans. Dielectr. Electr. Insul., vol. 11, no. 3, pp. 261–270, 2004, doi: [10.1109/TDEI.2004.1306724](https://doi.org/10.1109/TDEI.2004.1306724).
- [93] M. J. Degerstrom, B. K. Gilbert, and E. S. Daniel, “Accurate resistance, inductance, capacitance, and conductance (RLCG) from uniform transmission line measurements,” in 2008 IEEE-EPEP Electrical Performance of Electronic Packaging, Oct. 2008, pp. 77–80, doi: [10.1109/EPEP.2008.4675881](https://doi.org/10.1109/EPEP.2008.4675881).
- [94] “MATLAB R2019a.” The MathWorks inc., Natick, Massachusetts, 2019.
- [95] J. James, M. Albano, D. Guo, and A. M. Haddad, “Application of Multiple Modelling Techniques for Analysis of Very Fast Transient Overvoltages in GIS,” IEEE Dielectr. Electr. Insul. Eng., 2018, doi: [10.1109/ICHVE.2018.8642189](https://doi.org/10.1109/ICHVE.2018.8642189).
- [96] B. Gustavsen, “Computer code for rational approximation of frequency dependent admittance matrices,” IEEE Trans. Power Deliv., vol. 17, no. 4, pp. 1093–1098, Oct. 2002, doi: [10.1109/TPWRD.2002.803829](https://doi.org/10.1109/TPWRD.2002.803829).
- [97] ABB, “Type EXLIM-P Surge Arresters.”, Available online: <https://library.e.abb.com/public/>
- [98] Classified author, “Surge Counter Investigation Report,” 2012.
- [99] Classified author, “400kV S/S Surge counter Report,” 2018.
- [100] A. Haddad, J. Fuentes-Rosado, D. M. German, and R. T. Waters, “Characterisation of ZnO surge arrester elements with direct and power frequency voltages,” IEE Proc. A (Physical Sci. Meas. Instrumentation, Manag. Educ., vol. 137, no. 5, pp. 269–279, Sep. 1990, doi: [10.1049/ip-a-2.1990.0043](https://doi.org/10.1049/ip-a-2.1990.0043).

- [101] Classified author, “ PD coupler constructional arrangement. Drawing NO H2P7472,” 2008.
- [102] “Advanced Design System.” Keysight, 2017, [Online]. Available: <http://edadownload.software.keysight.com/>(accessed on 3 February 2020).
- [103] “Modelithics v18.1.” Modelithics inc, Tampa, Florida, [Online]. Available: <https://www.modelithics.com/>.
- [104] J. Wang, J. Yang, and R. Luo, “Non-contact transient high-voltage measurement with self-integrating D-dot probe,” *Int. J. Appl. Electromagn. Mech.*, vol. 47, no. 3, pp. 837–845, Mar. 2015, doi: [10.3233/JAE-140111](https://doi.org/10.3233/JAE-140111).
- [105] “Prodyn Technologies, Home of High Quality EM Sensors » D-Dots (Electric Field Sensors).”, Available online: <http://www.prodyntech.com/>(accessed Oct. 10, 2018).
- [106] J. Wang, W. Ding, and A. Qiu, “Capacitive sensor for fast pulsed voltage monitor in transmission line,” *Rev. Sci. Instrum.*, vol. 90, no. 3, p. 035107, Mar. 2019, doi: [10.1063/1.5050276](https://doi.org/10.1063/1.5050276).
- [107] CIGRE WG 1.60, “Traceable measurement techniques for very fast transients,” 2016.
- [108] D. M. Pozar, *Microwave engineering*. USA: John Wiley & Sons, Ltd, 2012.
- [109] J. Smajic, *NAFEMS - How to perform Electromagnetic Finite Element Analysis?* 2016.
- [110] J. M. Jin, *Theory and Computation of Electromagnetic Field*. John Wiley and Sons, 2010.
- [111] “Using Perfectly Matched Layers and Scattering Boundary Conditions for Wave Electromagnetics Problems | COMSOL Blog.” www.comsol.com (accessed Mar. 08, 2022).
- [112] A. Morched, B. Gustavsen, and M. Tartibi, “A universal model for accurate calculation of electromagnetic transients on overhead lines and underground cables,” *IEEE Trans. Power Deliv.*, vol. 14, no. 3, pp. 1032–1038, Jul. 1999, doi: [10.1109/61.772350](https://doi.org/10.1109/61.772350).

- [113] British Standards Institution., “BS EN 60071-4:2004 - Insulation co-ordination - Part 4:Computational guide to insulation co-ordination and modelling of electrical networks,” 2004.
- [114] B. Gustavsen and A. Semlyen, “Rational approximation of frequency domain responses by vector fitting,” *IEEE Trans. Power Deliv.*, vol. 14, no. 3, pp. 1052–1061, Jul. 1999, doi: [10.1109/61.772353](https://doi.org/10.1109/61.772353).
- [115] S. Grivet-Talocia and B. Gustavsen, *Passive macromodeling*. Hoboken, NJ, USA: Wiley, 2015.
- [116] S. Boyd, V. Balakrishnan, and P. Kabamba, “A bisection method for computing the H_∞ norm of a transfer matrix and related problems,” *Math. Control. Signals, Syst.*, vol. 2, no. 3, pp. 207–219, Sep. 1989, doi: [10.1007/BF02551385](https://doi.org/10.1007/BF02551385).
- [117] A. Semlyen and B. Gustavsen, “A Half-Size Singularity Test Matrix for Fast and Reliable Passivity Assessment of Rational Models,” *IEEE Trans. Power Deliv.*, vol. 24, no. 1, pp. 345–351, Jan. 2009, doi: [10.1109/TPWRD.2008.923406](https://doi.org/10.1109/TPWRD.2008.923406).
- [118] B. Gustavsen, “Fast Passivity Enforcement for Pole-Residue Models by Perturbation of Residue Matrix Eigenvalues,” *IEEE Trans. Power Deliv.*, vol. 23, no. 4, pp. 2278–2285, Oct. 2008, doi: [10.1109/TPWRD.2008.919027](https://doi.org/10.1109/TPWRD.2008.919027).
- [119] P. Triverio et al., “Stability, Causality, and Passivity in Electrical Interconnect Models,” 2007, doi: [10.1109/TADV.2007.901567](https://doi.org/10.1109/TADV.2007.901567).
- [120] Jianfang Zhu and Dan Jiao, “Fast Full-Wave Solution That Eliminates the Low-Frequency Breakdown Problem in a Reduced System of Order One,” *IEEE Trans. Components, Packag. Manuf. Technol.*, vol. 2, no. 11, pp. 1871–1881, Nov. 2012, doi: [10.1109/TCPMT.2012.2203135](https://doi.org/10.1109/TCPMT.2012.2203135).

10 APPENDICES

A - RELEVANT PARAMETERS WHEN INVESTIGATING ELECTROMAGNETIC WAVE PROBLEMS	213
B - NUMERICAL ELECTROMAGNETIC ANALYSIS	216
C - CIRCUIT BASED MODELLING FOR VFTs AND TEVs IN ATP-EMTP	220
D - DISCONNECTOR 'MODELS' CODE	224
E - GIS FINITE ELEMENT MODEL CONVERSION TO BLACKBOX MACROMODELS	234
F - DATA ACQUISITION AND CALIBRATION TECHNIQUES	236
G - FURTHER MEASUREMENT RESULTS	238

A - RELEVANT PARAMETERS WHEN INVESTIGATING ELECTROMAGNETIC WAVE PROBLEMS

VFTs and TEVs can reach extremely high magnitudes and the threats to insulation are obvious. These threats need to be studied in detail. To study VFTs and TEVs effectively, concepts need to be utilised from multiple engineering disciplines. The frequencies involved are more commonly associated RF or EMC engineering and thus it makes sense to investigate the propagation and coupling aspects using methodology more common to those disciplines. For example, grounding, at least in the traditional sense, is not completely relevant, VFTs and TEVs propagate as waves and a ground can no longer be considered as a remote point far away, it be any metallic structure or resistive medium. Also, given the broad spectrum associated, awareness of near field and far field behaviour is required. Some of the parameters and concepts that are necessary for a full understanding of very high frequency electromagnetic phenomenon are presented to aid explanations in further sections.

When describing transmission and reflection of electromagnetic waves at high frequencies, where voltages and currents are not easily quantifiable, scattering parameters (S-parameters) are commonly used [108]. S-parameters, such as the two port S-parameters shown in Equation A.1, are matrices that hold the complex transmission and reflection coefficients, fully describing the transmission line effects over any frequency range, in terms of magnitude and phase.

$$\begin{bmatrix} b_1 \\ b_2 \end{bmatrix} = \begin{bmatrix} S_{11} & S_{12} \\ S_{21} & S_{22} \end{bmatrix} \quad (\text{A.1})$$

For a two port device, S11 and S22 represent the reflection coefficients at ports 1 and 2 respectively (also termed return loss), whereas S12 and S21 are the transmission coefficients for one port to another (also termed insertion loss) and are in most cases reciprocal. A one port device has only reflection coefficients. S-parameters have no units but are often expressed in dB. S-parameters are also straight-forward to convert to other forms including Z, Y and ABCD parameters. One port S-parameters can be converted to input impedance using Equation A.2.

$$Z_{in} = \frac{S_{11} * Z_c + Z_c}{1 + S_{11}} \quad (\text{A.2})$$

Impedance has multiple interpretations when considering high frequencies. When modelling a transmission line approximation for a transient study or to energise a port within a finite element model, the characteristic impedance of a line, cable or bus, calculated according to Equation A.3, is an important parameter when modelling for high frequency transient studies. The characteristic impedance of a conductor is based on its geometry and material characteristics at a specific location. For an infinite line without discontinuities the characteristic impedance equals the input impedance. If considered lossless, the characteristic impedance can be simplified to Equation A.4 and considered as a function of the geometry and space only. When a wave is propagating between a conductor and its return path, changes in characteristic impedance are points in which reflections occur. To evaluate the characteristic impedance, assuming a conductor/return path extends to infinity, the line integral of the electric field between a conductor and ground or two conductors (voltage) is divided by the line integral of the magnetic field following a closed loop around or between conductors (current), as shown in Equation A.5.

$$Z_c = \sqrt{\frac{R + j\omega L}{G + j\omega C}} \quad (\text{A.3})$$

$$Z_c = \sqrt{\frac{L}{C}} \quad (\text{A.4})$$

$$Z = \frac{-\int E \, dl}{\oint H \, dl} \quad (\text{A.5})$$

The harmonic grounding impedance is the ratio of peak voltage and current seen at a point looking into a system at a specific frequency, as shown in Equation A.6. Evaluation of the harmonic grounding impedance of a system provides a clear indication of its response over the frequency range, identifying possible resonances in the system. Magnitude and phase characteristics are conserved. There are many variations of the harmonic input impedance, for understanding the impedance of a transmission line, including resonances, Equation A.7 applies.

$$Z(\omega) = \frac{V(\omega)}{I(\omega)} \quad (\text{A.6})$$

$$Z(\omega) = Z_0 * \tanh(\gamma l) \quad (\text{A.7})$$

The transient impedance is considered the only accurate unit of measurement for characterisation of a grounding system under high frequency surges [46], usually applied to the characterisation of grounding systems. There are two definitions that exist for the characterisation of the transient impedance: impulse impedance and surge impedance. The impulse grounding impedance is defined as the ratio of the peak voltage across a device to the peak current injected at the origin of the grounding device [59], as given in Equation A.8.

$$Z_{impulse} = \frac{V_{peak}}{I_{peak}} \quad (\text{A.8})$$

The surge impedance, is defined as the ratio of the instantaneous voltage and current, as given in Equation A.9(A.9)[4].

$$Z(t) = \frac{V(t)}{I(t)} \quad (\text{A.9})$$

An essential parameter for describing the propagation of an electromagnetic wave is the propagation constant. It is a complex quantity describing the attenuation and phase change along a conductor, as shown in Equation A.10. The phase constant is also used to extract the velocity of the mode and the effective mode index.

$$\gamma = \alpha + j\beta \quad (\text{A.10})$$

The effective mode index is ratio of the wavenumber of free space and the phase constant of a propagation mode as shown in Equations A.11 and A.12. It used in mode analysis as the basis for a mode search. For a strictly TEM mode in a lossless system, the calculated phase constant is equal to the wavenumber of free space (k_0), i.e., an effective mode index of 1. The effective mode index scales with the square of the relative permittivity [83].

$$\eta_{eff} = \frac{k_0}{\beta} \quad (\text{A.11})$$

$$k_0 = \frac{2\pi}{\lambda} \quad (\text{A.12})$$

B - NUMERICAL ELECTROMAGNETIC ANALYSIS

Field-theory based methods, known collectively as Numerical Electromagnetic Analysis, can be adopted for further insight into high frequency electromagnetic phenomenon. NEA methods for high frequency studies solve full Maxwell's Equations, through the solution of the wave equation or a derivation there of, providing invaluable information about wave propagation and field interactions for arbitrary complex, or simplified geometries and material characteristics. Results are elucidated through vector or contour plots, and data can be readily extracted for analysis.

NEA methods are computationally demanding, making it quite challenging to analyse the interaction between components and larger systems. For this reason, NEA can also be used for the extraction of equivalent electrical parameters for discrete elements of an electrical system for representation using circuit-based methods. NEA methods are also not subject to the same limitations and assumptions as with traditional EMTs, particularly with regards to solving for the higher order propagation modes that are possible at very high frequencies. Some NEA methods such as the method of moments, permit only the representation of relatively basic structures, whereas techniques like FEM and FDTD allow more complex geometries to be simulated.

The finite element method, more specifically, vector FEM, has a distinct advantage over other numerical methods due to its flexibility in handling complex geometries and isotropic or anisotropic material characteristics. It can be applied to both linear and non-linear 2D and 3D problems.

FEM is a numerical method of finding approximate solutions for a given boundary value problem (BVP), i.e. a set of second order PDEs and boundary conditions describing a specific set of physics.

FEM involves the discretisation of an equivalent integral form (weak form) of a BVP. The weak form of a BVP is formulated using either the variational method (Ritz method) or the weighted residual method (Galerkin's method) [109]. For a 3D vector electromagnetic wave problem, a weak form of the wave equation shown in Equation (B.1) is solved. A weak form obtained by the variational method is shown in Equation (B.2) [109]. The solution of the wave equation provides details of forward and reflected, propagating waves.

The wave equation is formulated for the electric field due to the convenience of imposing boundary conditions for the electric field on conducting surfaces, however, the magnetic field is found through constitutive relations.

$$\nabla \times \mu_r^{-1}(\nabla \times \bar{E}) - k_0^2(\epsilon_r - \frac{j\sigma}{\epsilon_0\omega})\bar{E} = \mathbf{0} \quad (\text{B.1})$$

$$\begin{aligned} & \frac{1}{2} \iiint \left[\frac{1}{\mu_r} (\nabla \times \bar{E}) \cdot (\nabla \times \bar{E}) - k_0^2 \epsilon_r \bar{E} \cdot \bar{E} \right] dV \\ & + \iint \left[jk_0 \sqrt{\frac{\epsilon_r}{\mu_r}} (\mathbf{n} \times \bar{E}) \cdot (\mathbf{n} \times \bar{E}) + 2jk_0 \sqrt{\frac{\epsilon_r}{\mu_r}} \bar{E} \cdot \bar{E}_{inc} \right] dS \end{aligned} \quad (\text{B.2})$$

Discretisation is achieved through meshing. A mesh consists primarily of triangular or tetrahedral elements which divide a component into much smaller elements. The finite element method solution is computed by solving a weak form of the equation over all elements. The equations across each element are known as shape functions [83]. Shape functions are usually of linear, cubic or quadratic type. Higher order elements, such as the quadratic shape function, provide a more accurate result, at the cost of additional computational resource. Mesh elements have additional nodes, the number of which depend on the shape function. The product of the number of elements, number of nodes and the number of unknowns is known as the number of degrees of freedom (DoF). The number of DoF will give some indication of the size of the problem and the computational requirements needed to solve. The overall process results in a large system of linear equations which can be solved numerically.

When it comes to defining a mesh, for wave problems, merely achieving a good geometric representation and high resolution across material domains is not sufficient. To achieve an accurate solution, the number of elements required also depend on the wavelengths present. Generally, a minimum of six elements are required across the smallest wavelength under analysis. Consideration of the wavelengths in lossy materials must be given, as discussed in a later section.

As the finite element method solves a BVP, appropriate boundary conditions are required to provide a known quantity and truncate or simplify the modelling domain. The perfect electric conductor shown in Equation (B.3) forces the tangential component of the electric field to zero. The PEC is usually used to represent a lossless conductor or

return path, however it can also be used to impose symmetry for magnetic fields if exploiting symmetries in models to reduce the computation requirements.

$$\bar{n} \times \bar{E} = 0 \quad (\text{B.3})$$

The perfect magnetic conductor boundary condition, shown in Equation (B.4) sets the tangential magnetic field and surface current to zero, enforcing a very high impedance boundary. The PMC boundary can also impose symmetry for electric fields.

$$\bar{n} \times \bar{H} = 0 \quad (\text{B.4})$$

An impedance boundary condition, expressed in Equation (B.5) can account for conductor/material losses without the need to mesh the conductor.

$$\sqrt{\frac{\mu_r}{\epsilon_r - j\sigma/\omega}} \bar{n} \times \bar{H} + \bar{E} - (\bar{n} \cdot \bar{E})\bar{n} = (\bar{n} \cdot \bar{E}_s)\bar{n} - \bar{E}_s \quad (\text{B.5})$$

When considering the boundaries of a model it is essential that unintentional reflection of waves does not occur as the accuracy of the solution is degraded. A PML is essentially an additional domain surrounding a modelling domain to mimic an open boundary. A PML adds attenuating domains so that reflections, regardless of frequency, mode or incident angle are significantly reduced [110], through stretching the coordinate system in the defined area.

A scattering boundary, described by Equation (B.6) is an alternative method to a PML, for the prevention of reflections from incident plane waves. A scattering boundary is not as effective as a PML for higher incident angles, however reflections are considerably attenuated [111]. Scattering boundaries can also be used to excite an electric or magnetic field with varying incidence.

$$n \times (\nabla \times \bar{E}) - jkn \times (\bar{E} \times \bar{n}) - \frac{1}{2jk_0} \nabla \times (\bar{n}\bar{n} \cdot (\nabla \times \bar{E})) = 0 \quad (\text{B.6})$$

Numerous other boundary conditions exist, but of the remaining, a noteworthy boundary is the port boundary. A port boundary can provide excitation of a model or terminate a model according to a specified impedance and mode, via eigenmode analysis. A port boundary will automatically compute the S-parameter matrix based on the number of ports and the transmission and reflection between them. There are a number of port types within COMSOL, most of which require normalisation with a specified characteristic impedance. A numeric port will compute the characteristic mode

of the fields in plane, searching for modes around a specified mode index or range. Ports can be combined with a PML to absorb other modes.

Finite element analysis permits eigenvalue analysis of arbitrary geometries, for the purpose of the identification of propagation modes (eigenmode analysis/modal analysis) or resonances (eigenfrequency analysis). Eigenfrequency analysis is useful for calculating the natural resonant points of cavities. The GIS has apertures throughout and eigenfrequency analysis may detect cavity resonances and antenna behaviour. Eigenmode analysis solves the wave equation for the complex propagation constant for a desired propagation mode. The eigenvalues of a solution are equal to complex propagation constants. Manual excitation of a model is not required, eigenmodes are calculated based on geometry, material characteristics and boundary conditions. As with modal analysis applied to the transmission line approximation, mode analysis can describe the fields between a conductor and its return path, however it is also used to find higher order modes of propagation.

Modes are identified according to their effective mode index, which related to the wavenumber and phase constant as shown in Equation (B.7). For TEM modes of propagation on lossless surfaces, the effective mode index is 1.

$$\eta_{eff} = \frac{k_0}{\beta} \quad (\text{B.7})$$

C - CIRCUIT BASED MODELLING FOR VFTS AND TEVS IN ATP-EMTP

Transmission line models

Due to the travelling wave nature of VFT, distributed parameter lines models are used not only to represent transmission lines, cables and even the GIB. Due to their stability and accuracy at lower frequencies, Bergeron models are often utilised. The Bergeron line model is initialised at a specified frequency and neglects frequency dependence.

It is possible to model the frequency dependent behaviour of transmission lines, traditionally through the use of J Marti, Noda or Semleyen. The J Marti and Semleyen are based on modal decomposition with a single transformation matrix initialised at a single frequency, therefore accuracy is affected. The Noda line model is a phase domain mode and there is therefore no concern over transformation matrices, however it relies on numerous curve fitting and recursive convolutions and can be numerically unstable, even at low frequencies. These line models, along with Carson's earth return theorem utilised from which outputs of the line and cable constants subroutines of LCC and cable constant routines are based, are reported to be unstable at very high frequencies, although, given the proposed decoupled propagation of internal VFTs and external TEVs, TLAs may be suitable for internal bus modelling only, provided numerical stability can be achieved.

TEV modelling

Oftentimes, advice provided in literature regarding the modelling for TEVs will suggest that the LCC routine can be used for this purpose of modelling the external GIB, incorporating the frequency dependent effects of ground resistivity on propagation velocity and attenuation. Furthermore it is advised that the consideration of an enclosure to ground propagation mode, ground straps and the earthing system all need to be considered [8].

As concluded in Chapter 3, care should be taken when considering using an EMT and more specifically TLAs when modelling for the purpose of TEVs. Using frequency dependent TLAs for TEVs is likely to lead to numerical error given the low frequency earth return theorems on which they are based. The Universal Line Model (ULM), While not available in ATP-EMTP standard library at present will perform far better at modelling TEVs. The ULM utilises vector fitting [112], to fit both transmission line

characteristic admittance and propagation matrices. A frequency dependent response is then included through Norton equivalent conductances using recursive convolution.

Gas to Air bushing

Modelling of a gas/air bushing would be dependent on type, gas filled or capacitively graded. A gas filled bushing could be simply represented by a gradually increasing surge impedance from that of the bus duct to the that of the transmission line. The model would consist of a number of transmission lines in series, each with varying surge impedance [8]. The lines should consider coupling to the enclosure and other losses (resistive, or radiated loss which result from coupling to adjacent structures). Advanced designs should also include the earthing system and any electrode shielding that is present [8]. The model for a capacitively graded bushing would require greater detail, with each grading element represented by its lumped or distributed parameters.

As the main source of coupling of internal VFTs and external Transient Enclosure Voltages (TEVs) [48], it is important to represent the bushing accurately. However, a simplified representation may be used in the absence of detailed information. In its simplest form, a gas filled bushing is simply represented as a gradual decrease in surge impedance from the impedance of the line/bus bar to the impedance of the Gas Insulated Bus (GIB), with the addition of a capacitance, representing the bushing capacitance to ground.

Overhead line tower geometry

Overhead lines (OHL) are also represented by their estimated geometrical characteristics using a LCC routines. The associated L6 tower models shown in Figure C.1 are also included for completeness. The first ten L6 towers are approximated as a conical tower with varying surge impedance according to height, as suggested in [88]. The remaining ~81km of overhead lines are represented as a single line. To avoid error, lines of significant length, modelled using the LCC routine, this final long line has to be initialised at a low frequency. In between each span the tower geometry must be modelled, due to its connection to the earthwire. For high frequency studies. as a minimum, transmission towers are modelled according to their characteristic

impedances at varying heights. The coupling between each phase-crossarm is modelled as a capacitance

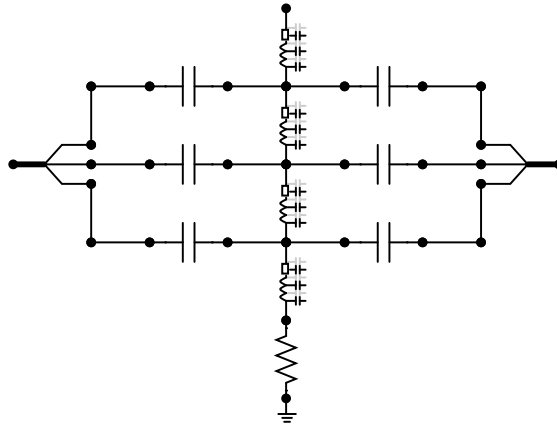


Figure C.1: L6 Tower representation.

Transformer model

A basic model of a power transformer considers only its capacitance to ground [15]. However, greater accuracy can be achieved by considering the frequency response of the transformer [113]. Where the transfer of surges onto the secondary winding are of concern, a far greater level of detail is required which should include inter-winding capacitances and secondary capacitance to earth [8].

Ground straps/download leads

A ground strap is characterised by a varying surge impedance along its vertical length. This can be achieved by dividing the ground strap into a number of sections, each with its own surge impedance in a similar fashion as the gas filled bushing [17]. A number of ground strap models were compared by Fujimoto et al. [48], each with varying complexity. It was found that a basic inductor model was adequate for straps with travel time less than the impulse rise time, while a non-uniform surge impedance more applicable for longer straps. This variation of surge impedance will lead to continuous reflections for the length of the strap. Analytically, a ground strap can be simplified by subdividing its length and calculating the value of characteristic impedance at the midpoint of each segment. More accurate download models are explored in Chapter 3 and 4.

Earthing system

At high frequencies, an earthing system has a complicated frequency dependence. Impedance of the electrode and soil resistivity/permittivity varies significantly over the frequency range. In addition to frequency, soil parameters can vary according to water content and structure and possibly current magnitude (soil ionisation). Due to this complexity, the earthing grid is often simplified in EMTP studies as a simple resistance, a series LC with parallel conductance branch or distributed parameter line [8].

D - DISCONNECTOR 'MODELS' CODE

DATA

Sop {dflt:0} -- switching operation 0 = opening 1=closing
Top {dflt:0.1}-- time start switching operation
eta {dflt:1}-- degree of field uniformity
p {dflt:5}-- pressure [bar]
gap {dflt:0.15}-- gap distance max [m]
Emax {dflt:89000}-- max critical field [kV/cm*bar]
spd {dflt:0.1}-- speed of operation [m/s]
arctmin {dflt:1e-6} --arcing time min
ichop1 {dflt:0}-- power freq chopping current
ichop2 {dflt:0}-- high freq chopping current
bdtime {dflt:20e-9} -- desired breakdown time in nanoseconds

INPUT

v1 {dflt:0}-- source voltage [V]
v2 {dflt:0}-- TCV [V]
-- current {dflt:0} -- current through TACS resistance

VAR

RA1 -- TACS controlled arc resistance
RE -- max arc resistance
Tau -- arc exponential decay constant
dst -- gap distance start of operation
den -- gap distance at end of operation
Vbc -- breakown voltage close

Vbcn -- negative breakdown voltage close
vbo -- breakdown voltage open
vbon -- negative breakdown voltage open
dcl --distance during closing
dop -- distance during opening
va -- input voltage
vb -- output voltage
narc1 -- current number of breakdowns
switcht -- actual time since start of switching
state -- 0 = open 1 = moving no arc 2 = arcing 3 = closed
arcing -- DS condition arcing
noarcclosing -- DS condition no arc
extinguish -- DS condition arc extinguished
noarcopening -- DS condition no arc
swclosed -- DS condition closed
swopening --DS condition opening
arct -- time start of arc
startarct -- time at start of arcing phase
vcon --
VbcalO -- final breakdown voltage opening
VbcalC -- final breakdown voltage closing
-- ds3ph --

OUTPUT

RA1 -- TACS controlled arc resistance [Ohms]--

HISTORY

RA1 {dflt:0}

-- current {dflt:0}

v1 {dflt:0}-- source voltage [V]

v2 {dflt:0}-- TCV [V]

-- ds3ph {dflt:0}

INIT

RE:=1E30

Tau:=0.6e-9/(20e-9/bdtime)

Vbc:=4e6

Vbcn:=-4e6

vbo:=155e3

vbon:=-155e3

dop:=0

dcl:=gap

va:=v1

vb:=v2

narc1:=0

arct:=0

switcht:=0

startarct:=0

Vbcalo:=0

Vbcalc:=0

IF Sop=0 THEN

dst:=0

```

den:=gap
state:=3 -- closed initially --
RA1:=0
ELSE
dst:=gap
den:=0
state:=0 --open initially --
RA1:=RE
ENDIF

ENDINIT

EXEC

--errors
IF bdtme>100e-9 OR bdtme<1e-9 THEN
ERROR
write('Simulation Error - Breakdown time (bdtme) must be between 1ns - 100ns');
STOP
ENDIF

IF timestep>bdtme*0.2 THEN
ERROR
write('Simulation Error - reduce simulation timestep to less than'bdtme*0.2!')
STOP
ENDIF

```

```
vcon:=abs(v1-v2)
```

```
IF Sop=0 AND
```

```
  t>Top THEN
```

```
    dop:= spd*(t-Top)
```

```
    --
```

```
    IF dop>gap THEN
```

```
      dop:=gap
```

```
    ENDIF
```

```
    --
```

```
    IF dop=0 THEN
```

```
      state:=3 --closed initially
```

```
    ENDIF
```

```
    --
```

```
ELSE
```

```
  dop:=0
```

```
ENDIF
```

```
--
```

```
Vbo:=(Emax*p*eta*dop)*1000
```

```
VbcalO:=(Emax*p*eta*gap)*1000
```

```
Vbon:=-Vbo
```

```
--
```

```
IF t>Top AND Sop=0 THEN -- start of DS state loop
```

```
  arcing:=false
```

```

noarcopening:=false

extinguish:=false

swopening:=false

--

IF state=0 THEN --if switch open
    RA1:=RE -- max resistance no arc
    noarcopening:=true

ELSIF state=1 THEN

    IF Vbo<abs(v1-v2) THEN
        narc1:=narc1+1
        arcing:=true

    ENDIF

ELSIF state=2 THEN
    arct:=arct+timestep
    startarct:=backtime(arct, 0)
    RA1:= 0.5+RE*exp(-(t-startarct)/tau)

    IF arct>=arctmin THEN
        extinguish:=true
    ENDIF

ELSIF state=3 THEN

```

RA1:=0

swopening:=true

ENDIF

-- DS conditions

IF noarcopening THEN

state:=1

ENDIF

IF arcing THEN

arct:=0

startarct:=0

state:=2

ENDIF

IF extinguish OR swopening THEN

state:=0

ENDIF

ENDIF

--closing operation

--closing

-- gap distance

IF Sop=1 AND t>Top THEN


```

dcl:= dst-(spd*(t-Top))

IF  dcl<0 THEN
    dcl:=0
ENDIF

IF dcl=0 THEN
    state:=3
ENDIF

ELSE
    dcl:=gap
ENDIF

Vbc:=(Emax*p*eta*dcl)*1000 -- breakdown voltage closing
vbcn:=-vbc
VbcnC:=(Emax*p*eta*gap)*1000

IF  t>Top AND Sop=1 THEN
    arcing:=false
    noarcclosing:=false
    extinguish:=false
    --
    IF  state=0 THEN --if switch open
        RA1:=RE
        noarcclosing:=true
    ENDIF
    ELSIF state=1 THEN
        --

```

```
IF Vbc<abs(v1-v2) THEN
```

```
narc1:=narc1+1
```

```
arcing:=true
```

```
--CAP:=0
```

```
ENDIF
```

```
--
```

```
ELSIF state=2 THEN
```

```
arct:=arct+timestep
```

```
startarct:=backtime(arct, 0) -- time at start of arcing period
```

```
RA1:= 0.5+RE*exp(-(t-startarct)/tau)
```

```
--
```

```
IF arct>=arctmin THEN
```

```
extinguish:=true
```

```
--CAP:=1
```

```
ENDIF
```

```
--
```

```
ELSIF state=3 THEN
```

```
RA1:=0
```

```
ENDIF
```

```
--
```

```
-- DS conditions
```

```
IF noarcclosing THEN
```

```
state:=1
```

ELSIF arcing THEN

arct:=0 --reset arc time on first loop

startarct:=0

state:=2

ELSIF extinguish THEN

state:=0

ENDIF

ENDIF

ENDEXEC

ENDMODEL

E - GIS FINITE ELEMENT MODEL CONVERSION TO BLACKBOX MACROMODELS

The technique developed is implemented in MATLAB with the VF toolbox created by Gustavsen et al. [114]. The vector fitting method requires specification of an initial pole type. For the admittance matrices fitted, linearly spaced, complex poles were selected.

The next step is pole relocation through multiple iterations to achieve a better fit of the dominant poles of the response. Unstable poles are flipped to left half of the complex plane, guaranteeing stable poles. After the poles are obtained, the residues of Equation (5.9) are computed as a linear least-squares problem. While stable poles should revoke a good frequency response, an unstable time domain response is possible due to passivity violations. A truly passive system is one in which no energy is produced. A non-passive response can be generated due to small numerical errors, which is a known risk associated with the outputs from field solvers [115].

Passivity can be assessed using a Hamiltonian matrix [116], whereby the identification of purely imaginary eigenvalues constitutes a non-passive model. The size of Hamiltonian matrix can be significant can result in long computation times. For passivity assessment of admittance parameter representations, the VF toolbox builds a half size singularity test matrix, identifies non-passivity frequency bands by identifying singularities in the conductance matrix [117]. Fast residue perturbation [118] then perturbs elements of the residue and constant matrices until eigenvalues are positive, while minimising the change to the elements of the admittance matrix, thereby enforcing passivity. A further condition for stability of time domain responses is causality. A non-causal system is one in which a response precedes an input. Causality is a requirement for passivity and passivity enforcement through perturbation of eigenvalues should also ensure a causal model [119]. As a general note, when fitting some models generated for this thesis, it was observed that a considerable number of poles were identified in the lower frequencies of the computed spectrum, and for the first fit a somewhat noisy response. This was likely attributed to numerical errors as full-wave solutions are known to break down at lower frequencies [120]. Further to this, it was observed experimentally that model stability and transient response accuracy was improved by carrying out the initial fit and passivity enforcement directly on the S-

parameters representation prior to conversion to an admittance representation. This two-step fitting process had a minor impact on the frequency domain response.

An overview of the process to produce and verify blackbox models for ATP from high frequency finite element models is provided in Figure E.1

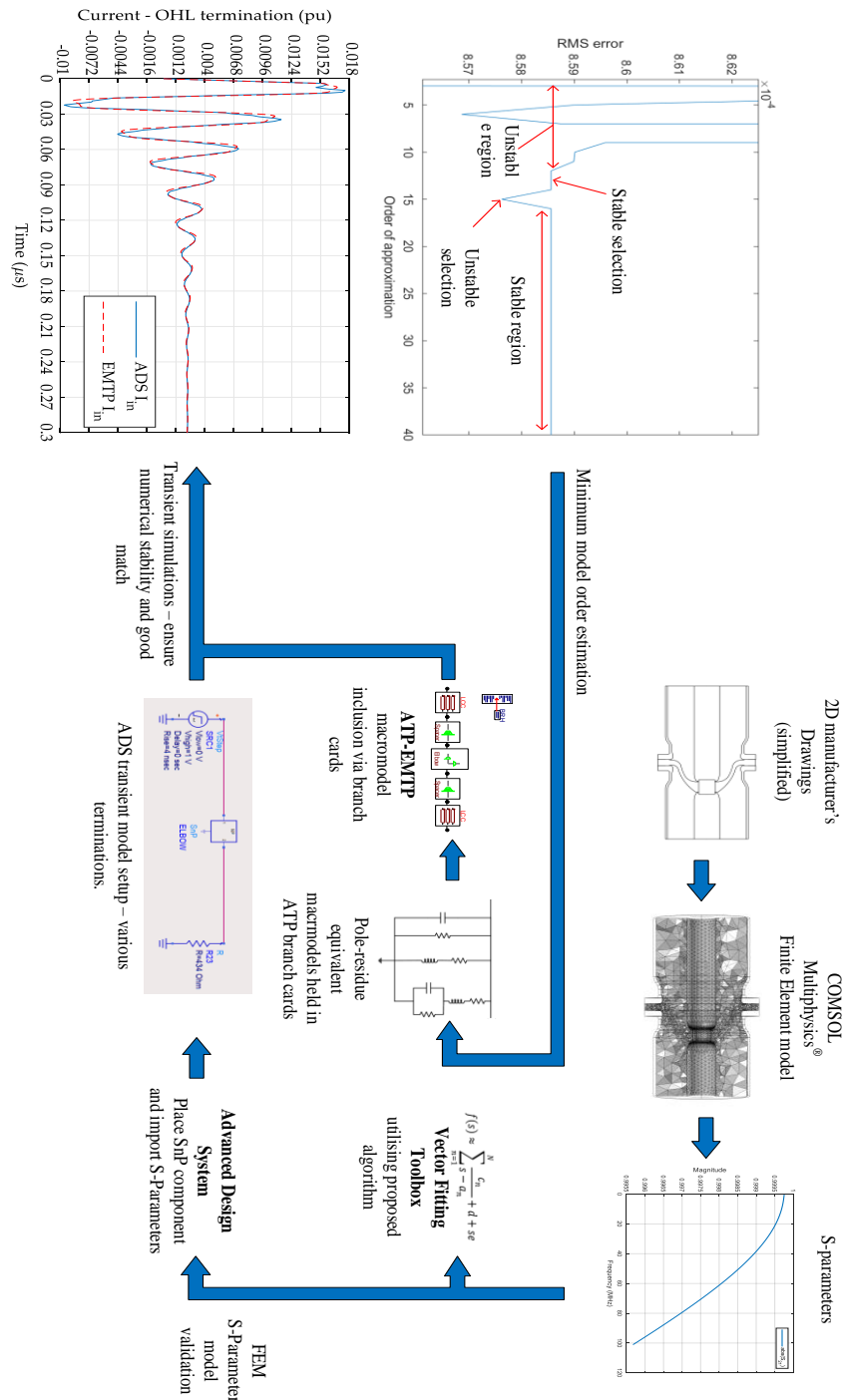


Figure E.1: GIS Blackbox Macromodel workflow for the study of VFTs in ATP-EMTP.

F - DATA ACQUISITION AND CALIBRATION TECHNIQUES

A good data acquisition system is essential for accurate measurements. The complete data acquisition system includes the sensor, cables, a recording device (oscilloscope), power supplies and shielding. As there are numerous considerations when choosing and oscilloscope for measurement of high frequency transients, the main considerations are given in Table F.1

Table F.1: Oscilloscope considerations.

<p>Sample rate</p>	<p>Nyquist criterion suggests that a system with a sample rate relating to twice the bandwidth of the signal to be measured should suffice. However, in reality, a sample rate at least five times the bandwidth is required. Therefore, a minimum 500MS/s will produce reasonable results.</p>
<p>Vertical resolution</p>	<p>As VFTs are oscillatory with numerous frequency components, the range of voltage magnitudes measured in a single capture could vary significantly. It is therefore essential to use a scope with a high vertical resolution, i.e. a minimum of 12 bit. Unfortunately, there is often a compromise between vertical resolution and sample rate.</p>
<p>Buffer</p>	<p>VFTs require a high sample rate and have a relatively long duration. To capture an entire disconnector operation, a very large buffer is required. As an alternative a high-speed digitiser system could avoid the limited memory issues of standalone oscilloscopes, by streaming data via high speed PCI links directly to a computer's RAM.</p>
<p>Channels</p>	<p>The larger the number of channels the greater number of simultaneous measurements that can be carried out. It is a great advantage for measurement of propagating waveforms when sensors placed at different locations are used to monitor the propagation. Measurements are easily synchronised. When synchronising triggers at the VFT timeframe with different</p>

	recording devices, it can be difficult to achieved an accurate synchronised trigger.
Trigger modes	The ability to trigger at different thresholds on different points of a waveform is an advantage. A very useful triggering function for multiple transient events over a long time is triggering in sequence mode. Sequence mode minimises the dead time between events by triggering, recording for a fixed interval and the rearming the trigger, awaiting the next transient event.

TEVs propagate along the outer surface of the enclosure, posing a risk to any devices that are connected via cables with screens bonded to the enclosure. As most of the measurement techniques planned are based on differential measurement, this connection can be avoided, with the exception of the UHF coupler, where the body of the N type connector is most likely bonded to the enclosure. As an extra precaution all cables should be fitted with ferrite cores clamped around the outer insulation. The oscilloscope and floating supply will be housed inside a grounded metallic case and maintain no direct contact with the case.

Correct calibration of measurement systems is vital for the accurate capture of waveform shapes and amplitude, both attributes are extremely important for the thorough evaluation of VFTs/TEVs. In addition to correct calibration of a measurement system, the measurement uncertainty introduced by the physical presence of the sensor and cabling needs to be accounted for [70].

G - FURTHER MEASUREMENT RESULTS

HFCT measurements 30/09/20

30th September 2020 HFCT measured values – amplitude and frequency content.

Switching scenario	C1		C2		C3	
	Max Amplitude (A)	Frequencies (MHz)	Max Amplitude (A)	Frequencies (MHz)	Max Amplitude (A)	Frequencies (MHz)
DS1 open*	73.6	10.7, 8.7, 13.7	64.7	17.4, 11.5, 8.7	63.5	5.0, 3.3, 17.5
DS2 open	5.2	13.3, 10.4, 7.4	7.4	25.3, 12.9, 5.1	3.7	4.9, 12.9, 25.3
Trapped charge dissipate CB1	51	13.4, 10.5, 17.1	10.2	12.4, 14.1, 5.3	28.6	12.5, 5.1, 17.4
<p>Note</p> <p>* waveform clipped due to scope range and scale (40V peak). Clipped signals have been corrected with and 4th order polynomial fit.</p>						

30th September 2020 HFCT measured values – number of transients and duration.

Switching operation	Max No of transients	Total duration (ms)	Surge counter incrementation					
			R _{pre}	R _{post}	Y _{pre}	Y _{post}	R _{pre}	B _{post}
DS1 open	191	122	41	41	235	235	142	142
DS2 open	95	159	41	41	235	235	142	142
Trapped charge dissipate CB1	8	1.2	41	41	235	235	142	142

HFCT measurements 02/07/19

2nd July 2019 HFCT measured values – amplitude and frequency content.

Switching Scenario	C1		C2		C3	
	Max Amplitude (A)	Frequencies (MHz)	Max Amplitude (A)	Frequencies (MHz)	Max Amplitude (A)	Frequencies (MHz)
DS1 close	9.0	10.5, 12.4, 8.7	8.0	12.1, 16.8, 14.8	5.6	5.2, 10.7, 15.2
DS2 close	23.8	13.5, 10.3, 18.1	45.9	13.2, 10.4, 16.2	22.3	5.0, 13.0, 10.4
CB1 close	21.6	12.4, 14.0, 17.3,	58.6	12.4, 14.2, 17.1	13.4	12.4, 14.1, 9.4
Note * waveform clipped due to scope range and scale (40V peak). Clipped signals have been corrected with and 4 th order polynomial fit.						

2nd July 2019 HFCT measured values – number of transients and duration.

Switching operation	Max No of transients	Total duration (ms)	Surge counter incrementation					
			R _{pre}	R _{post}	Y _{pre}	Y _{post}	B _{pre}	B _{post}
DS1 close	5	21	39	39	227	227	138	138
DS2 close	119	106	39	39	227	227	138	138
CB1 close	5	0.4	39	41	227	232	138	140

HFCT measurements 10/03/19

10th March 2019 HFCT measured values – amplitude and frequency content.

	C1		C2		C3	
	Max Amplitude (A)	Frequencies (MHz)	Max Amplitude (A)	Frequencies (MHz)	Max Amplitude (A)	Frequencies (MHz)
DS2 close	No capture	No capture	No capture	No capture	No capture	No capture
DS1 close*	No capture	No capture	72.0	11.6, 9.2, 14.6	No capture	No capture
CB1 close*	No capture	No capture	318.6	12.2, 14.0, 16.2	No capture	No capture
Note * waveform clipped due to scope range and scale (40V peak). Clipped signals have been corrected with and 4 th order polynomial fit.						

10th March 2019 HFCT measured values – number of transients and duration.

Switching operation	Max No of transients	Total duration (ms)	Surge counter incrementation					
			R _{pre}	R _{post}	Y _{pre}	Y _{post}	R _{pre}	B _{post}
DS2 close	No capture	No capture	39	39	227	227	138	138
DS1 close	175	151	39	39	227	227	138	138
CB1 close	5	1.2	39	39	227	227	138	138